A Three-Dimensional Damage Percolation Model

by

Oleg S. Orlov

A thesis

presented to the University of Waterloo

in fulfilment of the

thesis requirement for the degree of

Doctor of Philosophy

in

Mechanical Engineering

Waterloo, Ontario, Canada, 2006

I hereby declare that I am the sole author of this thesis. This is a true copy of the thesis, including any required final revisions, as accepted by my examiners.

I understand that my thesis will be made electronically available to the public.

Abstract

A combined experimental and analytical approach is used to study damage initiation and evolution in three-dimensional second phase particle fields. A three-dimensional formulation of a damage percolation model is developed to predict damage nucleation and propagation through random-clustered second phase particle fields. The proposed approach is capable of capturing the three-dimensional character of damage phenomena and the three stages of ductile fracture, namely void nucleation, growth, and coalescence, at the level of discrete particles.

The experimental work focuses on the acquisition of second phase particle field data and measurement of damage development during plastic deformation. Two methods of acquisition of three-dimensional second phase particle fields are considered. The first method utilizes three-dimensional X-ray tomography for the acquisition of real microstructural data. The second method involves statistical stereological reconstruction of second phase particle fields from two orthogonal metallographic sections of the as-received material. The reconstruction method is also used to introduce parametric

variation of key microstructural parameters to support a study of the effect of particle clustering and second phase constituent content on formability.

An *in situ* tensile test with X-ray tomography is utilized to quantify material damage during deformation in terms of the number of nucleated voids and porosity. The results of this experiment are used for both the development of a clustering-sensitive nucleation criterion and the validation of the damage percolation predictions.

The three-dimensional damage percolation model is developed based on the acquired second phase particle fields and the damage evolution characterization using the results of the *in situ* tensile test. Void nucleation, growth, and coalescence are modelled within the considered second phase particle field. The damage percolation model is coupled with a commercial finite element code, LS-DYNA.

The damage percolation model is applied to simulate the *in situ* tensile test as well as to study bendability. In particular, the effect of second phase particle field parameters on formability is examined. The volume fraction of *Fe*-rich and Mg_2Si particles is shown to be of critical importance in controlling the formability of aluminum alloy AA5182.

This study of microstructural heterogeneity using the damage percolation model has resulted in a more fundamental understanding of the processes of material degradation during deformation in the presence of second phase particles. The results of the study indicate a significant effect of second phase content on formability and provide practical recommendations to improve material formability in future alloy designs.

Acknowledgements

I would like to thank my supervisor Michael Worswick for his guidance and support through the course of my graduate studies.

I also would like to thank Dr. Eric Maire and Dr. Jerome Adrien from INSA de Lyon, France, for their help with X-ray tomography and *in situ* testing.

I appreciate the useful conversations I had with members of the Worswick group that contributed to the research.

I am grateful for financial support provided by Novelis Inc. through the Kingston Research and Development Centre (KRDC), the Natural Science and Engineering Research Council (NSERC), the Ontario Research and Development Challenge Fund, and the University of Waterloo, Department of Mechanical Engineering.

Contents

List of Tables

List of Figures

Chapter 1

Introduction

The need to reduce emissions and fuel consumption is the main driving force for lower vehicle weight in future generation automobile designs. One approach is to replace mild steel with aluminum alloys, which has promoted considerable interest in the application of aluminum in the automotive industry. However, the mechanisms and evolution of damage in aluminum alloys, as well as the effect of damage on formability, are not yet fully understood. Intermetallic second phase particles present in the material and their spatial distribution (clustering) play a crucial role in damage initiation and evolution. Therefore, the objectives of the proposed research are: (i) to develop a model, known as the 3D damage percolation model; and (ii) to perform supporting experiments that capture the effects of void/particle size and clustering on the damage within and formability of commercial 5xxx-series aluminum alloy sheet.

The traditional method to assess the limits of formability in sheet metal forming is the forming limit diagram (FLD) approach (Keeler and Backofen, 1963; Goodwin, 1968) (Figure 1.1a); however, this approach suffers one major drawback in that it does not take into account the effect of strain path. Although FLDs are normally strain-based, so-called stress-based FLDs can be used to account for strain path effects on formability (Stoughton, 2001) (Figure 1.1b).

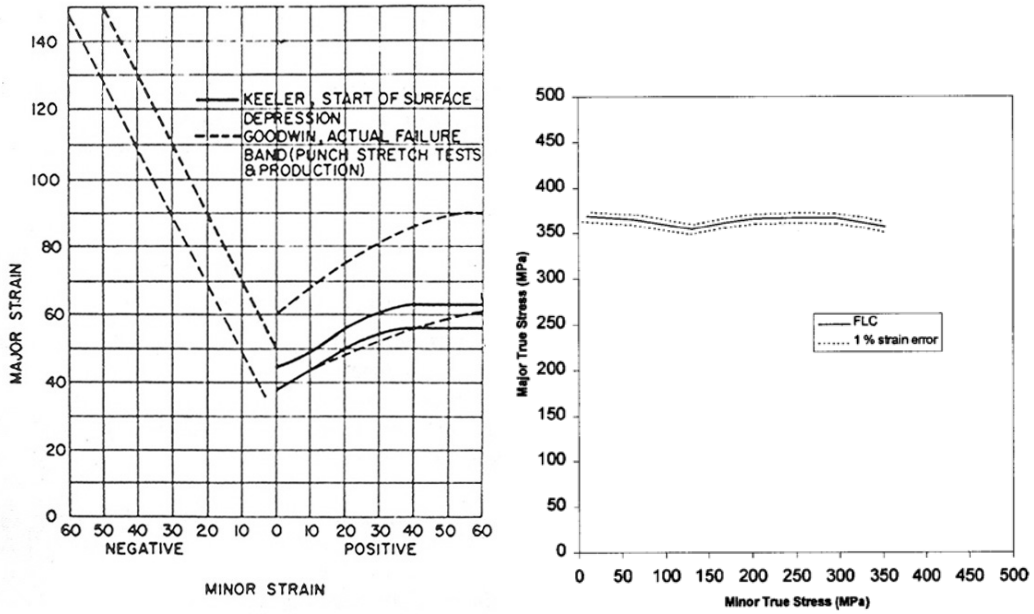

(a) (b)

Figure 1.1: Strain- (a) and stress- (b) based forming limit diagrams (Goodwin, 1968; Stoughton, 2001).

Not all sheet metal forming processes can be studied using the FLD approach, particularly those that introduce complicated strain paths due to multiple bending and unbending during forming (Worswick and Finn, 2000; Cinotti *et al.*, 2000). Moreover, the FLD approach involves applying a grid on the specimen surface, which is not practical for material that experiences high contact forces. Consequently, what is needed

is a method that is capable of taking into consideration complicated strain paths, through-thickness strain gradients, and microstructural degradation. Various material models are currently available. Some of these account for damage effects by considering void nucleation, growth, and coalescence at the continuum level (Gurson, 1975, 1977a,b,c; Tvergaard, 1981), but fail to account for material microstructural spatial heterogeneity.

Sheet material experiences extensive plastic deformation during commercial metal forming operations. Multiple bending and unbending of the material can occur at die features such as draw-beads that introduce a certain amount of damage and, in conjunction with the strains associated with stretching and drawing, may lead to rupture. It is essential to understand the mechanisms of material degradation and failure during such forming operations.

There are three main failure modes occurring during plastic deformation (Teirlinck *et al.*, 1988), namely, plastic collapse, shear fracture, and ductile fracture (Figure 1.2). The first mode is mostly observed in pure metals, whereas the second and third are typical for commercial purity metals and alloys containing inclusions such as second phase particles. This review is concerned with the latter types of failure since the formability of commercial aluminum alloys containing *Fe*- and *Mn*-rich second phase particles is studied here.

The process of material degradation inherent in the alloys of interest encompasses three major phenomena: void nucleation, growth, and coalescence. These processes generally occur simultaneously; as some voids are nucleating, others might be already growing and coalescing. The contributions of these processes to the onset of final failure can be different in various materials. In some alloys, nucleation is the mechanism controlling the onset of failure, whereas in others void growth and coalescence play a more important role.

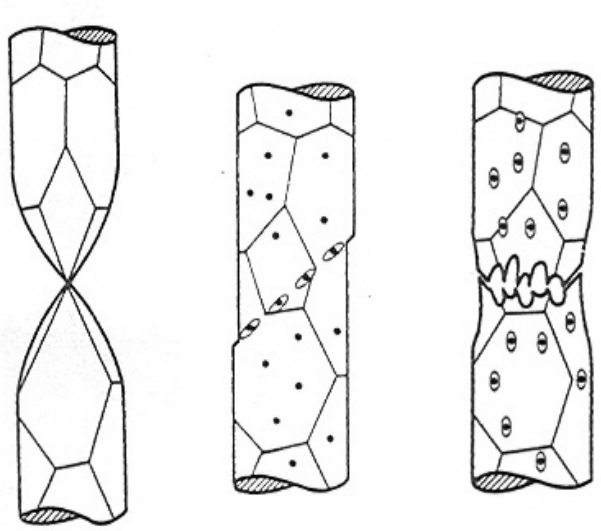

Figure 1.2 : Plastic collapse, shear fracture, and ductile fracture (Teirlinck *et al.*, 1988).

Material heterogeneity (second phase particle clustering) significantly affects the aforementioned phenomena of material degradation. More clustered particle fields tend to accumulate damage more easily; therefore, it is essential to account for the effects of particle clustering on void nucleation, growth, and coalescence when modelling ductile damage.

The following review of the literature pertinent to the current research first addresses the three primary stages of ductile damage, namely void nucleation, growth, and coalescence. This is followed by a discussion of so-called pressure sensitive or dilatant yield criteria (Section 1.4). The effect of microstructural heterogeneity on each aspect of ductile damage is then considered, followed by a summary of recent work on the damage percolation model.

1.1 Void Nucleation

Voids nucleate in systems containing second-phase particles by decohesion or particle cracking (Figure 1.3). This phenomenon has been observed and studied by numerous researchers (Puttick, 1959; Rogers, 1960; Cox and Low, 1974; Tanaka *et al.*, 1970; Van Stone *et al.*, 1985; Gurland and Plateau, 1963). There are a number of factors that can affect void nucleation (Goods and Brown, 1979) such as particle shape, size, orientation, stress state, particle strength, and particle-matrix interface strength.

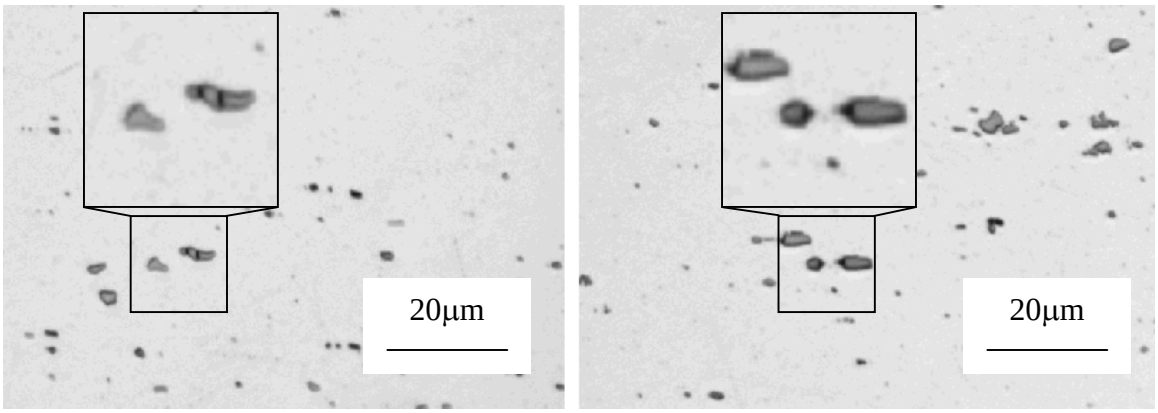

(a) (b)

Figure 1.3 : Void nucleation by particle cracking (a) and decohesion (b) in aluminum alloy AA5182.

There exist a number of theoretical descriptions of the cavity nucleation mechanism. There are two main approaches: the first is based on dislocation theory, used for particle-dislocation interactions and is applicable to small particles of 1 μm in diameter or less; the second approach employs continuum theory to describe the particle-matrix interaction and is used for particles larger than 1 μm.

Various researchers have proposed nucleation criteria that can be divided into three main categories: energy-based (Gurland and Plateau, 1963); stress-based (Thomson and Hancock, 1984); and strain-based (Goods and Brown, 1979) criteria. The energy criteria assume that an inclusion requires a certain amount of elastic energy to break the bond between the particle and matrix. These criteria have been proven to be sufficiently accurate to predict nucleation at smaller particles. For larger particles, this condition is a necessary, but not a sufficient criterion to fully describe void nucleation. The stress and strain criteria consider stress or strain as the governing parameter in void nucleation. According to these criteria, voids start to nucleate if the stress or strain in the material reaches a critical value. A better approach is to combine energy criteria and with a stress criterion (Fisher and Gurland, 1981a,b; Argon *et al.*, 1975; LeRoy *et al.*, 1981; Petch, 1961) or strain criterion (Tanaka *et al.*, 1970). In these cases, the energy criterion predicts void nucleation at smaller particles, and the stress or strain criterion is responsible for larger particles. Several analytical void nucleation models proposed over the last few decades are reviewed below.

Gurland and Plateau (1963) proposed one of the first nucleation models. They assumed that a particle fractures when the strain energy (U) stored in the inclusion exceeds the surface energy (S) of the newly formed crack surfaces, or

$$U \geq S \tag{1.1}$$

An approximate expression for the critical stress is

$$\sigma = \frac{1}{q}\left(\frac{E\gamma}{a}\right)^{1/2} \tag{1.2}$$

where σ is the applied uniaxial stress, q is the average stress concentration factor at the inclusion, γ is the specific surface energy of the crack, E is the weighted average of the elastic moduli of the inclusion and matrix, and a is the dimension of the inclusion.

Petch (1961) suggested a similar expression

$$(q\sigma - \sigma_0)^2 = \frac{E\gamma}{a} \tag{1.3}$$

where σ_0 is the friction stress of an unlocked dislocation.

Tanaka *et al*. (1970) proposed a cavity nucleation theory for a spherical inclusion in a plastically deforming matrix under uniaxial tension and showed that the energy approach of Gurland and Plateau (1963) is a necessary condition. The following expressions for the critical plastic strain were proposed:

$$\varepsilon_{crit} \geq \left(\frac{(7-5\nu)(1+\nu^*) + (8-10\nu)(1+\nu)\alpha}{10(7-5\nu)} \right)^{1/2} \text{- soft inclusion } (\alpha < 1) \tag{1.4}$$

$$\varepsilon_{crit} \geq \left(\frac{(7-5\nu)(1+\nu^*) + (8-10\nu)(1+\nu)\alpha}{10(7-5\nu)\alpha} \right)^{1/2} \text{- hard inclusion } (\alpha \geq 1) \tag{1.5}$$

where α is the ratio of Young's modulus of the inclusion to that of the matrix, ν and ν^* are the Poisson's ratios for the matrix and inclusion respectively.

Argon and Im (1975) also demonstrated that the above approach is valid and that the energy criterion is only a necessary condition.

Fisher and Gurland (1981) developed a model that is based on a combined critical normal stress requirement and an elastic energy requirement:

$$\sigma_n > \sigma_c \tag{1.6}$$

$$\Delta E > \Delta W \tag{1.7}$$

where σ_n is the normal stress at the particle-matrix interface, σ_c is the critical bonding stress of the interface, ΔE is the total energy released by formation of a crack, and ΔW is the energy associated with the particle-surface interface.

Argon *et al*. (1975) proposed a nucleation model based on a continuum analysis of deforming equiaxed particles. According to this model, nucleation occurs when the interfacial normal surface tractions (σ_{rr}) exceed the interfacial strength (σ_I) after the application of a critical plastic strain:

$$\gamma_c = \frac{\gamma_y m}{6^{3/2}}\left(\frac{\sigma_I}{K_0} - 1\right)^2 \tag{1.8}$$

where γ_y is the yield strain multiplied by $\sqrt{3}$, m is the Taylor factor, and K_0 is the yield stress in shear of the polycrystal.

Goods and Brown (1979) modified the earlier model of Brown and Stobbs (1976) and developed a formula for the critical strain for void nucleation at particles smaller than 1μm:

$$\varepsilon_{crit} = 1.7\frac{r}{b}\left(\frac{\sigma_I - \sigma_H - \sigma_0}{\mu}\right)^2\left(1 + 3f_v + \frac{f_v^{1/2}}{1.8}\right)^{-2} \tag{1.9}$$

where r is the particle radius, b is the Burger's vector, σ_I is the interfacial strength, σ_H is the hydrostatic tension, and f_v is the volume fraction of particles.

LeRoy *et al*. (1981) considered the condition that the critical normal stress value must be exceeded at the particle-matrix interface for void nucleation to occur:

$$\sigma_{loc} + \sigma_m = \sigma_c \tag{1.10}$$

where σ_{loc} is determined based on the local dislocation density, σ_m is the hydrostatic stress, σ_c is the critical normal stress.

Their model yielded the following formula for the nucleation strain

$$\varepsilon_c^{1/2} = \frac{1}{H_2}(\sigma_c - \sigma_m) \tag{1.11}$$

where H_2 is a constant.

The various void nucleation models occasionally contradict one another and give conflicting nucleation predictions. This is likely to be due to the fact that each model was developed for different alloy systems. However, there are several common conclusions that many authors have reached independently. Most agree that larger particles nucleate voids sooner than smaller ones (Cox and Low, 1974; Tanaka *et al.*, 1970; Van Stone *et al.*, 1985; Gurland, 1972). Larger particles contain more surface defects, having larger particle-matrix interfaces. Another common conclusion is that equiaxed inclusions are prone to particle-matrix decohesion, whereas nonequiaxed inclusions, especially those with high aspect ratios, tend to experience multiple fractures (Cox and Low, 1974; Goods and Brown, 1979; Agron *et al.*, 1975; Gurland, 1972; McMahon and Cohen, 1965).

Several researchers investigated the role of stress state on void nucleation (Cox and Low, 1974; Argon *et al*., 1975; Argon and Im, 1975; Argon, 1976). Work by

Hancock and Mackenzie (1976) suggests that the nucleation process is dependent on the stress state, while others suggest otherwise (Cox and Low, 1974).

1. 2 Void Growth

Void growth is the enlargement of cavities that are initially present or have nucleated from second-phase particles during material deformation (Puttick, 1959; Rogers, 1960; Cox and Low, 1974; Gurland and Plateau, 1963). Van Stone *et al*. (1985) suggested two distinct mechanisms for stable void growth. The first is solely controlled by plastic flow of the metal matrix (Floreen and Hayden, 1970), while the second is a combination of matrix plastic flow and particle-matrix decohesion (Rogers, 1960; Cox and Low, 1974). Void growth via the first mechanism tends to preserve spherical and ellipsoidal void shapes, whereas the second tends to results in irregular void shapes.

The effects of initial void size and stress state on the void-growth rate have received much attention from various researchers. Most of the models indicate that void growth rate increases with void size and is a strong function of stress triaxiality.

There have been numerous void growth models proposed. Gurland and Plateau (1963) suggested one of the first empirical relationships for void growth. They assume that the smallest curvature radius of an ellipsoidal void controls its growth. Their empirical formulae for void size in the directions parallel (*a*) and perpendicular (*b*) to major applied stress are

$$a = ka_i\left[e^{2(\varepsilon-\varepsilon_0)} - 1\right]^{1/2} \qquad b = a_i \tag{1.12}$$

where k is a constant, a_i is the initial void size, ε is the true strain, and ε_0 is the true strain at which voids first form.

There are also some dislocation models that assume that the void volume increases proportionally to the macroscopic strain (Broek, 1973; Brown and Embury, 1973; Ashby, 1966).

Continuum plasticity models of void growth include those by McClintock (1968), Rice and Tracey (1969), and Thomason (1993). McClintock (1968) investigated the growth of a cylindrical void in a rigid-plastic material under generalized plane strain. He gave the following formula:

$$\ln\frac{R}{R_0}=\frac{\sqrt{3}}{2(1-n)}\varepsilon\sinh\left(\frac{\sqrt{3}(\sigma_a+\sigma_b)(1-n)}{2\sigma}\right)+\frac{\varepsilon_a+\varepsilon_b}{2} \tag{1.14}$$

$$R=\frac{a+b}{2} \tag{1.15}$$

where R is the average void size, R_0 is the initial void size, a and b are the void sizes in the direction parallel and perpendicular to major applied strain, ε is the true strain, σ is the true flow stress corresponding to ε, σ_a and σ_b are the true stresses along the a and b axes, and ε_a and ε_b are the true strains along the a and b axes.

The studies by Brownrigg (1983), Sowerby (1986), Thomson and Hancock (1984), and Melander (1980) have provided experimental validation for McClintock's model. At the same time, Garrison and Moody (1987) noted that this model underestimates the extent of void growth, but confirmed the importance of stress triaxiality.

Rice and Tracey (1969) considered the growth and shape change of a spherical void in a rigid-plastic material subjected to a uniform remote strain rate field. The growth rate of a void in the x_1 and x_3 direction is defined as

$$\dot{R}_1 = \left(D - \frac{1+E}{2} \right) \dot{\varepsilon} R_0 \tag{1.16}$$

$$\dot{R}_3 = \left(D + 1 + E \right) \dot{\varepsilon} R_0 \tag{1.17}$$

$$D = 0.588 \sinh\left(\frac{\sqrt{3}\sigma^{\infty}}{2\tau_0} \right) + 0.008\nu \cosh\left(\frac{\sqrt{3}\sigma^{\infty}}{2\tau_0} \right), \tag{1.18}$$

$$\nu = \frac{-3\dot{\varepsilon}_{II}^{\infty}}{\dot{\varepsilon}_{I}^{\infty} - \dot{\varepsilon}_{III}^{\infty}} \tag{1.19}$$

where R_0 is the void initial size, $\dot{\varepsilon}$ is the strain rate in the x_3 direction, σ^{∞} is the remote mean normal stress, τ_0 is the yield shear stress, ν is the Lode variable, and $\dot{\varepsilon}_{I}^{\infty}$, $\dot{\varepsilon}_{II}^{\infty}$, $\dot{\varepsilon}_{III}^{\infty}$ are the principal components of the remote strain rate field. It can be seen that stress state (stress triaxiality), represented by D, affects the growth of voids.

LeRoy *et al*. (1981) modified the model of Rice and Tracey (1969) to account for deformation history and calculated the amplification factor, 1+*E*, for the case of uniaxial tension:

$$1 + E = \frac{2e^{\frac{3}{2}\varepsilon}}{2e^{\frac{3}{2}\varepsilon} - 1} \tag{1.20}$$

Thomason (1993) utilized the model of Rice and Tracey (1969) and suggested a model for the case of perfectly plastic non-hardening material with initially spherical voids:

$$\frac{V_c}{V_0} = 1 + V_f \left[\left(\frac{abc}{a_0 b_0 c_0} \right) - 1 \right] \tag{1.21}$$

where V_c is the current volume of the cell, V_0 is the initial volume, V_f is the initial volume fraction of microvoids, a, b, c and a_0, b_0, c_0 are the current and initial geometries (semi-axes) of the void.

Budiansky *et al*. (1982) generalized the studies of McClintock (1968) and Rice and Tracey (1969) and considered an isolated void in an infinite block of viscous material subjected to remote axisymmetric stress. A power-law viscous material model was utilized.

Fleck and Hutchinson (1986) developed a void growth model for conditions similar to those in shear bands. They considered an isolated void in a block of material undergoing shearing and hydrostatic tension. The void growth relationships for spherical voids are:

$$\frac{\dot{V}}{\dot{\gamma} V} = \left\{ \frac{1}{n} \left| \frac{\sigma_m}{\tau} \right| + \frac{(n-1)(n+0.6137)}{n} \right\}^n \operatorname{sgn}\left(\frac{\sigma_m}{\tau} \right) \tag{1.22}$$

$$\text{high triaxiality } \left| \frac{\sigma_m}{\tau} \right| > 1$$

$$\frac{\dot{V}}{\dot{\gamma} V} = k(n) \frac{\sigma_m}{\tau} \approx \sqrt{n} \frac{\sigma_m}{\tau} \tag{1.23}$$

$$\text{low triaxiality } \left| \frac{\sigma_m}{\tau} \right| \leq 1$$

where V is the void volume, $\dot{V}$ is the volume change rate, $\dot{\gamma}$ is the remote shear strain rate, σ_m is the mean stress, n is the hardening exponent, $k(n)$ is a known function, and τ is the shear stress.

1. 3 Void Coalescence

Void coalescence is the final stage of failure of ductile materials and it occurs after void nucleation and growth. During this process, the ligaments between neighbouring voids experience localization of plastic deformation (Figure 1.4). Pardoen and Hutchinson (2000) distinguished two coalescence mechanisms: tensile (normal separation) and shear localization. The former mechanism deals with the uniaxial straining mode, whereas the shear mode is favoured by low stress triaxiality, low strain biaxiality, and low strain and strain rate hardening.

Van Stone *et al*. (1985) and Rosenfield (1968) pointed out that void coalescence is the most difficult stage to investigate experimentally since it occurs rapidly and catastrophically. When voids begin to link, they quickly turn into a crack (Figure 1.5). It is noted that before the experimental investigations of the 70s, there were several concepts of possible void coalescence mechanisms: necking down of the matrix between voids; formation of a series of secondary voids in the region of localized shear between large voids; formation and propagation of fine cracks between voids; and rupture when voids reach some critical size relative to inter-void spacing. Experimental investigation by Beachem (1963) has suggested that there are three modes of void coalescence: normal rupture, shear rupture, and tearing.

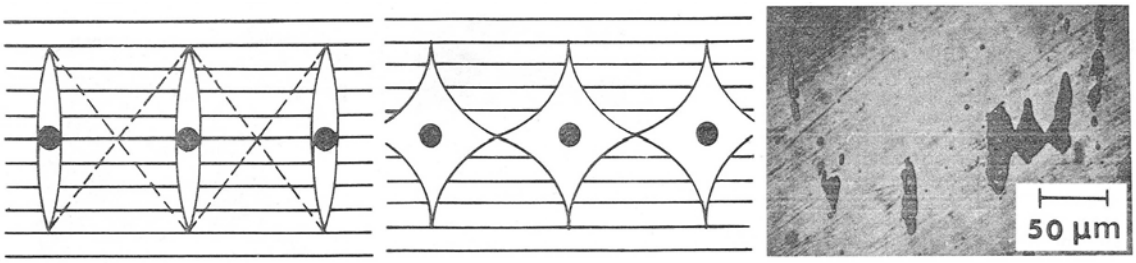

(a) (b) (c)

Figure 1.4: Void coalescence (Goods and Brown, 1979): (a) – condition for the onset of local necking (Brown and Embury, 1973), (b) – cross section after local necking (Brown and Embury, 1973), (c) – microscopic evidence (Puttick, 1959).

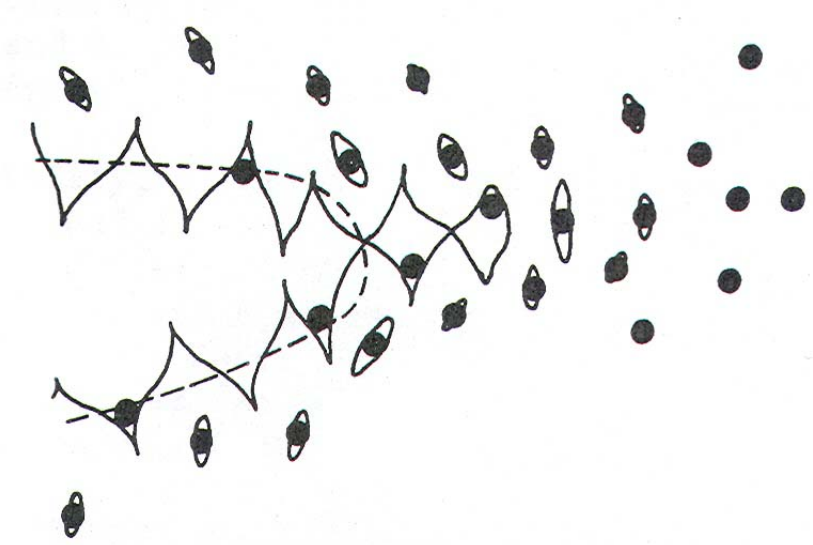

Figure 1.5: Ductile crack propagation due to void coalescence (Brown and Embury, 1973).

According to various researchers, void coalescence is sensitive to such parameters as stress triaxiality (Bandstra *et al.*, 1998; Bandstra and Koss, 2001; Hancock and Thomson, 1985; Thomson and Hancock, 1984; Ragab, 2000; Yamamoto, 1978; Benzerga, 2002), material hardening (Hancock and Thomson, 1985; Thomson and Hancock, 1984; Ragab, 2000; Bourcier *et al.*, 1984; Bandstra and Koss, 2004), and void

distribution (Bandstra *et al.*, 1998; Hancock and Thomson, 1985; Thomson and Hancock, 1984; Yamamoto, 1978; Bourcier *et al.*, 1984; Hancock and Mackenzie, 1976; Thomason, 1990; Dubensky and Koss, 1987; Magnusen *et al.*, 1988).

The influence of hardening on failure mode has a significant effect. It was found (Bourcier *et al.*, 1984; Ragab, 2000) that shear localization takes place in low-hardening materials; whereas, tensile rupture is more likely to occur in materials with strong strain hardening. Hancock and Thomson (1985) view the process of ductile failure as a competition between the destabilizing influence of void growth and the effect of strain hardening in inhibiting strain localization. Bandstra and Koss (2004) in their study of void growth and coalescence within tensile bars containing blind-end holes (Figure 1.6) pointed out that the limit load within the inter-void ligaments is reached at strains close to the strain hardening exponent. They conclude that a void coalescence criterion should strongly depend on strain hardening.

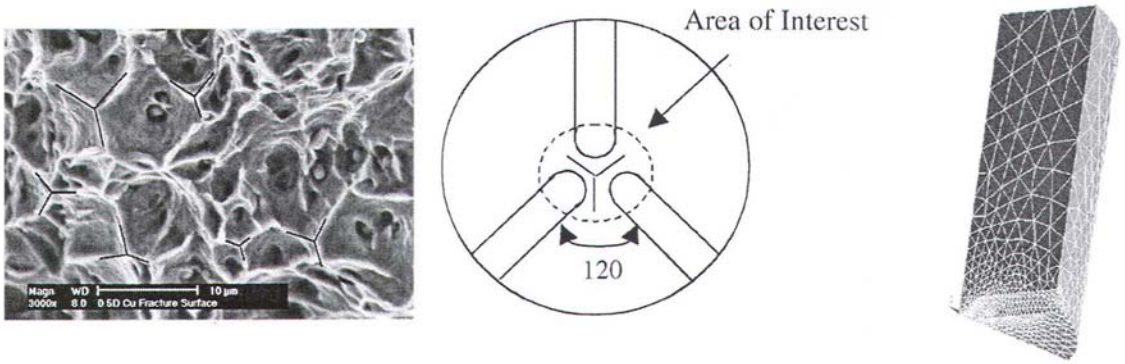

(a) (b) (c)

Figure 1.6: Ductile fracture surface formed by clusters of three voids (a), cross section of the studied specimen with three holes (b), and finite element model of a tensile bar containing holes (c) (Bandstra and Koss, 2004).

Tvergaard (1981, 1982) noted that increases in material porosity affect plastic flow stability and can lead to the onset of shear band bifurcation. The effect of void distribution on void coalescence and damage localization has been controversial for a long time (Yamamoto, 1978; Rice, 1976). One hypothesis states that deformation localization occurs due to material softening from void growth (Rudnicki and Rice, 1975); another assumes that instability within the plastic flow field occurs first. Bandstra and Koss (2001) employed a different approach; they concluded that softening due to a secondary population of voids can help to promote strain localization between two primary voids, but does not directly cause the localization. Growing primary voids are responsible for strain localization that accelerates damage processes within a localized band.

Shear banding between two neighbouring voids has been studied extensively. Tvergaard (1990) considered its onset as a loss of ellipticity of the equation governing incremental equilibrium (Hill, 1962; Rice, 1976) and stated that the critical strain for such an event was very sensitive to the constitutive law (Rudnicki and Rice, 1975). According to his study, solids with smooth yield surfaces and normality of the plastic flow rule are more resistant to localization. To reach the state at which bifurcation into a shear mode is possible (Figure 1.7), it is necessary to develop a vertex on the yield surface. It was pointed out that the onset of localization was very sensitive to material heterogeneity.

One of the fundamental contributions to the study of void coalescence belongs to Thomason (1968, 1981, 1985, 1993), who has developed a theory of ductile fracture based on the concept of coalescence of voids by internal necking. The theory takes into account the effects of material anisotropy, stress triaxiality, and void volume fraction. According to Thomason, internal necking is prevented if the mean tensile stress to cause the flow in the internal neck is higher than the yield stress. Plastic flow is continued and the voids grow until the constraint factor (mean stress to yield stress ratio), which is a

function of the ligament geometry between the voids, is reduced sufficiently for coalescence to begin.

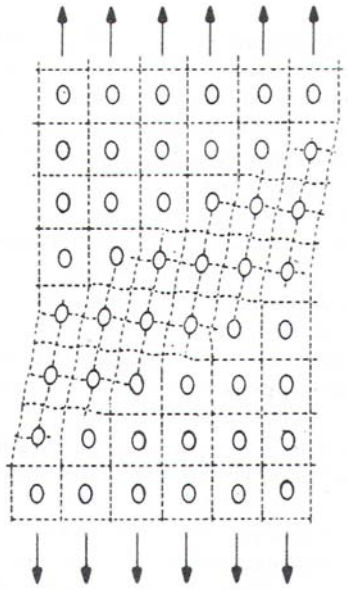

Figure 1.7: Shear band bifurcation mode found numerically for a periodic array of cylindrical voids (Tvergaard, 1990).

Thomason (1968) assumed that void coalescence occurs on the weakest sheet of microvoids and established sufficient conditions for the stability of macroscopic incompressible-plastic flow in the presence of microvoids. Following the development of Thomason's two-dimensional void coalescence model, a three-dimensional model of ductile fracture (Thomason, 1981) was developed for a rigid non-hardening plastic solid, containing a regular distribution of spherical microvoids. The model provides expressions for the plastic-limit load that controls the onset of localized internal necking of a sheet of microvoids. The condition for ductile fracture by plastic limit-load failure can be written as

$$\left(\frac{\sigma_n}{Y}\right)_{\lim} = \left(\frac{\sigma_n}{Y}\right)_{crit} \tag{1.24}$$

or

$$\left(\frac{\sigma_n}{Y}\right)\left(1-V_f\right)^{-1}\left(1-\left(\frac{3\sqrt{\pi}}{4}V_f^{2/3}\right)\left(\frac{b}{b_0}\right)\left(\frac{c}{c_0}\right)e^{\varepsilon_1}\right) = \frac{\sigma_m}{Y} + \frac{3+\nu}{3\sqrt{\nu^2+3}} \tag{1.25}$$

$$\frac{\sigma_n}{Y} = \frac{0.1}{\left(\frac{a}{d}\right)^2} + \frac{1.2}{\left(\frac{b}{b+d}\right)^{1/2}} \tag{1.26}$$

where σ_n is the mean stress, Y is the yield stress, $\left(\frac{\sigma_n}{Y}\right)_{\lim}$ is the limit-load constraint factor, and $\left(\frac{\sigma_n}{Y}\right)_{crit}$ is the critical constraint factor, V_f is the void volume fraction, a, b, c and d are the void dimensions (Figure 1.8), b_0 and c_0 are the initial void dimensions, and ν is the Lode parameter.

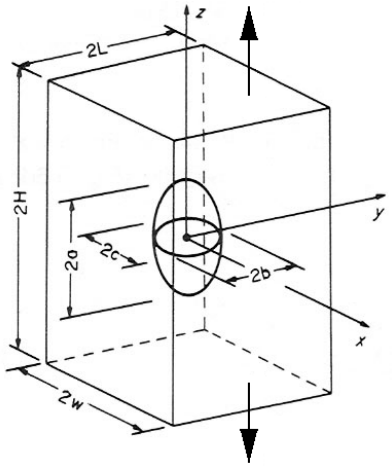

Figure 1.8: Thomason's three-dimensional unit cell (Thomason, 1990).

This work was later complemented with a two-dimensional plane strain model (Thomason, 1985) of void growth and coalescence in a rigid-plastic solid, containing distributions of voids of different sizes and non-uniform spatial arrangement (Figure 1.9).

The development of void coalescence criteria has received considerable attention in a number of studies. Most of the criteria for void coalescence take either void geometry and inter-void spacing, or void volume fraction as critical parameters.

McClintock (1968) proposed a criterion according to which coalescence occurs when the average void size reaches the average void spacing. Rosenfield and Hahn (1966) modified McClintock's model and suggested that there is a maximum stable average void size (D).

$$\sigma D^{\frac{1}{2}} = K \tag{1.27}$$

where σ is the stress level in the material and K is a material constant.

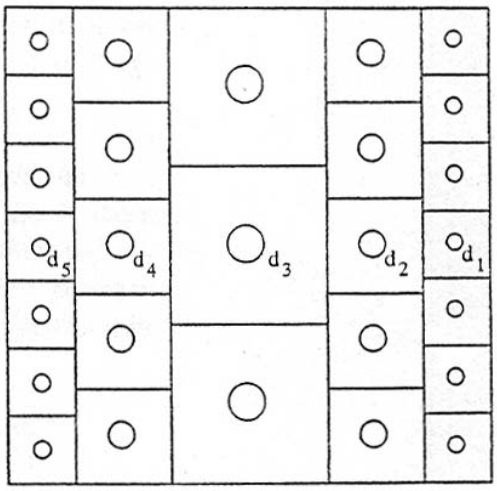

Figure 1.9: Multiple-void unit cell with variations in void size and spacing (Thomason, 1993).

Hancock and McKenzie (1976) obtained a formula for the void volume fraction (*f*) required for localization as a function of stress-state:

$$f = \left[0.56 \exp\left(\frac{3\sigma_m}{2\bar{\sigma}} \right) \right]^{-1} \tag{1.28}$$

where σ_m is the mean stress and $\bar{\sigma}$ is the effective stress.

In this relationship, the critical void volume fraction is directly dependent on the stress triaxiality, $\frac{\sigma_m}{\bar{\sigma}}$. As triaxiality increases, lower levels of void volume fraction are needed to trigger the coalescence process and fracture occurs sooner.

Budiansky *et al*. (1982) considered the void growth and collapse in viscous solids and calculated an estimate of the strain required to enlarge the voids in a solid to the point where coalescence occurs.

$$\frac{\varepsilon_{cr}}{c} = \left(\frac{\dot{V}}{\dot{\varepsilon} V} \right)_f^{-1} \qquad \text{for} \qquad \left(\frac{\dot{V}}{\dot{\varepsilon} V} \right)_f \leq 3 \tag{1.29}$$

and

$$\frac{\varepsilon_{cr}}{c} = \frac{1}{\left[1 + \frac{2}{3} \left(\frac{\dot{V}}{\dot{\varepsilon} V} \right)_f \right]} \qquad \text{for} \qquad \left(\frac{\dot{V}}{\dot{\varepsilon} V} \right)_f \leq 3 \tag{1.30}$$

with

$$c = \ln\left[\frac{(b/w)_{cr}}{(b/w)_0}\right]^2 \tag{1.40}$$

where ε_{cr} is the critical strain, V is the void volume, $\dot{V}$ is the rate of void volume change, $\dot{\varepsilon}$ is the strain rate, and b/w is the void dimension to void spacing ratio. Their approach is similar to that of McClintock (1968) for cylindrical voids. A minor drawback of this approach is that it neglects the interaction between the voids and considers each void to be isolated in an infinite block.

Pardoen and Hutchinson (2000) proposed a coalescence model based on the model by Thomason (1990). They considered the mechanism for tensile plastic localization in the inter-void ligaments. One of the assumptions is that diffuse plasticity assists localized deformation within the ligament while the material outside the ligament is unloaded elastically.

Brown and Embury (1973) established that two neighbouring voids grow in the direction of the major tensile axis and coalesce when their sizes become comparable with the ligament length between them. The mechanism of the failure or ligament necking was explained as the development of slip planes between the voids.

LeRoy *et al*. (1981) also employed the approach of Thomason (1968). They postulated the following void coalescence criterion for their model of ductile fracture.

$$2R_3^f = \phi\lambda \tag{1.41}$$

where $2R_3^f$ is the void length, λ is the nearest neighbour spacing, and ϕ is a material constant (close to unity).

Rousselier (1987) considered deformation at fracture to be independent of void size and spacing. The critical parameter according to his study was void volume fraction. A criterion for ductile fracture, which implicitly depends on void volume fraction, has been developed using the results for isolated spherical void growth by Rice and Tracey (1969).

$$\int_1^2 0.283 \exp\left(\frac{3\sigma_m}{2\sigma_{eq}}\right) d\varepsilon_{eq}^p = \ln\left(\frac{R}{R_0}\right)_c \tag{1.42}$$

where σ_m is the mean stress, σ_{eq} is the Von Mises stress, ε_{eq}^p is the equivalent plastic deformation, $\left(\frac{R}{R_0}\right)_c$ is the critical ratio of void growth. States 1 and 2 correspond to void nucleation and fracture, respectively. Oyane (1972) and Norris *et al.* (1978) have developed similar criteria.

It should be noted that most of the models above have been developed for steels. Aluminum alloys have inferior ductility compared to that of steels. Thus, the above-mentioned coalescence criteria should be employed with care when examining aluminum alloys, as in the current research.

1.4 Dilational Yield Criteria

Gurson (1975, 1977a,b,c) developed a constitutive relation that describes the process of ductile failure by void nucleation, growth, and coalescence for porous ductile media. It is a unit-cell model (Figure 1.10) of damage-induced softening. A volume of porous material, large enough to be statistically representative of the properties of the

aggregate, was considered to have a homogeneous, incompressible, rigid-plastic von Mises matrix material. The yield function is given by

$$\Phi = \left(\frac{\sigma_{eff}}{\bar{\sigma}} \right)^2 + 2 f^* \cosh\left(\frac{3\sigma_m}{2\bar{\sigma}} \right) - 1 - f^{*2} = 0 \qquad (1.43)$$

where f^* is the effective void volume fraction, σ_{eff} is the von Mises effective stress, σ_m is hydrostatic stress, and $\bar{\sigma}$ is the matrix flow stress.

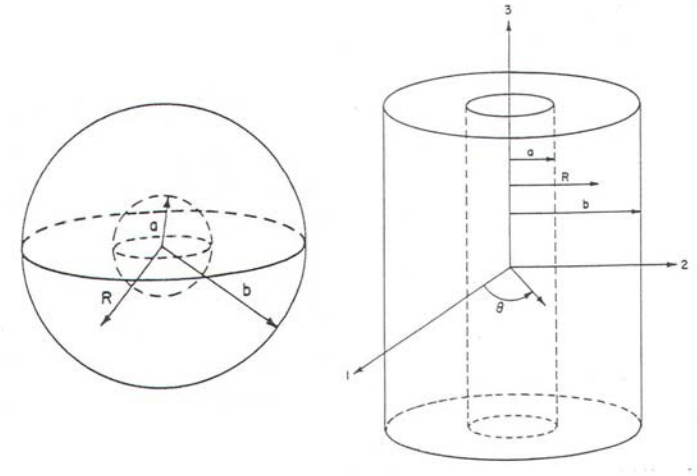

(a) (b)

Figure 1.10: Gurson's unit cells: spherical (a) and cylindrical (b) (Gurson, 1977c).

This model was modified by Tvergaard (1981) to account for void interaction effects during plastic deformation, who introduced "calibration" coefficients q_1, q_2, and q_3:

$$\Phi = \left(\frac{\sigma_{eff}}{\bar{\sigma}} \right)^2 + 2 f^* q_1 \cosh\left(q_2 \frac{3\sigma_m}{2\bar{\sigma}} \right) - 1 - q_3 f^{*2} = 0 \qquad (1.44)$$

Tvergaard and Needleman (1984) suggested that $q_1 = 1.5$, $q_2 = 1$, and $q_3 = q_1^2$ (Figure 1.11). (These three coefficients would equal unity in Gurson's original model).

The void growth rate depends on the hydrostatic component of the plastic strain rate tensor:

$$\dot{f}_{growth} = (1 - f)\dot{\varepsilon}_{kk} \tag{1.45}$$

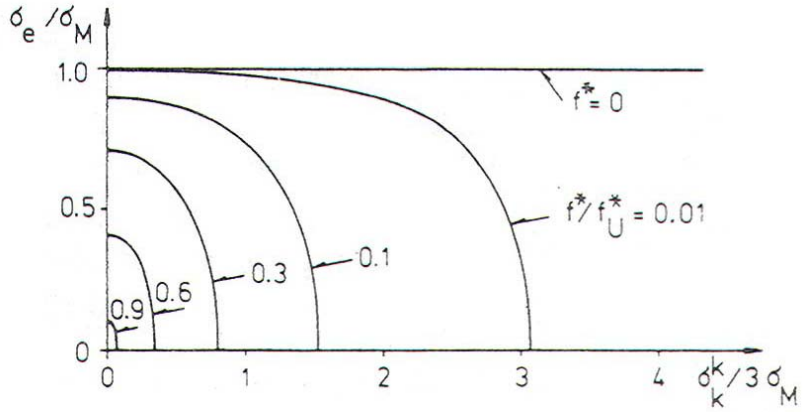

Figure 1.11: Yield surface (Tvergaard and Needleman, 1984).

As a consequence of adopting a pressure-sensitive yield criterion, there will exist a non-zero component of plastic volume change due to void growth. The total rate of increase in porosity is determined by summing the nucleation and growth rate of new and existing voids, respectively

$$\dot{f} = \dot{f}_{nucleation} + \dot{f}_{growth} \tag{1.46}$$

The void nucleation rate component may differ depending on the nucleation criterion adapted. Chen *et al.* (2003), in their study of AA5182 aluminum alloy, used a

criterion (Gurson, 1975) that assumes that voids nucleate at second phase particles and there is a normal distribution of nucleation strain for the total population of particles

$$\dot{f}_{nucleation} = A\dot{\varepsilon}^{p} \tag{1.47}$$

$$A = \frac{f_N}{s_N\sqrt{2\pi}}\exp\left[-\frac{1}{2}\left(\frac{\varepsilon^p - \varepsilon_N}{s_N}\right)^2\right] \tag{1.48}$$

where f_N is the volume fraction of void-nucleating particles, ε_N and s_N are the average and standard deviation of the nucleation strain, and ε^p is the effective plastic strain.

Tvergaard and Needleman (1984) introduced an "effective porosity" function into Gurson's model that accounts for the onset of void coalescence:

$$f^* = \begin{cases} f & \text{if } f \le f_c \\ f_c + \dfrac{f_u^* - f_c}{f_f - f_c}(f - f_c) & \text{if } f > f_c \end{cases} \tag{1.49}$$

where f^* is the effective void volume fraction, f is the void volume fraction in Gurson's model, f_c is the critical void volume fraction, f_u^* is the ultimate void volume fraction (loss of macroscopic stress carrying capacity), and f_f is the void volume fraction at final fracture. When $f^* = f_c$, void coalescence occurs, and the effective void volume fraction f^* takes into account the rapid increase of void volume fraction and loss of material strength due to coalescence (material failure).

Gologanu *et al.* (1993, 1994) extended Gurson's model to encompass a wide range of void shapes from needles to penny-shaped cracks by considering prolate (Gologanu *et al.*, 1993) and oblate (Gologanu *et al.*, 1994) confocal ellipsoidal voids. An

ellipsoidal void embedded in an infinite volume has been considered instead of Gurson's spherical and cylindrical voids.

Another important contribution to dilational yield criteria has been made by Rousselier (1987), who developed his model in the framework of the continuum thermodynamic theory. The plastic potential for the model is written:

$$F = \frac{\sigma_{eq}}{\rho} - R(\rho) + B(\beta)D\exp\left(\frac{\sigma_m}{\rho\sigma_1}\right) \tag{1.50}$$

where σ_{eq} is the Von Mises stress, ρ is the hardening variable, $R(\rho)$ is the hardening curve of the material, β is the damage variable, $B(\beta)$ is the damage term from the thermodynamic potential, D is a constant, σ_m is the mean stress, and σ_1 is a constant .

The models by Gurson and Rousselier have been developed using different approaches, but show analogy in the plastic potentials.

1.5 Second Phase Particle Clustering

Microstructural heterogeneity in the form of second phase particle clustering has a critical controlling effect on damage evolution. It affects all three stages of material degradation: void nucleation, growth, and coalescence. Closely spaced particles tend to nucleate voids sooner at lower nucleation strains (Fisher and Gurland, 1981a, b). The nucleated voids experience accelerated void growth (Thomson *et al.*, 1999), and the coalescence of such voids is more likely to occur (Thomson *et al.*, 2003). Most of the available theoretical models of damage processes do not consider clustering and assume

the microstructure to be periodic in nature. However, a significant body of research has been devoted to the investigation of the effect of second phase particle clustering on material damage evolution.

The effect of second phase particle clustering on nucleation has received attention in the works of various researchers (Fisher and Gurland, 1981a, b; Argon and Im, 1975; Kwon and Asaro, 1990; Thomson *et al.*, 1999, 2003). These studies confirm that clustering promotes void nucleation at lower strains. Accelerated void formation was attributed to elevated constraint on local plastic flow between closely spaced particles, leading to higher stresses.

A number of studies of the effect of clustering on void growth has been considered the interaction of closely spaced voids of equal size (Geltmacher and Koss, 1996; Forero and Koss, 1994; Goto and Koss, 1996) or distinctly different diameters (Marini *et al.*, 1985; Perrin and Leblond, 1990; Tvergaard and Needleman, 1996). In the case of voids of the same diameter, there is a significant increase in void rate growth if the voids are located within a distance of about one void diameter. In the case of voids of different diameters, the growth of the smaller void is accelerated. A numerical study by Thomson *et al.* (1999) showed that high hydrostatic stress further increases growth rates in regions of particle clustering, and that denser particle clusters exhibit strong sensitivity to cluster orientation relative to the principal loading direction.

Various researchers (Geltmacher and Koss, 1996; Perrin and Leblond, 1990; Tvergaard and Needleman, 1996; Dubensky and Koss, 1987) have investigated the role of particle clusters during void coalescence. These experimental investigations have included consideration of two-dimensional plates with holes representing voids in the matrix (Dubensky and Koss, 1987) (Figure 1.12). The plates were loaded in uniaxial tension to study the coalescence paths. The coalescence of two adjacent voids proved to be very sensitive to relative spacing and orientation, occurring preferentially between

voids oriented transverse to the direction of loading. The strain at which macroscopic fracture occurs was different for the cases of uniformly versus randomly distributed voids. The ductility of the specimen with uniformly distributed voids was reported to be two or three times higher (Dubensky and Koss, 1987), indicating that clustering has a deleterious effect on ductility. Magnusen *et al.* (1988) confirmed that the localization event during void coalescence is triggered and controlled by the location and shape, as well as size, of adjacent voids. It was also noted that ductile fracture was an evolutionary, sequential process in the presence of a random distribution of voids, but it is an abrupt process when the void array has a regular distribution. Bandstra *et al.* (2004) later complimented this research with finite element simulations of strain localization between voids leading to void coalescence (Figure 1.13).

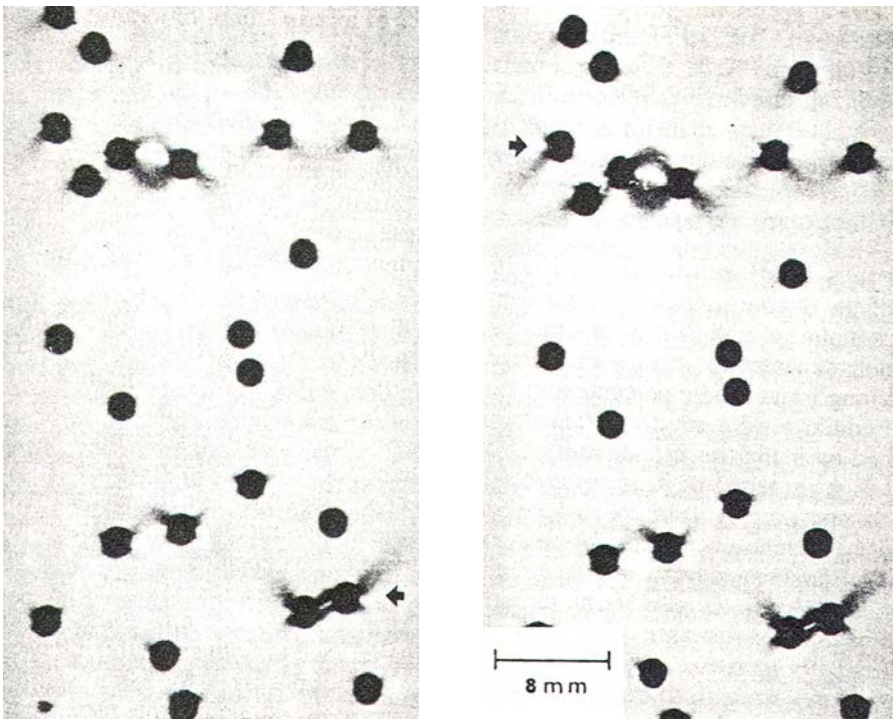

Figure 1.12: Hole coalescence in plates (Dubensky and Koss, 1987).

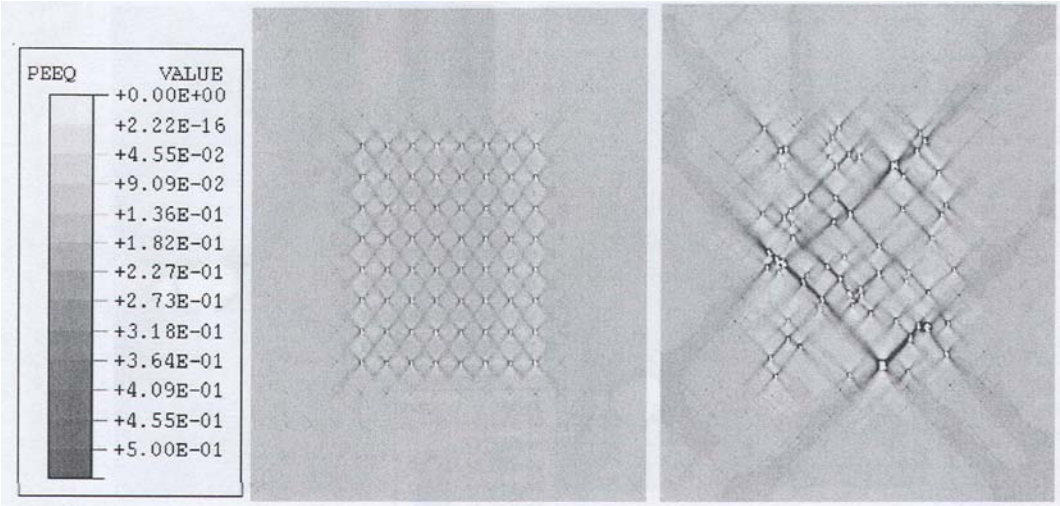

Figure 1.13: Equivalent plastic strain plots for regular (a) and random (b) void arrays (Bandstra and Koss, 2004).

There have also been considerable efforts to characterize particle distributions and quantify particle clustering (Wray *et al.*, 1983; Spitzig et al., 1985; Burger *et al.*, 1988; Pilkey *et al.*, 1998). Pilkey *et al*. (1998) employed Dirichlet tessellation of metallographic samples (Figure 1.14) to extract certain geometric attributes of the tessellation cells, which can act as strong indicators of clustering. Inter-particle dilational spacing frequency plots were found to provide one of the most useful descriptions of particle spatial distribution. Based on these plots, it was possible to identify different levels of clustering: clusters of particles (first order clusters), clusters of first order clusters (second order clusters), and so on. The results of this work were later used as an input into the damage percolation model described in the next section.

Another way to characterize spatial arrangement and heterogeneity of microstructural features is to use two-point correlation functions (Corson, 1974; Gokhale and Drury, 1994; Tewari *et al.*, 2004). Unbiased techniques have been developed based on these functions to characterize three-dimensional particle distributions using two-dimensional metallographic sections.

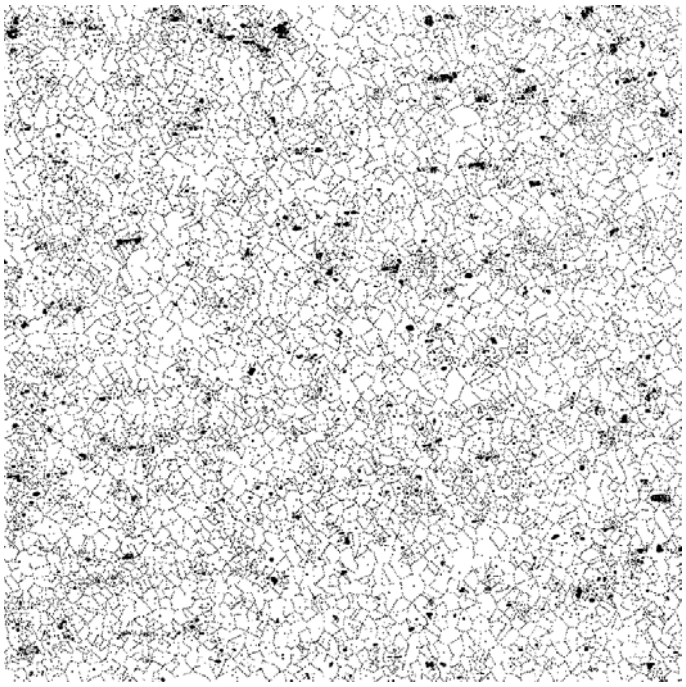

Figure 1.14: Tessellated particle field of an AA5182 aluminum alloy specimen rolling direction section (Worswick *et al.*, 2001).

1.6 The Damage Percolation Model

One shortcoming of the majority of damage models developed to-date is an inability to account for real second phase particle distributions; instead, current models often utilize unit cell or periodic particle distribution assumptions that ignore the random-clustered character of real microstructures.

One of the earliest attempts to overcome these shortcomings was by Tonks (1994) who modelled the evolution of disordered initial void distributions in materials undergoing ductile damage. This work considered void growth and coalescence under tension at different strain rates. Two-dimensional plane strain simulations utilized

rectangles as void shapes instead of circles for the sake of simplicity. This study addressed ductile fracture transition from a propagating crack at quasi-static loading conditions to dispersed damage nucleating at multiple random sites under high strain rate loading, as observed in real tensile tests. The results of this study revealed that fracture occurs by long localized cracks (Figure 1.15a) and widespread random damage (Figure 1.15b) at low and high strain rates, respectively, and can be modelled using this approach. It was possible to calculate and compare the strains at fracture for the two cases. The fracture strain was smaller during loading at low rates of strain. The modelled mechanisms of damage initiation and evolution under different strain rate conditions fall into a greater area of knowledge known as a random continuum site percolation theory (Stauffer, 1985).

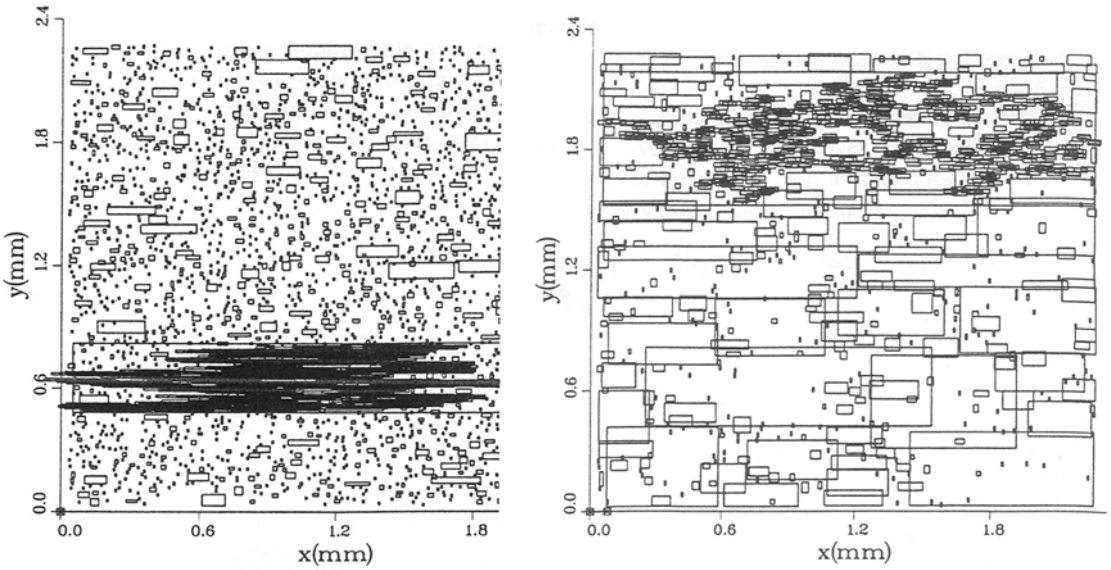

(a) (b)

Figure 1.15: Void link-up and ductile fracture: (a) crack developed at quasi-static loading and (b) random damage percolation at loading under high rates of strain (Tonks, 1994).

Worswick *et al.* (1998, 2000, 2001) have developed a two-dimensional percolation model that is capable of predicting damage evolution within materials using measured microstructural data (Figure 1.14), such as the distribution of size and inter-particle distance within second phase particle fields. Chen *et al.* (2003) modified the original 2D damage percolation model to be applicable to various sheet metal forming processes modelled using two-dimensional finite element (FE) models. This version of the 2D damage percolation model mapped second phase particle field images onto a finite element mesh and utilized one-way coupling to the FE model using the results of the FE simulation to predict damage evolution in the component being modelled (Figure 1.16).

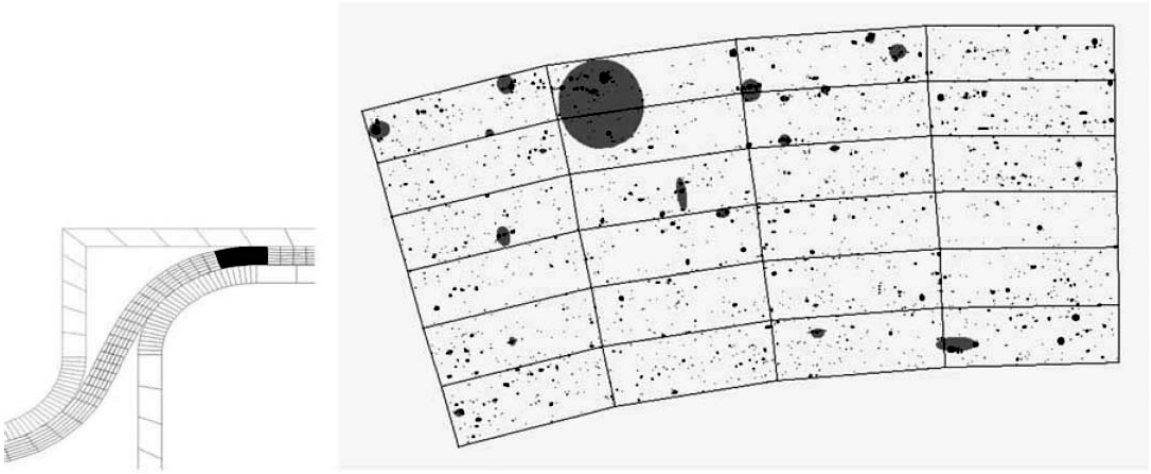

Figure 1.16: Damage prediction in AA5182 aluminum alloy during stretch flange forming using the two-dimensional DPM (Chen *et al.*, 2003).

The two-dimensional damage percolation model considers damage evolution within materials containing second phase particles. The models of Worswick *et al.* (2001) and Chen *et al.* (2003) import two-dimensional particle distributions obtained from

optical microscopy and simulate the evolution of damage associated with void nucleation, growth, and coalescence during a forming process. Damage is introduced through void nucleation via particle cracking or debonding from the matrix material (Puttick, 1959; Rogers, 1960; Gurland and Plateau, 1963). The subsequent growth of nucleated voids occurs during the plastic deformation of the matrix (Puttick, 1959; Rogers, 1960; Gurland and Plateau, 1963). Void coalescence precedes final material failure and occurs primarily within particle clusters, yet still remains a stable process over much of the deformation history (Rogers, 1960; Beachem, 1963; Rosenfield, 1968). A critical catastrophic event occurs with the linkup of damage across two or more void clusters. At this stage, coalescence spreads as a chain reaction across the bulk of material leading to final rupture. By utilizing two-dimensional particle distributions, the model is able to address the effect of microstructural heterogeneity (clustering of second phase particles) on damage evolution.

A number of shortcomings of the two-dimensional damage percolation model exist. It is not capable of capturing ongoing damage processes in the direction orthogonal to the 2D plane. In stretch flanging operations, for instance (Cinotti *et al*., 2000), due to limitations of the 2D model, concurrent occurrence of radial and circumferential cracks that are orthogonal to one another cannot be captured. Also, the effect of second phase particle clustering can be captured best in the long-transverse metallographic section. In other sections, e.g. short-transverse section, second phase particle clustering is much weaker due to the nature of cold-rolled microstructure. This fact imposes constraints on the use of the 2D damage percolation model. Finally, voids are represented by ellipses (Worswick *et al.*, 2001; Chen *et al.*, 2003) in two-dimensional sections used for damage percolation modelling. These ellipses correspond to cylindrical surfaces in three-dimensions, which is not the case in reality.

1.7 Current research

Understanding the damage mechanisms involved in sheet metal forming operations is important for material and part optimization and failure prediction. It is well accepted that the deformation of ductile materials, such as 5xxx-series aluminum alloy sheet, involves the nucleation, growth, and coalescence of voids, as well as shear localization, prior to final failure.

It is evident from the foregoing review that numerous studies have addressed the factors controlling ductile damage within the context of continuum damage or periodic unit cell assumptions. The effect of random and/or clustered particle distributions has only recently been addressed and requires further work. In particular, the work of Worswick, Chen, and Pilkey (Worswick *et al.*, 1998, 2001; Chen *et al.*, 2003) is limited to a two-dimensional assumption and the three-dimensional character of second phase particle fields must be introduced.

The next step to build upon the current understanding of ductile fracture would be to model and accurately predict the deformation behaviour and damage evolution of materials by considering fully three-dimensional second phase particle distributions that incorporate second phase particle clustering effects. This goal is achievable by developing a three-dimensional version of the damage percolation model that is capable of incorporating measurements of real microstructures.

As a part of the current study, the damage percolation approach has been extended to three-dimensions. The development of a new three-dimensional damage percolation model has several advantages over the more conventional unit cell damage models, which assume that the material microstructure is homogeneous and periodic, and the 2D percolation model of Chen *et al.* (2003), which is limited to damage modelling in one plane and does not account for the three-dimensional nature of real material

microstructures. The proposed model is used for studying the damage processes in an anisotropic rolled sheet material and may be potentially incorporated into a commercial FEM package, such as LS-DYNA.

Another important aspect of this research has been the acquisition of 3D second phase particle fields. Techniques have been developed to reconstruct 3D particle distributions from orthogonal 2D plane sections using a statistical reconstruction method. Direct acquisition of three-dimensional second phase particle fields and damage development also has been performed using X-ray tomography of *in situ* tensile samples. These 3D particle fields have been used to validate both the particle field reconstruction method and the 3D damage percolation predictions.

The specific objective of this research is to understand the role of microstructural heterogeneity on damage processes via:

- Microstructural characterization of real 3D second phase particle fields
- Extension of the 2D damage percolation code to 3D and implementation of two-way coupling with a finite element code to simulate damage development and constitutive softening within 3D particle fields
- Validation of the predictions against measured damage evolution
- Parametric study of the effect of clustering on damage development and material formability using the 3D percolation model

The balance of this thesis is organized in the following manner. Chapter 2 presents the work on characterization of the as-received AA5182 aluminum alloy sheet microstructure using optical microscopy and X-ray tomography. This includes the reconstruction of three-dimensional second phase particle fields from two-dimensional metallographic sections. Chapter 3 presents the application of *in situ* X-ray tomography to measure damage evolution in deforming tensile samples. Chapter 4 provides a description of the three-dimensional damage percolation model and algorithms. The

application of the three-dimensional damage percolation model to simulate the tensile test is presented in Chapter 5. Chapter 6 presents a parametric investigation into predicted damage development within materials reconstructed with varying clustering characteristics. The simulation of a bend test, as another example of a forming process, is presented in Chapter 7. The conclusions and recommendations stemming from this research are given in Chapter 8.

Chapter 2

Microstructure Characterization and Reconstruction of Second Phase Particle Fields

A key requirement in being able to predict damage development within real materials is the acquisition of suitable 3D particle field information comprising particle size and spatial arrangement data. This was not a problem in previous research considering a two-dimensional model, such as that developed by Worswick *et al.* (1998, 2001) and Chen *et al.* (2003), since standard 2D images from metallographically sectioned specimens are sufficient.

Several techniques are available for the acquisition of 3D images of solid objects including X-ray tomography (Maire *et al.*, 2001), serial sectioning (Li *et al.*, 1999), and acoustic methods. However, these methods often have relatively low spatial resolution or are highly work intensive and time consuming.

One key aspect of the current research is the development of appropriate reconstruction techniques so that three-dimensional second phase particle fields can be generated for input to the 3D damage percolation model. As described in the following, statistical techniques are used to reconstruct 3D particle fields from measured particle fields obtained from orthogonal 2D sections. There are two aspects to the reconstruction method. The first is the generation of a representative set of 3D particles with appropriate size and aspect ratio distributions. The second is the placement of these particles within the 3D volume while capturing the random-clustered nature of real particle fields.

In order to assess the quality of the reconstructed second phase particle fields, a number of direct 3D measurements of AA5182 aluminum alloy sheet were obtained using tomographic techniques. These tomographic images provide direct information about the spatial relationships between particles and damage, for example, and were also used to aid in selection of appropriate techniques to introduce particle clustering within the reconstructed fields.

The current chapter is organized in the following manner. First, the methods adopted for the acquisition of 2D optical and 3D tomographic images of the AA5182 second phase particle fields are presented. Next, the method to reconstruct the three-dimensional second phase particle fields is outlined. Finally, the results of reconstruction of the second phase particle field size distributions and spatial arrangement are presented and compared with measurements from the 3D tomographic images.

2.1 Microstructural data acquisition and characterization

Digital images of the AA5182 microstructure were obtained using either optical image acquisition from two-dimensional metallographic sections or fully three-dimensional synchrotron radiation tomography. All measurements were done on 1mm-thick AA5182 sheet. The chemical composition of the studied aluminum alloy is shown in Table 2.1. This material is produced by casting in large ingots, after which the ingots are scalped and preheated for hot rolling (Gupta *et al.*, 2001). They are processed in a hot-rolling line and rolled to a thickness between 2 and 5 mm (referred to as reroll). Cold rolling to a thickness of 1 mm follows cooling of the reroll. AA5182 sheet is supplied in the annealed "O4" temper.

The optical images were obtained from two-dimensional long- and short-transverse sections (Figure 2.1), which were used for reconstruction of the three-dimensional second phase particle fields. In order to facilitate comparison between the optical and tomographic measurements, 2D sections were also extracted from the 3D tomographic images. The methods used to obtain both types of images are outlined in the following.

Table 2.1: Chemical composition of AA5182 (all component quantities are in percent of weight).

Mg	*Si*	*Cu*	*Fe*	*Mn*	*Zn*	*Cr*	*Ti*
4.5	0.08	0.05	0.27	0.35	0.05	0.03	0.1

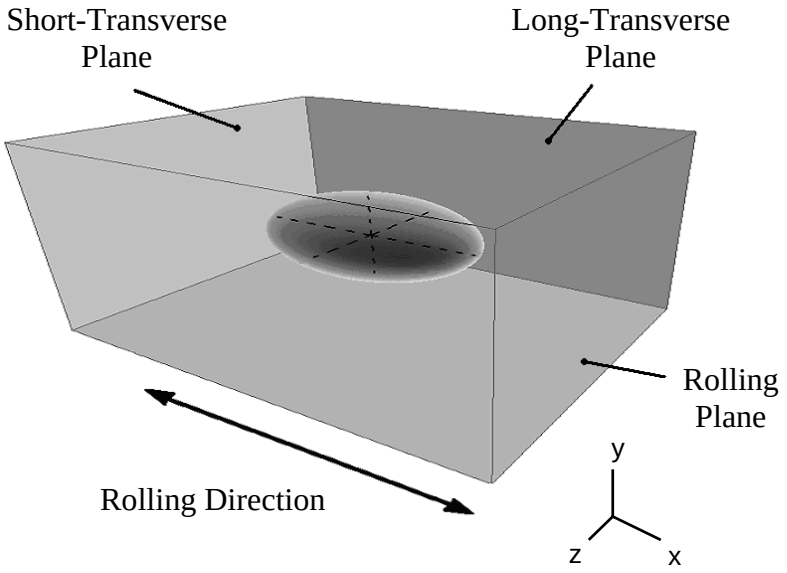

Figure 2.1: Particle orientation in the material.

2.1.1 Two-dimensional optical micrographs

Two-dimensional images of specimen sections in two orthogonal planes, long- and short-transverse, were obtained using optical microscopy. Specimens were cut in the rolling and orthogonal-to-rolling directions (Figure 2.2) from AA5182 sheet to obtain long- and short-transverse planes, respectively, and were cold mounted with epoxy resin and wet ground up to 4000 grit *SiC* paper. The next step of the specimen preparation was 3 μm and 1 μm diamond polishing, after which final polishing was performed using a 0.05 μm colloidal silica suspension.

Greyscale (8-bit) micrographs were captured using an Olympus BH2-UMA optical microscope equipped with a Photometrics CoolSNAP CCD camera from Roper Scientific Inc. The image size comprised 1392x1040 pixels. A 20x objective lens allowed for an image resolution of 0.303μm (Figure 2.3). The overall inspected areas were

4350x776μm and 4348x780μm for the long- and short-transverse sections, respectively, which correspond to image sizes of 14356x2561 and 14350x2574 pixels.

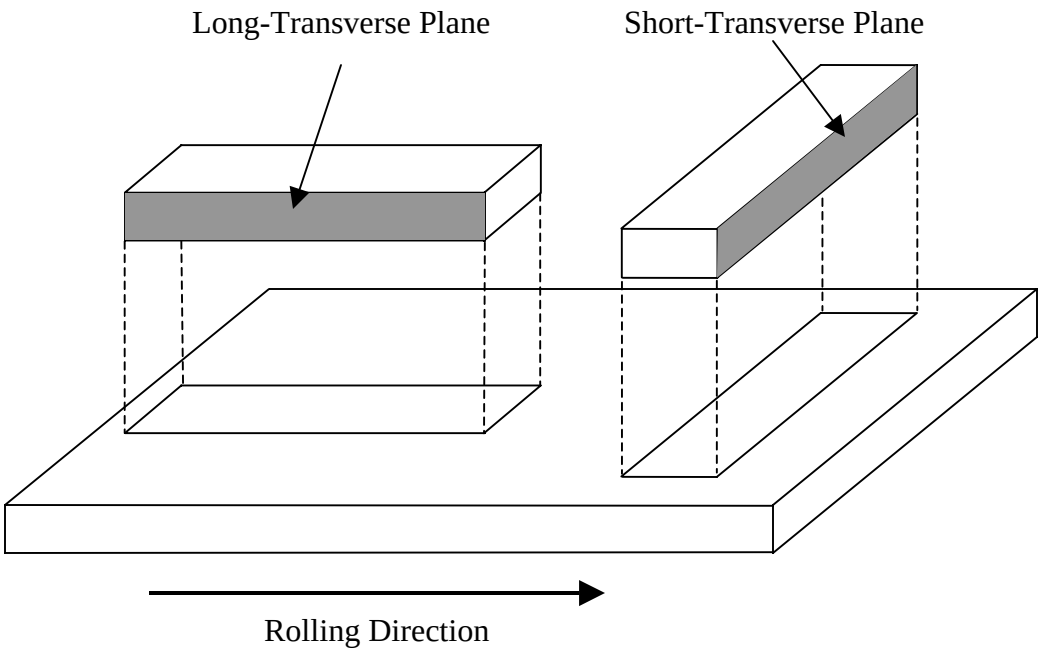

Figure 2.2: Specimens cut from AA5182 sheet to obtain long- and short-transverse metallographic planes.

A tessellation program developed by Lievers (2004) was used for microstructure characterization. This software performs thresholding of the original grey-scale images to separate particles from background. Next, the particles in the section are approximated as ellipses, calculating the area fraction of the second phase, tessellating the obtained image (Figure 2.4), and calculating the in-plane inter-particle distance distribution of the second phase particle population. The results of the measurements of particle ellipse major and minor axes are presented in the form of size distributions of the ellipse axes in the long- and short-transverse sections (Figures 2.5 and 2.6).

The aluminum alloy AA5182 considered in the current work contains two types of second phase particles, *Fe*-rich and Mg_2Si. It was not possible to distinguish between the two particle types using optical microscopy since the phases were of similar shades of grey. The entire population of second phase particles and voids (Table 2.2) was considered for three-dimensional size and shape reconstruction (as discussed later) without discriminating amongst the three object types.

Table 2.2: AA5182 optical micrograph data.

Metallographic Section	Number of Particles per mm^2	Second Phase Area Fraction	Average Particle Area (μm^2)	Maximum Particle Area (μm^2)
Long-Transverse	1637	0.0103	5.45	93.1
Short-Transverse	1843	0.0100	6.29	164.7

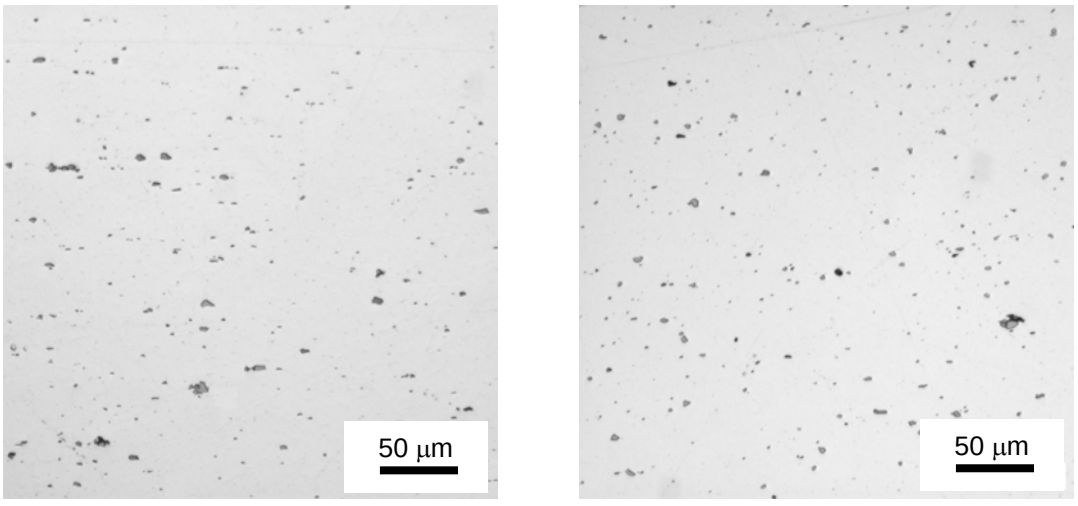

(a) (b)

Figure 2.3: Optical micrographs of AA5182 specimen long- (a) and short- (b) transverse sections.

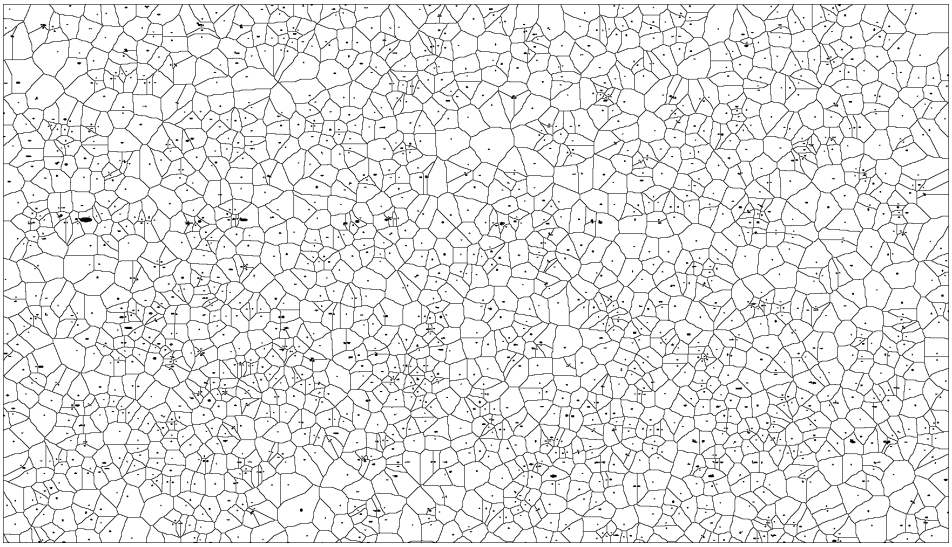

Figure 2.4: AA5182 specimen long-transverse micrograph section tessellation.

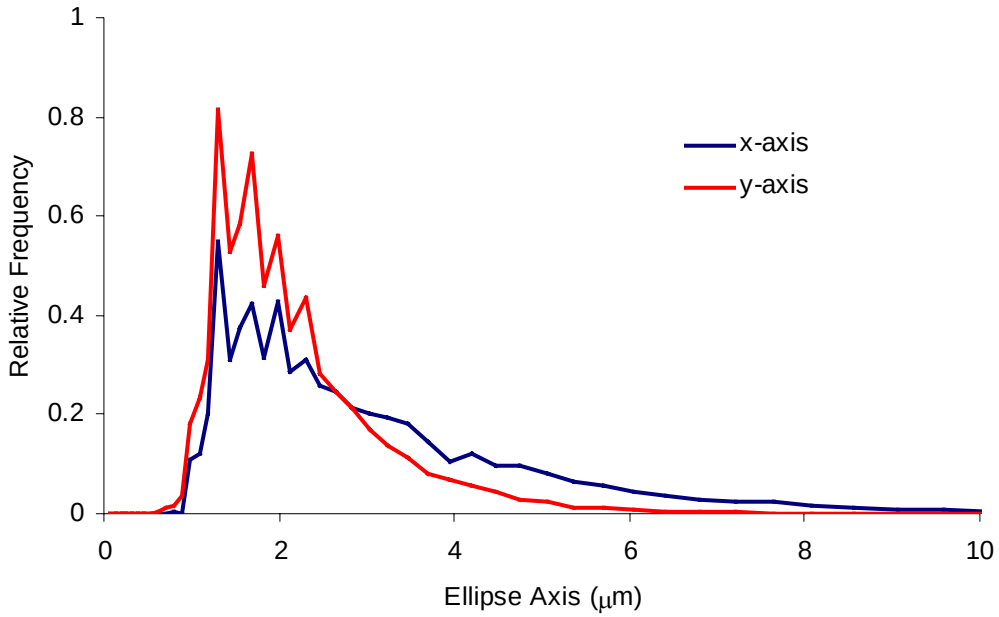

Figure 2.5: Ellipse axis distributions in the long-transverse section obtained with optical microscopy.

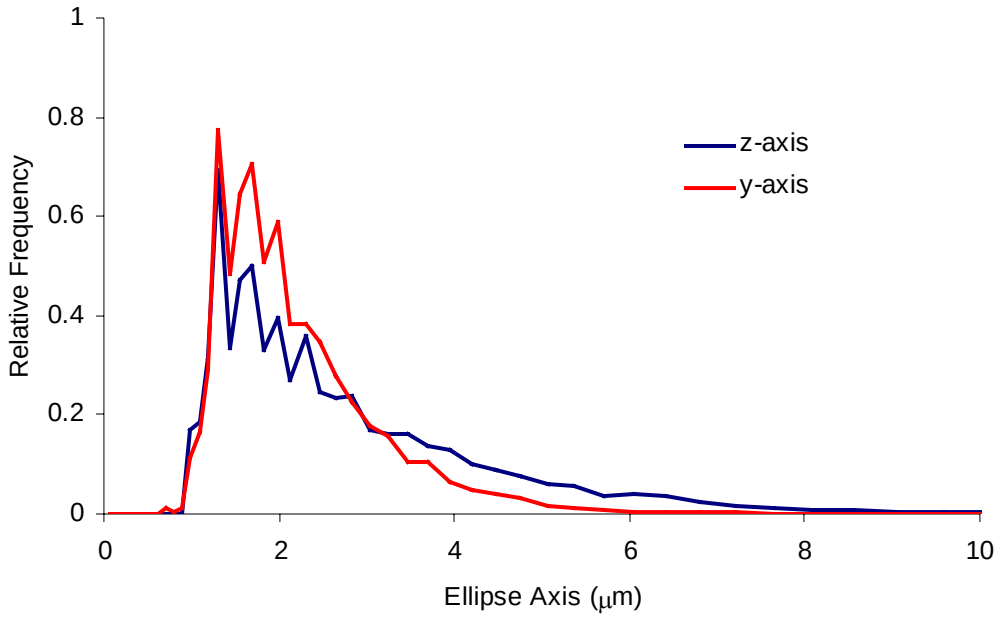

Figure 2.6: Ellipse axis distributions in the short-transverse section obtained with optical microscopy.

2.1.2 Three-dimensional X-ray tomographic images

Three-dimensional tomographic images of the AA5182 sheet were obtained at the European Synchrotron Radiation Facility in Grenoble, France. A monochromatic beam with high photon flux was used for the acquisition of greyscale images with a voxel resolution of 0.7 μm. Multiple two-dimensional projections were taken while rotating the specimen. The projections then were used for the reconstruction of the three-dimensional microstructure. The scanned volume of the material was 1000x1000x580μm. The shape of the aluminum alloy AA5182 specimenis shown in Figure 2.7. More details of this method are given by Maire *et al.* (2001).

The acquired three-dimensional tomographic images cannot be used in their original form since they have defects and specimen boundary surfaces produced during

image acquisition (Figures 2.8). Figure 2.8 shows an image of the as-received microstructure, which contains a defect in the middle of the image due to the rotation of the specimen during the tomographic data acquisition. To correct the problem, sub-volumes of good quality were cut from the three-dimensional images and pasted together to make a volume of comparable size to be used in the damage percolation model. Four defect-free sub-volumes have been used to construct a material volume of good image quality. The resulting cross section of the corrected material volume is 896x896 μm instead of the original 1000x1000 μm.

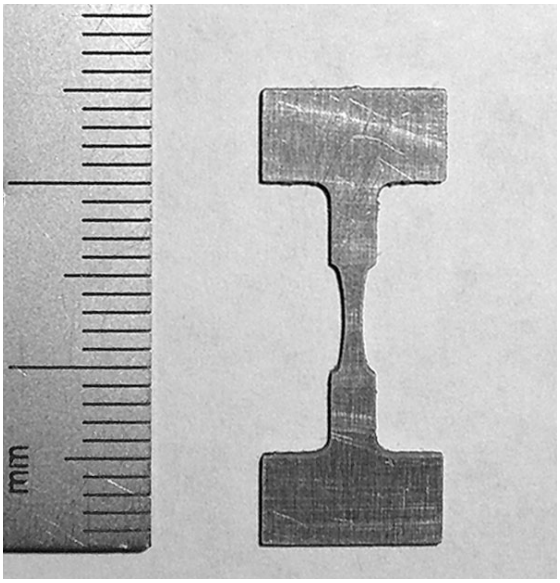

Figure 2.7: AA5182 tensile specimen.

The obtained tomographic images represent 256-grey-shade voxel arrays in which the grey levels correspond to different material X-ray permeability. Four different phases can be distinguished: matrix material, voids, and second phase particles of two types (*Fe*-rich and Mg_2Si) (Figure 2.9). The overall distribution of the grey shades in the images and the different zones of interest are shown in Figure 2.10. It can be seen that the grey scale levels of the void and Mg_2Si particle bands are adjacent to each other to the left on

the plot, whereas the *Fe*-rich particles are in the right side. Thresholding is used to distinguish second phase particles and voids from the matrix material, as well as the two particle types, within the greyscale images. The Mg_2Si particles are dark grey and *Fe*-rich particles are white. Voids are represented in the image by dark areas with a dark grey outline. There arises a problem of distinguishing this outline from the Mg_2Si particles that are of a similar shade of grey. Therefore, there are three thresholds that need to be set to distinguish between: (i) voids and Mg_2Si particles; (ii) Mg_2Si particles and the matrix; and, (iii) the matrix and *Fe*-rich particles.

The original grey-scale voxel array was thresholded within the following grey-scale intervals: 0 – 36 (voids), 37 – 85 (Mg_2Si particles), and 185 – 255 (*Fe*-rich particles). These intervals were chosen visually.

Grey-scale intervals corresponding to voids and Mg_2Si particles are adjacent in the distribution of the grey shades (Figure 2.10). The transition from a void to the matrix material, outlining of the same grey shades as Mg_2Si particles, can be misinterpreted as a Mg_2Si particle. A technique was developed to eliminate the outlining around voids. Thresholded voids are enlarged until they overlap the “shells” around them, after which the thresholding of the now exclusively dark grey Mg_2Si particles can be performed. The results of the thresholding procedure are summarized in Table 2.3 and shown in Figures 2.9 and 2.11.

In particle clusters, voids often nucleate between two or more adjacent particles of different types (Figure 2.12). Voids that nucleate through particle cracking are located between two halves of a cracked particle (Figure 2.13). In the case of matrix decohesion, voids nucleate at particle-matrix interfaces orthogonal to the rolling direction. Nucleation of voids through both mechanisms can be seen to occur at the same particle (Figure 2.14).

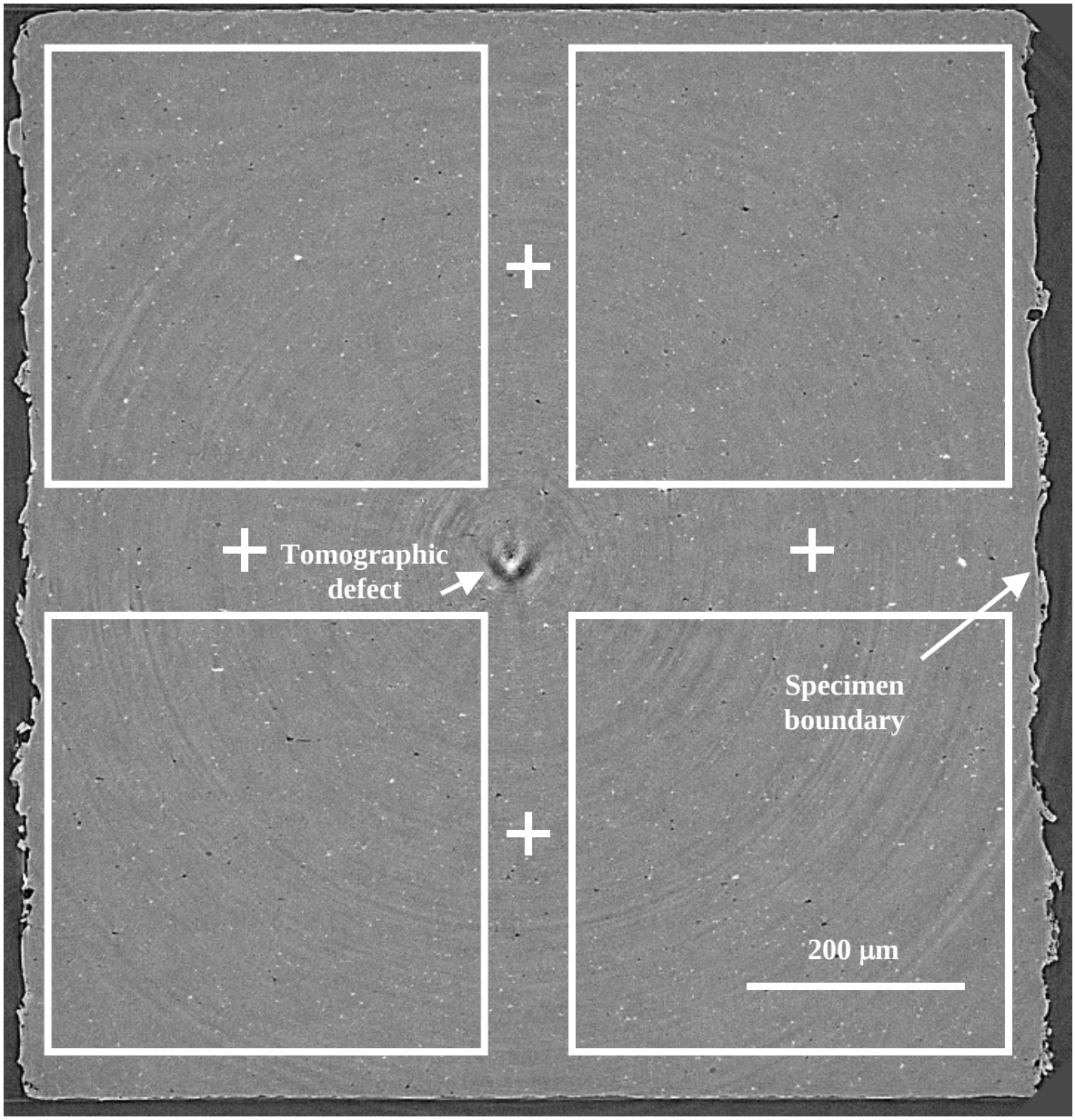

Figure 2.8: Section of the three-dimensional material volume (as-received AA5182): assembly of a tomographic image with regions of better quality.

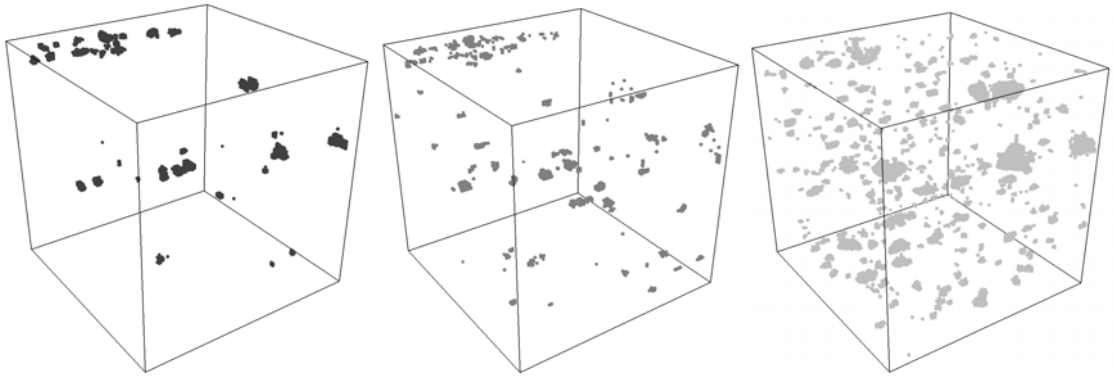

(a) (b) (c)

Figure 2.9: Thresholded images (70x70x70μm volume): (a) – voids, (b) - *Mg_2Si* particles, (c) – *Fe*-rich particles.

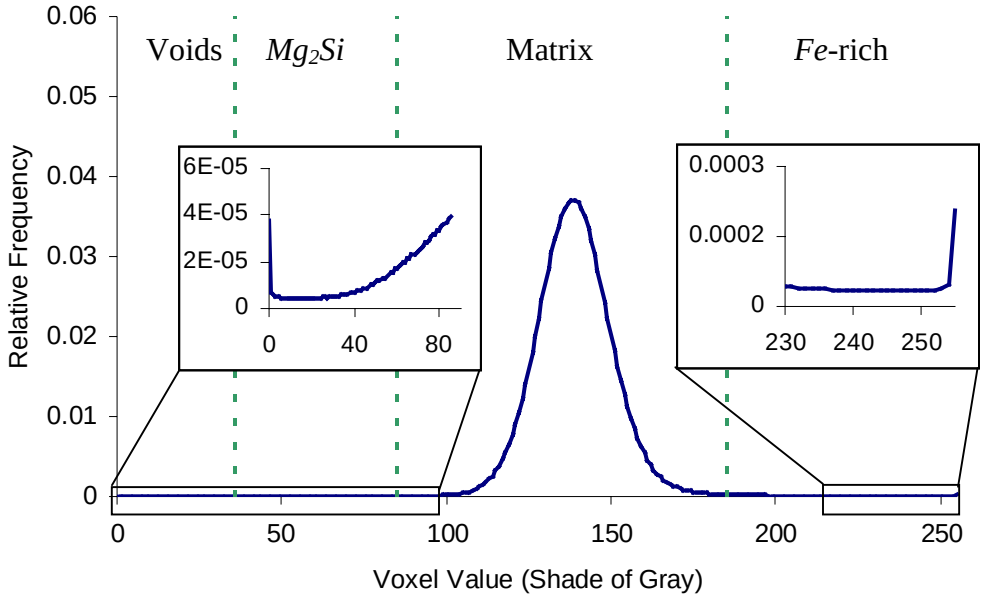

Figure 2.10: Grey scale range. Void and *Fe*-rich particle intervals contain peaks.

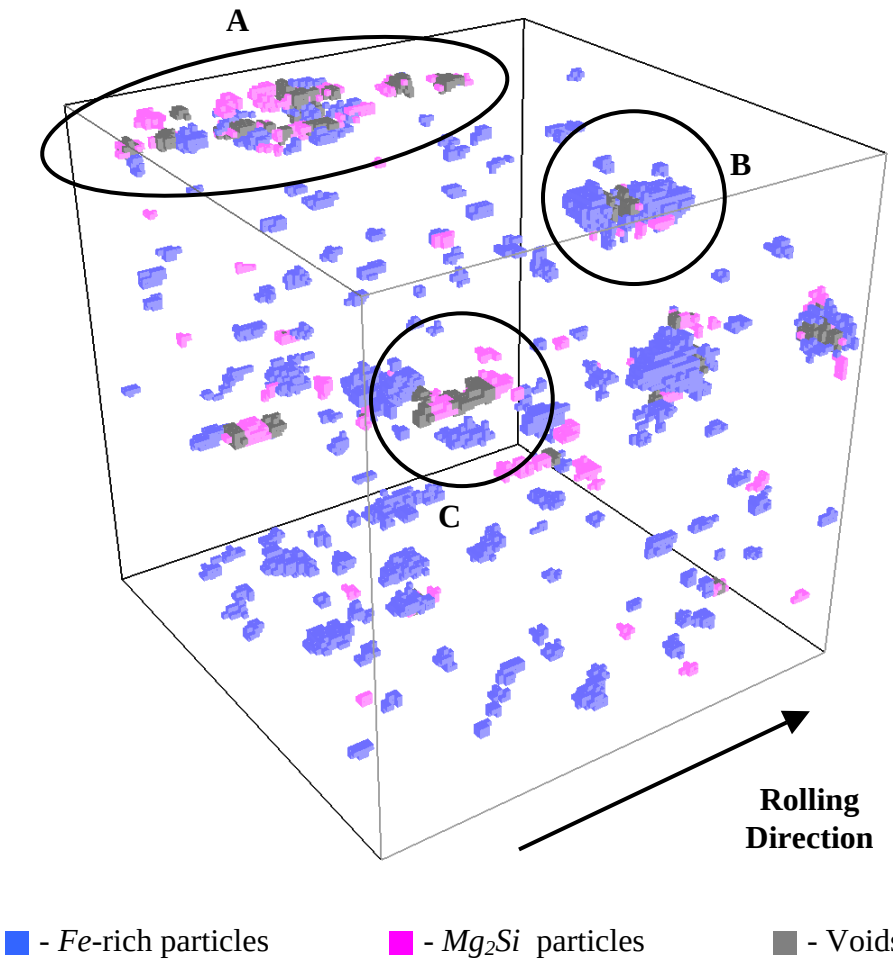

Figure 2.11: Undeformed AA5182 sheet (70x70x70μm Volume). A – particle/void cluster. B – fractured *Fe*-rich particle with void. C - fractured *Mg_2Si* particle with void.

Table 2.3: Volume fractions of *Fe*-rich particles, *Mg_2Si* particles, and voids.

Fe-rich	*Mg_2Si*	Voids
0.00483	0.000485	0.000529

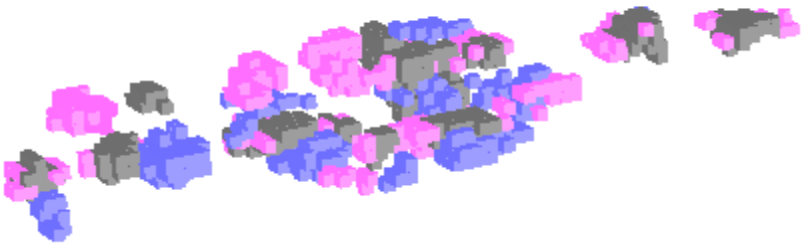

■ - *Fe*-rich particles ■ - Mg_2Si particles ■ - Voids

Figure 2.12: Particle/void cluster in undeformed AA5182 sheet (Detail A of Figure 2.11).

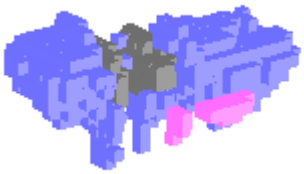

■ - *Fe*-rich particles ■ - Mg_2Si particles ■ - Voids

Figure 2.13: Fractured *Fe*-rich particle with void in undeformed AA5182 sheet (Detail B of Figure 2.11).

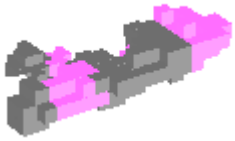

■ - *Fe*-rich particles ■ - Mg_2Si particles ■ - Voids

Figure 2.14: Fractured *Mg_2Si* particle with void in undeformed AA5182 sheet (Detail C of Figure 2.11).

2.1.3 Microstructure characterization

2.1.3.1 Particle/void size and shape

There are three types of objects stored that correspond to the two types of second phase particles and voids after thresholding. To incorporate these data into a damage model, it was elected to represent the particles as ellipsoids according to the assumption that particles and voids are ellipsoids of general form sometimes locally aligned (clustered) in the rolling direction (Figures 2.11 and 2.12). Due to hot rolling, second phase particles are compressed in the through-thickness direction and elongated along the rolling direction.

In order to determine representative ellipsoids for groups of voxels corresponding to each particle, the method utilized by Lievers (2004) was employed. In general, this method involves the solution of a covariance matrix *C*:

$$C = \sum \begin{pmatrix} X_i^2 & X_i Y_i & X_i Z_i \\ Y_i X_i & Y_i^2 & Y_i Z_i \\ Z_i X_i & Z_i Y_i & Z_i^2 \end{pmatrix} \tag{2.1}$$

where

$$X_i = x_i - \bar{x} \qquad Y_i = y_i - \bar{y} \qquad Z_i = z_i - \bar{z} \tag{2.2}$$

$$\bar{x} = \frac{1}{k}\sum_{i=1}^{k} x_i \qquad \bar{y} = \frac{1}{k}\sum_{i=1}^{k} y_i \qquad \bar{z} = \frac{1}{k}\sum_{i=1}^{k} z_i \tag{2.3}$$

and x_i, y_i, and z_i are the voxel coordinates; $\bar{x}$, $\bar{y}$, and $\bar{z}$ are the center-of-mass coordinates of the ellipsoid; and k is the number of voxels in the thresholded particle.

The ratios of eigenvectors λ_1 , λ_2, and λ_3 of matrix *C* are related to the axes of the ellipsoid, *a*, *b*, *c*, according to the following relationship:

$$\lambda_1 : \lambda_2 : \lambda_3 = a^2 : b^2 : c^2 \tag{2.4}$$

Equation 2.4 provides the ellipsoid aspect ratios. The ellipsoid volume is determined from the sum of the voxel volumes comprising the particle, after which these ratios can then be used to calculate the ellipsoid axes.

It was assumed that the entire population of approximated ellipsoids of second phase particles and voids can be considered to have their axes aligned with the image axes, that is, directions perpendicular to the long-, short-transverse and rolling planes. In this case, only the values from the main diagonal (Equation 2.1) need to be accounted for:

$$\left(\sum_{i=1}^{k} X_i^2\right) : \left(\sum_{i=1}^{k} Y_i^2\right) : \left(\sum_{i=1}^{k} Z_i^2\right) = a^2 : b^2 : c^2 \tag{2.5}$$

An example of the approximation of the second phase particles and voids as ellipsoids is shown in Figures 2.15 – 2.18. The corresponding part of the original second phase particle field represented by agglomerations of voxels is shown in Figures 2.11 – 2.14. The results of the approximation of the entire second phase particle field as ellipsoids are shown in the form of probability density plots of the distributions of the feature size along each axis in Figures 2.19 – 2.21. It can be seen that in the *Fe*-rich and Mg_2Si particle plots, the X-axis curve is shifted to the right from the Y- and Z- axis curves. The Z-axis plot is also shifted to the right relative to the Y-axis plot. These observations indicate that, on average, the ellipsoid X-axes are the most elongated, followed in magnitude by the Z-axes and Y-axes. Therefore, the assumption that the

particles are elongated along the rolling direction and compressed in the through-thickness direction due to hot rolling can be considered appropriate.

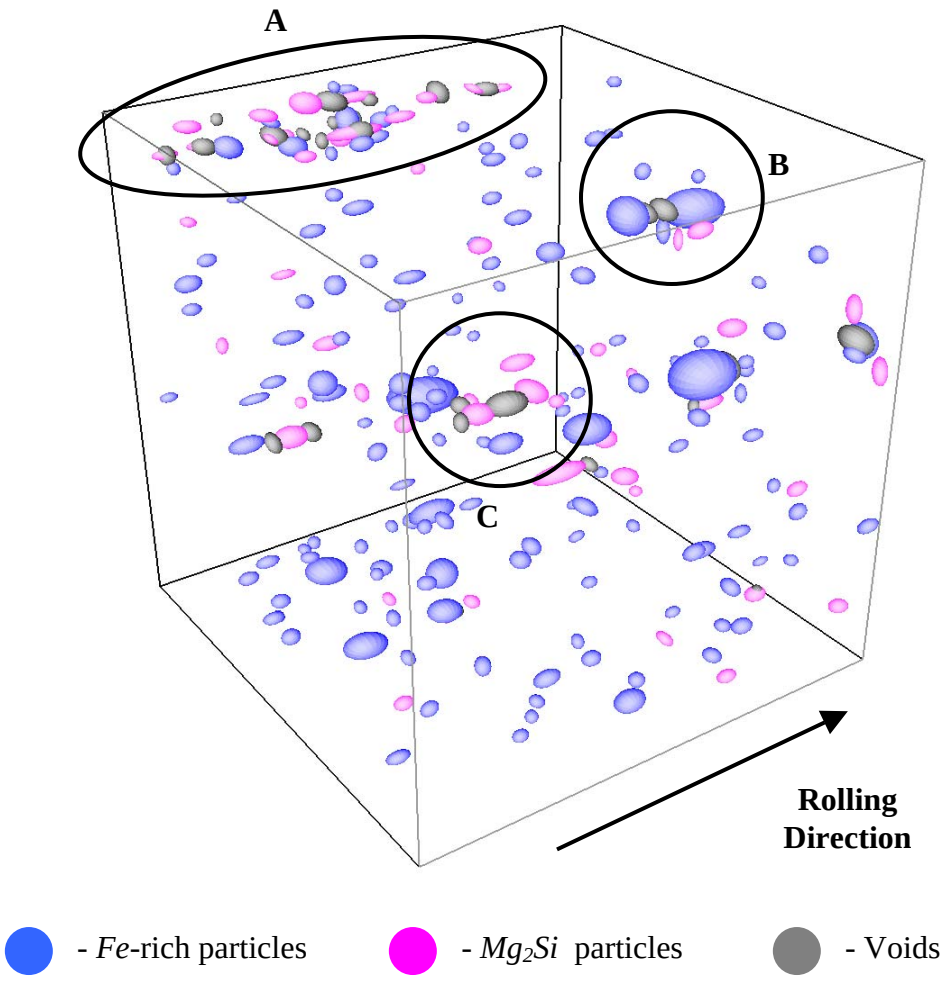

Figure 2.15: Ellipsoid representation of second phase particle field in Figure 2.11 in undeformed AA5182 sheet (70x70x70μm Volume). A – particle/void cluster. B – fractured *Fe*-rich particle with void. C - fractured *Mg_2Si* particle with void.

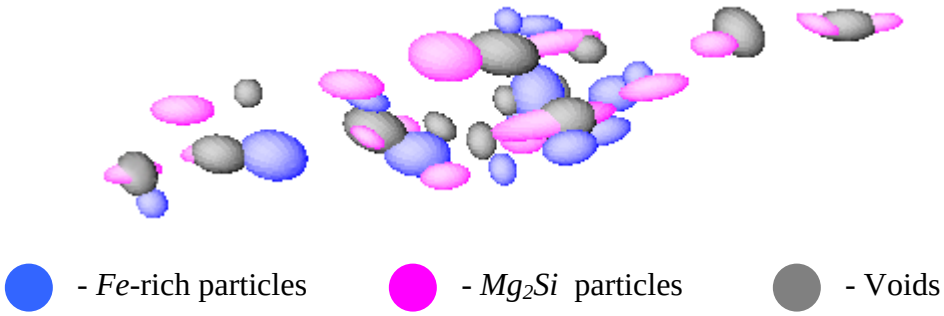

Figure 2.16: Ellipsoid representation if particle/void cluster in undeformed AA5182 sheet (Detail A of Figure 2.15).

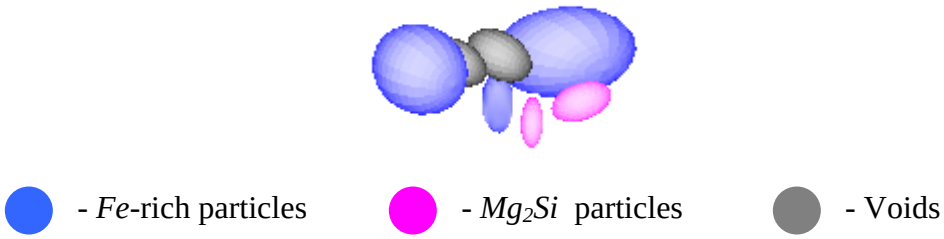

Figure 2.17: Ellipsoid representation of fractured *Fe*-rich particle with void in undeformed AA5182 sheet (Detail B of Figure 2.15).

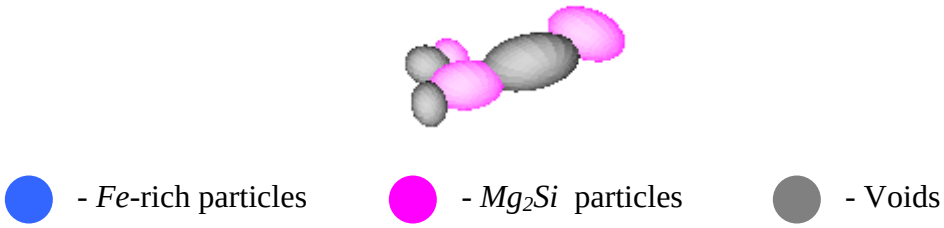

Figure 2.18: Ellipsoid representation of fractured *Mg_2Si* particle with void in undeformed AA5182 sheet (Detail C of Figure 2.15).

The void axis plots show a different preferred orientation compared to the particle data. Here, the voids are elongated along the Z-axis. This difference from the particles can be explained by the fact that most of the voids in as-received AA5182 are due to second phase particle decohesion and fracture during the cold rolling process (Figure 2.10). Thus, the voids represent the empty inter-particle volume between the two parts of the original particle and have a shape close to that of a thin disk. Thus, voids are typically oriented perpendicular to the rolling direction. Voids are mostly associated with such second phase particles.

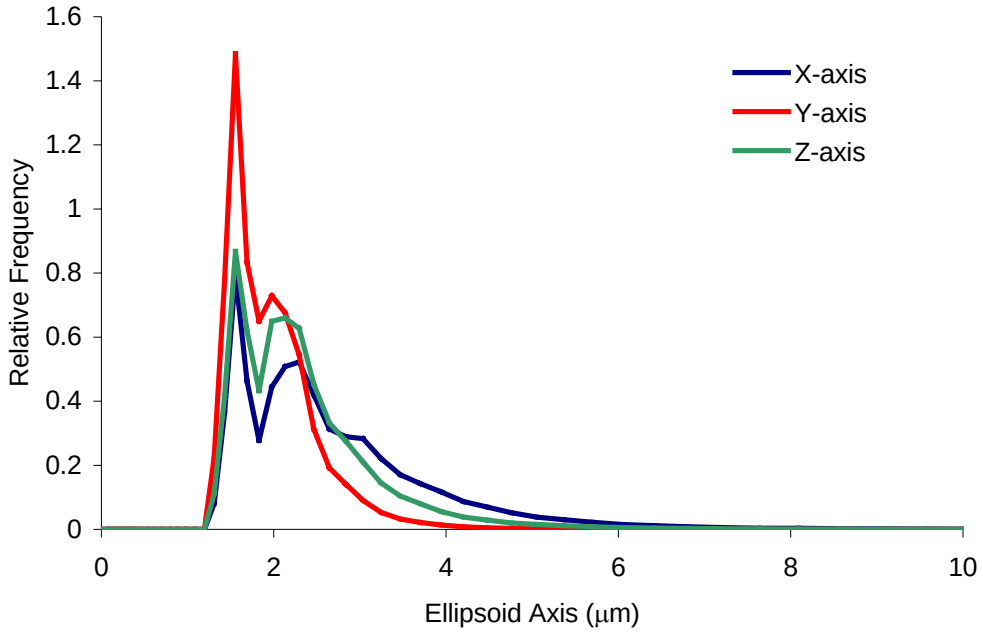

Figure 2.19: Distribution of *Fe*-rich particle axes.

The three-dimensional second phase particle field consisting of ellipsoids calculated from the tomography data was also used to obtain two-dimensional sections in the long- and short-transverse sections. This method of particle and void elliptical section acquisition was chosen, as opposed to thresholding of raster (consisting of pixels)

sections of the original voxel array, because the resolution of the 3D voxel images (0.7μm) does not allow for adequate ellipse shape approximation. The area of a pixel (0.7μm x 0.7μm) in an image obtained through voxel array sectioning is more than 5 times larger than the area of an optical micrograph pixel (0.303μm x 0.303μm). The ellipsoid sectioning method, however, allows elliptical sections of any size to be obtained and better captures the left side of an ellipsoid axis distribution (e.g. Figures 2.22 and 2.23 compared to Figures 2.5 and 2.6), which is crucial for accurate ellipsoid reconstruction. Figures 2.22 and 2.23 are based on the results of an image analysis performed on the collected two-dimensional sections using the tessellation program developed by Lievers (2004).

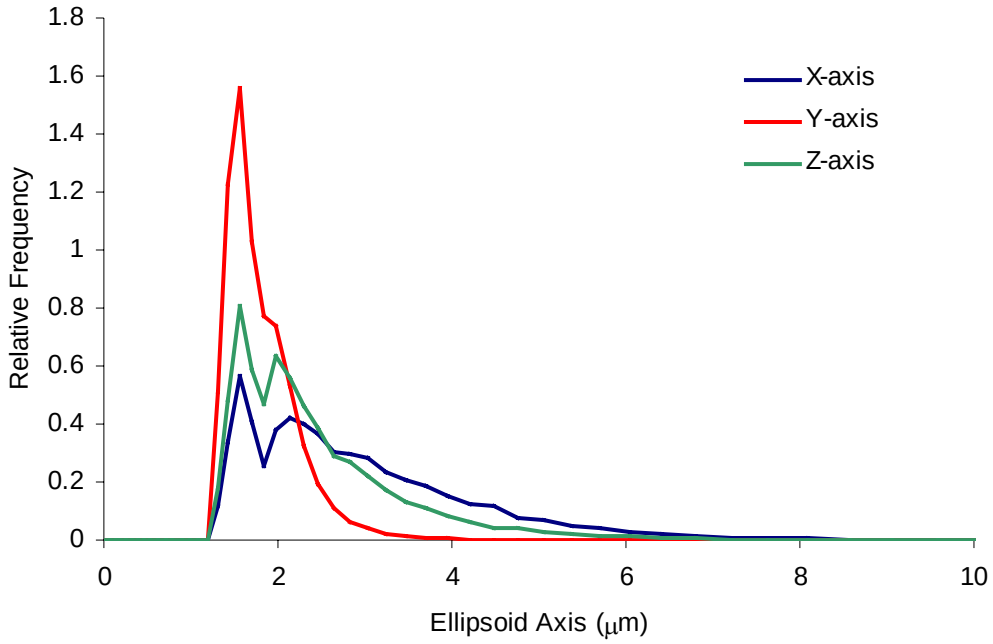

Figure 2.20: Distribution of *Mg_2Si* particle axes.

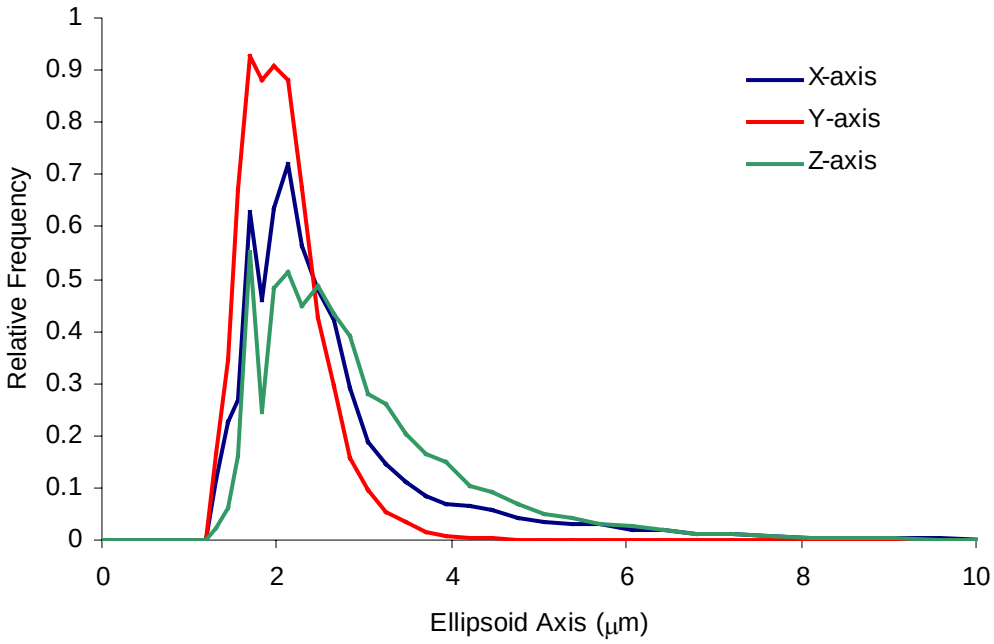

Figure 2.21: Distribution of void axes.

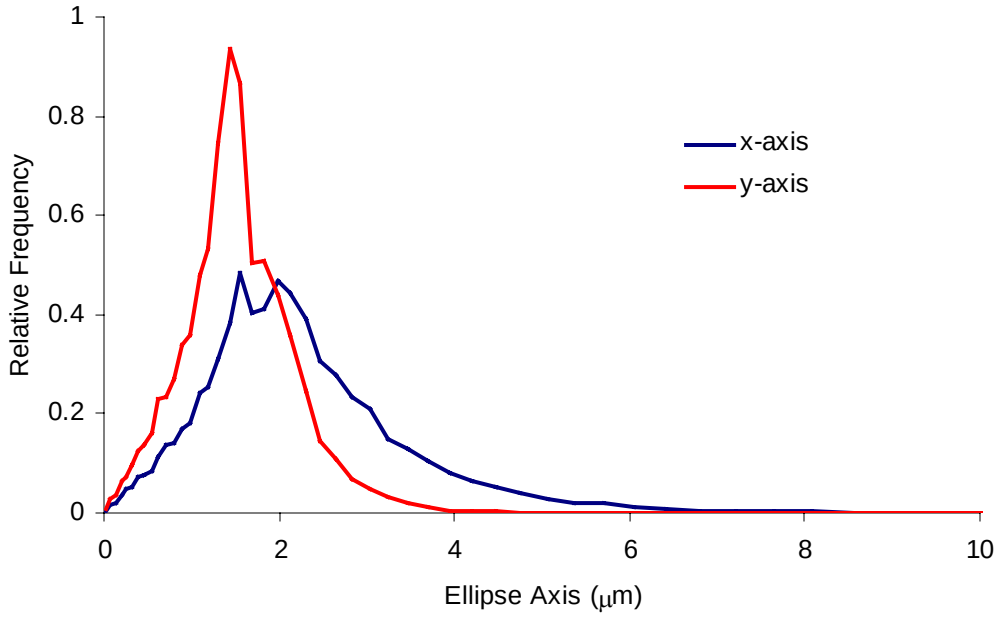

Figure 2.22: Distributions of *Fe*-rich particle ellipse axes in the long-transverse section obtained with X-ray tomography.

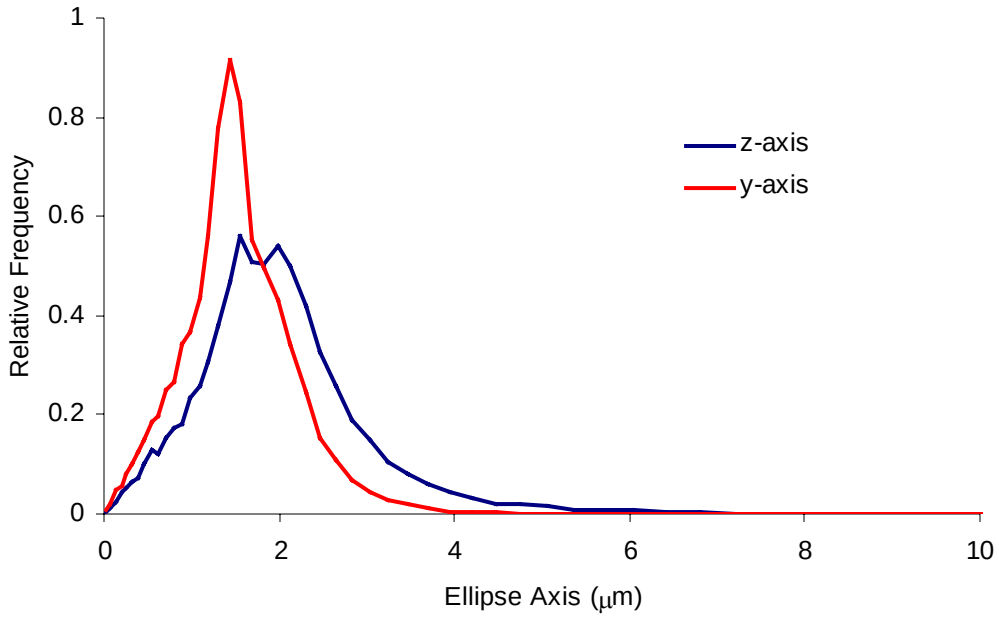

Figure 2.23: Distributions of *Fe*-rich particle ellipse axes in the short-transverse section obtained with X-ray tomography.

2.1.3.2 Particle-void clustering

The entire thresholded second phase particle field was represented as three sets of ellipsoids corresponding to voids, Mg_2Si particles, and *Fe*-rich particles using Equation 2.5. This acquired population of three-dimensional ellipsoids, as positioned within the considered volume, was then tessellated with a matrix erosion method using in-house software (Figure 2.24). The centroids of all ellipsoids were placed in a voxel array of the same size as the original tomographic image and the matrix between the centroids was eroded until the newly formed boundaries met a neighbouring boundary. This process enables information concerning particle nearest neighbours to be collected.

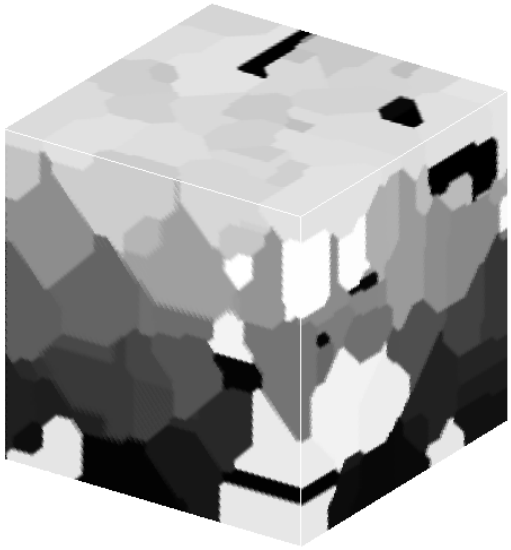

Figure 2.24: Second phase particle field spatial tessellation (70x70x70μm volume).

The three-dimensional tessellations provided information about second phase particle field spatial (3D) clustering in the form of an inter-particle distance (IPD) distribution, which was calculated as the minimum of all the IPDs between the particle and its nearest neighbours. This information along with the inter-particle distance distributions in the long- and short transverse planes was used for the development of the clustering model used in the reconstruction method.

The second phase particle fields acquired from the 3D tomographic images and their 3D tessellations have been used to estimate the degree of particle and void clustering. It has been established (Table 2.4) that the majority of the second phase particle field objects in AA5182 are *Fe*-rich particles (about 83%). Mg_2Si particles add another 10%, which are primarily clustered with each other and *Fe*-rich particles. Almost all voids are in clusters since they nucleate from fracture of second phase particles during cold rolling of the sheet material. The voids represent about 7% of the objects in the AA5182 second phase particle field. Inter-particle distance distributions have been calculated separately for the three types of objects to allow later particle reconstruction of

one type at a time. The first IPD distribution considered only *Fe*-rich particles. The second IPD distribution was calculated for Mg_2Si particles taking into account not only particles of this type, but also *Fe*-rich particles. Finally, the IPD distribution for voids was calculated taking into account objects of all three types. The results of the IPD calculations are shown in Figure 2.25. Also shown, is the expected distribution of a hypothetical random particle field for comparison purposes.

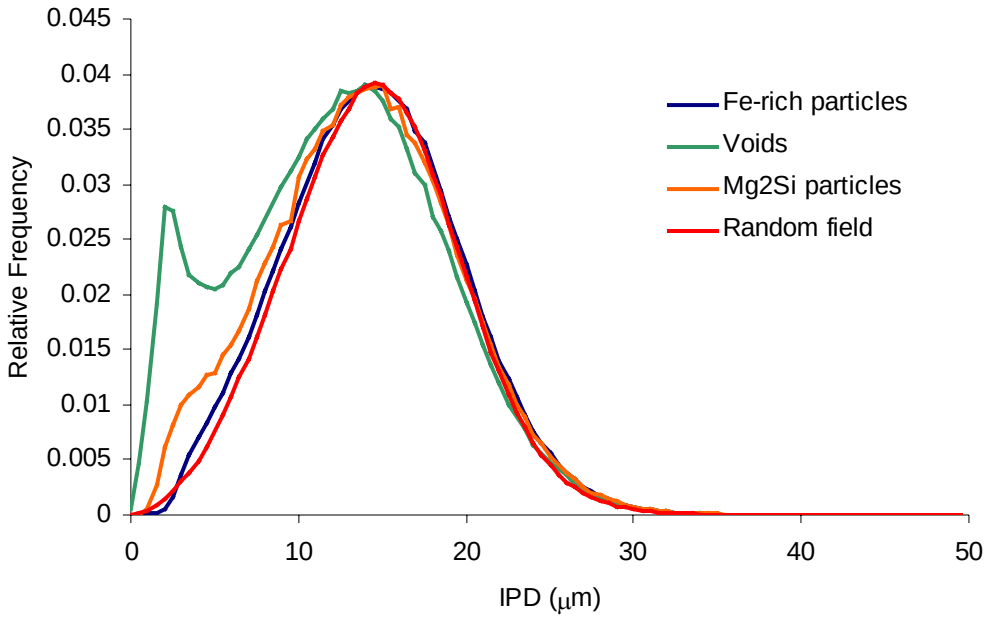

Figure 2.25: Second phase particle field object IPD distributions.

Table 2.4: 3D second phase particle field objects (numbers per 1 mm^3).

Fe-rich	Mg_2Si	Voids	*Fe*-rich PVI	Mg_2Si PVI
659127	77045	55889	28103	33439

The following assumptions can be adopted based on examination of the data in Figure 2.25. The *Fe*-rich particles can be considered to be randomly distributed. Only minor deviations of their IPD distribution from that of an absolutely random particle field exist. The Mg_2Si particles show a certain degree of clustering with each other and with *Fe*-rich particles. The void IPD distribution has a strong peak at roughly 2-4 μm, confirming the assumption that these objects are highly clustered. The low IPD values result from their proximity to second phase particles due to nucleation via matrix decohesion or particle fracture.

The analysis of the tomographic data showed that there is almost the same number of particle-void interfaces (PVI) as the number of voids in the material (Table 2.4). This observation suggests that virtually all of the voids have nucleated from second phase particles during cold rolling. The percentages of the voids adjacent to *Fe*-rich and Mg_2Si particles also were obtained from the tomographic images and consisted of about 46% and 54%, respectively.

2.2 Material reconstruction

2.2.1 Second phase particle size and shape reconstruction method

Many researchers have attempted to address the problem of reconstructing 3D objects within an opaque body based on data from 2D sections since the beginning of the twentieth century. Some of the fundamental work has been carried out by Wicksell (1925) who has developed relations for the determination of spheroid diameters from the measurement of circular section diameters. This work was later extended to the case of

ellipsoids of rotation (Wicksell, 1926). The particles of interest were prolate or oblate ellipsoids, with constant form or shape. The developed relations were shown to be true regardless of eccentricities and axis orientation of the corpuscles. The solution was also adapted for the case of a non-analytical expression for circular section diameter distributions, since this data is usually represented in terms of a series of numerical values obtained from direct measurements.

One of the later attempts to characterize spheroid fields composed of ellipsoids of revolution was performed by Cruz-Orive (1976). This work considered prolate or oblate ellipsoids with variable principle semi-axes. With the introduction of an ellipse eccentricity parameter and taking minor and major semi-axes as the size parameters for prolate and oblate ellipsoids, respectively, the whole population of ellipses in the section was represented by a bivariate distribution. Cruz-Orive (1978) later extended this work with a discrete version using size-shape histograms.

The 3D particle field reconstruction method employed in the current work is a modified version of Wicksell's (1925, 1926) and Cruz-Orive's (1976, 1978) techniques for image acquisition of 3D objects. It is capable of determining the statistical distributions of ellipsoid dimensions in 3D space using 2D section data obtained from two orthogonal planes of the specimen. The relation between the size distribution of spherical objects and their sections developed by Wicksell is presented below.

An opaque body containing a large number of spherical or ellipsoidal particles was considered (Wicksell, 1925). The particles are of different sizes, but their spatial distribution density and size distribution are considered to be the same in all parts of the body. The diameter distribution of the particles is expressed in terms of the diameter distribution of the circles found on a section of the body. The following notation was introduced: $F(r)$ - the frequency function of the diameters *r* of the particles, $f(r)$ - the frequency function of the diameters of the particles cut by the section plane, and $\phi(x)$ -

the frequency function of the diameters *x* of the circular sections in the section plane. The solution for the distribution of particle diameters was obtained by Wicksell (1925), in the following form:

$$F(r) = -\frac{2rr_0}{\pi}\int_x^R \frac{d\left(\frac{\phi(x)}{x}\right)}{\sqrt{r^2 - x^2}}\frac{dx}{\sqrt{x^2 - r^2}} = \frac{2rr_0}{\pi}\int_0^{\sqrt{R^2-r^2}} P(\sqrt{l^2 + r^2})dl \qquad (2.6)$$

where $P(x) = -\frac{1}{x}\frac{d\left(\frac{\phi(x)}{x}\right)}{dx}$.

The Cruz-Orive's method has been designed for non-equiaxed ellipsoids of revolution, prolate or oblate, whereby only two dimensions defining the ellipses are required to statistically characterize the entire bulk population. In order to correlate data obtained from the two perpendicular sections and reconstruct three-dimensional ellipsoids, certain assumptions are made. Second phase particles in sheet metal fabricated through a rolling process are assumed to be close to oblate and elongated along the rolling direction. All particles are regarded as triaxial ellipsoids whose principal axes correspond to directions orthogonal to the long- transverse, short-transverse and rolling planes (Figure 2.1) of the sheet. Since two ellipsoid axes are considerably larger than the third axis through the thickness of the sheet, a reasonable degree of accuracy can be obtained from using an ellipsoids-of-revolution assumption on each of the orthogonal sections. Here, ellipsoid axes are denoted as *X*, *Y*, *Z* and section ellipse axes as *x*, *y*, *z*. The two orthogonal sections (long- and short-transverse) of a specimen both contain information about one common ellipse axis *y* that can be used to relate the acquired size distributions from the two sections. With these assumptions, the distributions of 3D particle dimensions can be reconstructed from 2D metallographic data.

The technique developed by Wicksell (1926) is based on the assumption that the ellipsoids are of constant shape. However, in the current study, the aspect ratio of the ellipses varies; therefore, it is necessary to divide them into shape classes. Since sections are made orthogonal to the ellipsoid axes, the aspect ratios of the ellipses and the original ellipsoids are identical. The bivariate distributions of the ellipse dimensions are transformed into bivariate distributions of the size and shape parameters. The shape parameters are $1-\left(\frac{y}{x}\right)^2$ and $1-\left(\frac{y}{z}\right)^2$ for the long- and short-transverse sections, respectively. The values of the shape parameters vary from 0 to 1, indicating a circle when 0 or a very elongated ellipse as unity is approached. The dimensions of the ellipses are of log-normal distribution. Therefore, it is convenient to use a logarithmic scale when dealing with such distributions. The size parameters are the *x* and *z* axes, since they are the major axes of the ellipses and are required for calculating the ellipsoid axes in Wicksell's procedure. In the case of *y* being the major axis, it was swapped with the corresponding minor axis to keep the shape parameter within the 0 – 1 range. The acquired data were converted from the axis-axis distributions into size-shape distributions. The ellipse size-shape distributions were used as bivariate histograms or two-dimensional arrays. The obtained arrays can be thought of as sets of one-dimensional arrays with size probability density functions representing each shape class. Therefore, Wicksell's procedure can be applied to each row of shape class independently. By merging the resulting univariate distributions of the shape classes into one two-dimensional array, a bivariate ellipsoid size-shape distribution for each section is obtained.

Following this step, size distributions of ellipsoids of rotation can be reconstructed using data from either of the two orthogonal sections. In addition, the two bivariate distributions contain sufficient information to reconstruct three-dimensional

ellipsoid particle population. It is noted that the *Y*-axis is the common axis and is included implicitly in both distributions. One of the ellipsoid bivariate distributions is converted back in the form of an axis-axis distribution.

In brief, the three-dimensional ellipsoid reconstruction technique is as follows:

1. Generation of size and shape parameters using the size-shape distribution of the long-transverse section
2. Determination of the *X* and *Y* ellipsoid axes, and
3. Generation of the *Z*-axis from known *Y*-axis using the converted *Z*-*Y* distribution.

Other important material parameters that relate to the ellipsoid size-shape distribution are the number of particles per unit volume and particle volume fraction. The reconstruction procedure should be performed with reasonable care and precision, as a change in one parameter will inevitably affect the other. A source of inaccuracy may be due to numerical integration using small numbers of size-shape classes in the Wicksell procedure. If distortion of the size-shape distribution is unavoidable, either the number of particles or the particle volume fraction parameter should be fixed, and the other parameter will be determined by the size-shape distribution. The number of particles was fixed during the reconstruction procedure. This parameter affects the resulting IPD distribution of the reconstructed field, which is used to assess particle clustering. It is necessary to use equal numbers of particles in the reconstructed particle field and the original measured particle field in order to obtain IPD distributions that can be compared.

The microstructure reconstruction software ultimately allows the production of particle fields of any volume with characteristics representing that of the materials sampled on two orthogonal planes. The generated 3D particle field can be tested for resemblance to the original field by taking 2D sections along the long- and short-transverse planes and comparing the size-shape distributions and inter-particle distance

plots to those of measured from the real metallographic sections of the material. What remains is to position the particles and voids within the volume, as described in the next section.

The sensitivity of the proposed second phase particle size and shape reconstruction method to parameters that affect results, namely the threshold grey-scale levels, of reconstruction is discussed in Appendix A. In general, the deviation in the thresholds does not affect dramatically most of the output ellipsoid axis distributions. The threshold T_1 has the highest influence on the output particle/void fields. This leads to the change in material porosity; however, the actual porosity is a very small quantity for this material

2.2.2 Second phase particle placement and clustering

Real second phase particle fields display a form of random-clustered IPD distribution; hence, it is necessary to establish parameters describing this distribution for use in particle placement within the 3D reconstruction algorithm. A certain portion of the particles are located close to each other, forming particle clusters. Cluster shape and inter-particle distance within clusters need to be specified. In the current work, a “chain-like clustering” model (Everett, 1993) was utilized to simulate the stringer-like clustering observed in the rolled sheet microstructure (Figure 2.11). Stringers are assumed to be oriented along the rolling direction. They are generated as a series of particles located along some path in the rolling direction. The main parameter in generating chain-like clusters is the probability that the next generated particle is placed next to the current. Also, if a generated particle belongs to the stringer, it is located within a specified solid angle oriented relative to the rolling direction (Figure 2.26), in this case 40 degrees was

adopted as the maximum solid angle (as discussed later in Section 2.3.2). The distance between adjacent particles is defined by a specified inter-particle distance distribution. Thus, stringers may consist of objects of different types. A special rule exists for voids in clusters. They are placed adjacent to the previous particle in order to simulate or mimic particle fracture and decohesion observed in the actual microstructure.

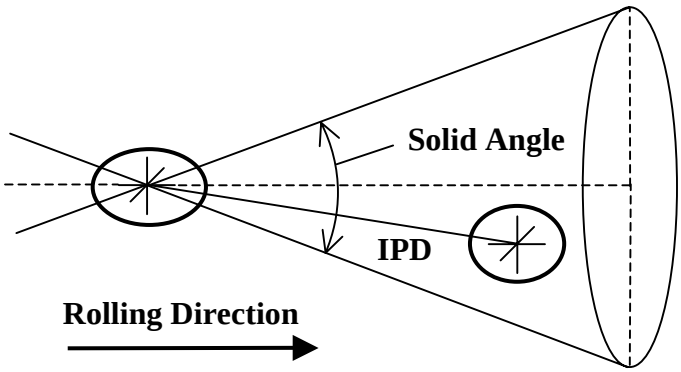

Figure 2.26: Placement of clustered particles.

The adopted particle placement procedure is summarized as follows (Figure 2.27). The first step was the placement of *Fe*-rich particles randomly within a prescribed volume. For each *Fe*-rich particle, three ellipsoid axes were generated using reconstructed *Fe*-rich particle ellipsoid axis distributions. Each particle was then placed randomly within the volume of interest. This subroutine was repeated until the maximum number of *Fe*-rich particles that can be accommodated the volume was reached. A similar procedure was performed for Mg_2Si particles with the only difference that Mg_2Si particles could be placed next to *Fe*-rich particles and already created Mg_2Si particles with a certain probability *p* governing cluster membership. If a Mg_2Si particle belonged to a cluster according to *p*, an IPD value and a random orientation within the solid angle were

generated. The IPD values were considered to follow a normal distribution, which was calibrated through a parametric study, as discussed later. The placement of Mg_2Si particles stopped when the maximum number of these particles in the volume was reached. Finally, void ellipsoids were generated using the reconstructed void ellipsoid axis distributions and placed adjacent to second phase particles of both types until the maximum number of voids in the volume was reached.

2.3 Second phase particle field reconstruction results

For comparison purposes, the reconstruction technique was applied using section data acquired using both optical microscopy and X-ray tomography. Unfortunately, key differences exist in the treatment of the second phase particle populations acquired using the two techniques. The optical technique could not distinguish between particle types, whereas the X-ray tomography could detect *Fe*-rich and Mg_2Si particles separately. The optical method was also unable to reliably distinguish voids from particles. Nevertheless, the following outlines the results of particle/void size and shape reconstruction from the two image types and the calibration of the various parameters chosen to capture material clustering. Reconstructed voids and second phase particles as well as their spatial distribution are compared to those from direct 3D tomography measurement of the original material. An example of a reconstructed field is shown in Figures 2.28 and 2.29.

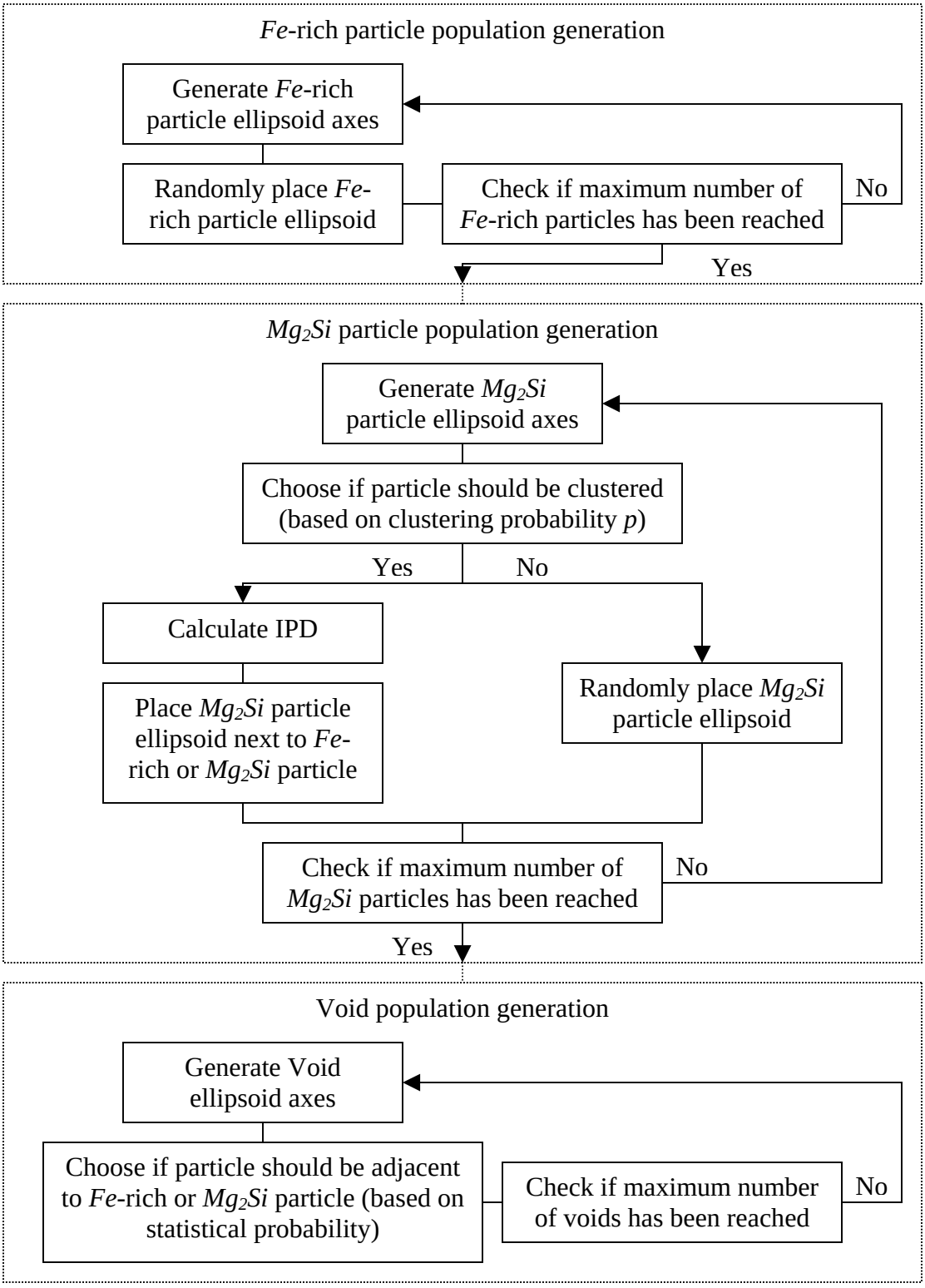

Figure 2.27: Second phase particle field reconstruction algorithm.

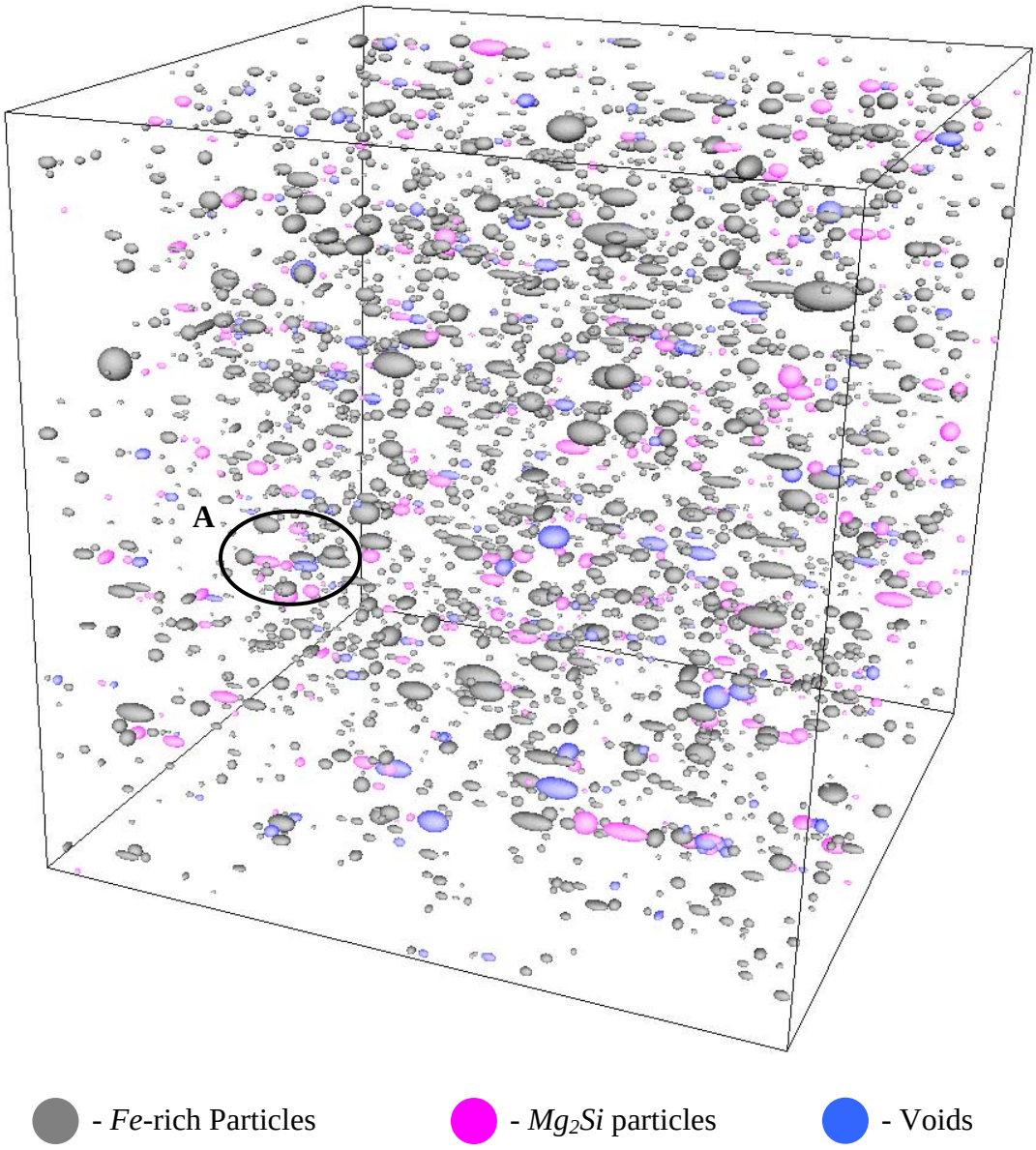

Figure 2.28: Reconstructed second phase particle field based on data from orthogonal sections of the second phase particle field acquired using X-ray tomography (200x200x200 μm, p=80%, m=0.7μm, σ=3μm). A – particle/void cluster.

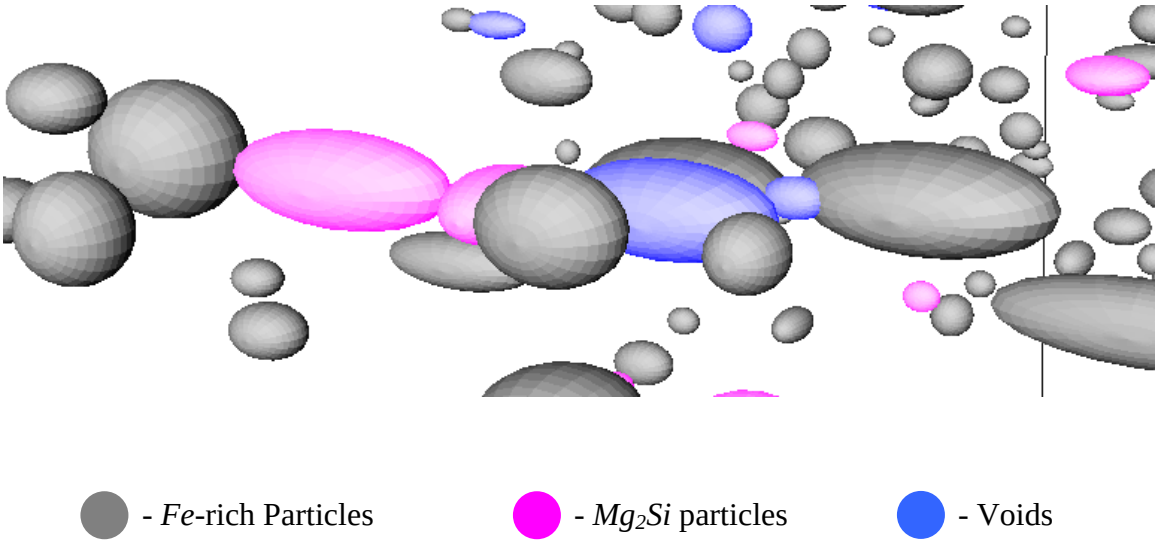

Figure 2.29: Particle/void cluster (Detail A of Figure 2.23).

2.3.1 Second phase particle size distribution reconstruction

The comparisons of the measured and reconstructed ellipse axis distributions in the long- and short-transverse sections are shown in Figures 2.30 – 2.36. The comparisons are provided both for the entire population of objects reconstructed from optical micrographs and for the *Fe*-rich particle population (consisting of about 83% of the total number of objects and defining the shape of cumulative ellipse axis distributions) reconstructed from the tomographic images (Figures 2.30 – 2.33). The respective comparisons of *Fe*-rich particle ellipsoid axis distributions are presented in Figures 2.34 – 2.36. Generally speaking, the reconstructed particle dimensions capture the trends of the original particle field. There is, however, a major discrepancy between the ellipse and ellipsoid axis distributions obtained from the optical micrographs and those obtained from the tomographic images.

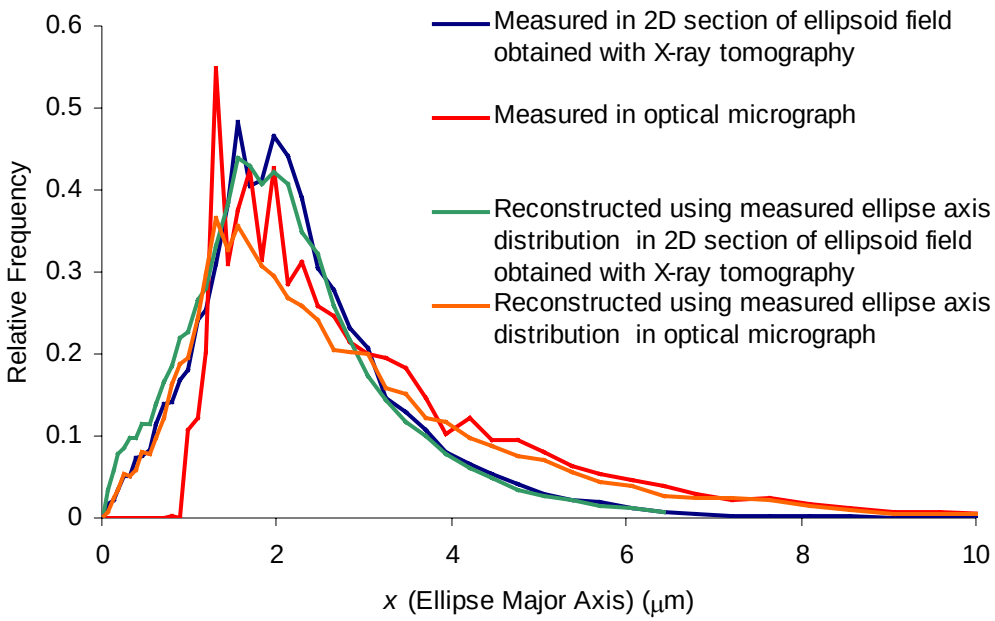

Figure 2.30: Distributions of measured and reconstructed ellipse major axes in the long-transverse plane.

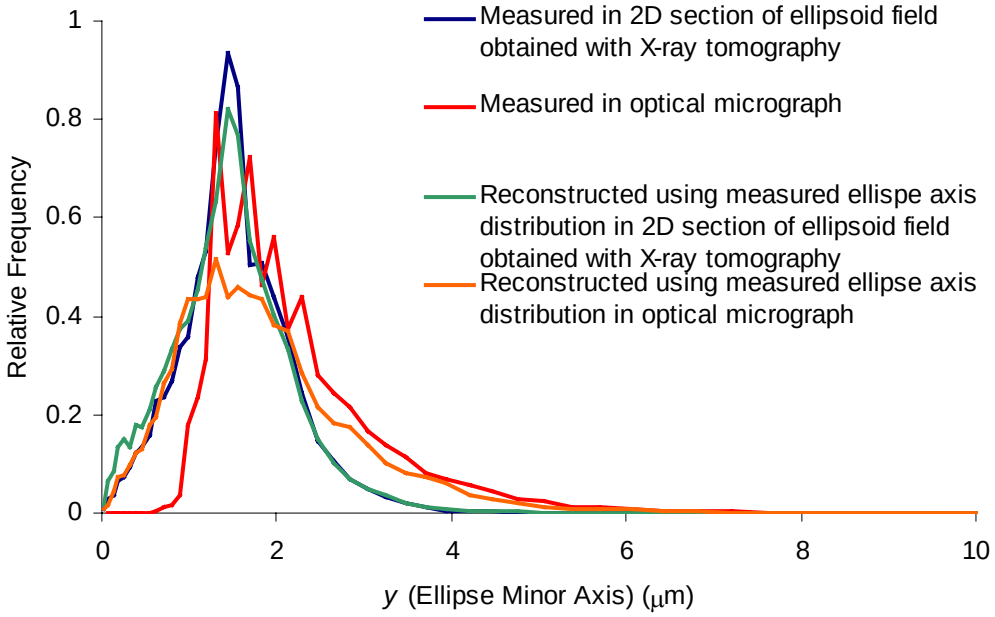

Figure 2.31: Distributions of measured and reconstructed ellipse minor axes in the long-transverse plane.

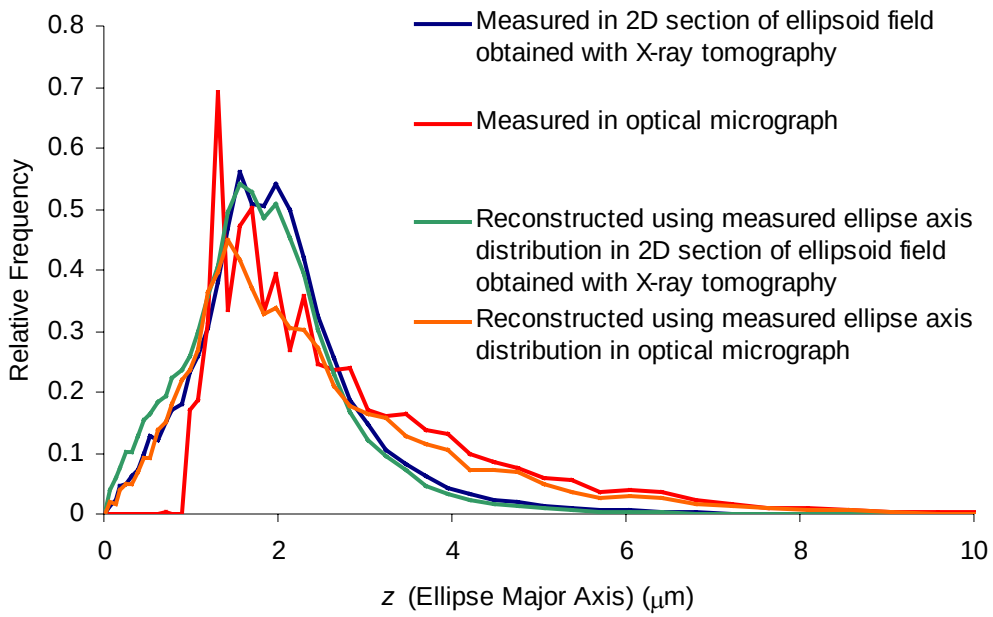

Figure 2.32: Distributions of measured and reconstructed ellipse major axes in the short-transverse plane.

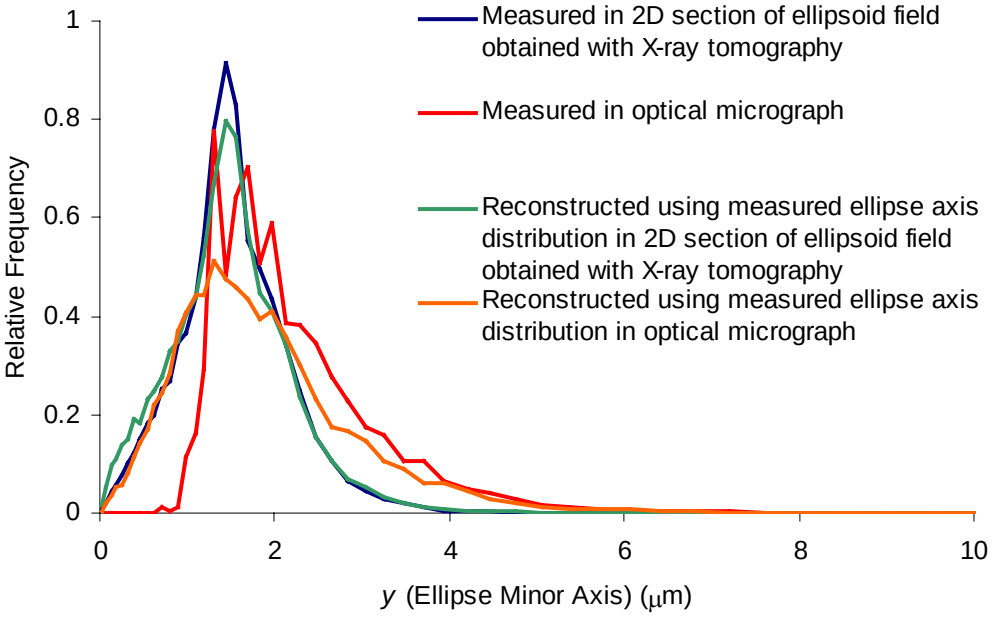

Figure 2.33: Distributions of measured and reconstructed ellipse minor axes in the short-transverse plane.

The curves in Figures 2.30 – 2.33 corresponding to the measured results in optical micrographs have zero ordinate values in the left-hand side of the plots because the plots were produced using raster images (consisting of pixels and, thus, discrete), whereas all of the other curves were obtained by sectioning particles approximated with ellipsoids. While processing the 2D raster images, smaller particles of sizes under a certain threshold value of 0.36 μm^2 are removed since their shapes cannot be properly captured with low numbers of pixels. When the truncated input ellipse distributions are used, the reconstruction method produces section ellipse size distributions slightly deviating from the corresponding distributions obtained by sectioning the tomography-based 3D particle field. However, the measured and reconstructed results of both 2D ellipse and 3D ellipsoid sizes based on the tomographic data are in reasonable agreement suggesting that the proposed method is adequate for the considered problem of particle field size-shape reconstruction.

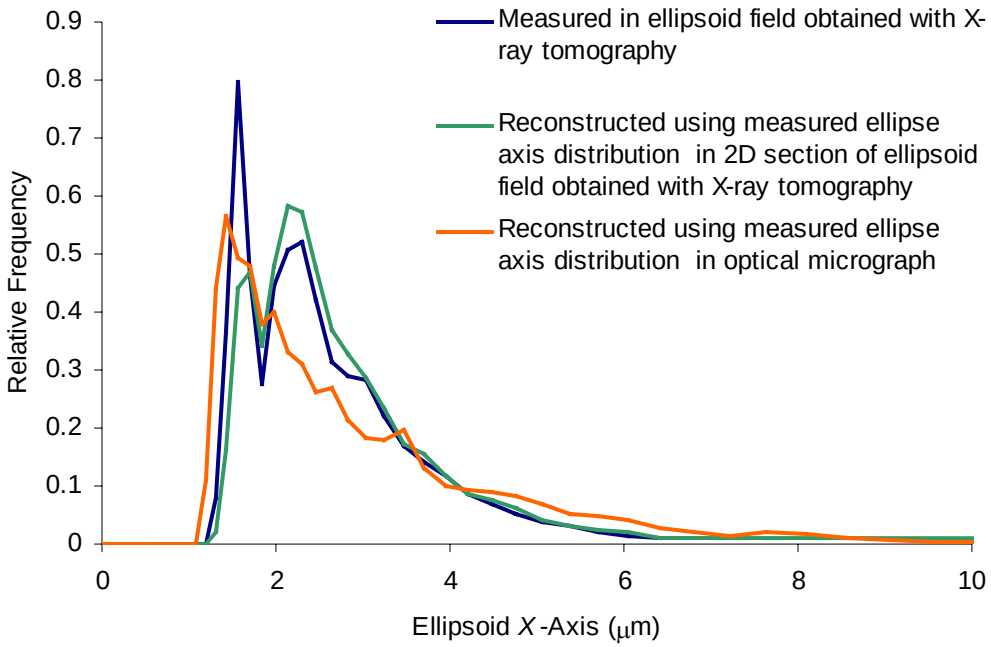

Figure 2.34: Distributions of measured and reconstructed ellipsoid X-axes.

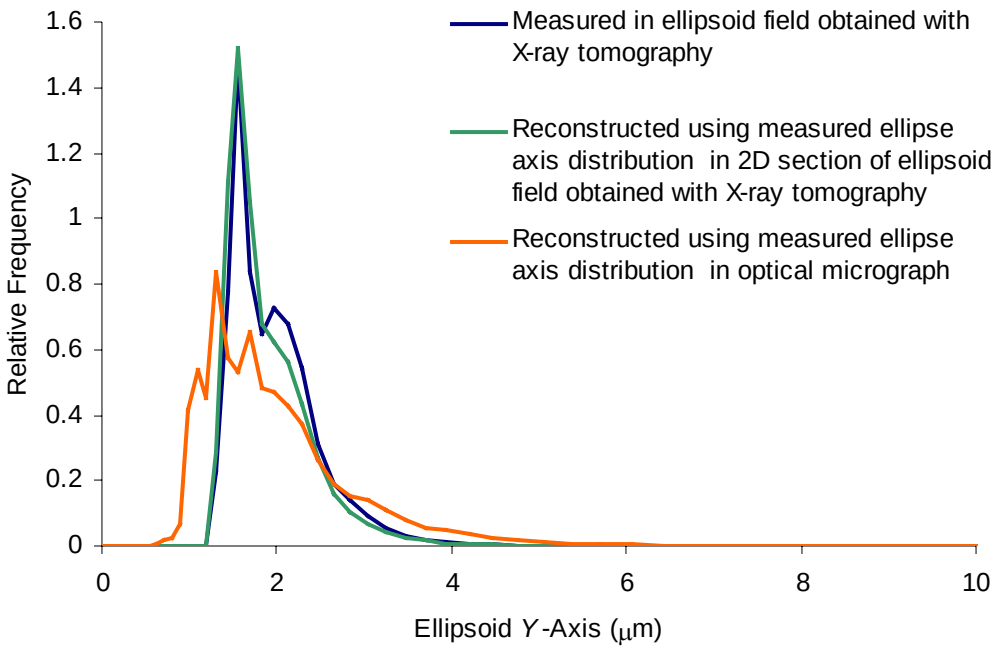

Figure 2.35: Distributions of measured and reconstructed ellipsoid *Y*-axes.

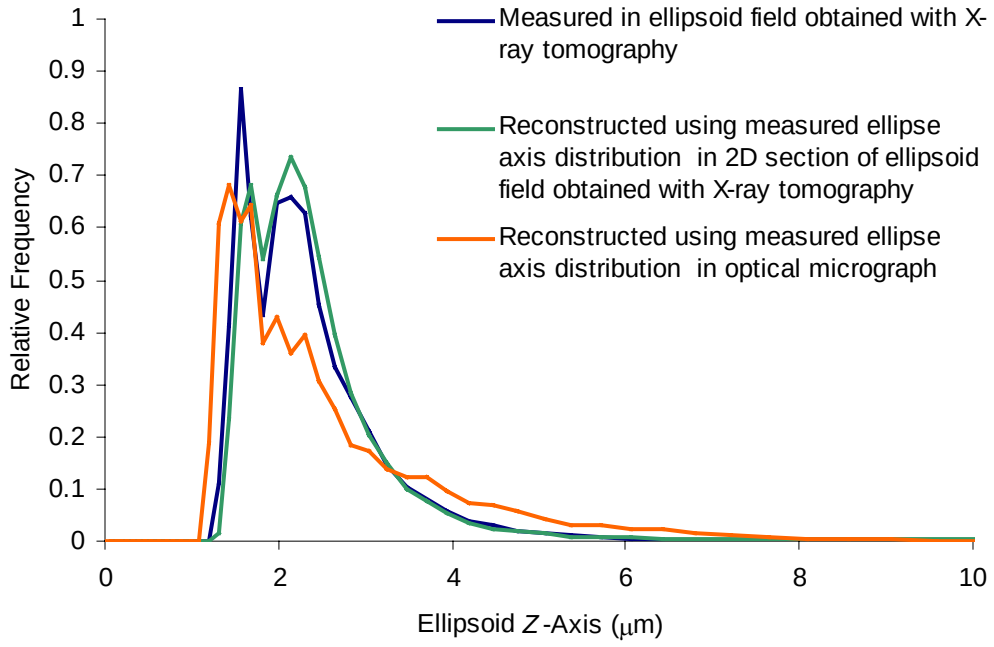

Figure 2.36: Distributions of measured and reconstructed ellipsoid *Z*-axes.

2.3.2 Second phase particle spatial arrangement reconstruction

The solid angle relative to the rolling direction that defines particle stringer geometry (Figure 2.26) was varied within the range from 0 to 70 degrees. The results of the study showed that the angle had no significant effect on the resulting IPD distributions. An arbitrary value of 40 degrees has been chosen for the cluster solid angle for all reconstructions.

It was assumed that the IPD distribution of Mg_2Si particles in a cluster followed a normal distribution. This required two additional parameters (mean particle spacing, m, and standard deviation, σ) to be established. A parametric study was undertaken to select the IPD normal distribution parameters and the clustering probability for the Mg_2Si particles. The ranges of the sought parameters, namely, m, σ, and p were 0 – 3μm, 0 – 4μm, and 0 – 100%, respectively. A set of second phase particle field reconstructions was created using these clustering parameters in order to match the Mg_2Si particle IPD distribution of the reconstructed particle fields with that of the particle field obtained with X-ray tomography. The results of the parametric study indicated that m=0.7μm, σ=3μm, and p=80% provided a suitable distribution for the Mg_2Si particles (Figure 2.37).

The particle placement procedure is the same for second phase particle field reconstruction using optical micrographs for which there was no distinction between the size-shape distributions of the different object types. All three object types utilize common size distributions. The clustering percentage, IPD parameters, and ratios of voids adjacent to *Fe*-rich and Mg_2Si particles are used the same as described above.

The measured and predicted inter-particle distance distributions of the reconstructed 3D second phase particle fields are shown in Figures 2.38 and 2.39. Figures 2.38 and 2.39 show the in-plane IPD distributions taken for the long- and short-transverse section. The smaller numbers of particles in optical micrographs than in X-ray

tomography images and reconstructed particle fields resulted in distribution curve scatter. Nevertheless, the trends of the measured optical data distributions can be examined. The chosen clustering algorithm mainly affects the ellipse arrangement in the long-transverse plane (Figure 2.38). The short-transverse plane shows measured and predicted inter-particle distributions similar to a random spatial particle arrangement (Figure 2.39). This is consistent with the measured IPD distributions confirming the cluster shape assumption.

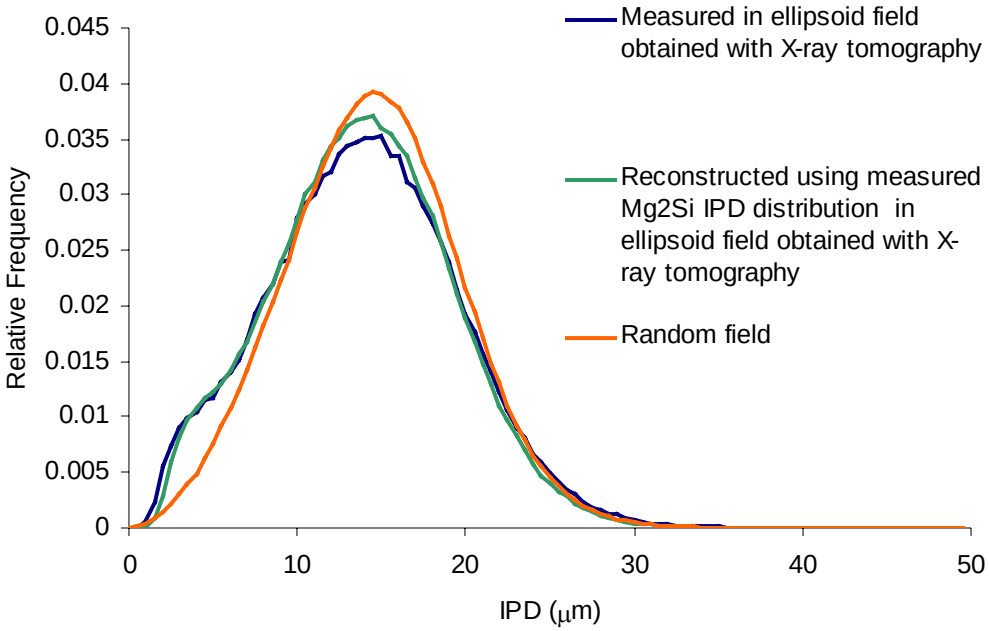

Figure 2.37: Comparison of measured and reconstructed *Mg_2Si* IPD distributions.

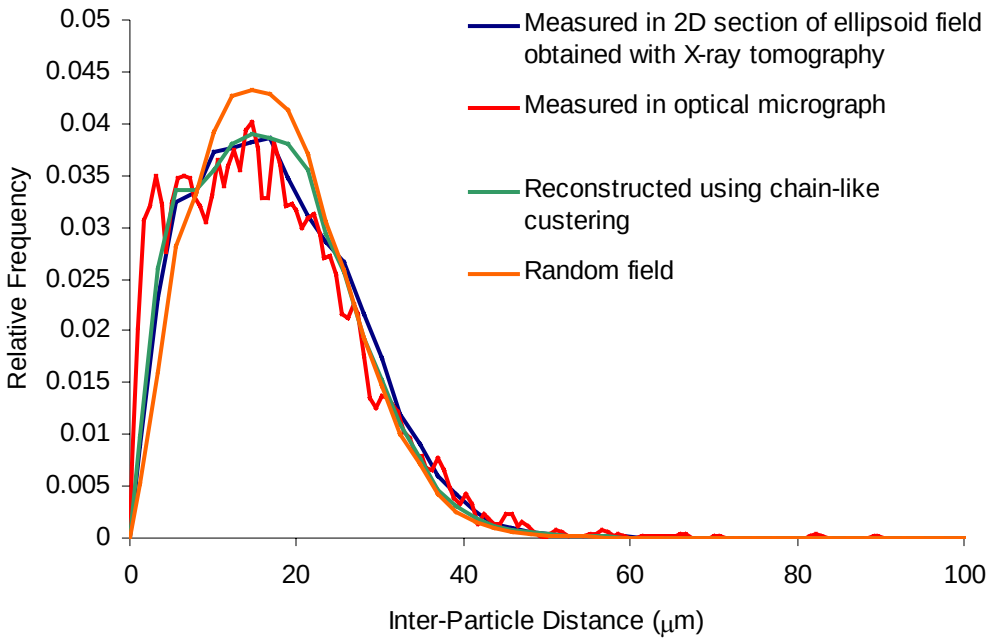

Figure 2.38: Measured and reconstructed inter-particle distance distributions in the long-transverse plane.

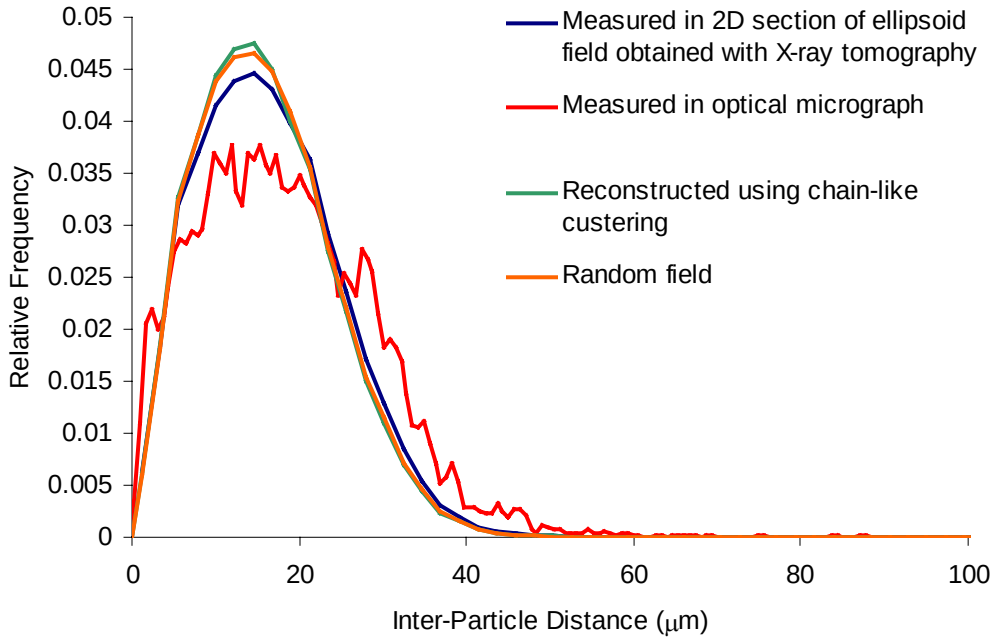

Figure 2.39: Measured and reconstructed inter-particle distance distributions in the short-transverse plane.

Summary

This chapter has presented approaches for second phase particle field characterization and reconstruction. A statistical stereological method of reconstruction of second phase particle and void fields in AA5182 has been developed. Both two- and three-dimensional metallographic images obtained with optical microscopy and X-ray tomography have been utilized for material characterization and the measurement of second phase particle and void sizes, shapes, and spatial arrangement (clustering). The information from the two-dimensional material sections has been used as an input into the particle size distribution reconstruction model. Measured particle clustering in the form of inter-particle distance distributions in both two-dimensional metallographic sections and three-dimensional tomographic images have been used for the development of a particle clustering model and determination of its parameters. The three-dimensional microstructural images have been used for the validation of the particle-void size, shape, and clustering predictions. The measured and predicted results are in relatively good agreement. Finally, the method has allowed creation of a representative material volume that can be used as input for damage evolution simulations using the three-dimensional damage percolation model.

Chapter 3

Characterization of Damage in Deformed AA5182 Sheet

In order to quantify the damage progression within the AA5182 material studied, *in situ* X-ray tomography experiments were performed. These experiments used the same tomographic facilities introduced in Chapter 2 (Maire *et. al*, 2001), with the addition of an *in situ* tensile testing apparatus. The experiments allow critical examination of how damage develops within the bulk of material and the proximity of damage to features such as particle clusters, for example. In addition, the *in situ* damage measurements are used later in this thesis (Chapter 5) to assess the predictions of the 3D damage percolation model.

3.1 *In situ* tensile test with X-ray tomography

In situ tensile testing, utilizing X-ray tomography, was conducted at the European Synchrotron Radiation Facility. The specimen, shown in Figure 2.7a, was tested in tension in a step-wise fashion and X-ray computed tomography was used to obtain three-dimensional images of the material microstructure at the end of each loading step. The specimen geometry has been developed to promote strain localization in the middle of the specimen (Figure 2.7a). Thus, plastic deformation during the test was confined to the narrowest region of the specimen. Four three-dimensional images of the studied region of strain localization have been obtained, corresponding to the four different loading (elongation) steps: 0 mm (undeformed material), 0.2 mm, 0.39 mm, and 0.81 mm. The 0 mm sample corresponds to the as-received images presented in the previous chapter. The scanned volume of the as-received AA5182 was 1000x1000x580μm and the resolution was 0.7 μm. The change of the considered volume dimension in the out-of-plane (tensile) direction due to tensile loading was accounted for. For the four acquired tomographic volumes, this dimension was 580μm, 586μm, 641μm, and 686μm. The curves of load versus displacement corresponding to the three loading stages are shown in Figure 3.1. Necking in the thinnest region of the specimen was observed at the end of the last loading stage.

The as-received tomography image corresponding to zero displacement is shown in Figure 2.8. The images corresponding to the deformed samples are shown in Figures 3.2 – 3.4. The corrected tomographic images are thresholded using the same procedure as described in Chapter 2. The resulting volumes containing second phase particles and voids are tessellated to create a list of nearest neighbours for each object in the second phase particle field and calculate the inter-particle distances. These lists are used

subsequently to characterize the effect of second phase particle clustering on damage initiation and evolution. They are also employed by the damage percolation model to limit the coalescence check algorithm to consider only the nearest objects that could potentially coalesce with the considered object.

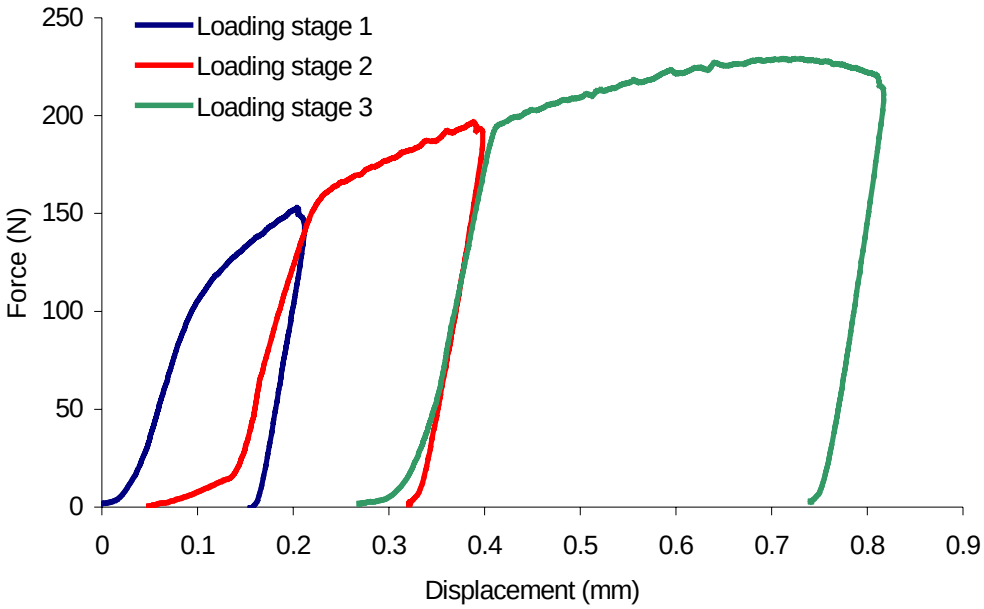

Figure 3.1: *In situ* tensile test curves of load versus displacement (three stages).

It should be noted that the deformation mode can be considered to be uniaxial tension for the first two loading stages or three material states: undeformed (0 strain), after the first stage (0.054 strain), and after the second stage (0.099 strain). At the last loading stage, there can be distinguished two regions with different stress states (Figure 3.5). The material in the middle of the specimen experiences a state with higher stress triaxiality; whereas, the surrounding material is in uniaxial tension. The average plastic strain has been calculated for both of these regions. The strain values of 0.368 and 0.394 correspond to the outer and inner material, respectively. Thus, five different strain states were considered for microstructural characterization: 0, 0.054, 0.099, 0.368, and 0.394. More details on the calculation of strain and stress triaxiality are provided in Chapter 5.

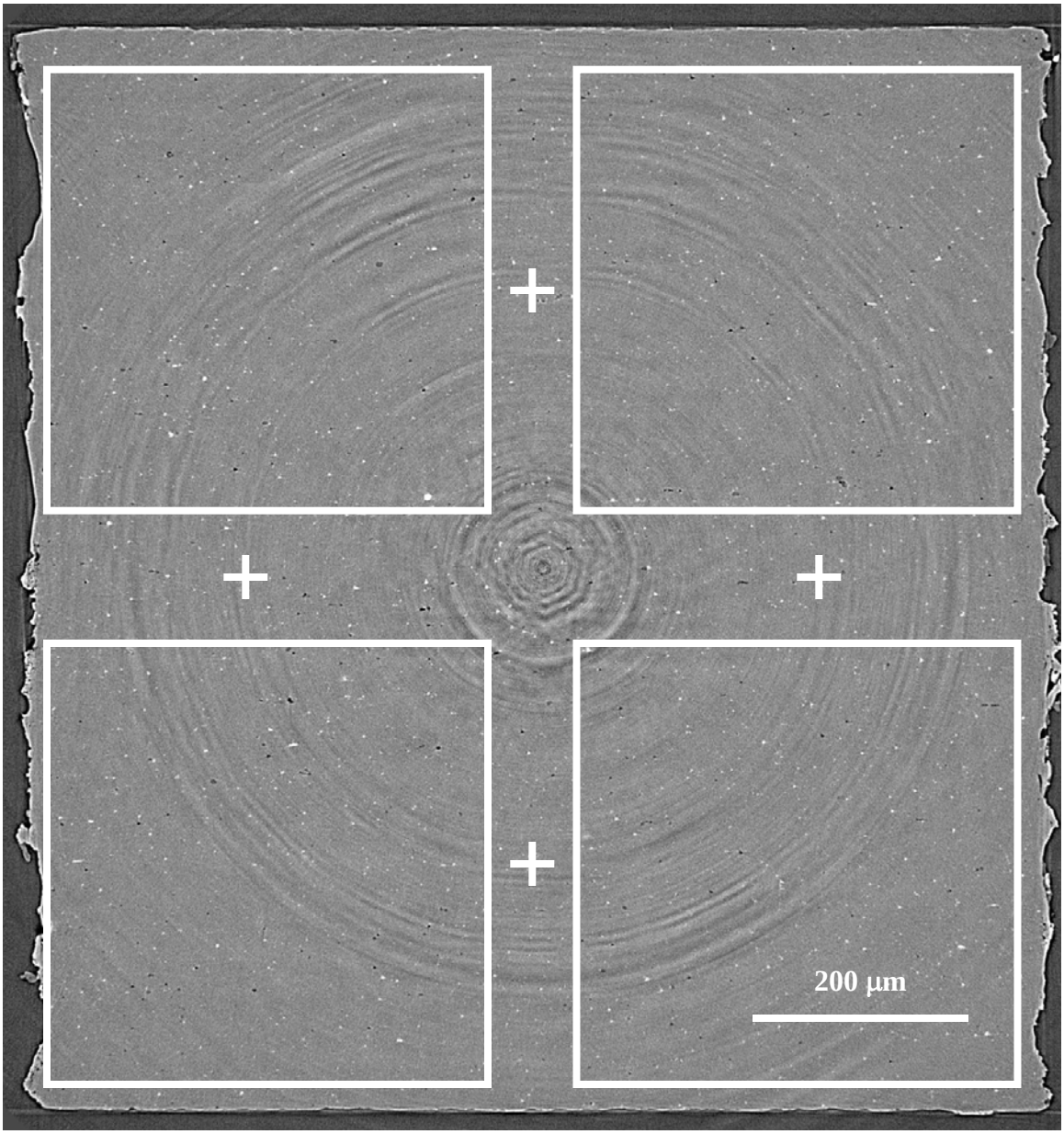

Figure 3.2: X-ray tomographic specimen cross-section after the first loading stage: assembly of a tomographic image with regions of better quality.

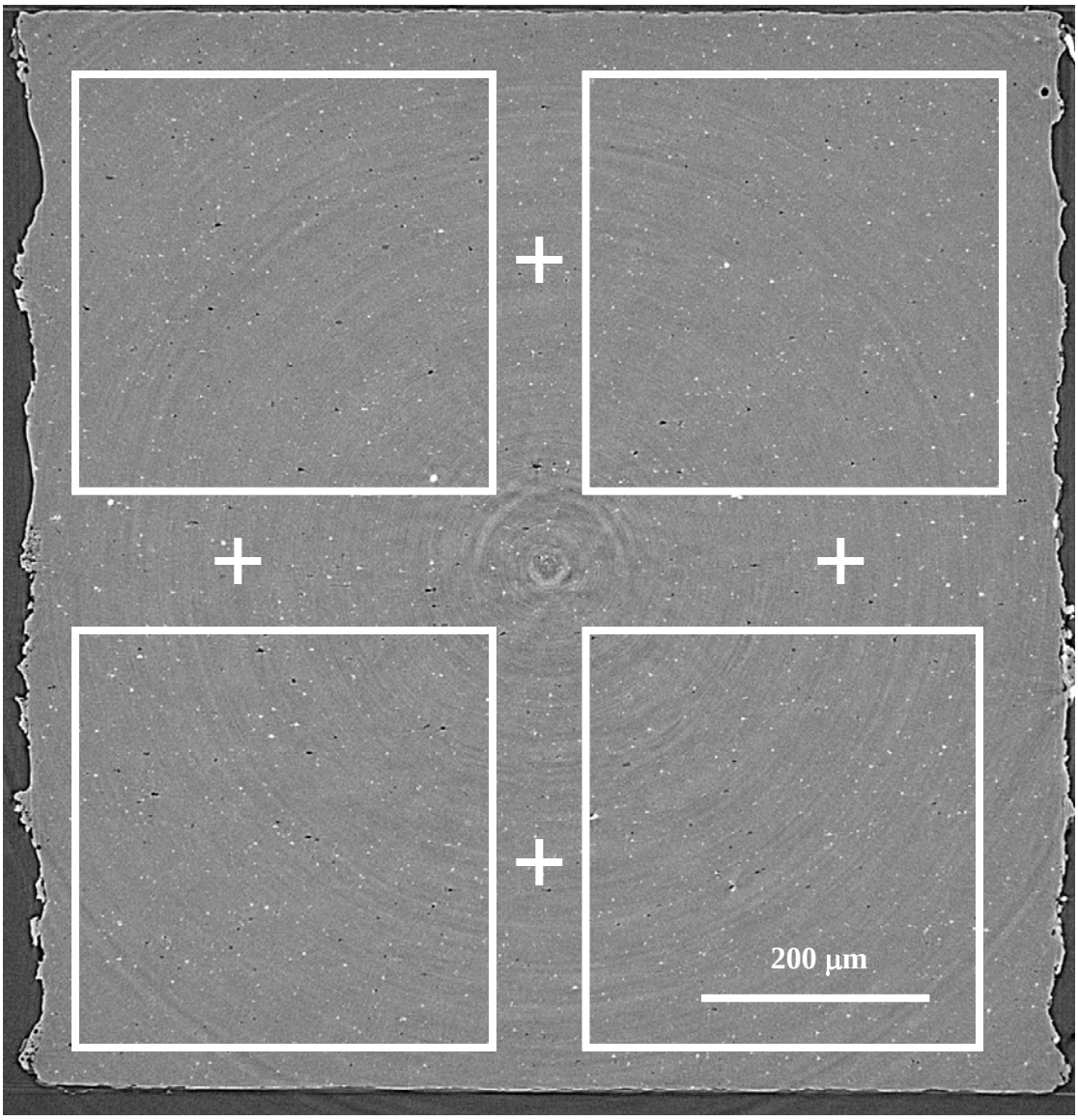

Figure 3.3: X-ray tomographic specimen cross-section after the second loading stage: assembly of a tomographic image with regions of better quality.

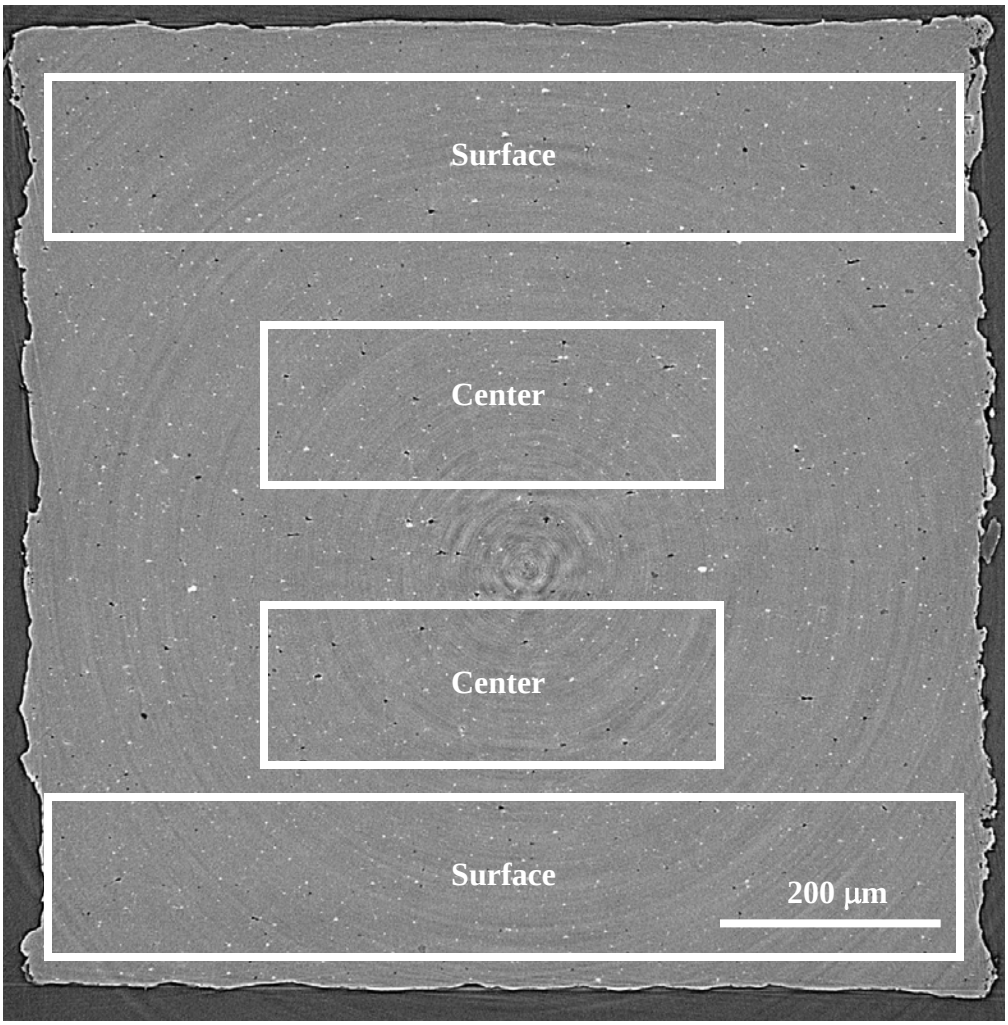

Figure 3.4: X-ray tomographic specimen cross-section after the third loading stage and regions with different stress triaxiality used for damage characterization.

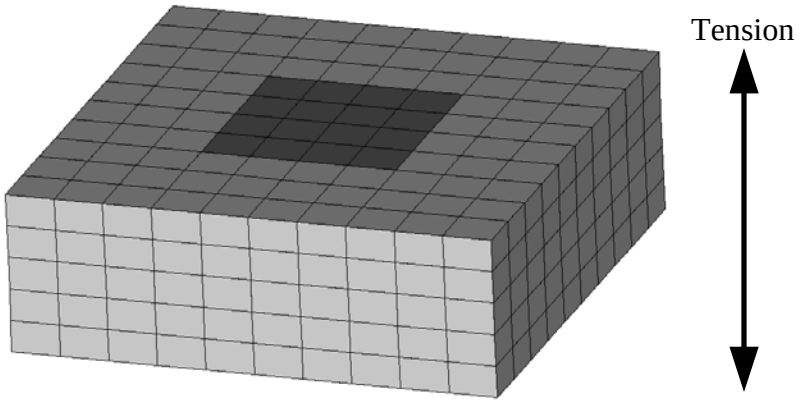

Figure 3.5: Specimen volume of interest. Darker elements represent the region of elevated stress triaxiality (up to 0.61). Material at surface is in uniaxial tension (stress triaxiality 0.33).

3.3 Material damage

3.3.1 Porosity measurement

The porosity within the *in situ* tensile specimen was measured for each strain state (Table 3.1). Figure 3.6 shows the measured porosity versus plastic strain at the corresponding loading stage along with 95% confidence intervals. The confidence intervals are calculated based on the set of measurements at the initial state (0) and after each of the three loading stages (states 1 – 3). The measurements were taken from volumes shown in Figures 2.8, 3.2, and 3.3 for the states 0, 1, and 2, respectively, and in Figure 3.4 for the state 3. Each image has two layers of such volumes making 8 volumes per image in total. This information is used for the validation of the void damage rules as well as for calibration of the coalescence criterion employed in the damage percolation model, as will be discussed in the next chapter.

Table 3.1: Tomographic data analysis results (voids and particle-void interfaces (PVI) per 1 mm^3).

Loading Stage	Volume (μm^3)	Porosity	Number of Voids	Number of *Mg_2Si* PVI	Number of *Fe*-rich PVI
	455x462x292	0.0005216	56279	33849	28638
	455x462x292	0.000525	55723	33441	27412
	455x455x292	0.0005755	59815	35680	30837
0	448x455x292	0.000519	54466	32413	27157
	462x462x292	0.0005317	55249	32596	28107
	434x462x292	0.0005087	54772	32969	25570
	455x455x292	0.0005437	56680	34270	29576
	448x455x292	0.000509	54129	32295	27528
	448x434x293	0.0005847	62795	36316	31529
	448x434x293	0.0005584	60410	24006	21867
	448x448x293	0.0006504	65793	37509	34230
1	448x448x293	0.0005654	59066	32497	31291
	448x434x293	0.0005575	59533	32914	29863
	434x434x293	0.0005691	61761	34193	29831
	448x448x293	0.0006026	64162	36421	32871
	441x448x293	0.0005532	58606	33117	29165
	455x455x320	0.000692	70783	37109	35873
	434x455x320	0.0006512	66326	36045	34197
	420x441x320	0.0007243	73036	38463	37335
2	420x441x320	0.0006608	65744	34388	35230
	434x434x320	0.0005057	53257	27705	23946
	434x434x320	0.0005151	55906	30222	24326
	434x434x320	0.0005577	57661	30785	26860
	434x434x320	0.0005329	53588	28798	25138
	791x175x343	0.001228	95788	36015	55034
3	812x161x343	0.0010669	94355	39161	50244
(surface)	770x196x343	0.0010731	86235	29981	43678
	742x189x343	0.0013079	102179	38232	59499
	392x175x343	0.001397	89631	29325	60392
3	406x154x343	0.0014812	97828	34086	65607
(center)	385x196x343	0.0022992	111657	36202	75996
	371x105x343	0.0021771	112562	33679	79257

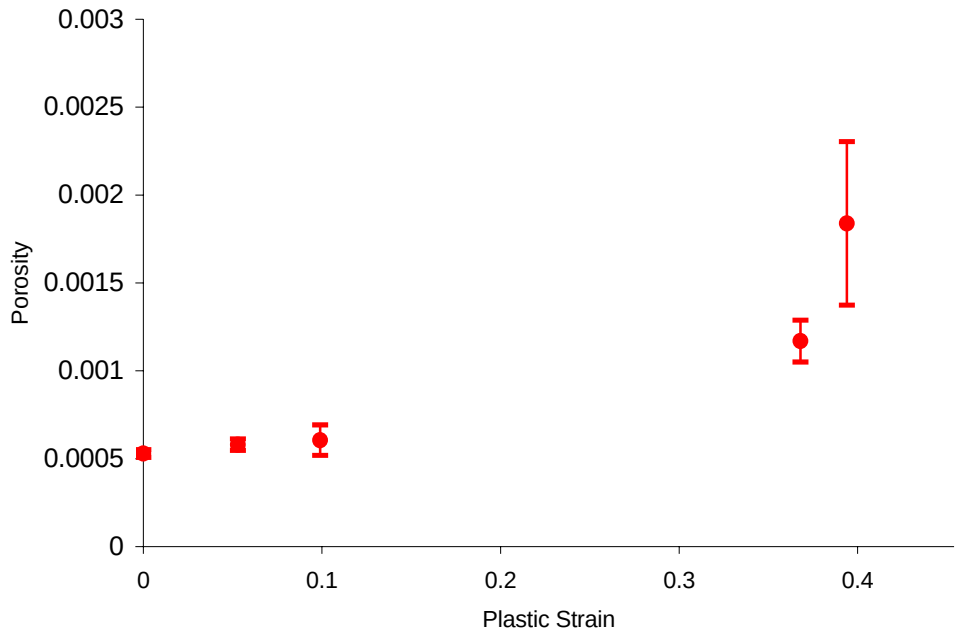

Figure 3.6: Measured porosity versus plastic strain.

It is observed from Figure 3.6 that the porosity remains low at the early stages of deformation. Significant increases in porosity occur in the last deformation increment, at which point the sample has passed the UTS point and necking has commenced. It should be noted that the overall porosity level remains quite low with maximum values less than 0.3%. This level is consistent with recent 2D section measurements (Smerd *et al.*, 2005).

3.3.2 Void nucleation characterization

The number of particle-void interfaces (PVI) per unit volume is adopted in the current work as a parameter describing nucleation of second phase particles. The calculation of PVI was done separately for each type of particle (Mg_2Si and *Fe*-rich particles) using specially developed in-house software. The results of the PVI calculations for each sub-region are presented in Table 3.1.

The minimum inter-particle distance (IPD) has been calculated for each particle as a measure of clustering (Pilkey *et al*., 1998). Particles that are a part of a cluster have lower values of IPD. The determination of which particles are members of clusters is controlled by a prescribed threshold level for cluster membership, which sets the upper limit for the IPD of particles that are considered to be members of clusters. In the limit, the entire population of second phase particles is included in the calculations when the threshold is set to exceed the maximum particle IPD value. By varying the cluster threshold IPD level, the dependence of the number of PVI on clustering, for example, can be examined. This relationship is examined in Figures 3.7 and 3.8 for the Mg_2Si and *Fe*-rich particle populations separately. Plotted are the number of PVI for particles within clusters as a function of the IPD threshold for cluster membership. It is evident from the data that void nucleation occurs preferentially at particles located within clusters.

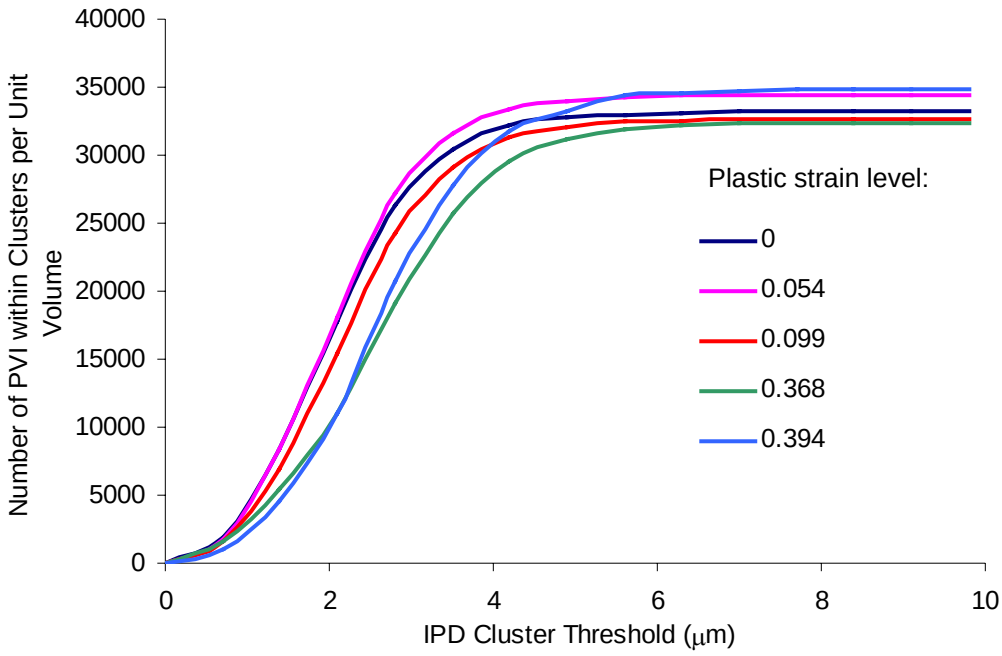

Figure 3.7: Number of PVI versus IPD for Mg_2Si particles.

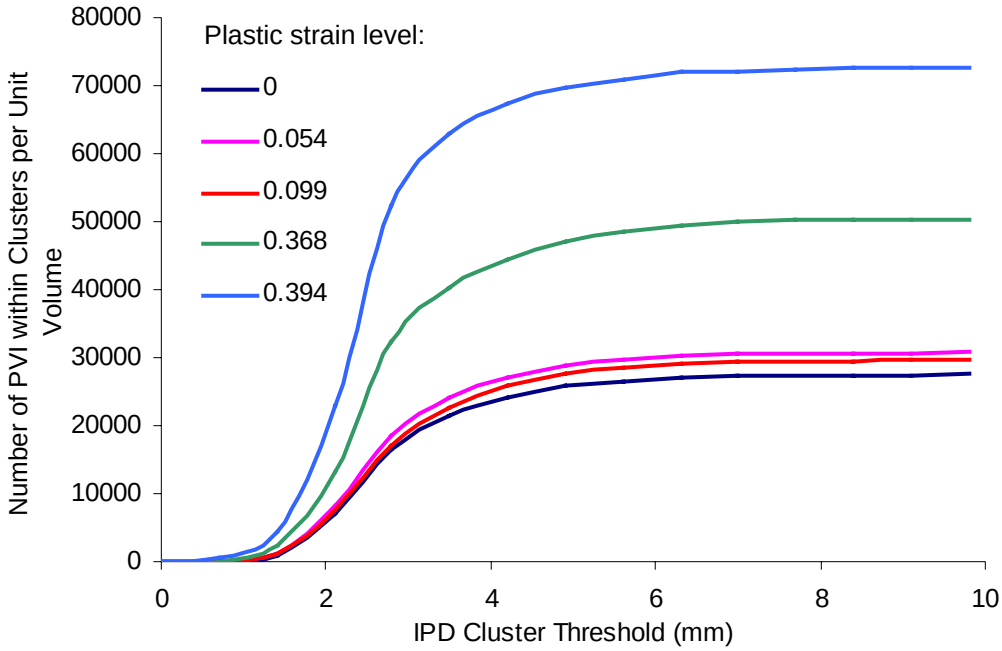

Figure 3.8: Number of PVI versus IPD for *Fe*-rich particles.

It can be seen from the plots that, in the case of the Mg_2Si particles, the number of PVI within clusters only depends on the cluster IPD threshold and shows no significant dependence on strain. In fact, the number of PVI remains almost the same throughout the entire process of deformation with only mild variations attributed to the size and location of the inspected volume (0.58 mm^3) and the material heterogeneity at that scale. Therefore, Mg_2Si particles are associated with only pre-existing voids nucleated during cold rolling.

There is a significant increase in the number of PVI within *Fe*-rich particle clusters with changing strain (Figure 3.8). Consequently, void nucleation during deformation of the as-received sheet is solely attributed to the *Fe*-rich phase. The curves in the picture exhibit a similar shape that can be characterized with probability density functions (PDF). By taking a derivative with respect to IPD and normalizing the data in

Figure 3.8, the PDF curves shown in Figure 3.9 are obtained. It is interesting to note that each of the normalized curves in Figure 3.9 follows almost the same pattern that can be described by a log-normal PDF,

$$f_I(x) = \frac{1}{xS_I\sqrt{2\pi}} e^{\frac{-\ln^2\left(\frac{x}{M_I}\right)}{2S_I^2}} \tag{3.27}$$

where x is the IPD, M_I = 2.6 (μm) is the mean value, and S_I = 0.38 (μm) is the standard deviation.

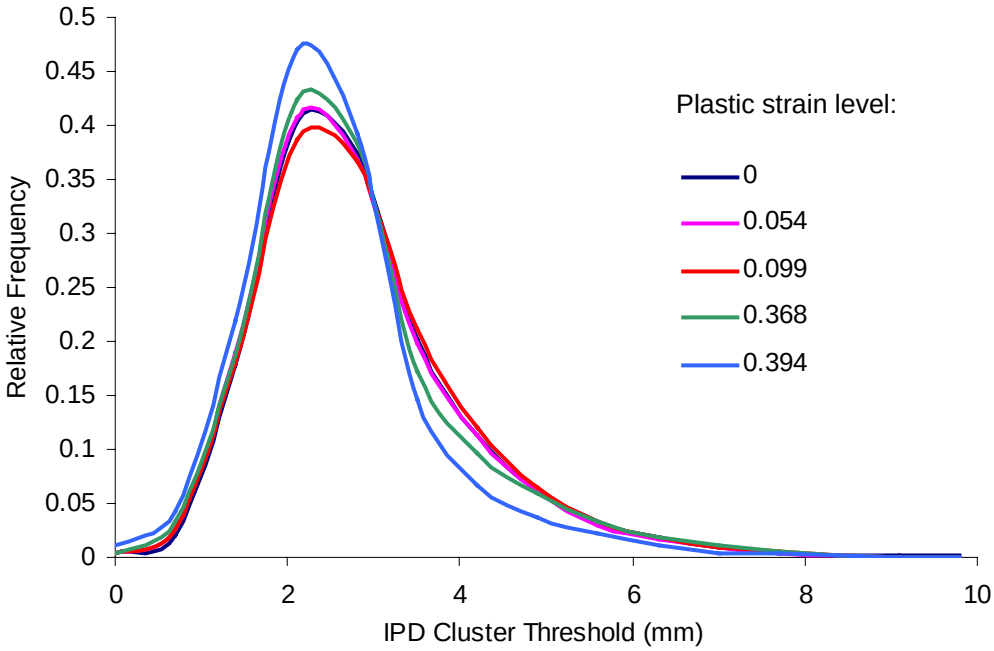

Figure 3.9: *Fe*-rich particle nucleation probability density functions for different plastic strain levels.

The dependence of the number of PVI on strain for the entire population of particles is shown in Figure 3.10. It is observed that there is no void nucleation during the first two loading stages; the slight difference in the values is attributed to material heterogeneity. The number of PVI increases rapidly during the last stage of deformation. The values are plotted for the two zones with different stress states (points marked Center and Surface in Figure 3.10): the material in the center of the specimen has higher stress triaxiality (up to 0.61) while the surrounding material is in uniaxial tension (0.33 triaxiality) (Figure 3.5).

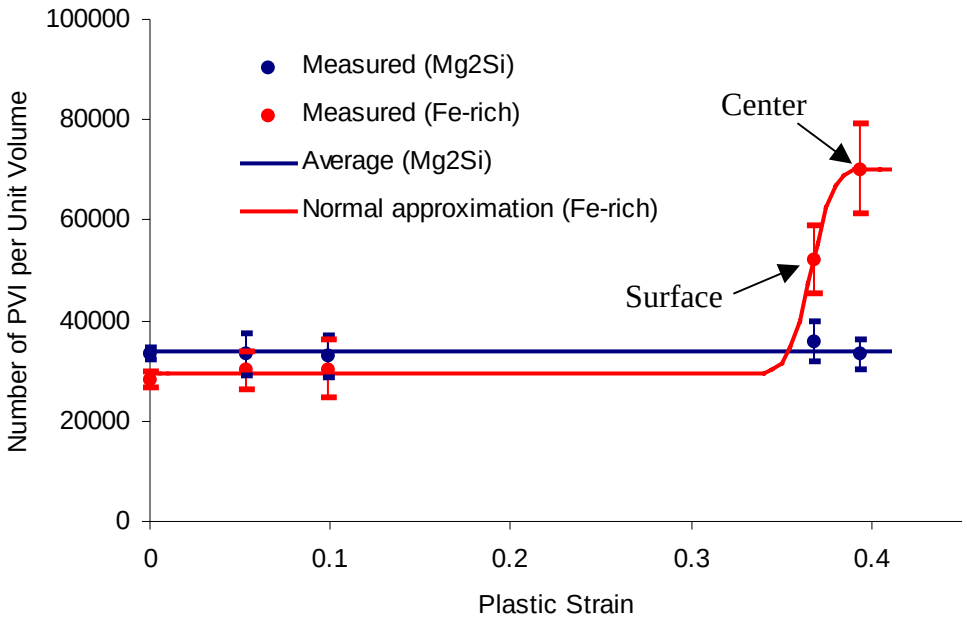

Figure 3.10: Number of PVI versus plastic strain.

Unfortunately, due to the limited availability of the *in situ* synchrotron radiation facility, measurements were not taken between strains of 0.1 and 0.35. Thus, a number of somewhat arbitrary assumptions had to be made regarding the void nucleation behaviour.

Void nucleation is assumed to occur within a relatively short interval at high plastic strains (0.3 - 0.4). This assumption is consistent with the results of Smerd *et al.* (2005). This interval corresponds to deformation after the Considere condition is met and necking starts to develop. High plastic strains in the neck lead to profuse void nucleation. An assumption of normal distribution for nucleation strain is adopted in the nucleation criterion (Gurson, 1975). Also, it is assumed that there exists a maximum number of voids that can nucleate. This assumption is similar to that of the volume fraction of particles that can nucleate voids in the model of Gurson (1975). This approach places a constraint on the maximum number of PVI that can be modelled within the DPM using the results of the *in situ* tensile test. Better estimates of the nucleation behaviour can be obtained by acquiring more measurement points during *in situ* tensile testing or by conducting tests with different loading types leading to higher plastic strains. Thus, the last point on the curve in Figure 3.10 is considered to be the maximum number of PVI before the onset of ductile rupture. The approximation of the evolution of the number of PVI is also shown in Figure 3.10 and corresponds to a normal distribution with the following PDF:

$$f_E(\varepsilon) = \frac{1}{S_E\sqrt{2\pi}} e^{\frac{-(\varepsilon - M_E)^2}{2S_E^2}} \tag{3.28}$$

where ε is the plastic strain, M_E = 0.32 is the mean value, and S_E = 0.03 is the standard deviation. Note also that this distribution is fit through all five points in Figure 3.10, including the two measured from the inner and outer regions of the sample at the highest strain level.

The initial number of *Fe*-rich PVI per unit volume and the total number of *Fe*-rich PVI per unit volume after deformation to a strain of 39.4% are 28,100 and 44,000, respectively, according to the collected data (Figure 3.8). The confidence intervals in Figure 3.10 (95%) are calculated based on the measurements at the four loading stages of Table 3.1. The cumulative probability density function of the number of PVI taking into account the clustering level, IPD, and plastic strain (Figure 3.11) can be written:

$$f(x,\varepsilon) = \frac{1}{xS_I S_E 2\pi} e^{\frac{-\ln^2\left(\frac{x}{M_I}\right)}{2S_I^2} + \frac{-(\varepsilon - M_E)^2}{2S_E^2}} \tag{3.29}$$

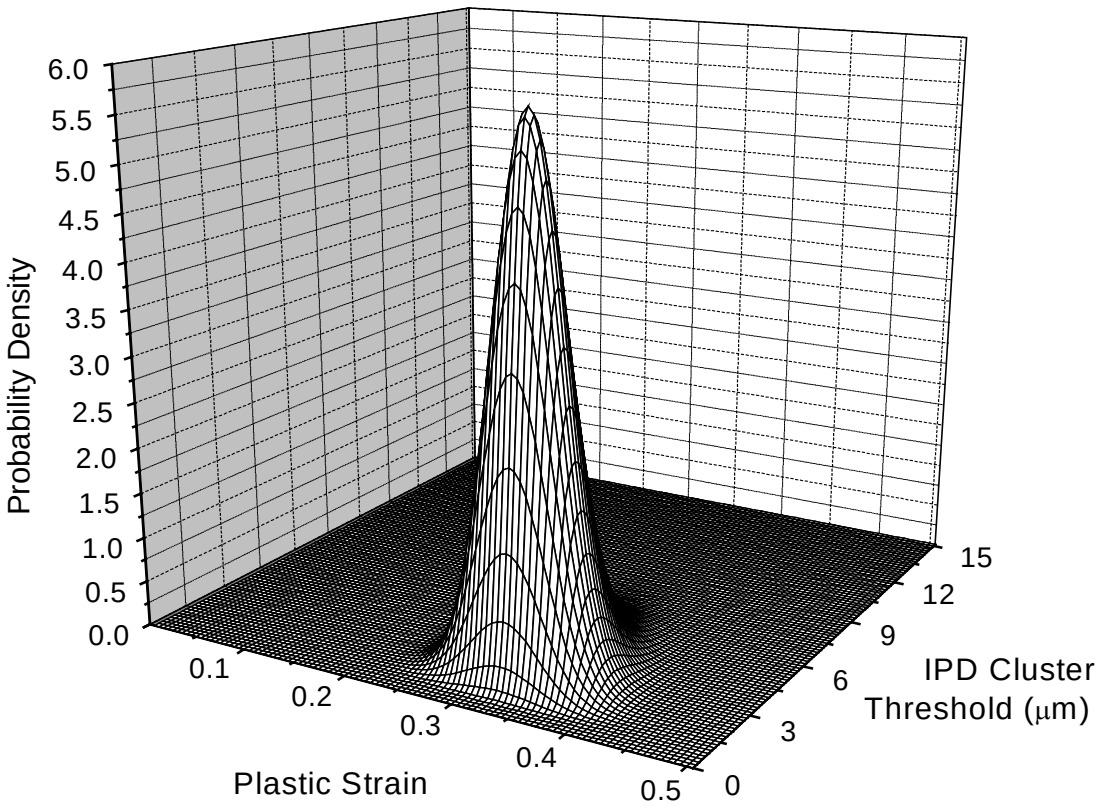

Figure 3.11: Probability density function of *Fe*-rich particle nucleation.

The evolution of the number of PVI (Figure 3.12) now can be approximated with the following formula.

$$P(x,\varepsilon)=\int_0^x \frac{1}{rS_I\sqrt{2\pi}} e^{\frac{-\ln^2\left(\frac{s}{M_I}\right)}{2S_I^2}} dr\left(A+B\int_0^\varepsilon \frac{1}{S_E\sqrt{2\pi}} e^{\frac{-(t-M_E)^2}{2S_E^2}} dt\right) \tag{3.30}$$

where A = 28100 and B = 44000.

The resulting PVI evolution (Figure 3.12) and its probability density function (Figure 3.11), which describe the *Fe*-rich particle nucleation process, are utilized in the development of the nucleation criterion discussed in the next chapter.

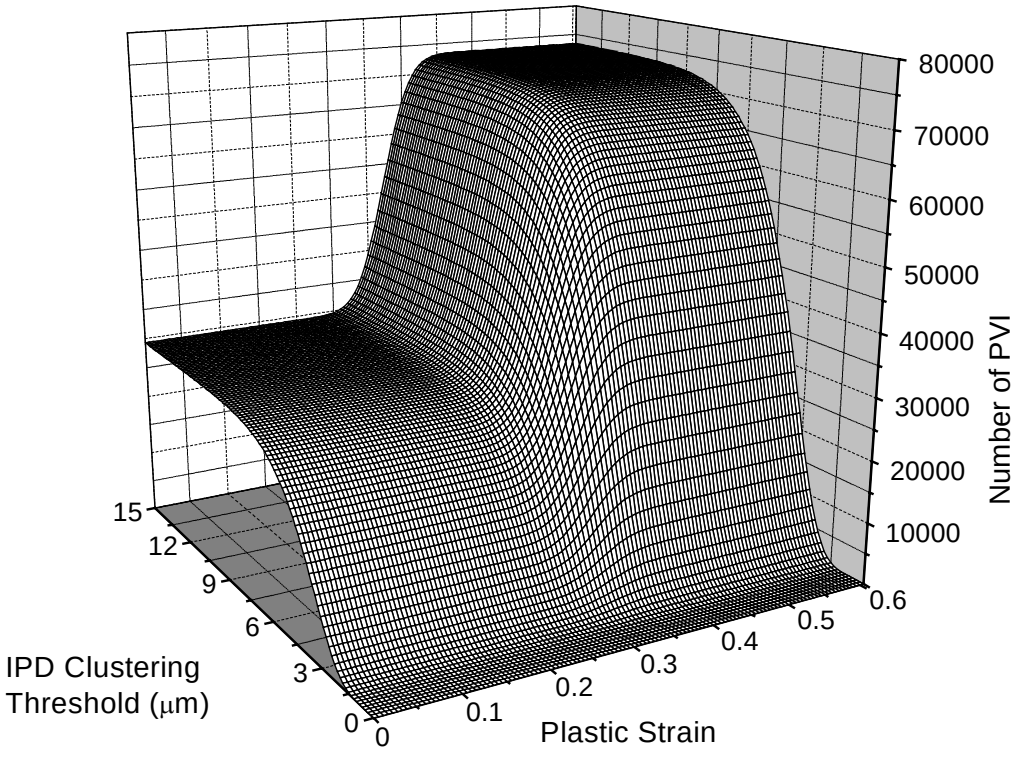

Figure 3.12: Number of PVI evolution approximation.

Summary

The *in situ* tensile test utilizing X-ray tomography has proven to be a useful source of information about material microstructure evolution. Three-dimensional images at different loading stages, together with finite element calculations of the plastic strain distribution in the studied material region, have provided an opportunity to establish the relationship between material damage parameters, second phase particle clustering and plastic strain. In addition to material porosity, a traditional measure of material damage, the number of particle-void interfaces has been used as a measure of void nucleation. The results of such measurements have provided quantitative information about void nucleation that can be used for the development of a void nucleation criterion for the three-dimensional damage percolation model.

Chapter 4

Three-Dimensional Damage Percolation Model

A key component of the current work is the development and application of a three-dimensional damage percolation model (DPM) to study the effects of void/particle size and spatial (clustering) distributions on the formability and damage in commercial 5xxx-series aluminum alloy sheet. Aluminum alloy AA5182, considered in this work, contains iron- and magnesium-based inter-metallic second phase particles. The mechanism of damage evolution and ductile fracture due to the second phase particles is well known and has been studied extensively. It consists of the three stages: void nucleation via particle-matrix decohesion and/or particle fracture, void growth, and void coalescence. The evolution of material damage in the form of increasing porosity has been previously accounted for through the development of dilational yield surfaces and functions describing porosity evolution (Gurson, 1975, 1977a,b,c; Tvergaard and

Needleman, 1984). Such models are typically based on a unit-cell approach that represents the material as a periodic array of identical cells. A major drawback of this method is that microstructural heterogeneity, which plays a crucial role in damage initiation and evolution, is not accounted for. To tackle this problem, the DPM has been developed by Worswick *et al.* (1998, 2000, 2001) and Chen *et al.* (2003), which predicts damage evolution based on real second phase particle field data. The model has since been extended into three dimensions (Orlov *et al.*, 2004, 2005, 2006 a, b) as part of the current research. The extension of this model into 3D space leads to a number of advantages, such as the capability of capturing sheet metal anisotropy or capturing the competitive aspects of ongoing damage processes developing in different directions.

Another aspect of the current research has been to extend the model to work in a fully coupled manner (two-way coupling) with a commercial finite element code, LS-DYNA (Hallquist, 1998). The finite element code is used to predict the strains and stresses present within a plastically deforming component, for which the DPM predicts damage development. In the fully coupled version, the GTN yield surface is adopted within the FE calculations to introduce constitutive softening effects due to damage. Thus, the DPM code passes damage to the FE code, which in turn passes updated stresses and strains to the DPM code. The input requirements for the fully coupled calculations comprise a finite element model of a forming process and a second phase particle field approximated with ellipsoids. This chapter presents the general algorithm of the DPM and discusses its principal functions. A sensitivity analysis of DPM predictions to various input parameters is provided in Appendix B.

4.1 DPM algorithm

The three-dimensional damage percolation model has been designed to capture microstructural heterogeneity effects during damage initiation and growth in alloys containing second phase particles. For this reason, the model is capable of handling multiple types of second phase particles, such the *Fe*-rich and Mg_2Si particles, and voids that are present in the commercial aluminum alloy AA5182 considered in the current research. In the current predictions, only one type of particle is assumed to be able to nucleate voids; however, the model can be easily modified to account for multiple nucleation criteria corresponding to different particle type populations. Based upon the observed nucleation behaviour presented in Section 3.3.2, *Fe*-rich particles are assumed to be the only objects producing voids through matrix decohesion and particle fracture. In addition, a certain number of pre-existing voids are assumed to be associated with the Mg_2Si particle population. These voids exist in the as-received material and are formed during the sheet cold rolling process. Pre-existing voids not associated with any particle type are also present in the material.

The three-dimensional damage percolation model utilizes various inputs created by ancillary software to model void nucleation from second phase particles and their subsequent development into a macro crack. These pieces of software are used to obtain or generate second-phase particle fields and criteria necessary to describe the material behaviour at the micro-scale during deformation. The procedures for processing raw tomographic data, second-phase particle field characterization, and reconstruction of particle fields of desired volumes with certain clustering characteristics (Figure 4.1) have been described in previous chapters. In the current research, two methods were used to acquire 3D second phase particle field data, as illustrated in Figure 4.1 The first method utilized raw 3D tomographic data to generate the required 3D particle field input data to

the DPM. The second method utilized 2D particle fields obtained from optical micrographs of orthogonal sections and the reconstruction algorithms presented in Section 2.2 to generate the required 3D particle fields.

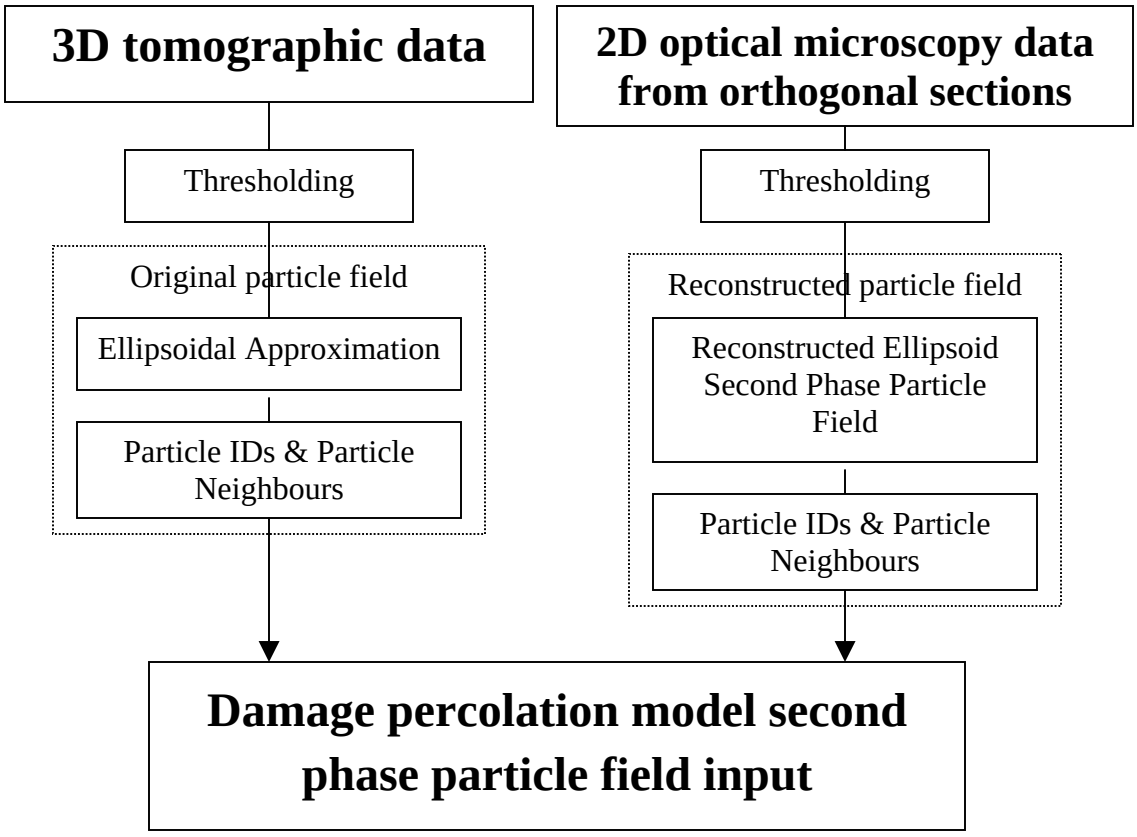

Figure 4.1: Flowchart showing the two routes used to generate second phase particle field input data for the DPM.

The second phase particle fields, along with ancillary information needed to describe particle nucleation preference (nucleation criteria taking into account particle size and spatial arrangement, for example) and particle nearest neighbour data, represents one part of the DPM input. The other part of the input is the finite element (FE) mesh and boundary conditions that are used in both the FE simulation and the DPM.

The structure of the three-dimensional damage percolation model is shown schematically in Figure 4.2, where major parts of the DPM can be seen: the DPM input, model initialization step, finite element simulation, damage modelling procedure, and model output subroutine.

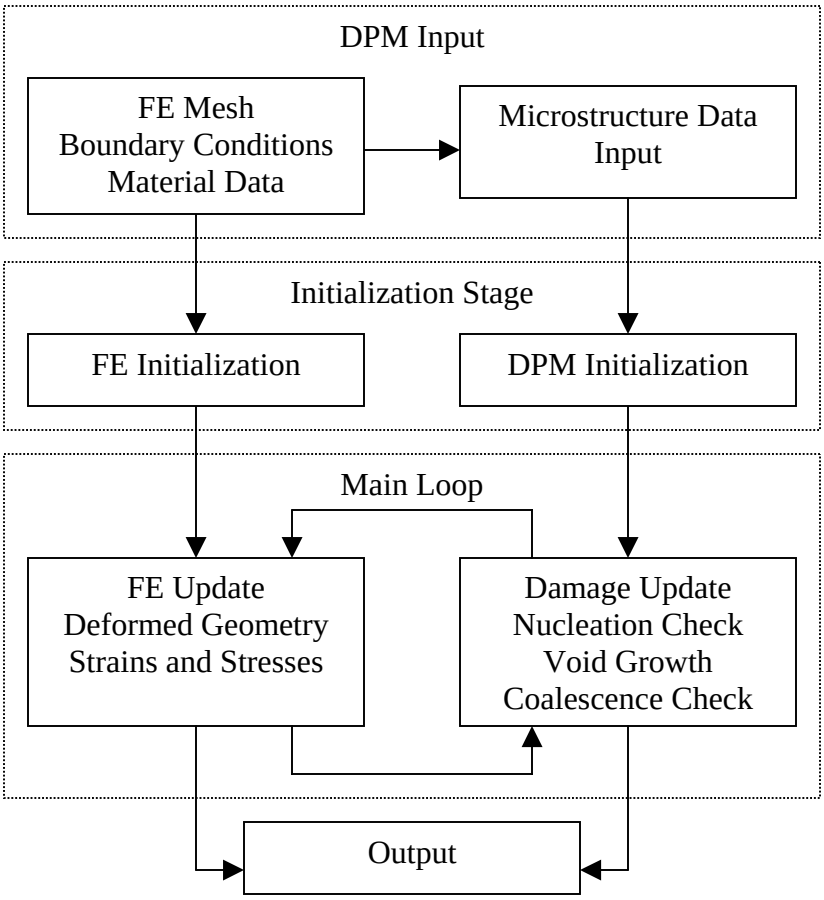

Figure 4.2: Three-dimensional damage percolation model algorithm.

The DPM is synchronized with the FE simulation. The entire forming process is divided into small loading steps. Information provided by a FE simulation step is utilized by the DPM, which performs damage evolution calculations for this step. The data produced by the DPM is in the form of a file listing calculated porosities for all of the

elements in the FE model. Each step is simulated with the FE code using the updated porosity distribution from the previous step, which results in local material softening. Material softening is accounted for in the GTN dilational yield surface (Equation 1.44). Thus, both the DPM and the FE simulation exchange information updating the material stress-strain state and porosity at each step. This kind of interaction is known as a “two-way loose coupling”. The interaction of the second phase particle field with the finite element model is discussed in more detail in the next sections.

4.2 DPM initialization step

Both the DPM and FE simulation require an initialization step. In this step, the DPM establishes a relationship between the second phase particle field (material microstructure) and the finite element mesh (model geometry).

Particle and void dimensions, centroid coordinates, rotations with respect to global coordinate axes, and minimum inter-particle distance (IPD) are provided as input data. Particles and voids are assigned a “parent element” and corresponding local coordinates within the element (Figure 4.3). These coordinates (s, t, and v) are subsequently used together with the element shape functions to update particle global location and orientation depending on the parent element location and orientation in space.

During initialization, the DPM creates a list of voids and particles that have nucleated (pre-existing) voids. This list is used later during the damage calculations.

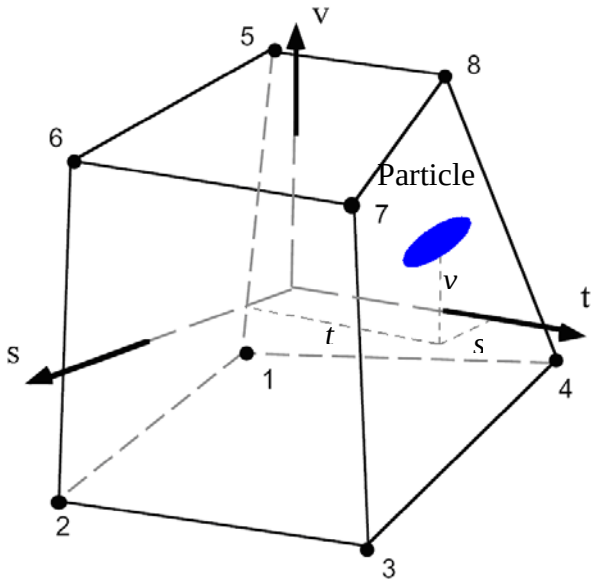

Figure 4.3: Particle inside its parent element with nodes (1-8) and local coordinate axes *s*, *t*, and *v*.

4.3 Finite element model

A finite element simulation was developed to simulate the *in situ* tensile test. The model employs the material properties of aluminum alloy AA5182 and a set of prescribed constraints and boundary conditions corresponding to the actual experiment.

The commercial explicit dynamic finite element code LS-DYNA (Hallquist, 1998) has been used for the calculations. The finite element model represents the geometry of the specimen utilized in the *in situ* tensile tests (Figure 4.6). The mesh of brick elements is refined at the region of strain localization to capture the non-uniform distribution of stresses and strains in the material. Ten elements were utilized through-thickness to better capture the through-thickness strain gradient. There are natural limitations to the choice of this number since a very small number of elements does not

allow adequate strain gradient resolution, and a larger number of elements leads to element size comparable to the sizes of second phase particles.

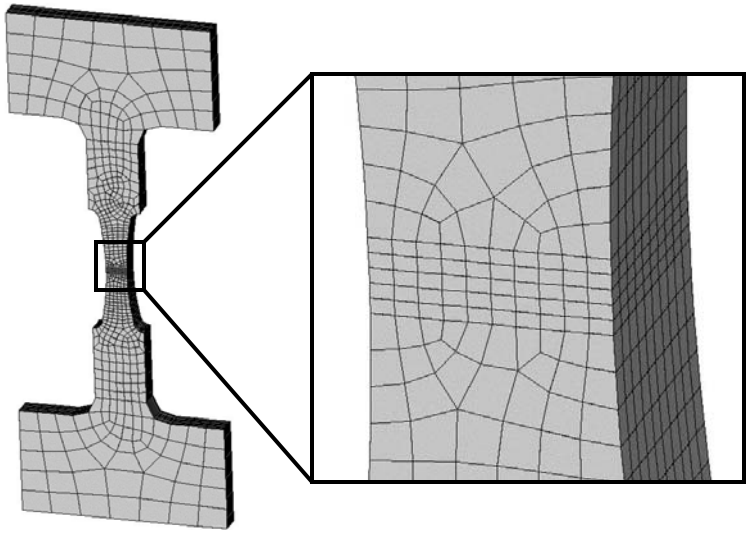

Figure 4.6: Tensile specimen finite element mesh.

The GTN material model (Equations 1.44 - 1.49) was utilized in FE simulations. This material model employs a dilational yield surface that takes into account material softening due to developing porosity. The parameters of Equations 1.44 - 1.49 that were used in the simulation are summarized in Table 4.1. Porosity calculated in the DPM was fed into the GTN yield function in the beginning of each elongation step. The FE code provided porosity evolution prediction during the elongation step until the next porosity update from the DPM was performed, as shown in Figure 4.7.

The material effective stress – effective strain curve used in the GTN material model was obtained via tensile testing of aluminum alloy AA5182 sheet and is shown in Figure 4.8. The material work hardening response is described with a piece-wise linear plastic model with the parameters shown in Table 4.2.

Table 4.1: GTN model parameters.

q_1	q_2	q_3	ε_N	f_N	S_N	f_0	f_c	f_f
1.5	1	2.25	1	0.0002	0.02	0	0.07	0.09

Table 4.2: Aluminum alloy AA5182 material parameters.

Density	Elastic Modulus (MPa)	Poisson Ratio	Yield Stress (MPa)
0.002643	$6.79 \cdot 10^4$	0.334	127.416

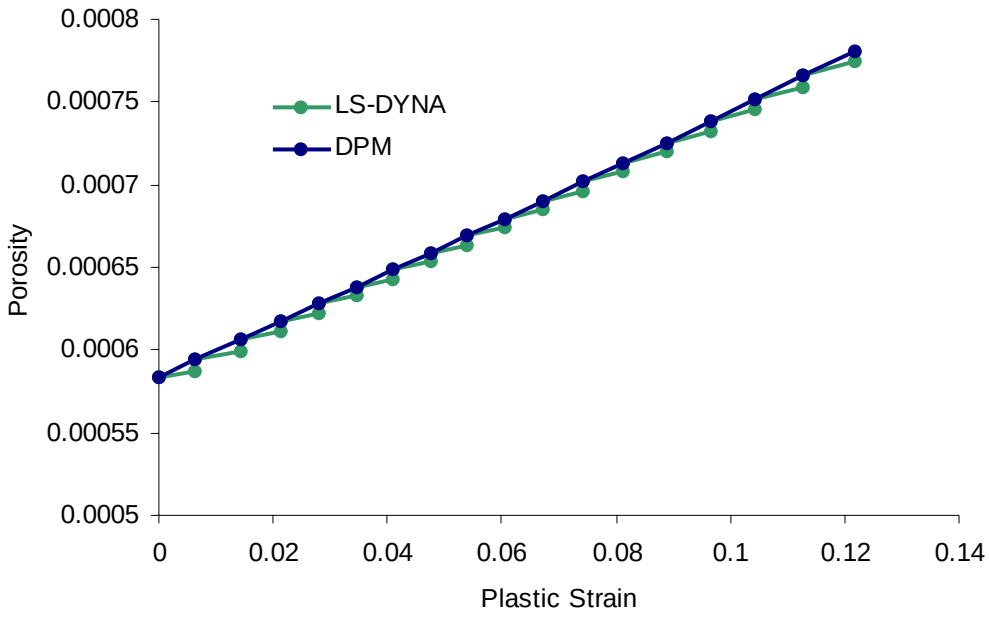

Figure 4.7: Porosity correction. The DPM provides initial porosity for each elongation step, while the GTN model predicts porosity evolution between updates.

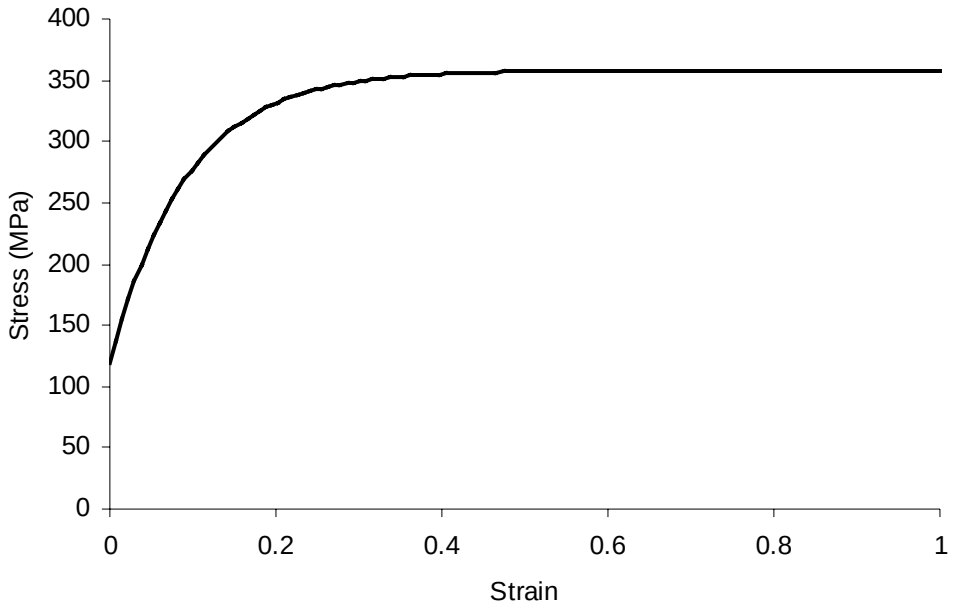

Figure 4.8: True stress versus effective plastic strain relationship for aluminum alloy AA5182.

The FE simulation is performed in a series of steps in order to allow the material damage update to be calculated in the DPM component of the simulation. Each loading step is performed by prescribing a constant velocity in opposing directions at the ends of the tensile specimen mesh. The duration of each step (elongation steps) is varied at different loading stages (this time step should not be confused with the explicit dynamic FEM solver time step). Small plastic strain increments are preferred later in the loading stage when voids coalesce and a small change in the stress-strain state may cause an abrupt void link-up leading to final material rupture. Therefore, the entire specimen loading consists of two parts. During the first part (up to 0.335 maximum plastic strain), the elongation step is 0.0269 mm. The deformation after this point is modelled with a finer elongation step of 0.00134 mm to better capture the void coalescence process. The

model has been subjected to tension with maximum displacement of 0.81 mm corresponding to that in the *in situ* tensile test (Figure 3.1).

4.4 Damage modelling

Damage initiation and growth modelling is performed for each load increment and comprises three parts. First, the second phase particles are checked to determine if they fulfil the conditions for void nucleation. Next, void growth is calculated for all pre-existing and nucleated voids. Finally, a void coalescence check is performed for all voids, including larger voids formed by coalescence of other voids.

4.4.1 Nucleation criterion

A nucleation check is undertaken for the entire particle population based on the updated element stresses and strains. Each particle has a minimum inter-particle distance (IPD) assigned, which is provided as part of the particle field input data and calculated as the smallest IPD between the particle and any of its nearest neighbours. The volume (size) of the particle and the minimum IPD are used to determine the strain necessary for the particle to nucleate a void (the nucleation strain is a function of particle size and clustering). The nucleation list is updated as particles nucleate voids.

The nucleation criterion for the second phase particle field has been developed based on the information provided by the tomographic images presented in Chapter 3. The main advantage of this criterion is that it is based upon on the exact numbers of

particle-void interfaces (PVI) obtained from the tomographic data and can differentiate between more versus less clustered regions.

The information necessary for this criterion has been obtained from the tomographic images at four different loading stages (including the undeformed state) during the characterization of material microstructure evolution in Chapter 3. The number of PVI per unit volume ($1mm^3$) has been adopted as a parameter describing second phase particle nucleation in the current work. The nucleation criterion considers *Fe*-rich particles as a source of nucleating voids. Mg_2Si particles do not nucleate voids during deformation, but are associated with pre-existing voids in the as-received state, as are the *Fe*-rich particles.

For the purpose of the current research, the nucleation criterion has been developed based upon the assumption that nucleation strain is a function of particle size (volume) and degree of clustering (IPD spacing). The dependency on clustering was shown in Chapter 3, while the importance of particle size has been demonstrated by numerous authors (Cox and Low, 1974; Tanaka *et al.*, 1970; Van Stone *et al.*, 1985; Gurland, 1972). The distribution of particle volumes is needed as an input into the nucleation criterion. The resulting two-dimensional particle volume relative frequency function is based on the *Fe*-rich particle population for the entire volume, as shown as a two-dimensional histogram in Figure 4.9.

The void nucleation criterion has been developed based on the nucleation probability density distribution (Figure 3.11) and the particle volume relative frequency function (Figure 4.9). Assuming that larger particles nucleate voids sooner and taking into account the total number of *Fe*-rich particles in the considered volume (C=154,514 in 896x896x292μm) and the number particles that nucleate voids during deformation (the difference between the numbers of *Fe*-rich PVI in the undeformed and necked material, B

= 44,000 in 896x896x292μm), a relationship between particle volume and its nucleation strain can be established with the following expression.

$$B\int_{0}^{E} f(x,\varepsilon)d\varepsilon = C\int_{V}^{\infty} f_v(x,v)dv \tag{5.1}$$

where $f(x,\varepsilon)$ is the nucleation probability density function (Figure 3.11), $f_v(x,v)$ is the particle volume relative frequency function (Figure 4.9), ε is the plastic strain, E is the nucleation strain, v is the particle volume, V is the minimum particle volume to initiate nucleation at strain E.

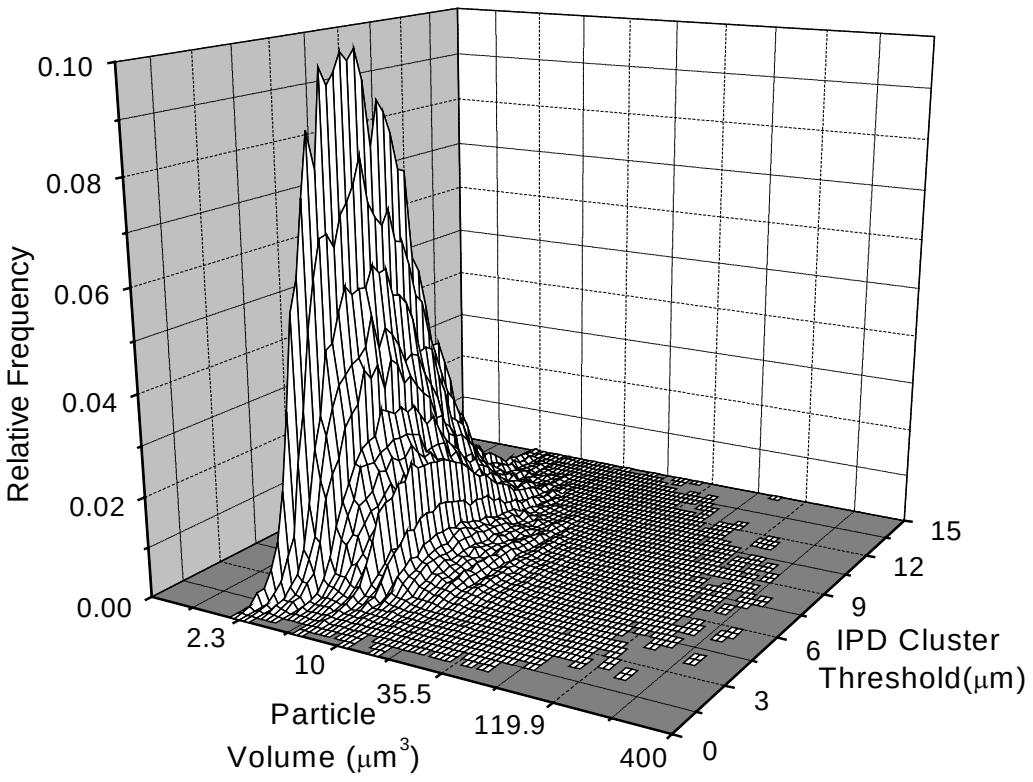

Figure 4.9: *Fe*-rich particle volume relative frequency function.

The essence of this nucleation criterion can be described as follows. For particles with IPD values falling into IPD class *x* (range from *int(x)* to *int(x)+1*), the left and right hand sides of Equation (5.1) provide relationships for the number of nucleated voids in IPD class *x* versus plastic strain ε (Figure 4.10) and the number of particles in IPD class *x* versus particle volume *v* (Figure 4.11), respectively. For a given plastic strain *E*, the number of nucleated voids (PVI) for the particle population in IPD class *x* corresponds to the area S_1 (Figure 4.10). These particles, represented by the area S_2 in the particle volume distribution plot in IPD class *x* (Figure 4.11), are located at the right end since larger particles are assumed to nucleate voids sooner. Thus, the minimum particle volume *V* to nucleate voids is determined for the values *x* and *E*. The obtained plastic strain *E* becomes the nucleation strain for particles of volume equal to or larger than *V*.

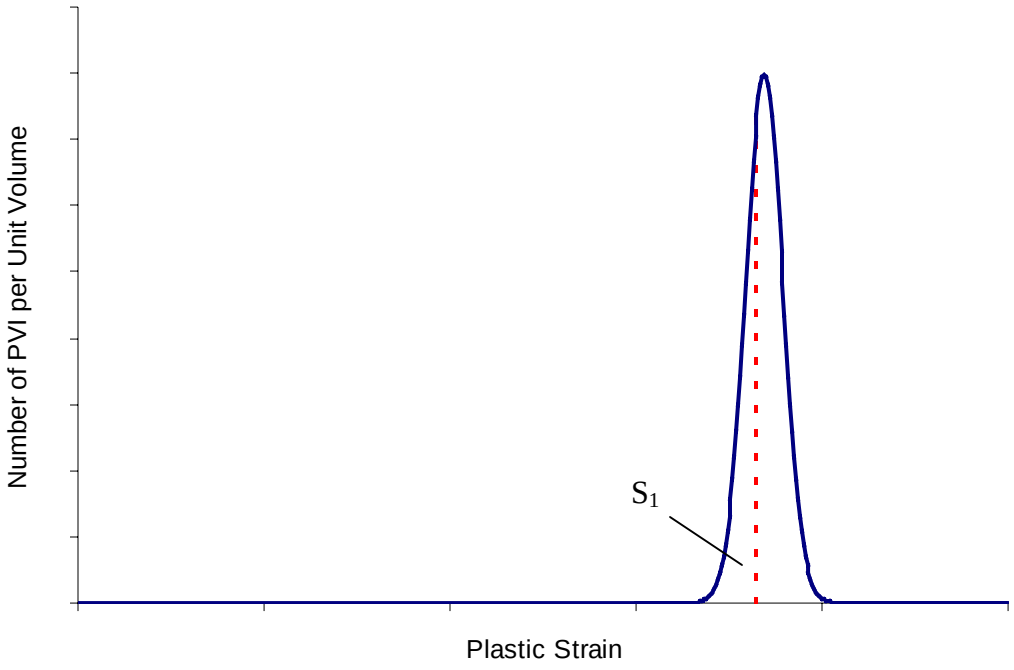

Figure 4.10: Number of nucleated voids of single IPD class per unit volume versus plastic strain.

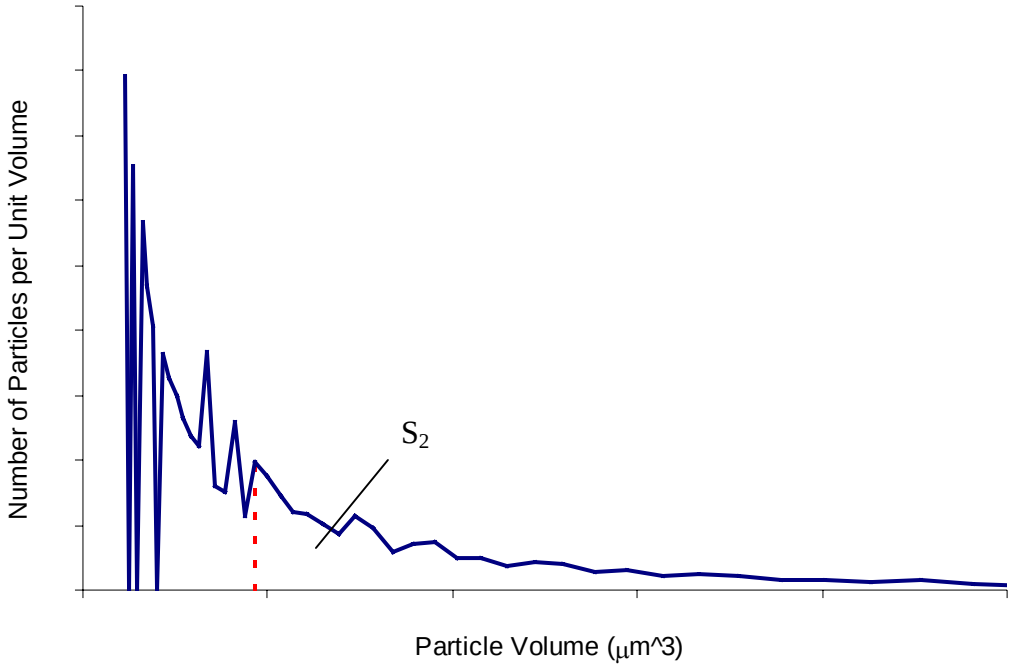

Figure 4.11: Number of particles of single IPD class per unit volume versus particle volume.

Equation (5.1) is used in a discrete mode with the histograms of the number of nucleated voids (obtained by multiplying the data shown in Figure 3.11 by the total number of nucleating *Fe*-rich particles in the considered volume, 10,314 in 896x896x292μm) and the particle volume distribution (obtained by multiplying the data shown in Figure 4.9 by the total number of *Fe*-rich particles in the considered volume, 154,514 in 896x896x292μm). Arrays of nucleation strains corresponding to different particle volumes and IPD have been generated. The histogram has been discretized into 50 classes or bins with the resulting cluster-sensitive nucleation criterion (surface) shown in Figure 4.12. The advantage of the current nucleation criterion is that it can be modified based on the number of IPD classes (bins) of interest. If the effect of clustering is to be suppressed, for example, then only one IPD class can be used such that the entire particle population is considered at once. The resulting treatment provides a one-dimensional

array of nucleation strains versus particle volume (Figure 4.13). This alternate single IPD treatment is referred to as cluster-insensitive in the following discussion, whereas the 50 IPD treatment is referred to as cluster-sensitive.

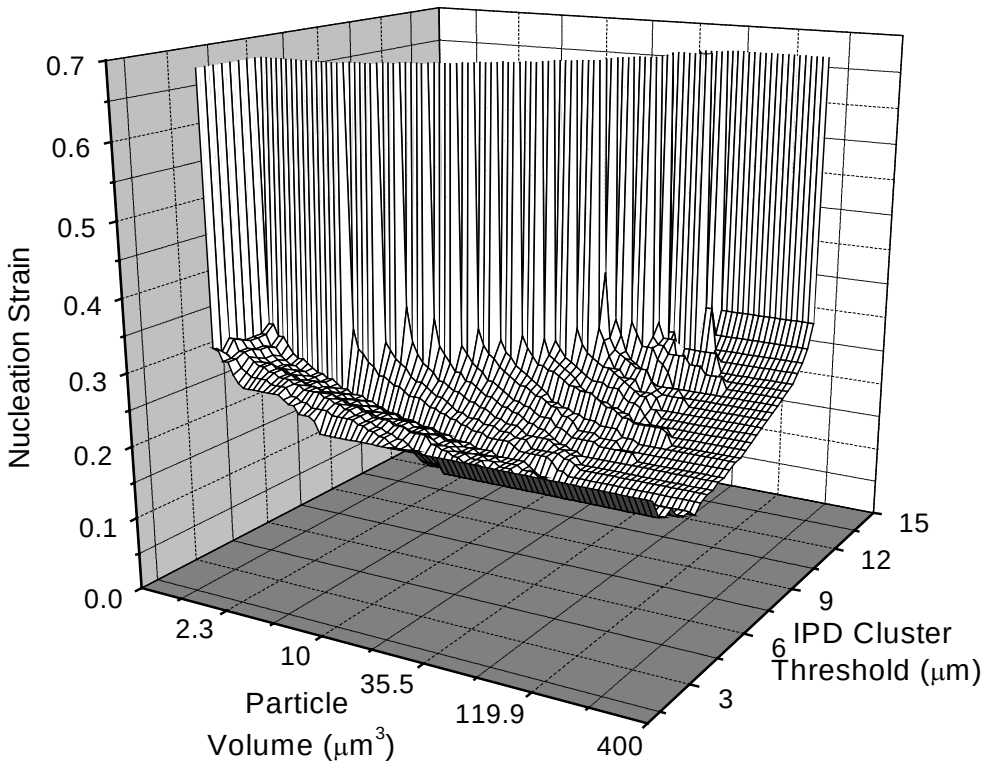

Figure 4.12: Nucleation criterion (50 IPD classes).

The number of particle volume classes (bins) has been chosen to be 100. This number, as well as the number of IPD classes, should be chosen to be high enough to describe the shape of the nucleation PDF surface. There exists a natural limitation for this number, the number of considered particles. Significant scatter in the data can occur if the number of particles is too small for the chosen number of classes.

According to the adopted nucleation criterion, only a portion of large particles nucleate voids during deformation. The nucleation strains for smaller particles is

generally not reached for the *in situ* tensile test since failure occurred prior to nucleation of these particles. Other material testing techniques, however, may be used to investigate void nucleation at higher plastic strains that exceed the maximum uniaxial tensile strain.

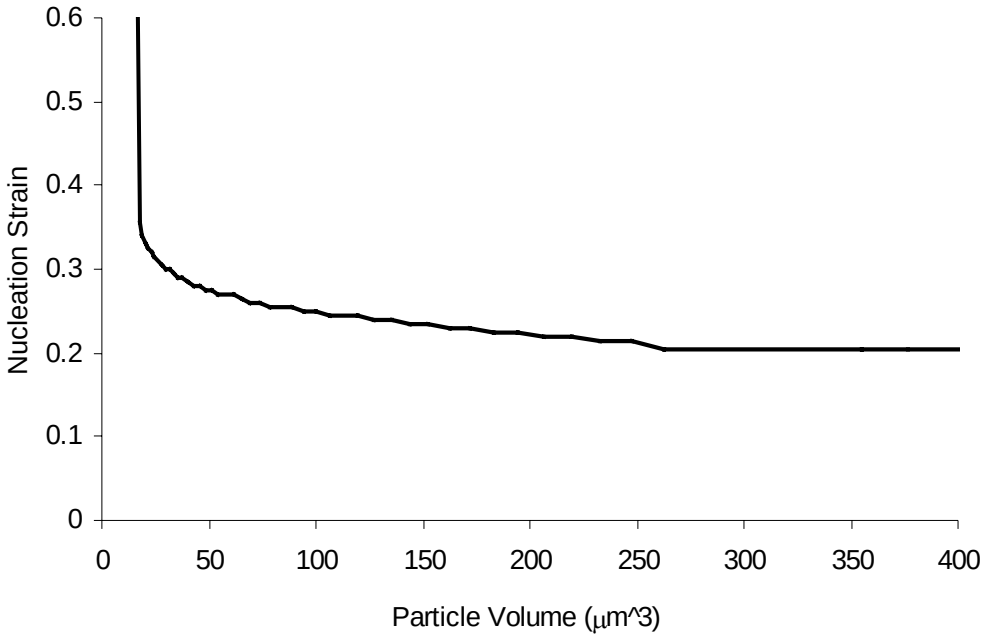

Figure 4.13: Nucleation criterion (1 IPD class).

In the current test, the fraction of *Fe*-rich particles that nucleate voids can be estimated using the particle volume distribution and a one-class nucleation criterion (Figure 4.14). Smaller particles that lie to the left of the vertical line in Figure 4.14 do not nucleate voids since their nucleation strains are higher than physically achievable in the *in situ* tensile test.

Another source of nucleating voids is associated with the process of void coalescence. The opening of a crack formed by void coalescence results in stress concentration at the boundary of the crack and subsequent void nucleation in the stressed region. Particles that are neighbours of coalescing voids are considered to nucleate voids,

as described in the crack propagation mechanism due to void coalescence shown in Figure 1.5 (Brown and Embury, 1973).

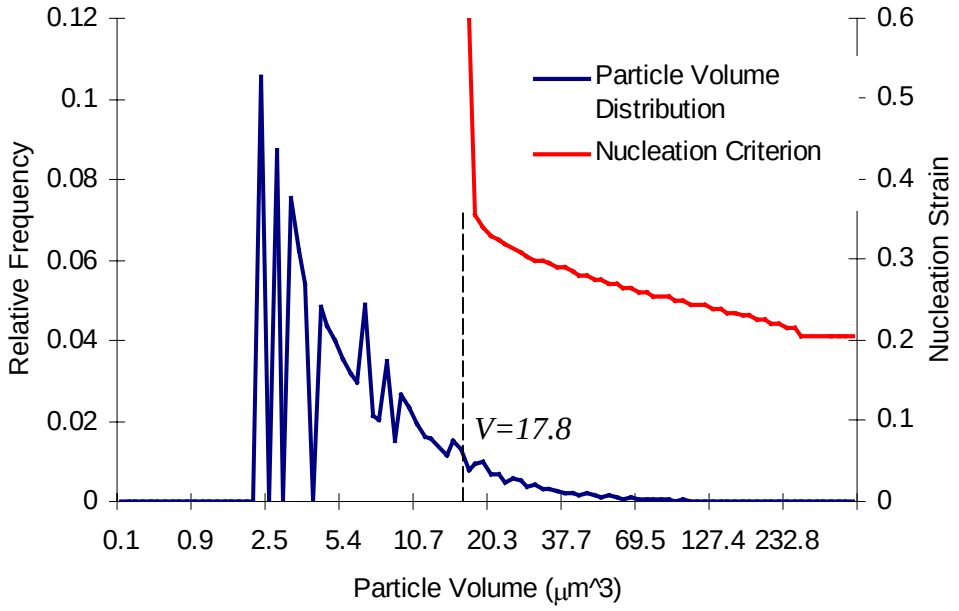

Figure 4.14: Minimum particle volume to nucleate voids. The left hand side of the particle volume distribution will not nucleate voids according to the nucleation criterion.

4.4.2 Void growth rule

The void growth rule utilized in the DPM provides rates of void expansion for various stress states defining the updated volumes of voids (the void growth rate is a function of plastic strain rate and stress triaxiality).

The principal difference in the treatment of nucleated voids in the damage percolation model and unit cell models, like the GTN model (Gurson, 1975, 1977a,b,c; Tvergaard and Needleman, 1984), is that in the latter models, particles that nucleate voids

are treated as voids of size equal to the original particle. The DPM considers nucleation to correspond to the instant of matrix decohesion from the particle (Figure 4.15). Thus, the volume of a nucleated void is zero at the onset of nucleation and it grows due to matrix material deformation, such that there is no abrupt increase in overall porosity. The original particle is considered to be inside the void. This approach imparts another important property of such a nucleation model: the void shape, if collapsed due to negative hydrostatic strain, can only return to the original particle shape and then start to grow from that shape under subsequent tensile deformation.

A void growth rule that accounts for void shape change and volumetric expansion due to high stress triaxiality has been developed based on the results of Thomson (2001). Figure 4.16 shows the results of the study in the form of a calculated void growth rate (f / f_0) as a function of strain (ε) and stress triaxiality (χ), where f is the void volume fraction and f_0 is the initial void volume fraction. These results are used in the DPM in the differential form shown in Figure 4.17. Thus, void growth is calculated based on the results for plastic strain increment and stress triaxiality updated by the finite element part of the simulation. The combined volume of each void with the inner particle that nucleated the void is considered for the void volume change calculation. The volume of the void is then calculated as the newly calculated volume less the volume of the inner particle (Figure 4.15).

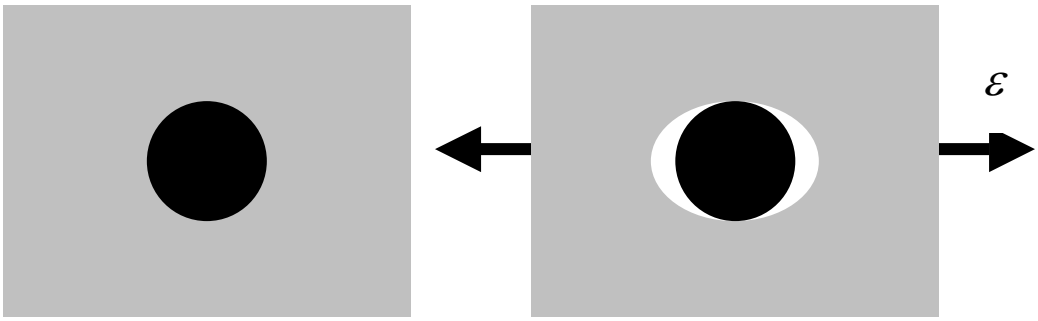

Figure 4.15: Void growth after matrix decohesion.

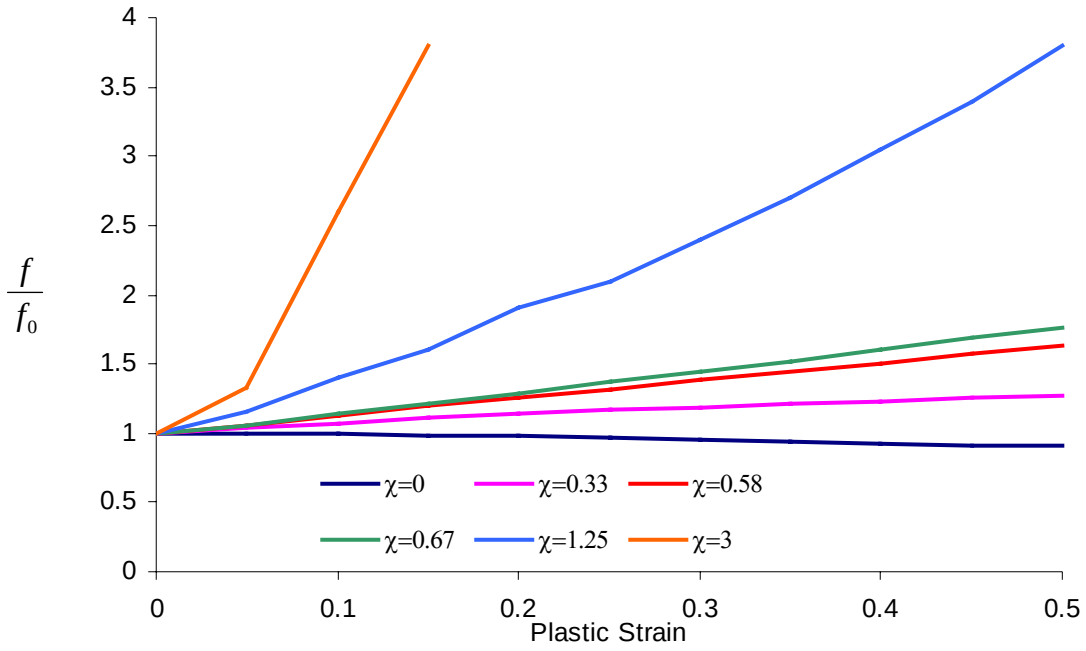

Figure 4.16: Void growth rule (Thomson, 2001).

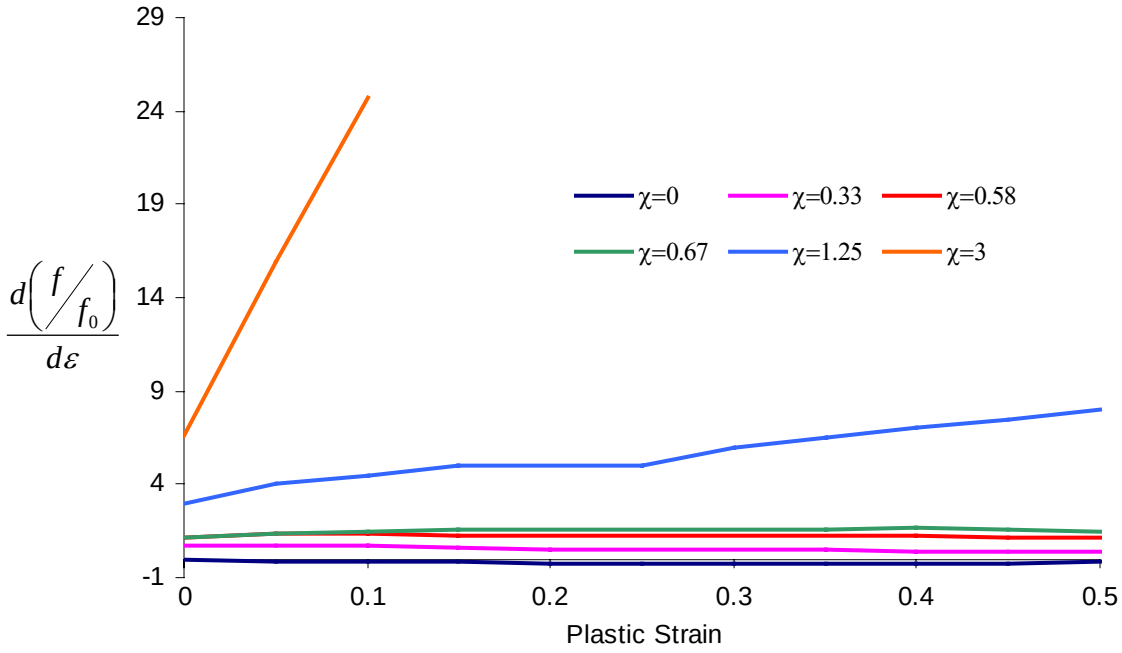

Figure 4.17: Void growth rate rule (based on the results of Thomson, 2001).

4.4.3 Coalescence criteria

A coalescence criterion is needed to model the final stage of ductile rupture. Among the important parameters that should be accounted for in a coalescence criterion, are void size and shape (void axis sizes), size of inter-void ligament, void orientation relative to the first principal stress and strain, and stress triaxiality.

Two coalescence criteria are considered that predict void-to-void and void-to-crack coalescence. The void-to-void coalescence criterion based on the limit load theory by Thomason (1969, 1981, 1985, 1990, 1993) has been utilized in the DPM. For void-to-crack coalescence, the geometric coalescence criterion by Brown and Embury (1973) has been utilized. The mechanism of void-to-crack coalescence is similar to crack propagation. This phenomenon is attributed to the irregular dimpled surface of newly formed cracks that can promote coalescence through stress concentration. The choice of the criterion of Brown and Embury (1973) for void-to-crack coalescence is due to its simplicity and ease of calibration of crack propagation rates.

4.4.3.1 Void-to-void coalescence criterion

The void-to-void coalescence criterion is based upon a comparison of the stress required to cause material flow in the internal neck between two voids to the current yield stress. The stress to cause the flow in the internal neck is a function of void geometry, inter-void distance, void orientation relative to the first principal stress, and triaxiality. The approach of Thomason (1981) is one of the most elaborate and comprehensive coalescence criteria available. The expressions for the condition for void coalescence by plastic limit-load failure and the constraint factor become (Thomason, 1981).

$$\left(\frac{\sigma_n}{Y}\right)(1-f)^{-1}\left(1-\left(\frac{3\sqrt{\pi}}{4}f^{2/3}\right)\left(\frac{b}{b_0}\right)\left(\frac{c}{c_0}\right)e^{\varepsilon_1}\right)=\frac{\sigma_m}{Y}+\frac{3+\nu}{3\sqrt{\nu^2+3}} \tag{5.2}$$

$$\frac{\sigma_n}{Y}=\frac{0.1}{\left(\frac{a}{d}\right)^2}+\frac{1.2}{\left(\frac{b}{b+d}\right)^{1/2}} \tag{5.3}$$

where σ_n is the mean stress, Y is the current yield stress, f is the void volume fraction, σ_1 is the first principal strain, a, b, and c are the void dimensions, d is the void spacing, b_0 and c_0 are the initial void dimensions, and ν is the Lode variable.

4.4.3.2 Void-to-crack coalescence criterion

The void-to-crack criterion is a version of the Brown and Embury (1973) criterion, as modified by Worswick *et al.* (1998). It compares the ratio of the ligament size between two voids to the void size. A material constant, δ, is introduced and compared to the ratio. Two voids coalesce to form a new crack or bigger void when the ratio of the ligament L between them to the void size D is less than a δ:

$$\frac{L}{D}<\delta \tag{5.4}$$

For the current research, the value of 0.7 was established for δ through a parametric study.

This criterion is used in a modified form (Pilkey *et al.*, 1998). The void size is defined as the average of the largest dimensions of the two voids.

$$D = \frac{\max(X_1, Y_1, Z_1) + \max(X_2, Y_2, Z_2)}{2} \tag{5.5}$$

where X_1, Y_1, Z_1, X_2, Y_2, and Z_2 are the axes of the two voids (Figure 4.18).

The ligament size is defined as

$$L = c - D \tag{5.6}$$

in which c is the center-to-center distance of the two voids.

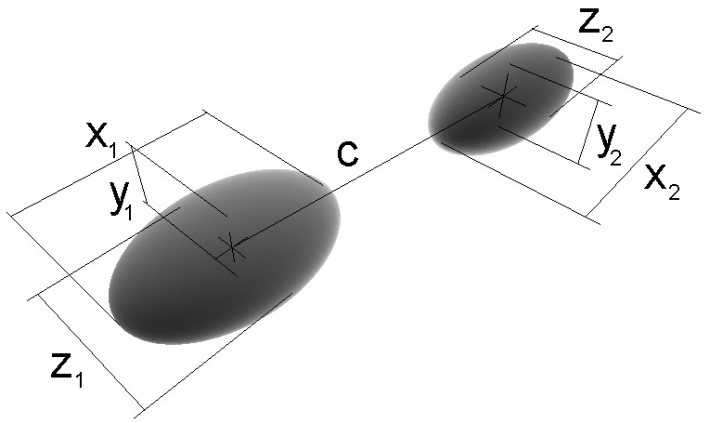

Figure 4.18: Coalescing voids.

4.4.3.3 Post-coalescence treatment

If two voids fulfil the requirement of void coalescence, a newly formed void geometry is calculated. Among various possible types of resulting void geometries and their calculation methods, a simple procedure has been employed that retains the geometric properties of the two coalescing voids (Figure 4.19). First, the direction

defined by the void centers (vector $\boldsymbol{\gamma}$), center-to-center distance c, and two coalescing void ellipsoid radii along $\boldsymbol{\gamma}$ (r_1 and r_2) are found. Initial rotations and the rotations imposed by the deformation process are accounted for in this procedure. The sum of the two radii and the center-to-center distance gives the first axis of the new ellipsoid ($c+r_1+r_2$). The second step attempts to find the maximum radii of the two voids in the planes perpendicular to the first direction and going through the void centers. The maximum value becomes the second ellipsoid semi-axis (r_3). The third ellipsoid axis is found as the maximum void ellipsoid radius in the direction orthogonal to the first two directions for the two coalescing voids (r_4). If the two coalescing voids have inner particles from which they nucleated, a particle of volume equal to the sum of the two original particle volumes is placed inside the new void. The shape of the inner particle is obtained by scaling the new void ellipsoid to reduce its volume to the calculated new particle volume. This step is performed since the DPM allows for one inner particle inside each void, which defines the minimum volume to which the void can shrink under compressive loading.

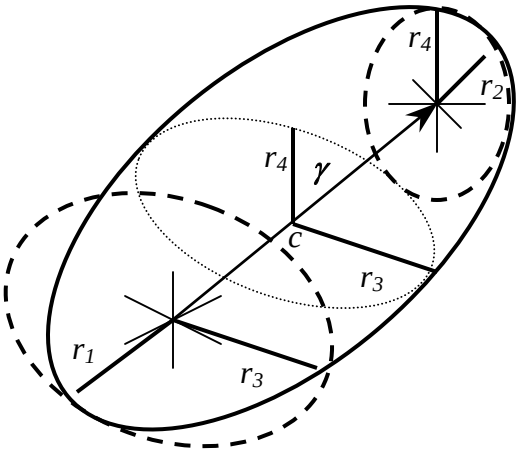

Figure 4.19: New void formed through coalescence of two voids.

After each coalescence event, a search is performed for a parent element to which the newly formed void can be assigned, in the same manner as was used for the initial particles and voids during the initialization stage of the DPM simulation. The new void is assigned the attribute of a newly coalesced void and is added to the nucleation list to be considered for further void growth and coalescence. The original two voids are discarded. The last step in the coalescence procedure is the creation of a nearest neighbour list for the new void. The list is constructed using the nearest neighbour lists of the original two voids except for discarded particles on those lists. The ID numbers of the two coalesced voids and the newly formed void ID number are saved for the purpose of monitoring coalescence propagation in the material during post processing.

4.5 Model output

Once the material damage modelling stage has been accomplished, the DPM simulation step can be considered finished, and the data obtained during the step is transferred to the next FE step. Three types of outputs exist. The first output is concerned with post processing. It comprises the model geometry and the predicted second phase particle field. Also, void and crack coalescence history are saved. The second type of output stores all of the code internal variables and arrays to be used in the next DPM simulation step. The nature of the DPM is incremental during a two-way coupled simulation, and the code is interrupted after every loading step to update element porosity and obtain the updated model geometry, stresses, and strains. Element porosity is calculated as the sum of all nucleated and coalesced void volumes less their inner particle volumes divided by the current element volume. Data from the current loading step is

transferred to the next step. The third type of the output creates an element porosity input necessary for the dilational yield function for the next FE simulation step.

Subsequent simulation will involve a FE step followed by a DPM step as in the algorithm loop shown in Figure 4.2. Each simulation utilizes data from the previous step (Figure 4.2). An alternative to this two-way coupling is one-way coupling in which the entire FE simulation is performed first, after which the DPM simulation runs in an internal loop using pre-calculated model geometry, stresses, and strains. In this case, element porosity and the dilational yield surface are not updated for every FE step. This approach was not used in the current research, but corresponds to the algorithm used by Chen *et al.* (2003).

Chapter 5

Simulation of the Tensile Test Using the Three-Dimensional Damage Percolation Model

This chapter presents results from application of the three-dimensional damage percolation model (DPM) to model damage initiation and evolution in the *in situ* tensile test. The damage initiation and evolution criteria adopted are those based on the material characterization work described in Chapter 3. These are used in concert with the second phase particle fields from the X-ray tomographic images as well as images obtained using the reconstruction method. Comparison of the DPM simulation results with measured material damage in the form of porosity and the number of nucleated voids; assessment of the nucleation predictions using cluster-sensitive and cluster-insensitive nucleation criteria; and estimation of the variability in the DPM predictions utilizing reconstructed second phase particle fields are the focus of this chapter.

5.1 Model input

As illustrated in Figure 4.2, a finite element model with a set of boundary conditions and material data (discussed in Chapter 4) and a second phase particle field are used as an input for the DPM. Within the *in situ* tensile test (Figure 2.7a), fracture was seen to develop in the plane orthogonal to the loading direction. Thus, the material volume simulated using the DPM corresponds to a slice across the middle of the specimen (Figure 3.5). The choice of this smaller modelled material volume with fewer second phase particle field objects results in a considerably shorter computational time.

The second phase particle fields used for the DPM calculations occupy a total volume of 896x896x292 μm. A second phase particle field obtained from the 3D tomographic images is used for calibration of the DPM (Figure 5.1). In addition, a set of 20 second phase particle fields was reconstructed from 2D optical micrographs. Comparison of the predictions using particle fields from the 3D tomography versus that obtained using the reconstruction algorithm allows determination of the variability of the DPM predictions due to the stochastic nature of the reconstruction method and material spatial variability.

The second phase particle field obtained using X-ray tomography consists of 185,676 objects. These objects include 154,514 *Fe*-rich particles, 18,061 Mg_2Si particles, and 13,101 voids. Note that smaller dispersoids are not considered in the DPM. Similar numbers of second phase particle field objects are observed in the reconstructed particle fields.

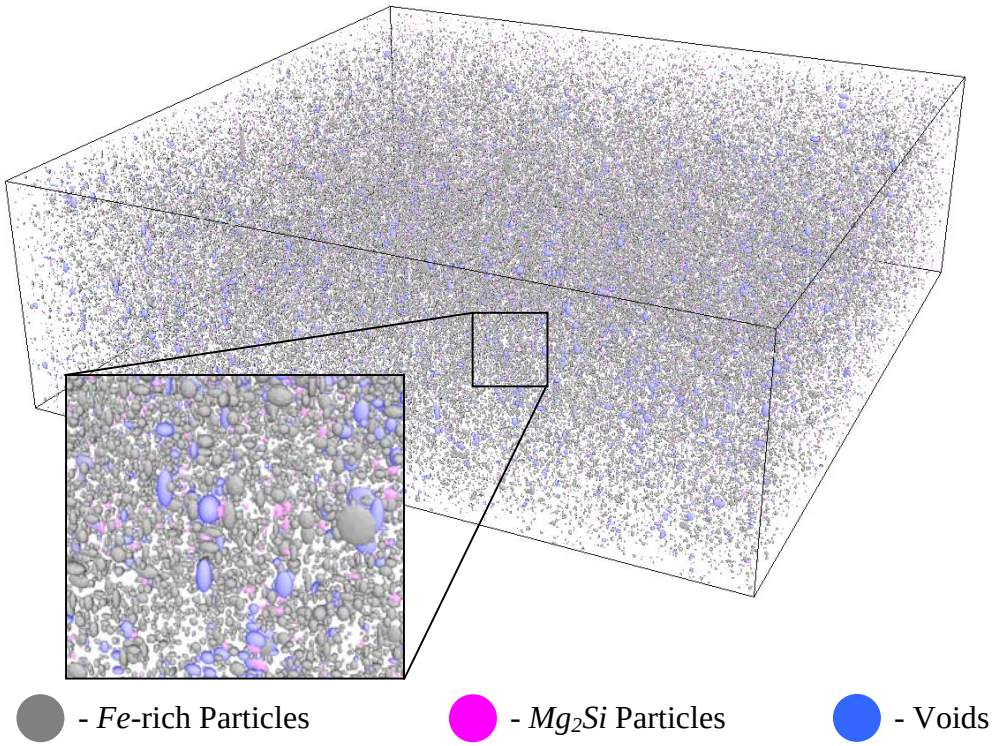

Figure 5.1: Second phase particle field (896x896x292μm volume). The large square is an enlargement of the smaller square.

5.2 DPM simulation results

Figure 5.2 shows the undeformed finite element mesh and the deformed mesh of three different states. The deformed states correspond to the onset of major events of material microstructure degradation. These include the state preceding the onset of the first void-to-void coalescence event (0.487 mm elongation), the state preceding the onset of the first crack-to-void or crack-to-crack coalescence event (0.804 mm elongation), and the state at the onset of inter-cluster coalescence leading to final material rupture (0.805 mm elongation).

The distribution of plastic strain for the four elongation states (including the undeformed state) is shown in Figures 5.3 – 5.6. A part of the volume in the plots has

been removed to show the plastic strain distribution inside the specimen. The plastic strain distribution in the first two plots (Figures 5.3, 5.4) is uniform; however it becomes non-uniform at higher levels of elongation (Figures 5.5, 5.6). In the latter case, necking occurs at the thinnest specimen cross section. The highest plastic strain is seen to develop in the middle of the considered material volume.

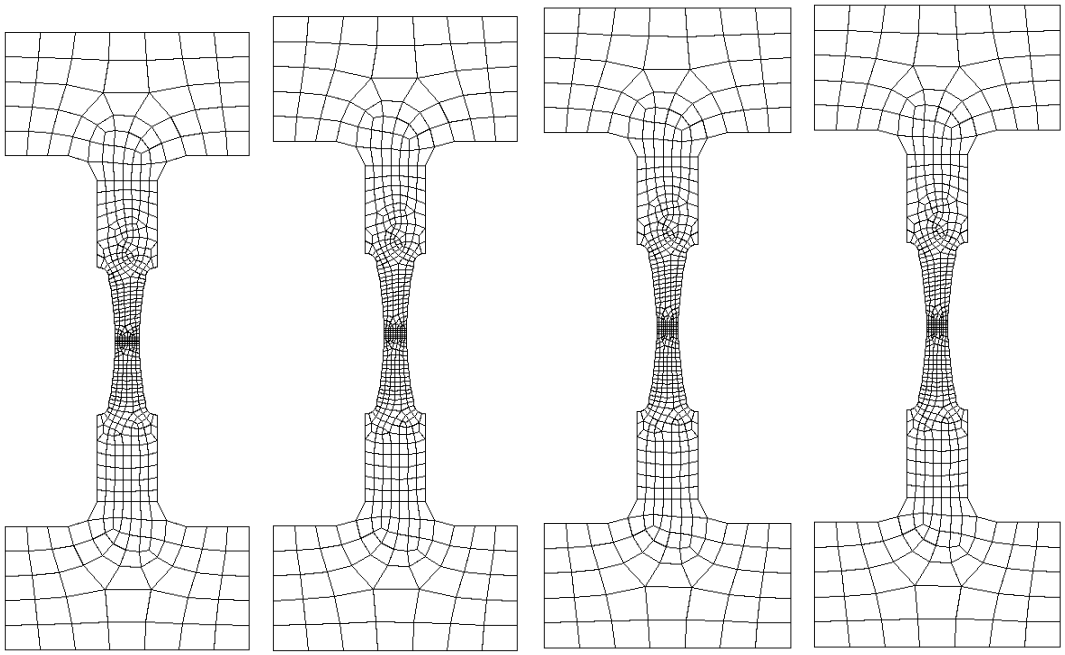

(a) (b) (c) (d)

Figure 5.2: Finite element mesh: (a) undeformed specimen, (b) 0.487 mm elongation, (c) 0.804 mm elongation, and (d) – 0.805 mm elongation.

The results of the FE simulation show that the stress state is predominantly uniaxial tensile until late into the deformation when necking initiates. Figure 5.7 shows the predicted triaxiality for elements in the center and at the surface of the sample, inner and outer regions shown in Figure 3.6, respectively. Also plotted in Figure 5.8 is the plastic strain at the same locations.

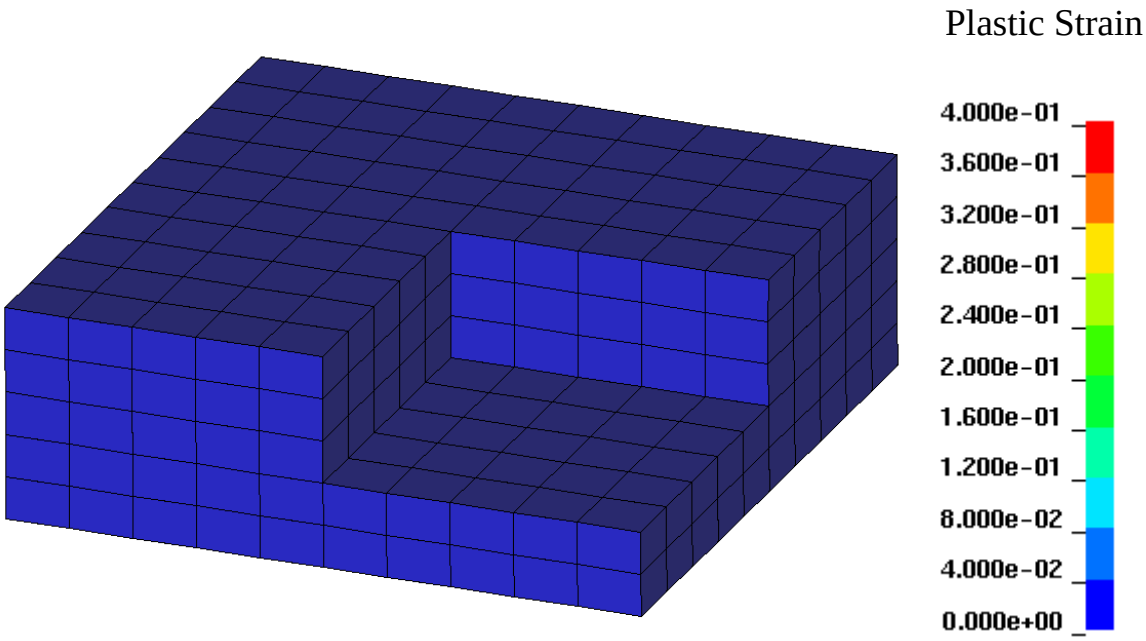

Figure 5.3: Distribution of plastic strain in undeformed material (896x896x292μm volume).

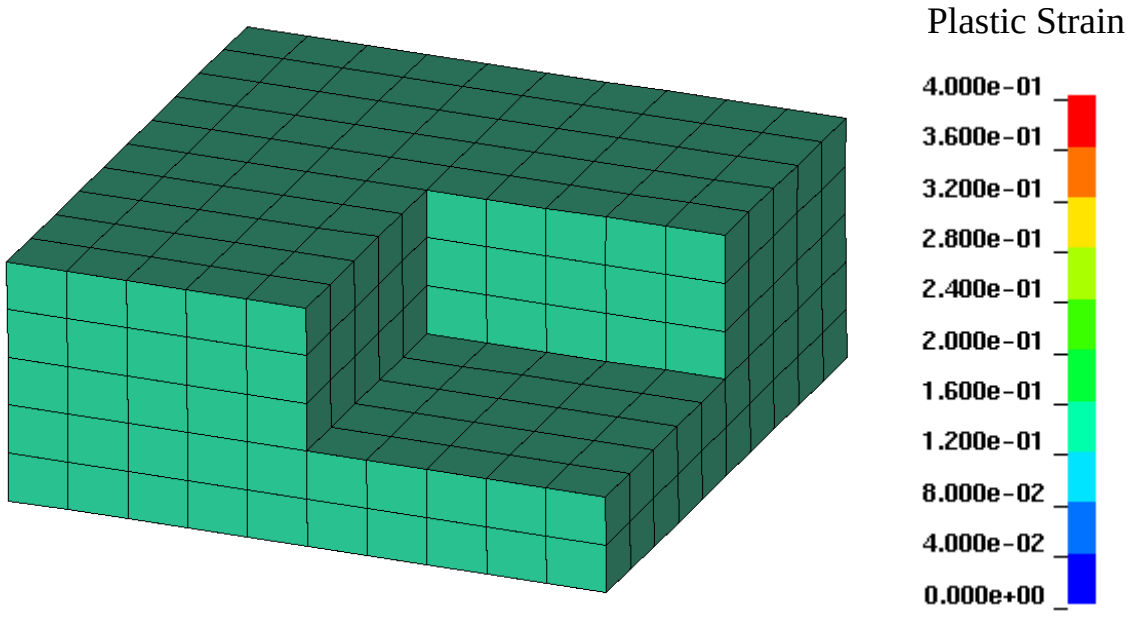

Figure 5.4: Distribution of plastic strain at 0.487mm specimen elongation. Material state preceding the first event of coalescence (896x896x292μm volume originally).

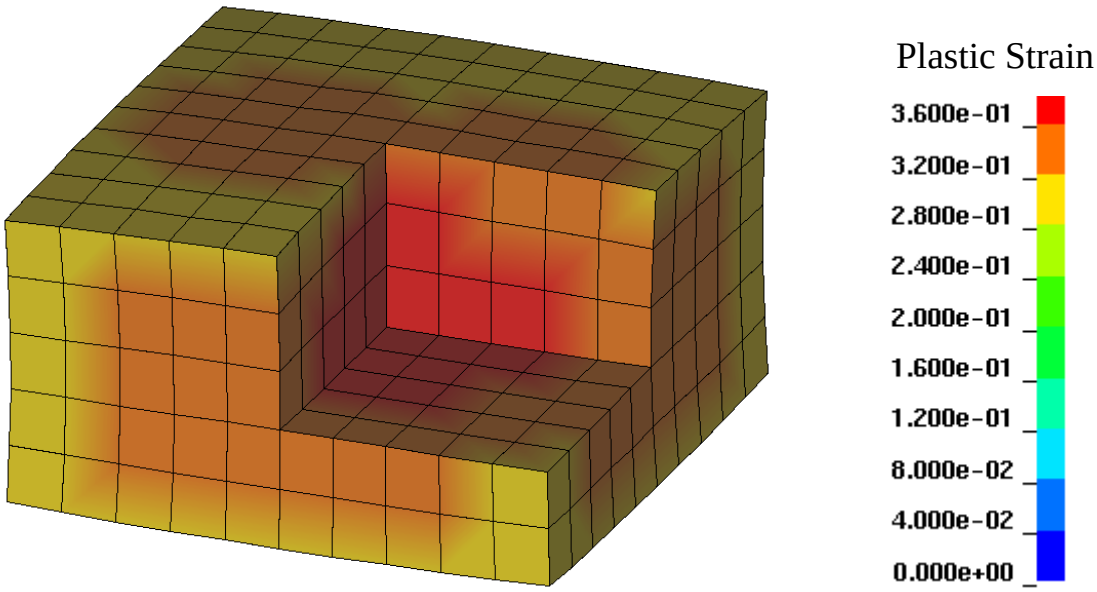

Figure 5.5: Distribution of plastic strain at 0.804mm specimen elongation. Material state preceding the first event of inter-cluster coalescence (896x896x292μm volume originally).

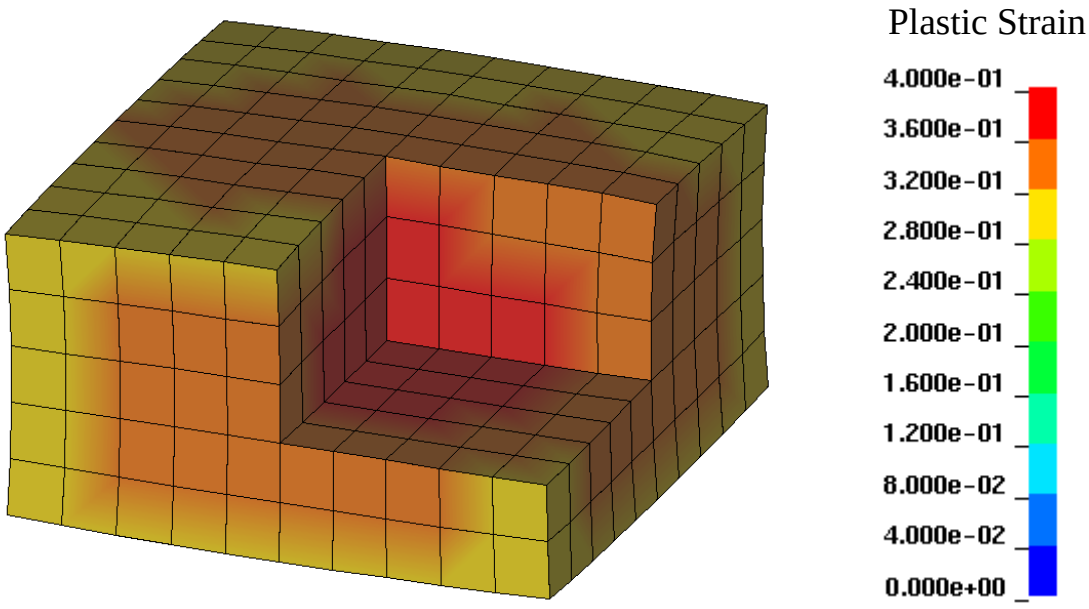

Figure 5.6: Distribution of plastic strain at 0.805mm specimen elongation. First event of inter-cluster coalescence. Subsequent deformation leads to widespread void/crack coalescence and final rupture (896x896x292μm volume originally).

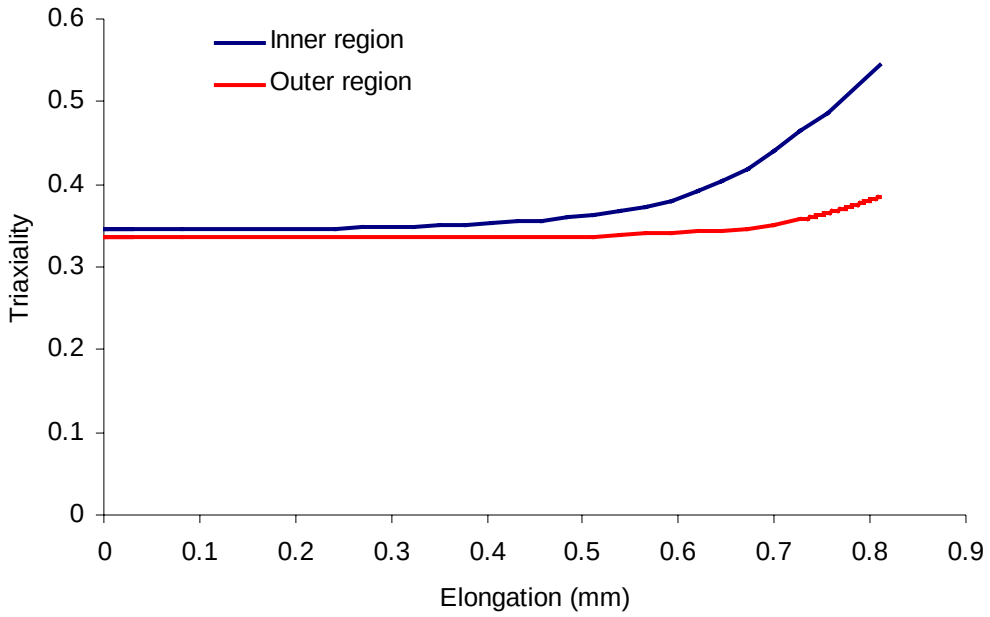

Figure 5.7: Stress triaxiality versus specimen elongation.

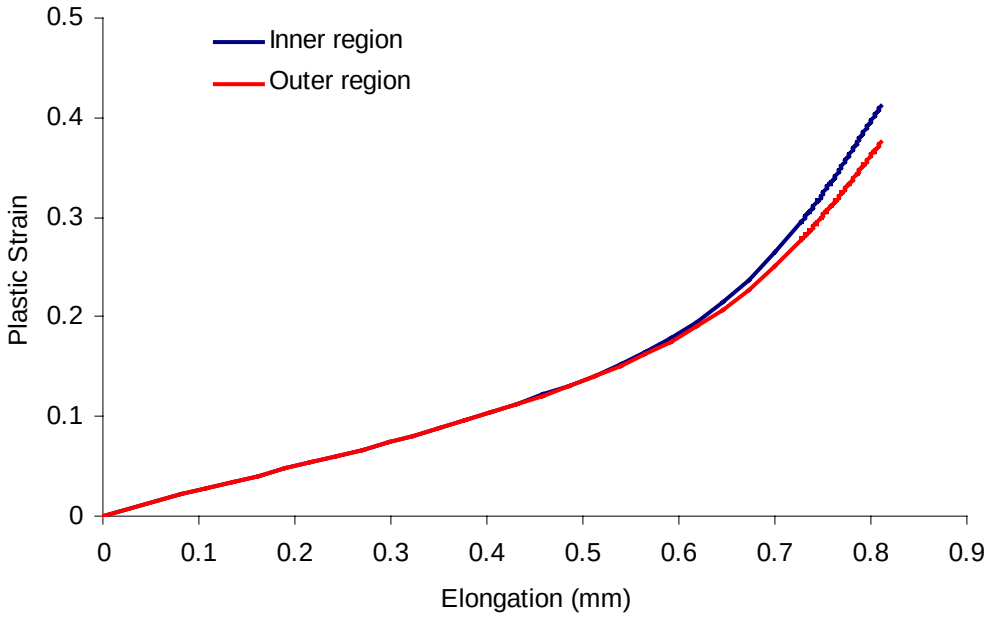

Figure 5.8: Average plastic strain versus specimen elongation.

The non-uniform distribution of material porosity due to the heterogeneous nature of the second phase particle fields is shown in Figures 5.9 – 5.12. A part of the volume in the plots has been removed to show the porosity distribution inside the specimen, which has an irregular character. Accelerated void nucleation and growth are observed to occur at the necked region and, in particular, in the middle of the specimen (Figures 5.11). The process of intra-cluster coalescence here does not lead to catastrophic failure. However, the coalescence mode that involves inter-cluster void-to-crack and crack-to-crack coalescence results in final ductile fracture. High plastic strain and stress triaxiality in the middle of the specimen causes more rapid void nucleation, growth, and coalescence than in the surrounding area.

The initiation and evolution of material damage within the considered volume can be seen in Figures 5.13 – 5.15. Initially, the material has only pre-existing voids produced during the manufacturing process (Figure 5.13). Pre-existing voids associated with Mg_2Si and *Fe*-rich particles are mostly produced during cold rolling. Voids not associated with any type of particle are likely formed during the casting process. As the material is deformed, more voids nucleate at *Fe*-rich particles through matrix decohesion and particle fracture (Figure 5.14). (Mg_2Si particles are considered to be inactive in the void nucleation criterion as discussed in Sections 3.3.2 and 4.4.1.) At large plastic strains in the range 0.3 – 0.4, void coalescence within particle clusters can be observed (Figure 5.15). At this point, the material has not lost its load carrying capacity and the deformation continues. Inter-cluster void-crack coalescence occurs at a plastic strain of 0.405 (averaged over the set of elements in the middle of the specimen). The crack propagation process leading to final fracture (Figure 5.16) is very rapid and requires only a small plastic strain increment to finish the rupture process.

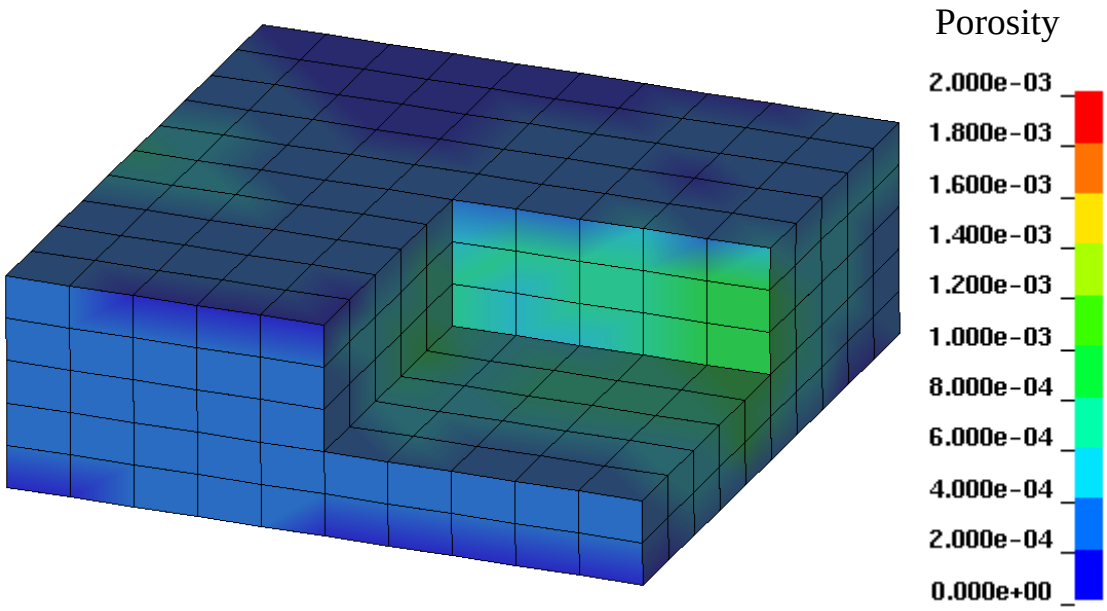

Figure 5.9: Distribution of porosity in undeformed material.

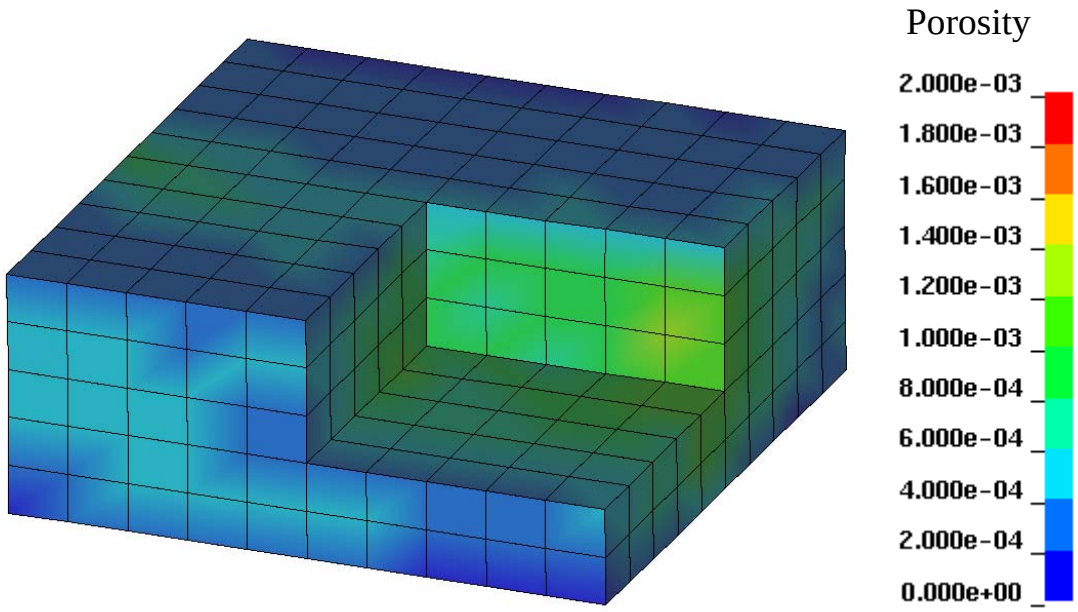

Figure 5.10: Distribution of porosity at 0.487mm specimen elongation. Material state preceding the first event of void-to-void coalescence (896x896x292μm volume originally).

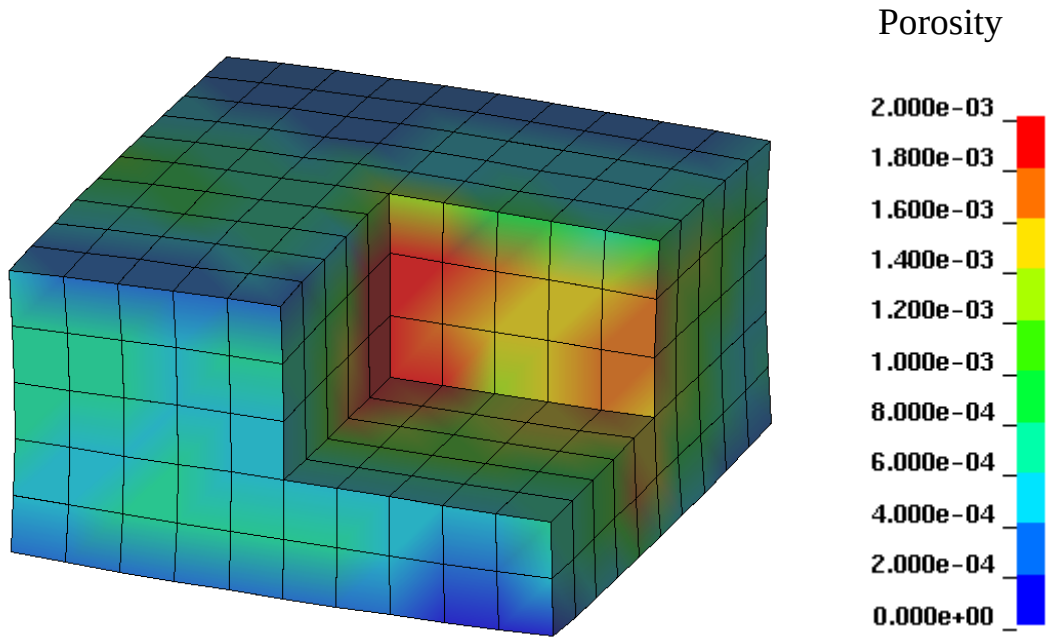

Figure 5.11: Distribution of porosity at 0.804mm specimen elongation. Material state preceding the first event of inter-cluster coalescence (896x896x292μm volume originally).

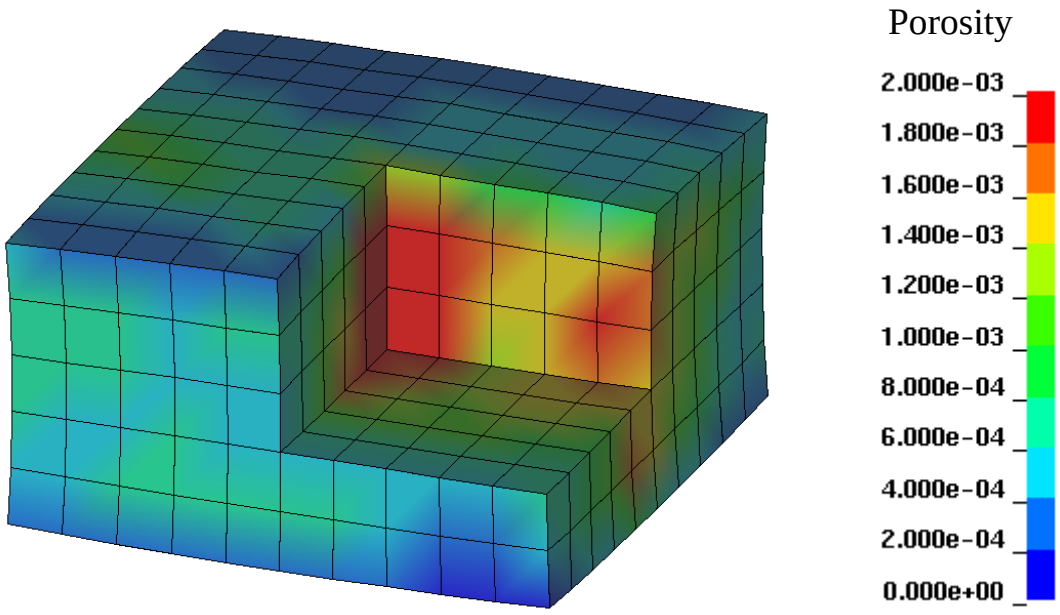

Figure 5.12: Distribution of porosity at 0.805mm specimen elongation. First event of inter-cluster coalescence. Subsequent deformation leads to widespread void/crack coalescence and final rupture (896x896x292μm volume originally).

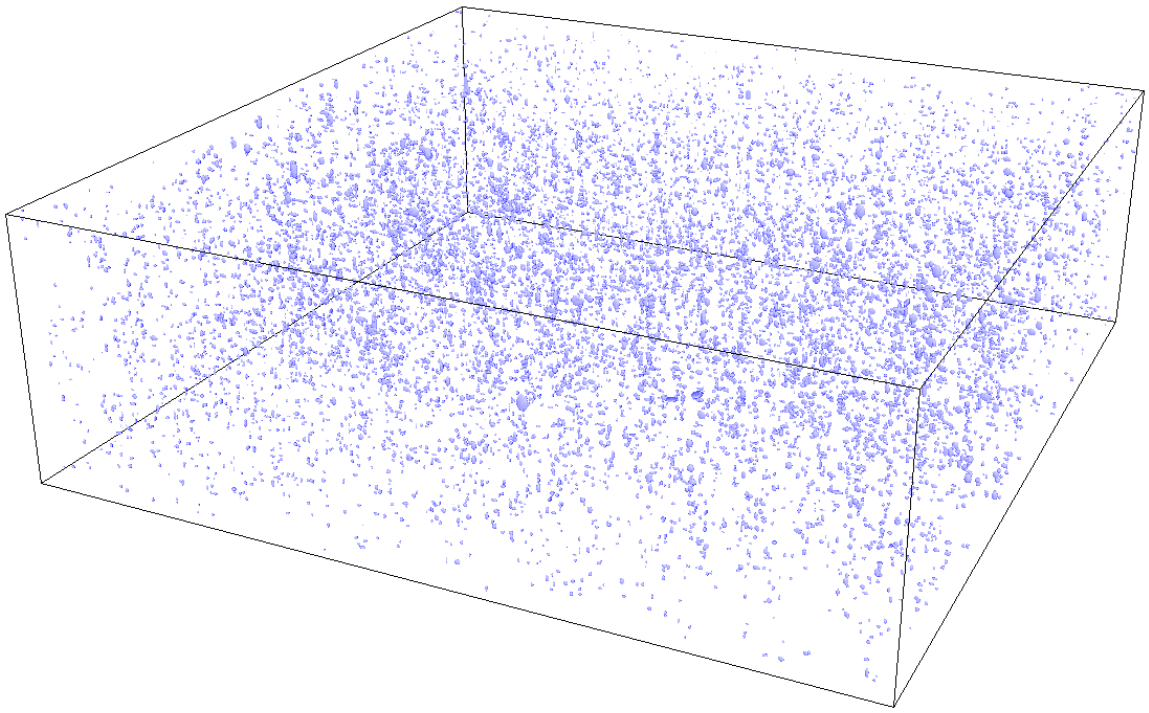

Figure 5.13: Nucleated voids in undeformed material (896x896x292μm volume).

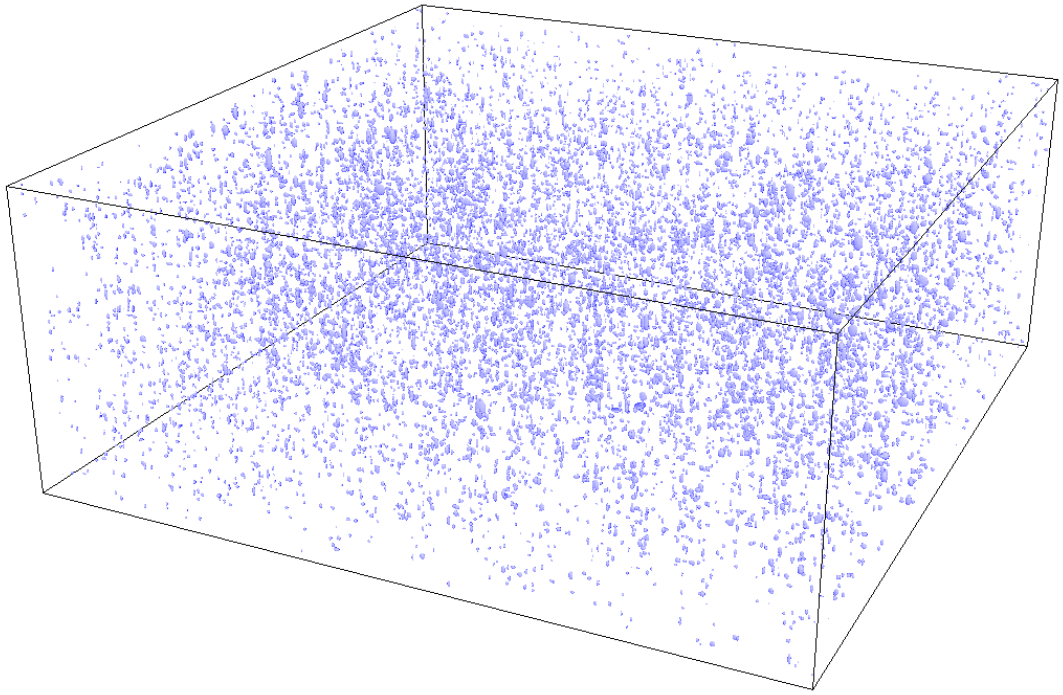

Figure 5.14: Nucleated voids at 0.487mm specimen elongation (0.132 maximum plastic strain). Material state before the first event of void coalescence (896x896x292μm volume originally).

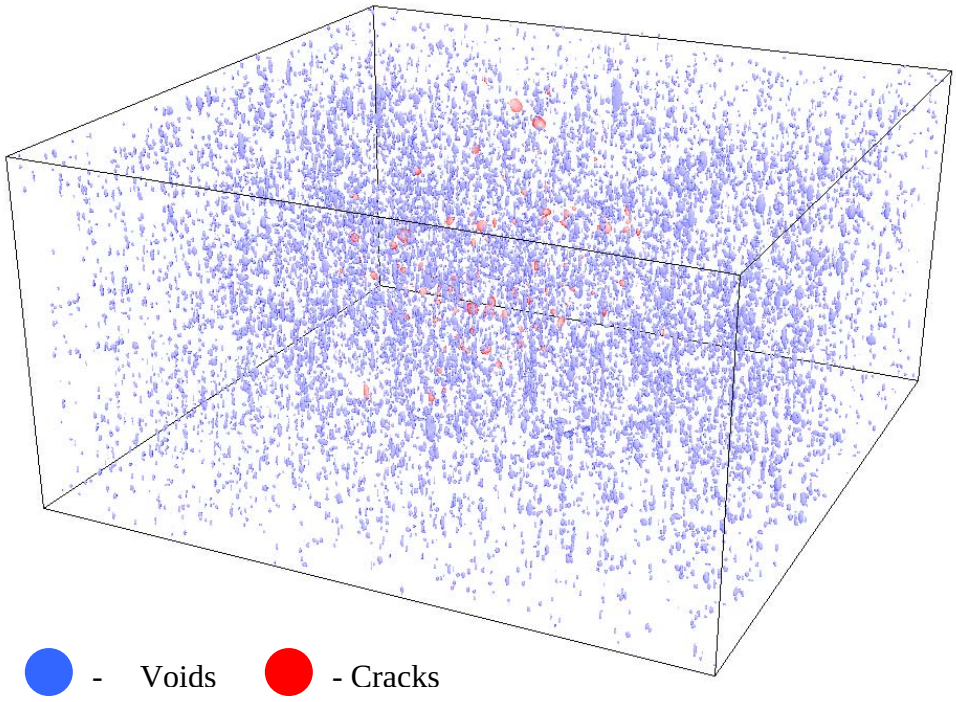

Figure 5.15: Nucleated voids and cracks at 0.804mm specimen elongation (0.403 maximum plastic strain). Void coalescence is confined to second phase particle clusters. (896x896x292μm volume originally).

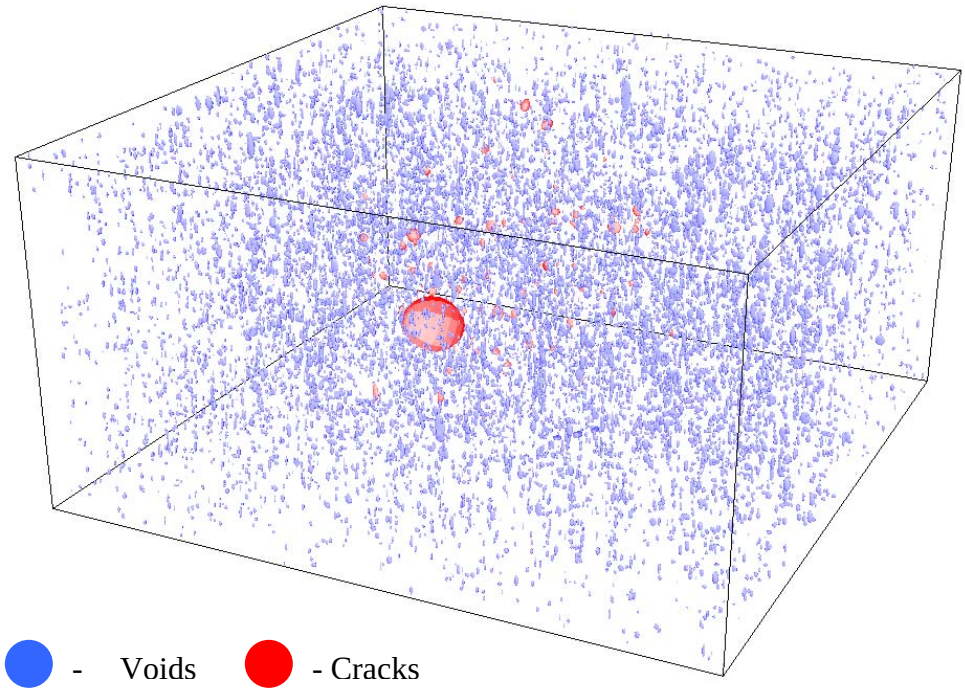

Figure 5.16: Nucleated voids and cracks at 0.805mm specimen elongation (0.405 maximum plastic strain). First event of inter-cluster coalescence. Subsequent deformation leads to widespread void/crack coalescence and final rupture (896x896x292μm volume originally).

The predicted void link-up process is shown in more detail in Figures 5.17 and 5.18. Figure 5.17 shows the coalescence of two voids, one of which is much larger than the other (Figure 5.17a). The resulting crack (Figure 5.17b) encompasses the two original voids and is then ready for coalescence with other voids and cracks.

Figure 5.18 serves to illustrate the propagation of void coalescence. Two images of the same region of the second phase particle field at two adjacent calculation steps are shown in Figure 5.18. The developing macro crack (Figure 5.18b) has swept through a number of neighbouring voids and cracks. At this moment, the size of the crack is comparable to the size of its parent element and the material loses its load carrying capacity.

Figure 5.19 shows the measured and predicted evolution of number of void-particle interfaces (PVI) per unit volume. The evolution of PVI numbers from two regions has been obtained, corresponding to the inner and outer regions of the sample, as indicated in Figure 3.6 and designated “Center” and “Surface,” respectively. These correspond to the material volumes used for the PVI measurements (Chapter 3). The PVI number predictions were averaged within the volumes for the comparison with the measured data. The initial vertical offset of the curves of the plot is due to material spatial variability. Both curves lie close to the points corresponding to different loading stage measurements. The curve for the outer region of the sample does not reach the maximum level of PVI numbers since the material experiences the stress-strain state of uniaxial tension and the effective plastic strain remains low in this region, which, in turn, delays void nucleation. The curve for the inner region of the sample closely resembles the PVI normal approximation curve.

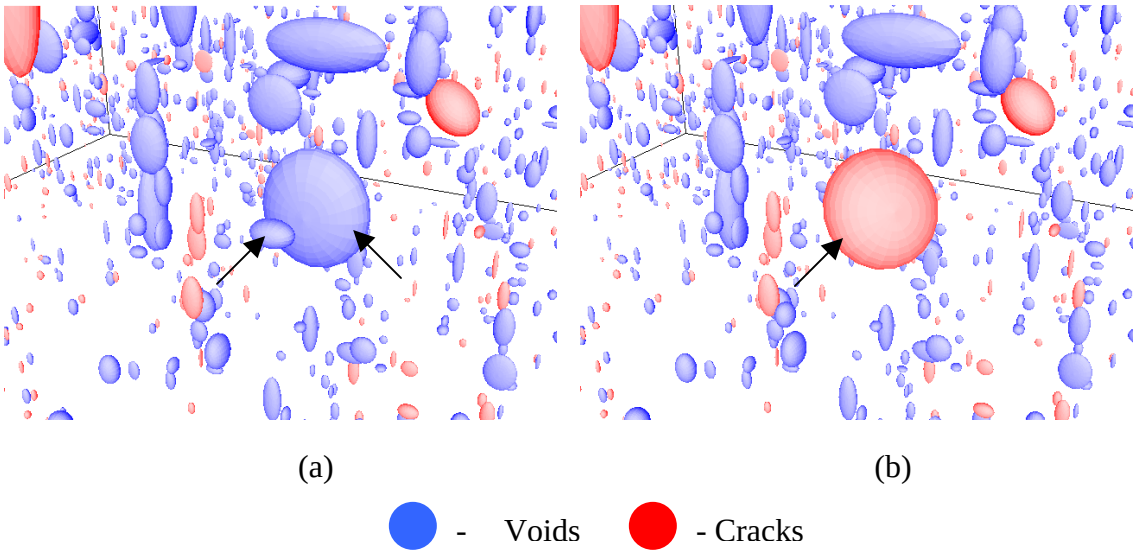

Figure 5.17: Void coalescence: (a) two coalescing voids (arrows); and (b) newly formed crack.

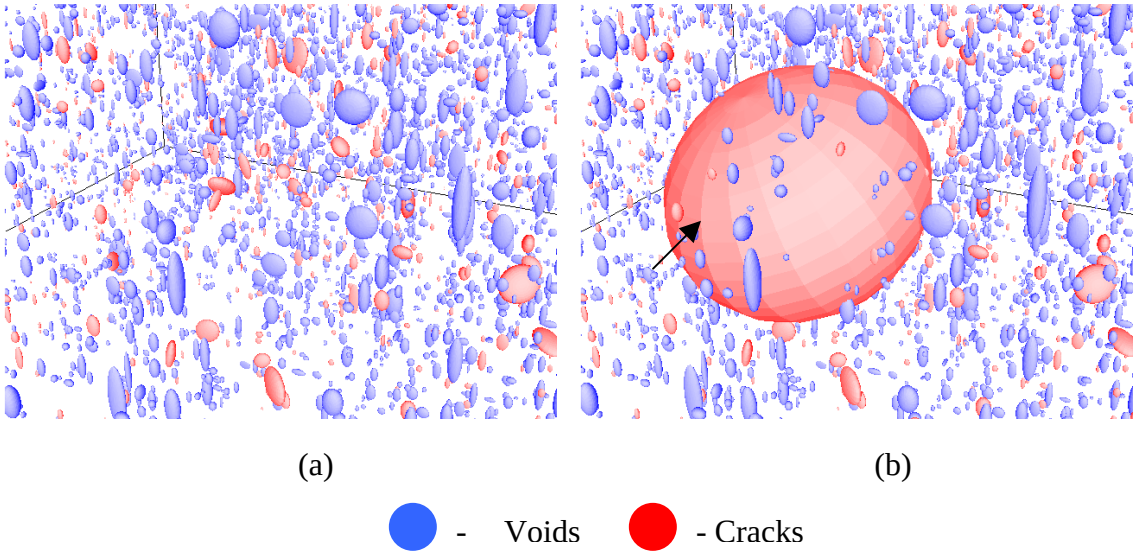

Figure 5.18: Development of macro crack: second phase particle field before (a) and after (b) macro crack initiation.

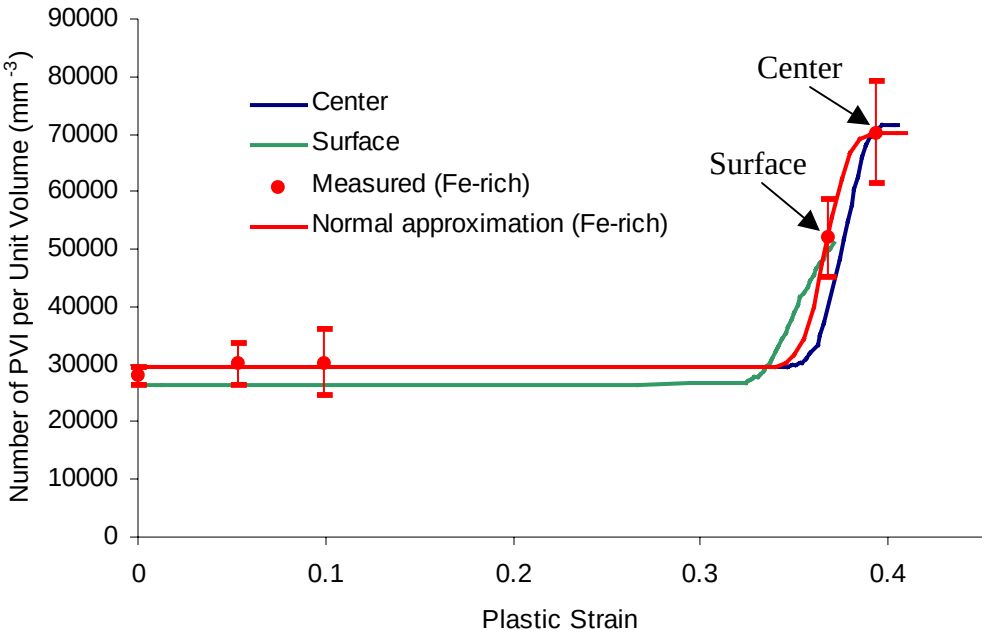

Figure 5.19: Number of nucleated voids per unit volume versus effective plastic strain.

5.2.1 Effect of clustering on void coalescence

One manner in which particle clustering can affect the damage process is in controlling where in the particle field does damage nucleate, which, in turn, can affect the spatial distribution of coalescing voids. To assess this effect, simulations were performed using two different nucleation criteria. In the first case, the nucleation criterion was that in Figure 4.12, in which the probability of void nucleation is a function of IPD or "nearest neighbour" spacing. The probability of nucleation increases for closely spaced particles, providing a cluster-sensitive nucleation criterion. In the second case (Figure 4.13), the effect of nearest neighbour spacing was suppressed to obtain a cluster-insensitive criterion.

The spatial distributions of nucleated voids for the two criteria are different. The cluster-sensitive nucleation criterion favors void nucleation in second phase particle clusters, whereas the cluster-insensitive class criterion imposes no such preference. In the later case, diffuse void nucleation can be observed, which makes it harder for newly formed voids to coalesce with other voids and cracks. Larger inter-void distances result in higher material formability due to delayed void coalescence.

The difference in void linkage rate in the simulations using the two nucleation criteria can be seen in Figure 5.20. The cluster-sensitive class nucleation criterion promotes void nucleation in particle clusters where inter-particle distances are smaller compared to the average IPD in the whole particle field. This lower spacing makes it easier for nucleated voids to coalesce with their neighbouring voids. Also, newly formed cracks cause void nucleation at their nearest neighbouring particles. The combined effect of clustering on nucleation and coalescence leads to a manifestation of the spatial arrangement of voids that results in higher damage accumulation rates and earlier fracture onset. The same mechanisms are in effect for the simulation with the clustering insensitive nucleation criterion; however, more uniform void nucleation in terms of spatial distribution and larger IPD results in impeded damage propagation.

5.2.2 Damage evolution in measured and reconstructed second phase particle fields

Figure 5.21 shows measured and predicted results for material porosity. The predictions of porosity evolution are compared for the simulations with clustering-sensitive and clustering-insensitive nucleation criteria, as well as with a simulation in which void coalescence was suppressed. The predictions using both nucleation criteria

were very close to the measured values for the first three strain states. The stress state of the last stage diverges from uniaxial tension as triaxiality increases in the specimen center. The higher triaxiality level promotes accelerated void growth and earlier onset of coalescence at particle clusters. Void coalescence starts to dominate the porosity evolution at this point. The high porosity measured in the center of the specimen is due to void coalescence in void-particle clusters.

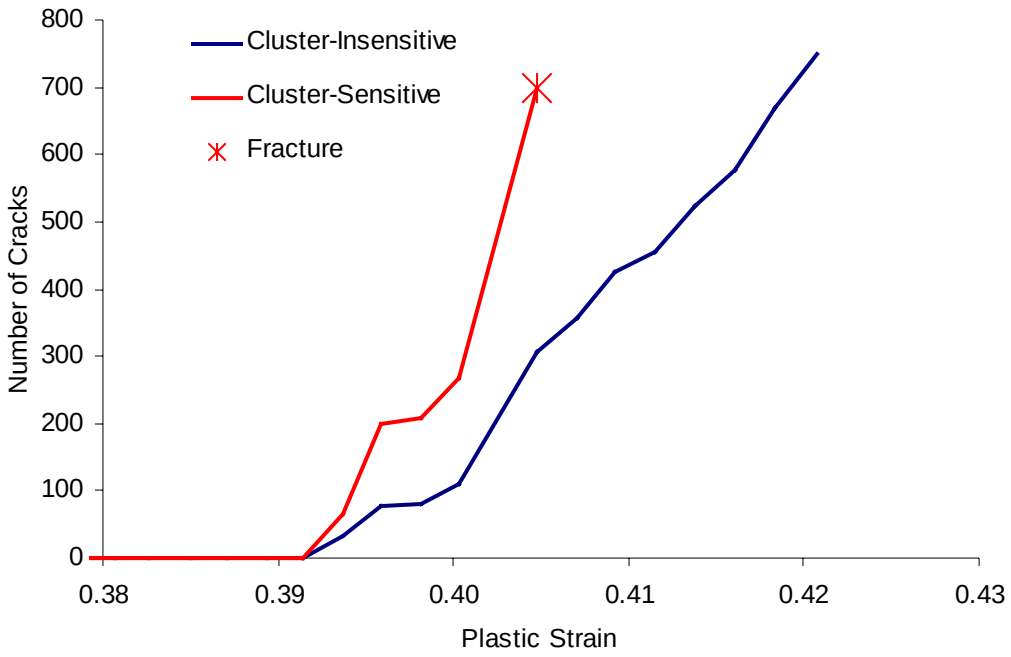

Figure 5.20: Coalescence predictions for cluster-insensitive and cluster-sensitive nucleation criteria.

The level of strain at onset of specimen rupture through the development of a macro crack is used to compare the DPM predictions of measured and reconstructed second phase particle fields. The comparison of the porosity evolution predictions in these fields and the moment of a macro crack initiation represented by the last point on each curve are shown in Figure 5.22. The overall behaviour of the two cases is similar.

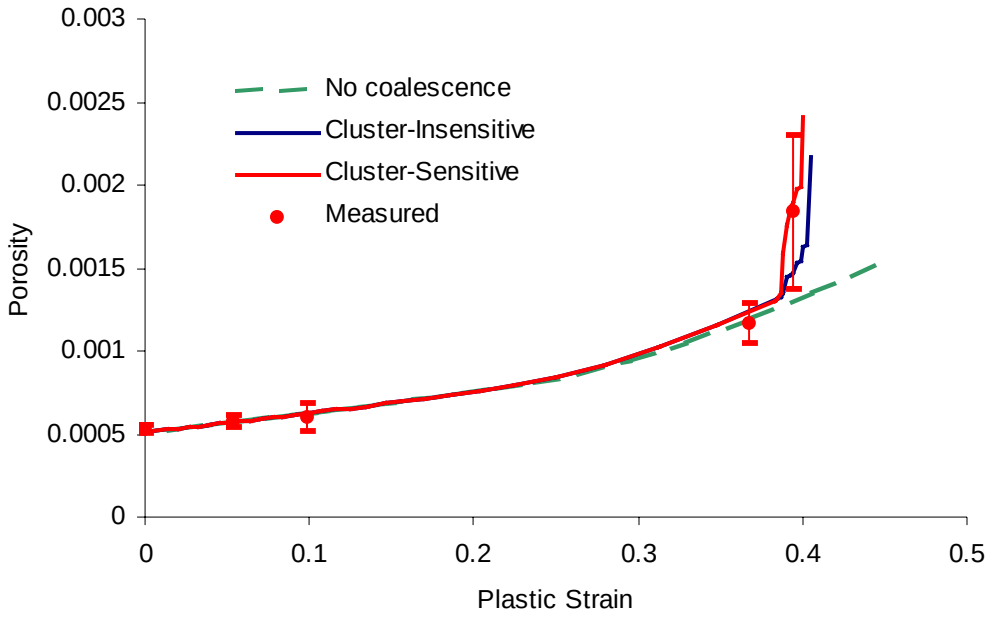

Figure 5.21: Porosity versus effective plastic strain.

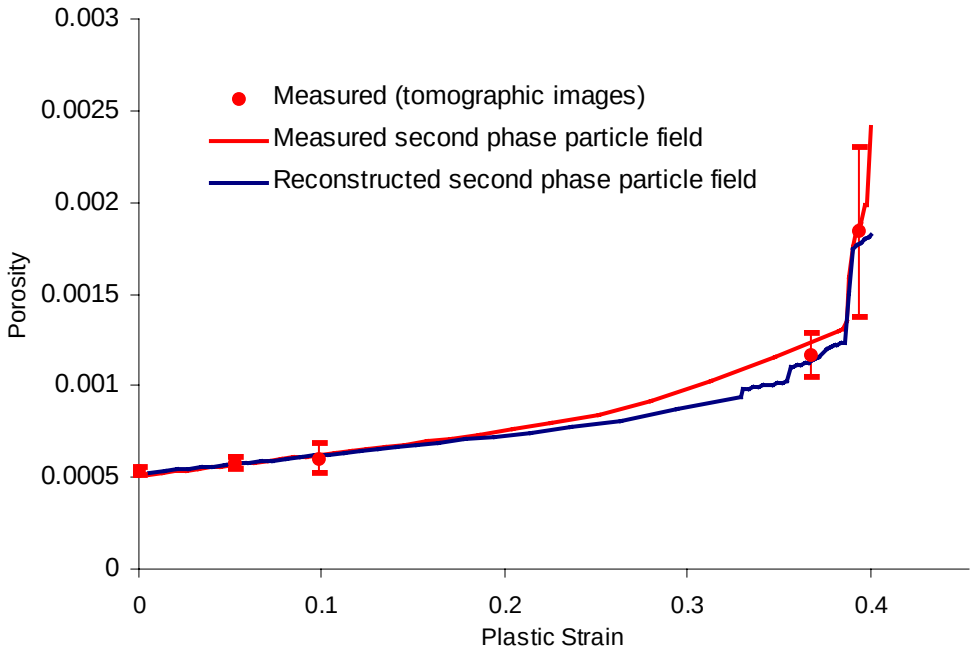

Figure 5.22: Porosity evolution in measured and reconstructed second phase particle fields.

Reconstructed second phase particle fields have a stochastic nature since they are reproduced using known size distribution probability density functions and a random number generator. This results in a certain variance in the predictions of material formability using the three-dimensional damage percolation model. In order to estimate the magnitude of this variance, a series of 20 DPM simulations using reconstructed second phase particle fields has been undertaken to calculate the mean and standard deviation of the plastic strain at the onset of fracture. Figure 5.23 shows five of the predicted porosity evolution curves and 95% confidence intervals of the predicted fracture strain. The predicted values of the fracture strain mean and standard deviation have been found to be 0.403 and 0.0079, respectively.

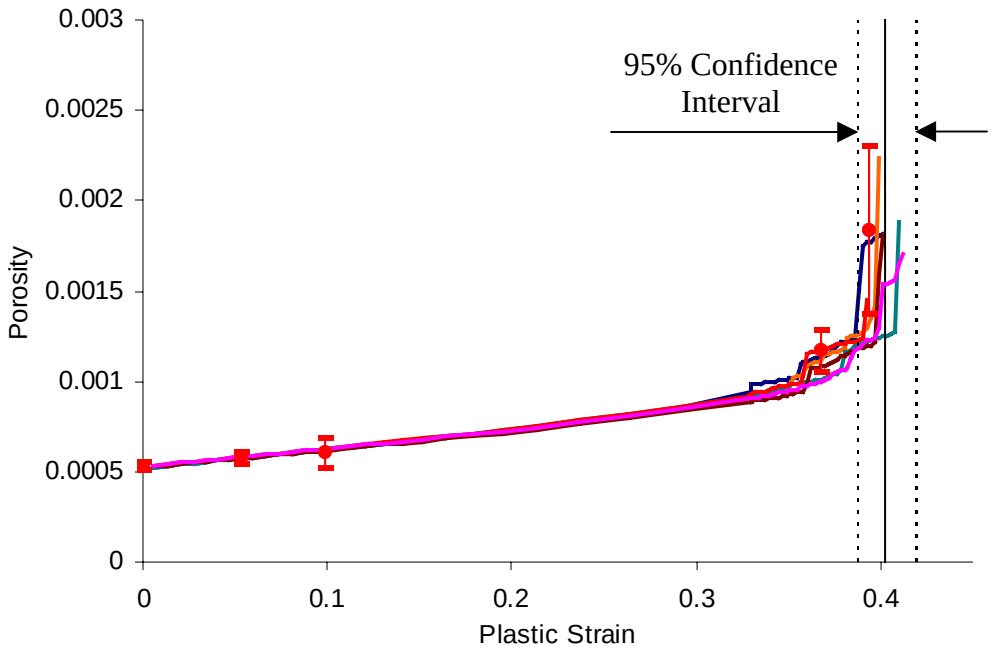

Figure 5.23: Porosity evolution in five reconstructed second phase particle fields with the same clustering parameters (p=80%, m=0.7, σ=3).

Chapter 6

Parametric Study of the Effect of Second Phase Particle Field Characteristics on Material Formability

The most attractive feature of the three-dimensional damage percolation model is its ability to consider the microstructural heterogeneity of materials containing second phase particles. Second phase particle fields inherit a certain degree of particle clustering as a result of the manufacturing processes used in production of the parent material. For example, aluminum alloy sheet is produced through a series of operations that includes casting, hot rolling, and cold rolling. In addition, second phase particle fields partly originate from particulate phases introduced in recycled scrap used for aluminum production. These contaminants represent a source of large second phase particles that are broken during hot and cold rolling and the resulting smaller particles form clusters oriented along the rolling direction.

Material formability depends on the degree of second phase particle clustering since it has been observed that damage initiating in the form of voids nucleating from second phase particles occurs more readily in particle clusters rather than stand-alone particles. Ideally, large hard particles should be widely spaced to avoid high stresses developed between closely spaced particles (Watt *et al.*, 1996). Second phase particle clustering affects all stages of damage initiation and evolution. Voids nucleate sooner in particle clusters (Fisher and Gurland, 1981a,b). Nucleated voids in clusters tend to grow faster with increasing plastic strain (Thomson *et al.*, 1999) and void coalescence in clusters occurs more easily (Thomson *et al.*, 2003). Smaller inter-particle ligament sizes as well as elevated stresses and strains in particle clusters favour void coalescence.

The size distribution of second phase particles is also of great importance. Gupta *et al*., (2001) noted that coarse and intermediate-sized particles significantly affect material mechanical properties. They manifest themselves through void nucleation via matrix decohesion and particle fracture in the cases of large equiaxed and nonequiaxed particles, respectively (Cox and Low, 1974).

Material formability depends on cluster size (Benson, 1995), which is a function of both overall second phase particle clustering and inter-particle distance distribution in clusters. Fracture strain decreases as the cluster radius increases and there exists a critical cluster radius within which fracture strain is relatively independent of the cluster size. Thus, when clusters are larger than the critical cluster radius, the material loses its ductility since it becomes easier for voids in different clusters to coalesce.

Different manufacturing conditions could affect second phase particle clustering parameters. For example, production of thinner sheet by multiple re-rolling would not only potentially break down more large particles (clustering percentage may change), but may also make stringers longer, thus affecting cluster inter-particle distance (IPD) distribution.

The control of material microstructural properties in terms of the degree of particle clustering, particle sizes, and particle cluster sizes and shapes should affect overall material performance and potentially lead to improved formability. To consider the importance of all of these parameters, the three-dimensional damage percolation model is applied to investigate the effect of microstructure alterations on the resulting material formability.

The microstructural properties of aluminum alloy AA5182 considered in the current research have been altered in a parametric fashion to study the effect of second phase particle clustering and particle size on formability. The study has concentrated on varying the parameters of the utilized clustering method in the material reconstruction technique and also the volume fraction of large second phase particles of the two types, *Fe*-rich and Mg_2Si. The changing clustering method parameters include the mean (m) and standard deviation (σ) of the particle IPD within clusters and the degree of clustering (p). The effect of introducing "improved" second phase particle fields containing finer particles that are less susceptive to void nucleation has been modelled by truncating the distributions of *Fe*-rich and Mg_2Si particles, thereby removing certain percentages of large particles. In the case of *Fe*-rich particles, only the particles that can nucleate voids have been considered. In the case of Mg_2Si particles, the entire population has been considered.

6.1 Effect of degree of particle clustering on formability

A series of second phase particle fields has been reconstructed with varying clustering probability parameter p (Figure 6.1). The parameter varied from 0%, which

corresponds to a completely random particle field, to 80%, which is the value that corresponds to the measured material microstructure, as determined through the parametric study described in Section 2.3.2. For this study, the parameters describing the cluster IPD distribution, namely the mean m and standard deviation σ, were the nominal values of 0.7 μm and 3 μm. Tensile tests of the second phase particle fields have been simulated with the three-dimensional damage percolation model. The resulting predicted porosity evolution is shown in Figure 6.2. The final points on each curve coincide with the predicted onset of material failure. At these points, macro cracks have developed and further material deformation leads to crack opening and fracture.

The results in Figure 6.2 show that material formability increases dramatically when the degree of material clustering decreases. The highest formability is achieved in the totally random second phase particle field. The numerical results for plastic strain at failure are shown in Table 6.1.

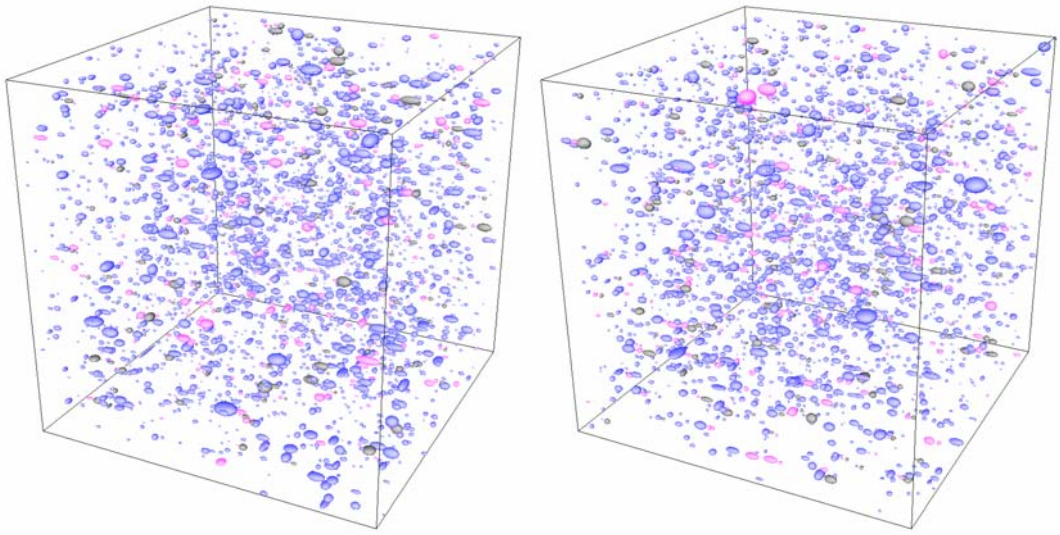

(a) (b)

Figure 6.1: Reconstructed second phase particle fields: randomly distributed (a) and clustered (p=80%) (b).

Table 6.1: Plastic strain at failure for materials with different degree of clustering.

Particle Clustering	Random (0%)	20%	40%	60%	80%
Plastic Strain at Failure	0.515	0.501	0.489	0.472	0.401

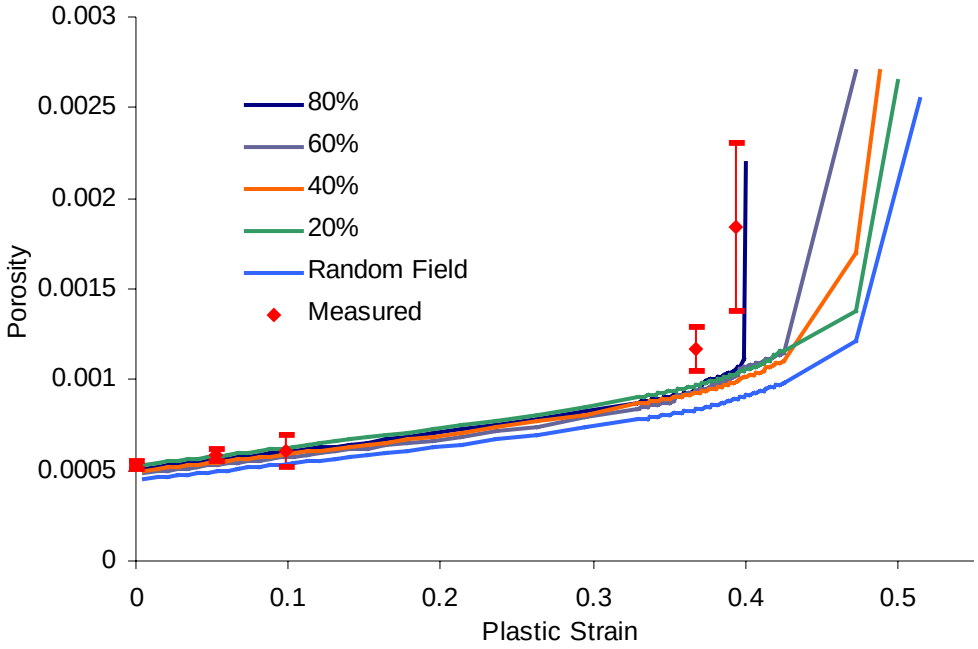

Figure 6.2: Porosity evolution in second phase particle fields with different particle clustering.

6.2 Effect of cluster inter-particle distance on formability

The effect of inter-particle distance (IPD) distribution within particle clusters on formability has also been investigated. The cluster IPD distribution has been considered

to be normal with two parameters that fully describe the shape of the IPD probability density function (PDF) curve, the mean m and standard deviation σ. It should be noted that only positive values of IPD are considered in the clustering method; thus, the distribution is truncated by the ordinate axis. The area under the PDF has to be equal to unity and thus the PDF curves were normalized. Parameter ranges of 0.7 – 2.8 μm and 3 – 10 μm have been considered for m and σ, respectively.

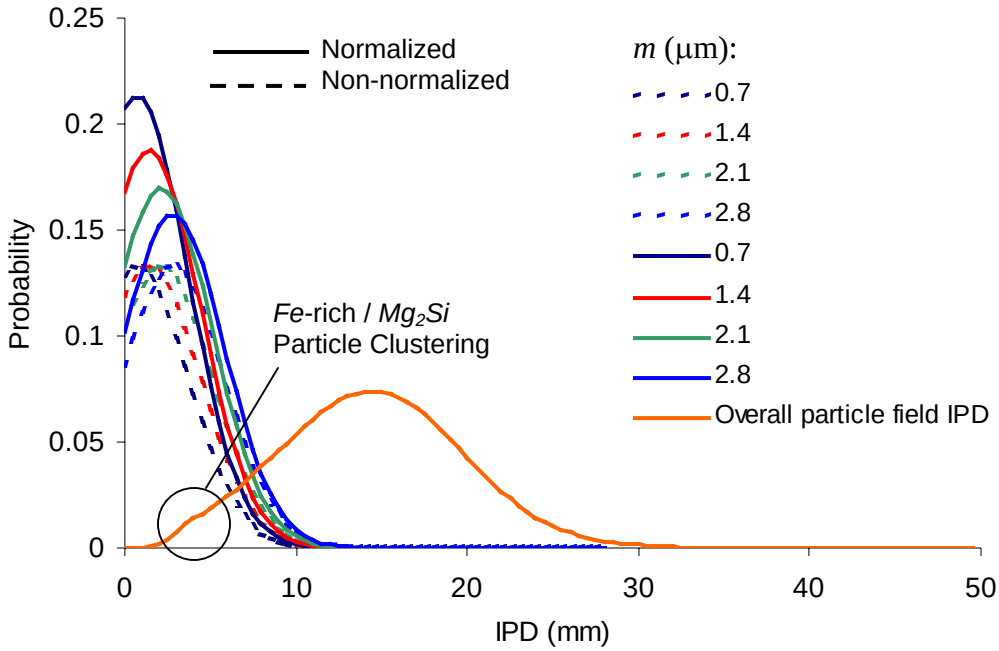

Figure 6.3: Cluster IPD distributions with changing mean *m* compared to the overall second phase particle field IPD distribution (σ=3μm).

An important observation can be made by comparing the cluster IPD distributions with the IPD distribution of the entire second phase particle field (Figures 6.3 and 6.4). The IPD distribution of the second phase particle field differs from that of a random particle field as was mentioned in Chapter 2. A small "bump" can be seen in the left-hand side of the curve (Figures 6.3 and 6.4) that represents particle clustering. Thus, it was

assumed that the cluster IPD values should be distributed around that region. Changing cluster IPD mean does not affect the cluster IPD distribution to the extent that its maximum values could lead to particle spreading as opposed to particle clustering (Figure 6.3). This would happen when maximum cluster IPD values are comparable with those of the second phase particle field IPD. Changing the cluster IPD standard deviation within its limits results in that kind of behaviour (Figure 6.4). Therefore, second phase particle fields with varying cluster IPD standard deviation have been discarded from the analysis. In the case of varying cluster IPD mean *m*, second phase particle fields with *m* equal to 0.7, 1.4, 2.1, and 2.8 μm have been constructed. The other clustering parameters were p=80% and σ=3 μm.

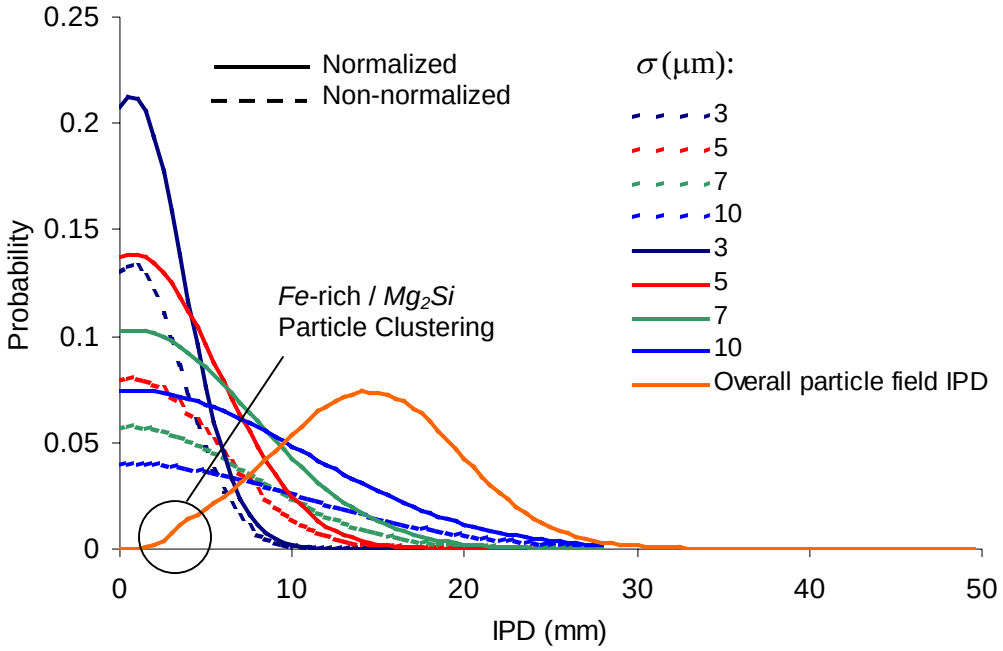

Figure 6.4: Cluster IPD distributions with changing standard deviation σ compared to the overall second phase particle field IPD distribution (m=0.7μm).

The results of damage percolation simulations using the second phase particle fields with varying cluster IPD mean are shown in Figure 6.5. Limiting plastic strain values corresponding to the considered cluster IPD distribution means are presented in Table 6.2. There does not appear to exist a strong relationship between plastic strain at failure and cluster IPD distribution mean, which is consistent with the notion that fracture strain is relatively independent of the cluster size within a certain critical cluster radius (Benson, 1995). The case of very large cluster sizes could be modelled by varying cluster IPD distribution standard deviation, which is not considered here since this case asymptotically approaches a random spatial particle distribution. Similar conditions have been simulated by second phase particle fields with low particle clustering in Section 6.1.

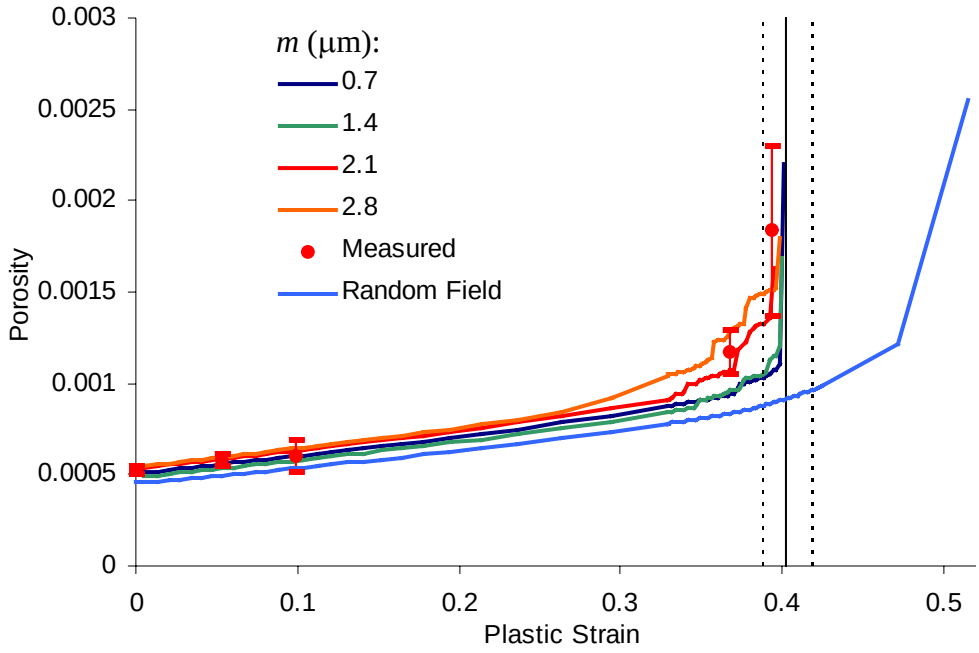

Figure 6.5: Porosity evolution in second phase particle fields with different cluster IPD mean *m*. Vertical lines represent the expected value of plastic strain at failure and 95.4% confidence interval for the original reconstructed second phase particle field (p=80%, m=0.7μm, and σ=3 μm).

Table 6.2: Plastic strain at failure for materials with different cluster IPD distribution mean.

m (μm)	0.7	1.4	2.1	2.8
Plastic Strain at Failure	0.401	0.400	0.395	0.399

6.3 Effect of maximum second phase particle size on formability

The effect of second phase particle size on material formability, in particular, the existence of large particles, has been investigated by considering reconstructed second phase particle fields (p=80%, m=0.7 μm, σ=3 μm) with various portions of large particle population removed. The resulting particle fields have been used in damage percolation simulations of the tensile test.

6.3.1 *Fe*-rich particles

Fe-rich particles represent the majority of second phase particles. However, most of these particles remain inactive during material deformation. Thus, only *Fe*-rich particles that can nucleate voids have been considered for the particle removal. The portion of nucleating particles can be determined by finding the minimum particle volume to nucleate voids according to the nucleation criterion, as shown in Figure 4.14. The particle volume distribution corresponding to this void-nucleating population is

shown in Figure 6.6. The obtained curve has been scaled so that the area under the curve equals to unity. The vertical lines in Figure 6.6 represent percentages of the particles remaining after the removal of large particles. Second phase particle fields with 50, 60, 70, 80, 90, and 100% of the number of nucleating particle have been considered for the damage percolation simulation.

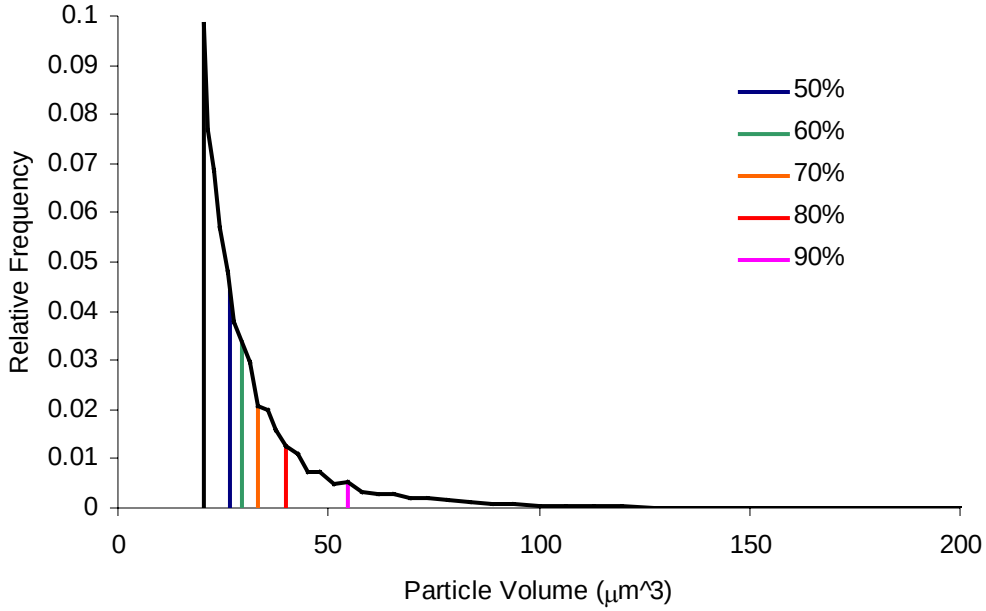

Figure 6.6: Truncated *Fe*-rich particle volume distribution (only particles that nucleate voids included).

The results of the simulations are shown in Figure 6.7. The corresponding numerical results for plastic strain at failure can be found in Table 6.3. The change in number of large *Fe*-rich particles significantly affects material formability. There is a proportional increase in plastic strain at failure with increasing numbers of removed large particles. The initial material porosity as well as its subsequent evolution is also seen to change since many large *Fe*-rich particles are associated with pre-existing and early-

nucleating voids. Removing large particles of this type at the manufacturing stage can contribute to lower initial material porosity and material softening during deformation. Ideally, the maximum particle size can be found that would allow void-free material deformation.

Table 6.3: Plastic strain at failure for materials with different *Fe*-rich particle content.

Fe-rich Particle Content	50%	60%	70%	80%	90%	100%
Fe-rich Volume Fraction	0.00382	0.00396	0.00408	0.00422	0.00441	0.00483
Plastic Strain at Failure	0.515	0.491	0.458	0.439	0.405	0.401

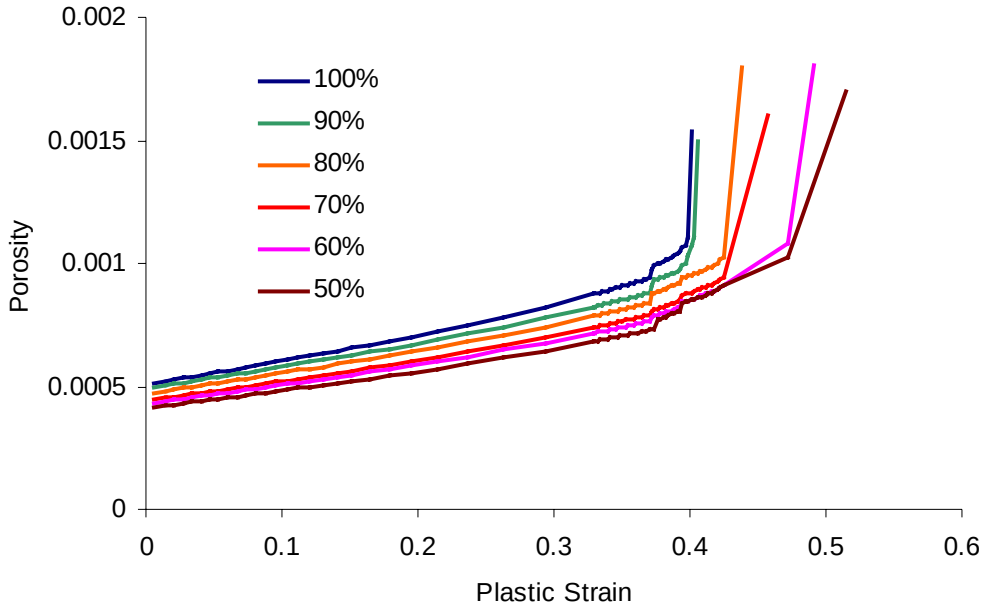

Figure 6.7: Porosity evolution in second phase particle fields with different *Fe*-rich particle content.

6.3.2 *Mg_2Si* particles

The procedure utilized for varying the content of large *Fe*-rich particles has also been applied to modify the *Mg_2Si* particle population. Particles of this type, however, are considered to have nucleated voids during cold rolling and to not nucleate voids during further material deformation. Thus, the entire population of *Mg_2Si* particles is considered here. Figure 6.8 shows the distribution of *Mg_2Si* particle volumes and the portions of the particle population corresponding to 60, 70, 80, 90, 95, and 100% of the overall number of such particles.

Results for damage percolation simulations of the tensile test with removed portions of large *Mg_2Si* particles are shown in Figure 6.9. The corresponding plastic strains at failure are summarized in Table 6.4. Several observations and conclusions made based on the current results are similar to those of the case of *Fe*-rich particles. Formability can be improved by controlling the maximum *Mg_2Si* particle size. Also, the initial material porosity changes since large *Mg_2Si* particles are sometimes associated with pre-existing voids.

The difference in the predictions for the two types of second phase particles, *Fe*-rich and *Mg_2Si*, can be seen in the region of void coalescence around 0.4 – 0.5 plastic strain. There is a distinct change in material behaviour as the percentage of remaining particles changes from 80% to 90%. It seems that *Mg_2Si* particles with pre-existing voids do not play a crucial role in damage development after 10 – 20% of the larger particles have been removed. Taking into account that 80% of these particles are in clusters with *Fe*-rich particles and voids, the observed abrupt change in formability can be explained. When large *Mg_2Si* particles are removed, there are fewer voids present in particle clusters. This postpones void coalescence in the clusters, leading to improved material formability.

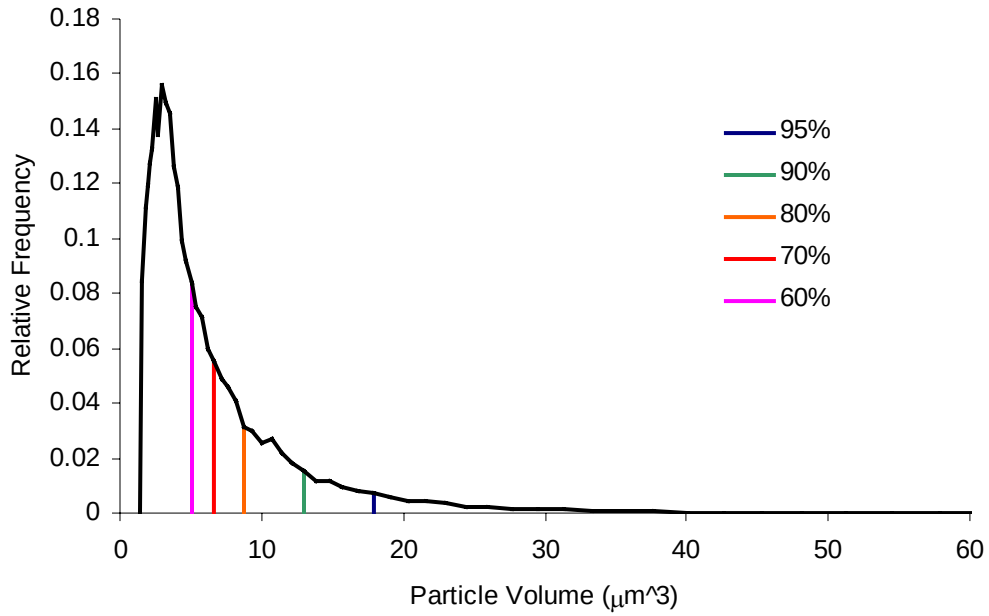

Figure 6.8: *Mg_2Si* particle volume distribution.

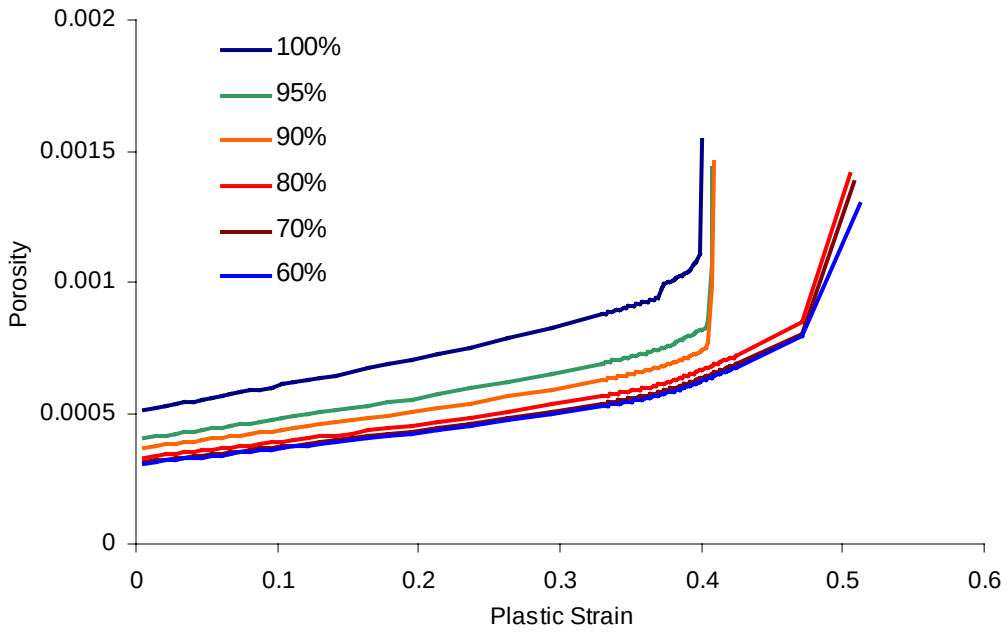

Figure 6.9: Porosity evolution in second phase particle fields with different *Mg_2Si* particle content.

Table 6.4: Plastic strain at failure for materials with different *Mg_2Si* particle content.

Mg_2Si Particle Content	60%	70%	80%	90%	95%	100%
Mg_2Si Volume Fraction	0.000103	0.000145	0.000186	0.000257	0.000326	0.00485
Plastic Strain at Failure	0.513	0.508	0.506	0.409	0.408	0.401

Summary

The three-dimensional damage percolation model has been used as a tool for material formability prediction in various "improved" second phase particle fields of aluminum alloy (AA5182). These microstructure alterations are possible due to potential improvements in the manufacturing processes used to produce metal sheet. The model is capable of formability prediction of a material with a newly designed microstructure. Among the important factors affecting material formability, the following have been found to have the highest impact. Second phase particle clustering significantly changes material formability by localizing damage initiation and evolution. Large second phase particles contribute to both higher initial porosity as well as accelerated damage initiation and evolution during material deformation. Controlling the populations of large *Fe*-rich and *Mg_2Si* second phase particles in material would allow significant material formability improvement.

Chapter 7

Application of the Three-Dimensional Damage Percolation Model to Simulation of Bending

The three-dimensional damage percolation model can be applied to model damage during different types of forming operations. Material formability during the *in situ* tensile test considered in the previous chapters, amongst many other sheet metal forming operations, is limited by the development of flow instability in the form of a neck. Damage through void nucleation, growth, and coalescence follows the onset of necking leading to ductile rupture. An alternative failure mechanism is observed during bending in which material formability is determined by the cooperative role of shear localization and damage initiating from second phase particles at the highly strained outer surface of a specimen (Figure 7.1). The sheet metal forming operation corresponding to this kind of bending deformation is known as hemming and is extensively used in the automotive industry to join outer skins and structural parts (Lievers *et al.*, 2003 b).

The formability of materials under bending has been studied with a specially designed cantilever bend test (CBT) (Selcuk and Rawlings, 1991; Lloyd *et al.*, 2002), as shown in Figure 7.2. During this test, a sheet material is bent over a mandrel with a small radius of curvature relative to the sheet thickness. The ratio of bend radius to sheet thickness (r/t) and the maximum angle up to which the material maintains its load carrying capacity are commonly used as measures of formability or bendability. The material at the outer surface of the specimen is extensively strained. The combined effect of shear bands and voids nucleating from second phase particles at the surface and surface irregularities leads to tearing and cracking and significantly affects material formability.

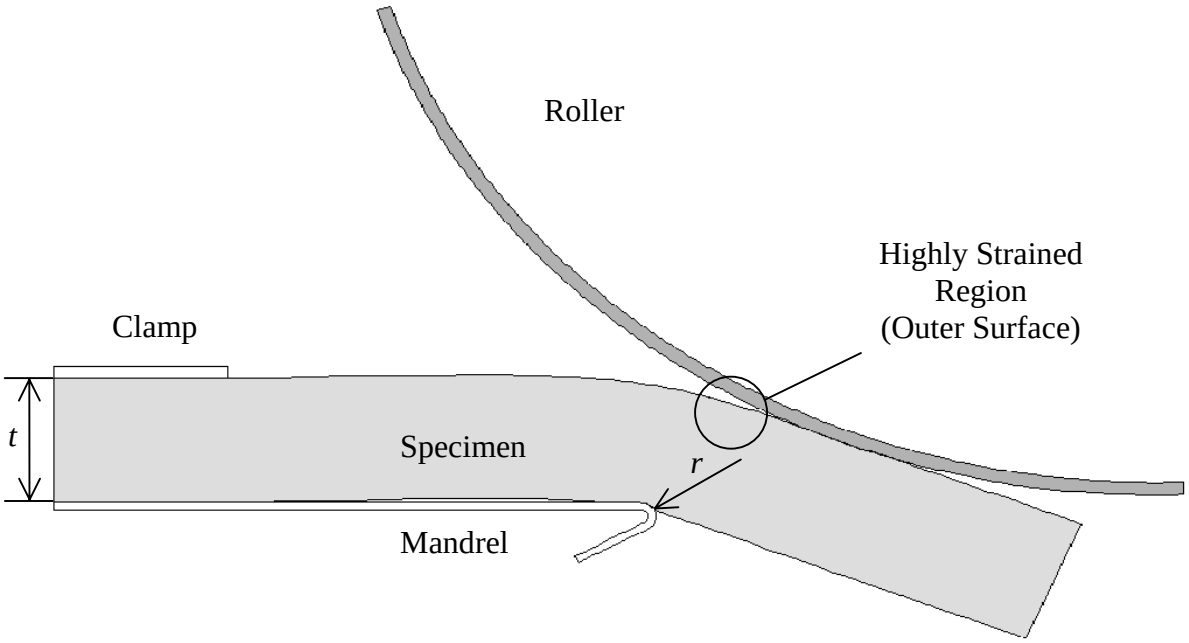

Figure 7.1: Specimen bent during a cantilever bend test.

The failure mode during a bending test includes several aspects (Lloyd *et al.*, 2002). First of all, there is surface roughening due to grain rotation. This process contributes to the development of shear bands originating at the outer strained surface of the specimen and propagating through the specimen thickness. On the other hand, second phase particles nucleate voids at the same highly strained outer specimen surface. The combined effect of these processes leads to the development of surface cracks and material failure.

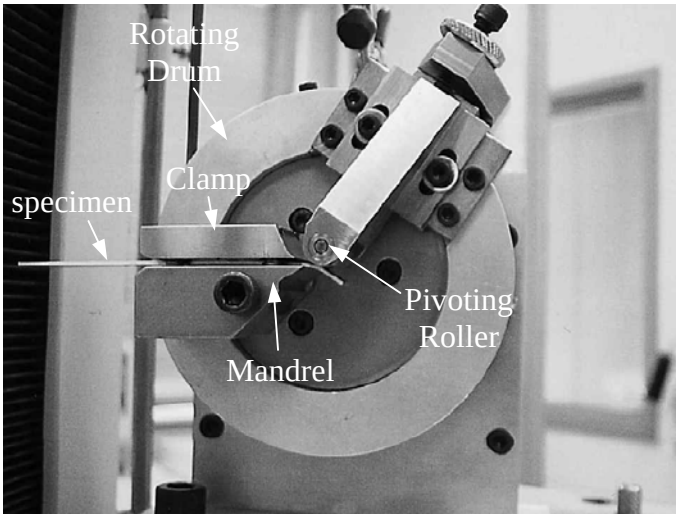

Figure 7.2: Cantilever bend test apparatus (Lloyd *et al.*, 2002).

The modelling of material failure during bending should account for all of the aforementioned processes. The roughening of the outer specimen surface is often modelled using crystal plasticity (Triantafyllidis *et al.*, 1982; Becker, 1992). Shear banding can be modelled using a finite element code with a bifurcation criterion triggering the onset of shear banding (Tvergaard, 1987; Lievers *et al.*, 2003 a, b). Finally, material damage due to second phase particle nucleation is normally modelled using dilational yield functions (Gurson, 1975, 1977a,b,c; Tvergaard and Needleman, 1984). It is still not clear how these various destabilizing processes combine to control material

behaviour under bending. An approach to modelling such damage processes that takes into account the various factors needs to be established. Much of the work in this area has concentrated on the shear localization aspect of bending; however, the damage component has not been properly modelled as yet. There are still doubts about which GTN parameters that should be used. Lievers *et al.* (2003 a), for example, conducted a parametric study to determine the effects of the parameters, yet their exact values have not been established.

The prospect of using the DPM in the context of this formability test is very promising since its damage initiation and evolution laws are based on real microstructural data and have been validated using the results of the *in situ* tensile test. A major advantage of the DPM lies in its ability to model damage development in varying microstructures not only in terms of the size, shape, and number of second phase particles, but also their spatial distribution. For example, it is known that the size and number of second phase particles, as well as the level of particle clustering, increase with *Fe* content level (Lievers *et al.*, 2003 b). Higher levels of *Fe* content result in inferior bendability.

The purpose of the research presented in this chapter is to model damage initiation and evolution in AA5182 sheet during bending and to provide an example of application of the DPM to the study of the effect of *Fe* content on the formability (bendability) of the material. DPM calculations that consider damage initiation and evolution in AA5182 can be coupled later with simulations taking into account other important factors like surface roughening due to grain rotation and shear banding that are crucial during bending. These factors, together with proper damage modelling, can account for all of the bending modelling aspects.

7.1 Model input

To provide input to the DPM, a second phase particle field and a finite element model of a bending operation have been utilized. During the bending of a sheet specimen within the cantilever bend test (CBT), there exists a region with the highest strains developing at the outer surface of the specimen (Figure 7.1). Using the approach similar to that of Lievers *et al*. (2003 a), a small block of material adjacent to the outer specimen surface is modelled.

7.1.1 Second phase particle field

The second phase particle field used to model the CBT (Figure 7.3) is that acquired with X-ray tomography and used to simulate the *in situ* tensile test presented in Chapter 5. The particle field was rotated to align with the sheet orientation considered in the FE bending model. Two sheet orientations were considered. In the particle field in Figure 7.3, the second phase particles are oriented orthogonal to the axis of bending. The bending of such a particle field is referred to as bending in the rolling direction, and this field has been used for the study of the effect of *Fe*-rich particle content on formability. Another second phase particle field (Figure 7.4) has been utilized to provide comparison of damage development during the loading of sheet material in directions along and orthogonal to the rolling direction. Second phase particles in this field are oriented parallel to the axis of bending. The bending of such particle field is referred to as bending in orthogonal-to-rolling direction.

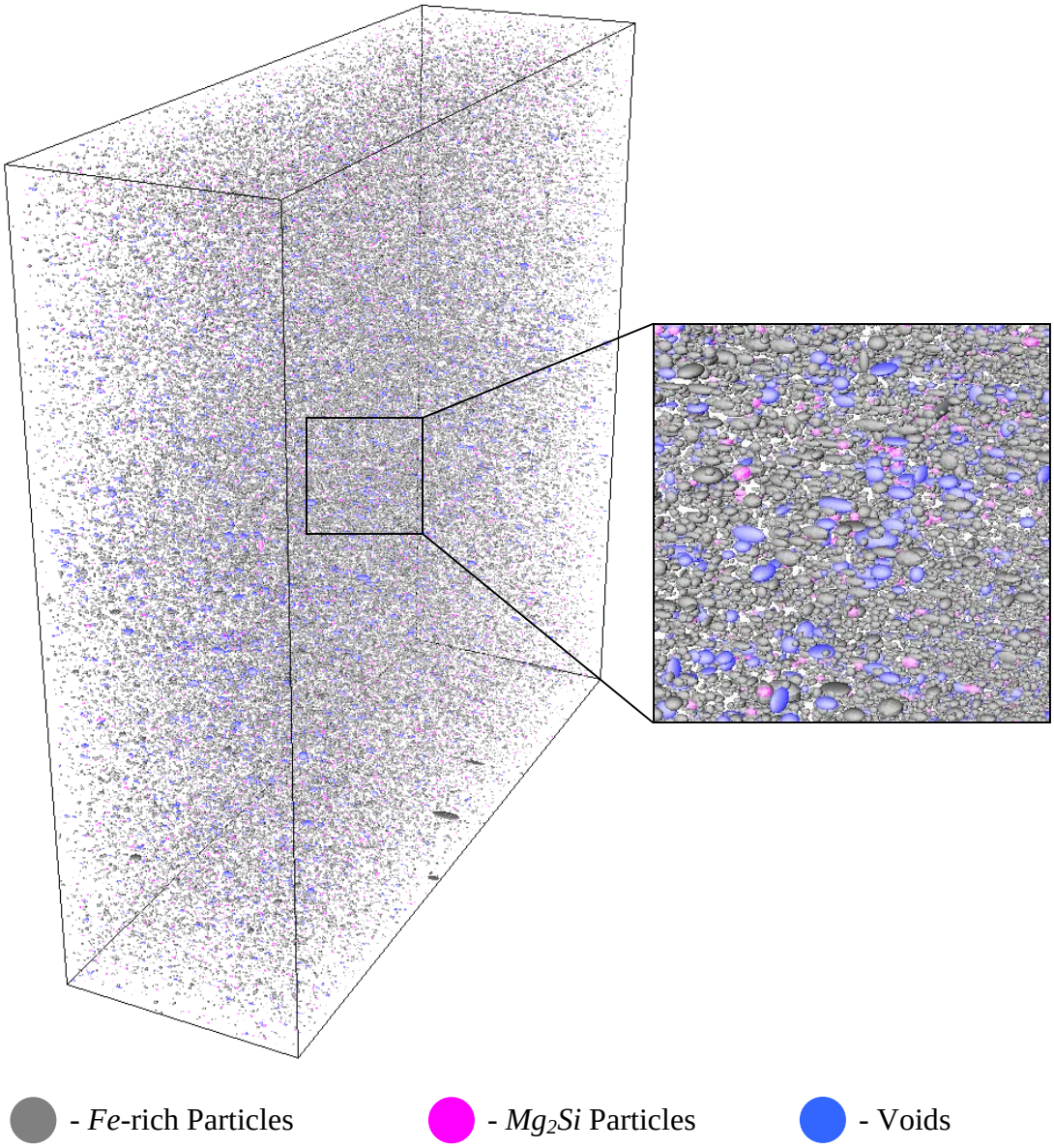

Figure 7.3: Second phase particle field (292x896x896μm volume) for the modelling of bending in the rolling direction. The large square is an enlargement of the smaller square.

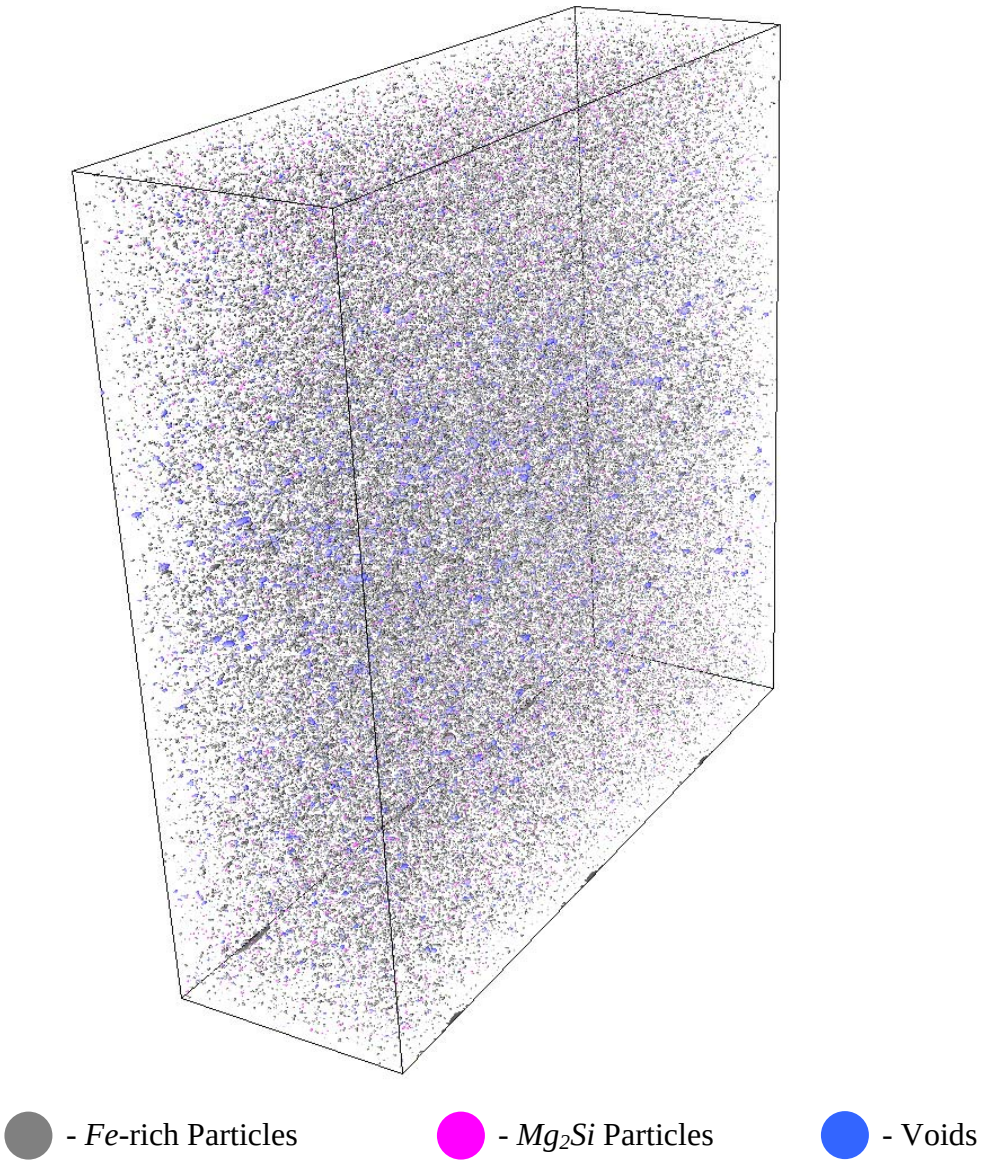

Figure 7.4: Second phase particle field (292x896x896μm volume) for the modelling of bending in the orthogonal-to-rolling direction.

Fe-rich second phase particles control the nucleation behaviour of the material during deformation since they comprise the nucleating phase, as implemented within the current framework of the DPM. The level of *Fe* content determines the maximum *Fe*-rich particle size and degree of clustering. The effect of *Fe* content level on AA5182 bendability is studied through the truncation of the *Fe*-rich particle population, as described in the previous chapter. The same levels of truncation were used in the bending model. The original second phase particle field with 50, 60, 70, 80, 90, and 100% of the number of *Fe*-rich particles that can nucleate voids (Figure 6.6) has been considered for simulations. Larger particles were removed during the truncation.

7.1.2 Finite element model

The finite element model used for the simulation of bending represents a volume of 292x896x896μm meshed with 10x16x16 (2560) brick elements (Figure 7.5). The region of interest comprises the four layers of elements at the top of the block. These elements have the highest plastic strains developing during deformation. Average plastic strain and porosity are calculated within this region.

The boundary conditions can be summarized as follows. The planes X=0 and Y=0 are restrained from translation in the X and Y directions, respectively. The planes Z=0 and Z=-*d* are restrained from translation in the Z direction. The plane X=*l* is assigned an angular velocity rotating the plane in the clock-wise direction around the edge X=*l*, Y=0.

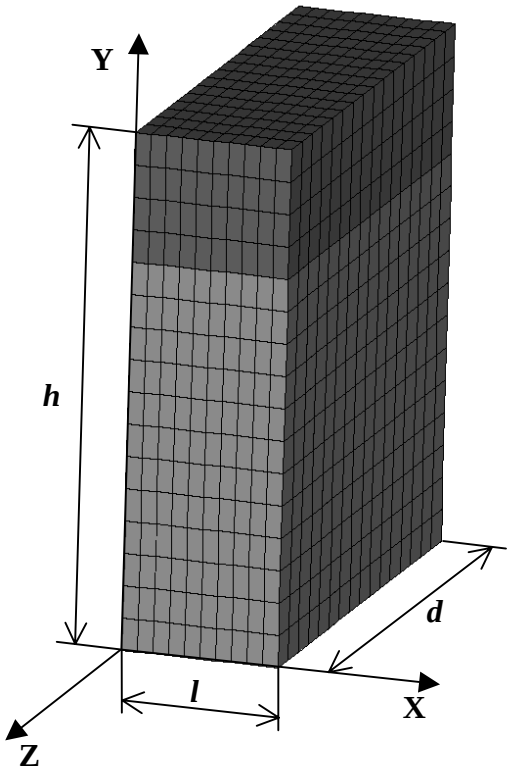

Figure 7.5: Modelled material volume under bending (*l*=282μm, *h*=896μm, *d*=896μm). Darker elements represent the region of interest.

7.2 DPM simulation results

7.2.1 The effect of *Fe*-rich content on formability

The results of the simulation in the form of porosity evolution in the region of interest with increasing plastic strain are shown in Figure 7.6. The corresponding numerical results for average plastic strain at failure calculated in the region of interest can be found in Table 7.1. As in the case of the tensile test, the variation in the population in *Fe*-rich particles significantly affects formability predictions. Material formability improves with the decreasing numbers of large *Fe*-rich particles.

There is a considerable change in the plastic strain at failure between the case of the intact (complete) particle field (100% *Fe*-rich particles used) and all of the other cases. This fact suggests that reducing the number of large *Fe*-rich particles that can nucleate voids by only 10% (8.8% decrease in *Fe*-rich volume fraction) results in significant increase in bendability.

Table 7.1: Plastic strain at failure during bending in the rolling direction for materials with different *Fe*-rich particle content.

Fe-rich Particle Content	50%	60%	70%	80%	90%	100%
Fe-rich Volume Fraction	0.00382	0.00396	0.00408	0.00422	0.00441	0.00483
Plastic Strain at Failure	0.400	0.393	0.392	0.391	0.390	0.363

The distribution of plastic strain in the material is shown in Figure 7.7. The highest plastic strains develop at the outer surface of the bent volume. The material at the bottom of the block does not experience large plastic strains due to the nature of the boundary conditions. The irregular distribution of porosity for the case of intact *Fe*-rich particle field in the undeformed condition and before the onset of ductile rupture is shown in Figures 7.8 and 7.9, respectively. At the bottom of the deformed block (Figure 7.9), due to compressive loading, voids do not tend to grow leading to porosity values close to zero. At the top of the block, extensive plastic deformation causes void nucleation, growth, and coalescence. More importantly, the original irregular porosity distribution pattern becomes more pronounced as seen by comparing Figures 7.8 and 7.9.

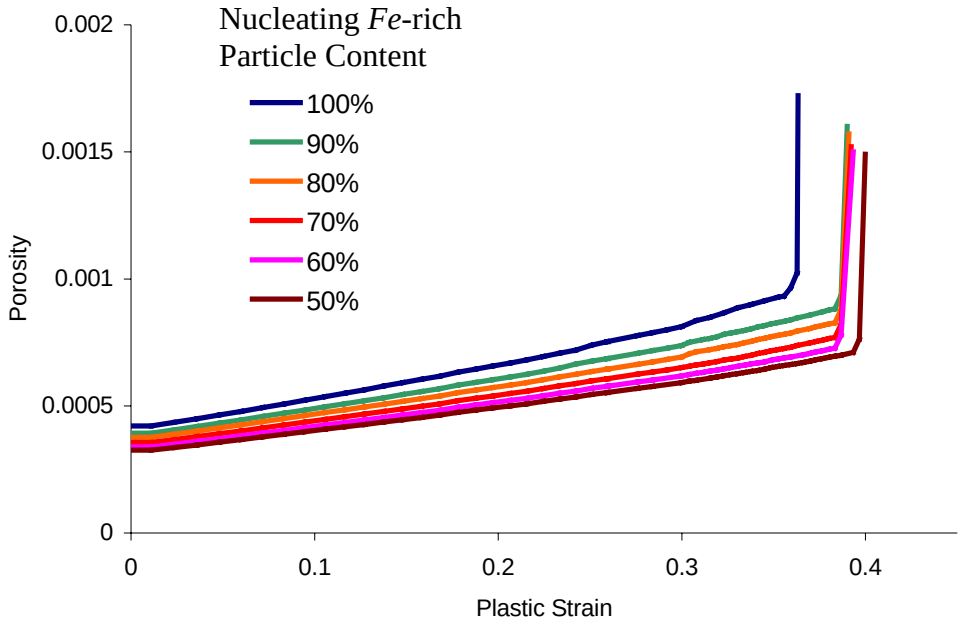

Figure 7.6: Porosity evolution during bending in the region of interest for second phase particle fields with different *Fe*-rich particle content (bending in the rolling direction).

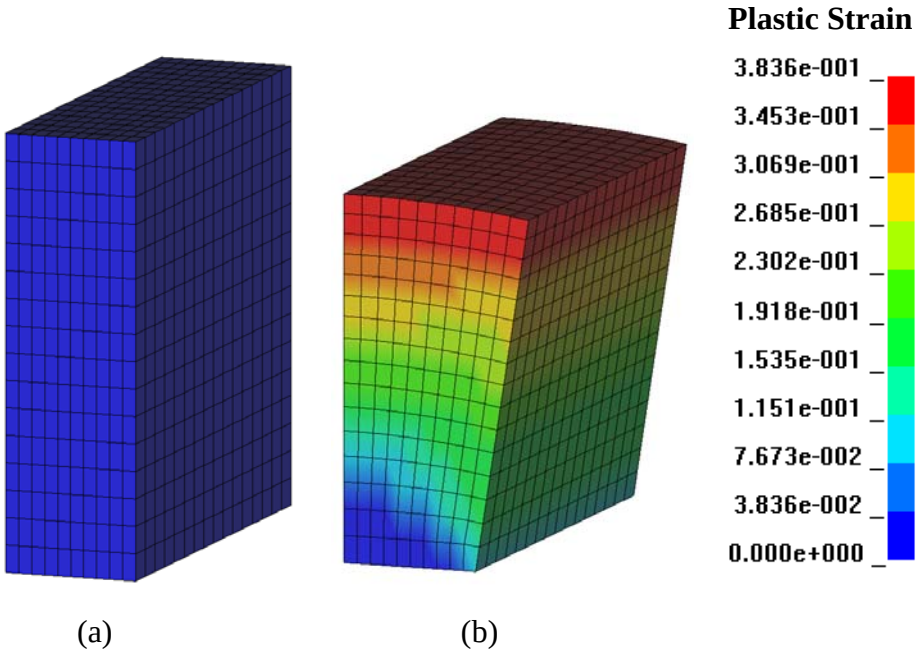

(a) (b)

Figure 7.7: Distribution of plastic strain in undeformed (a) and deformed (10.4 degree bend) (b) material (bending in the rolling direction).

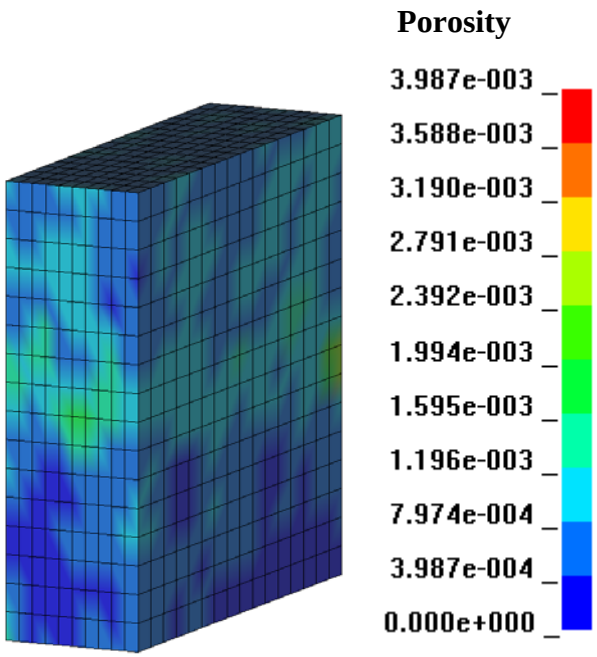

Figure 7.8: Distribution of porosity in undeformed material (100% *Fe*-rich particles, bending in the rolling direction).

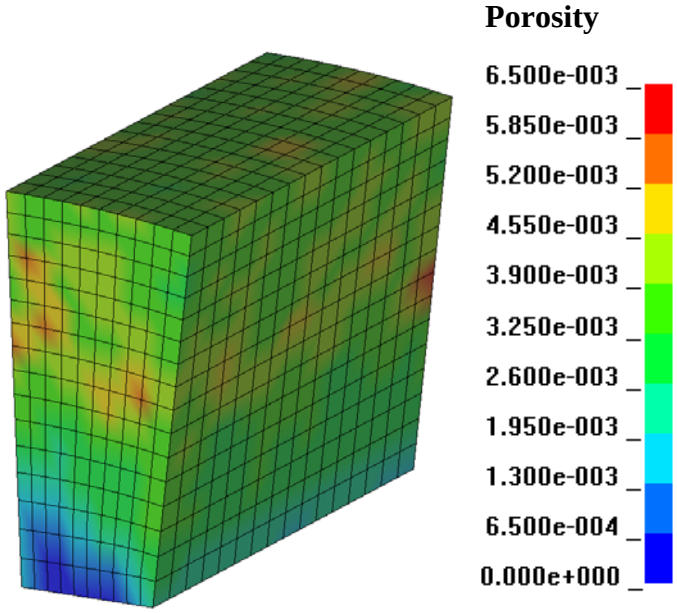

Figure 7.9: Distribution of porosity in deformed material (angular deformation 8.8 degrees, 100% *Fe*-rich particles, bending in the rolling direction).

In the current models, the prediction of ductile failure due to coalescence of voids nucleated from second phase particles in this region controls material bendability. Nucleated voids and cracks formed through void coalescence corresponding to the two extreme cases of 100 and 50% *Fe*-rich particle populations are shown in Figures 7.10 and 7.11, respectively. The comparison of these results can be summarized as follows. The original second phase particle field (100% *Fe*-rich particles) contains large *Fe*-rich particles that nucleate voids. Most of the time, such particles are clustered with other particles and voids. This fact facilitates void coalescence in clusters leading to final fracture at around 0.36 average plastic strain (angular deformation 8.8 degrees). For the case of 50% *Fe*-rich void-nucleating particles, fewer potential nucleation sites are present in the material. Many of these nucleation sites are also removed from particle clusters, which become smaller. This reduction impedes damage propagation and allows larger levels of deformation prior to failure. For this more dilute particle field, the average plastic strain reaches 0.4 (angular deformation 10.4 degrees). The increase in average plastic strain to failure over the 100% *Fe*-rich particle field case is about 4% strain.

7.2.2 The effect of material orientation

The results of the simulation that considers bending along the orthogonal-to-rolling direction (Figure 7.4) are presented below. The comparison of porosity evolution in the cases of bending in the rolling and orthogonal-to-rolling directions is shown in Figure 7.12. It is clear from this comparison that damage develops more rapidly in the case of the bending in the orthogonal-to-rolling direction. The numerical results for the plastic strains at failure are summarized in Table 7.2.

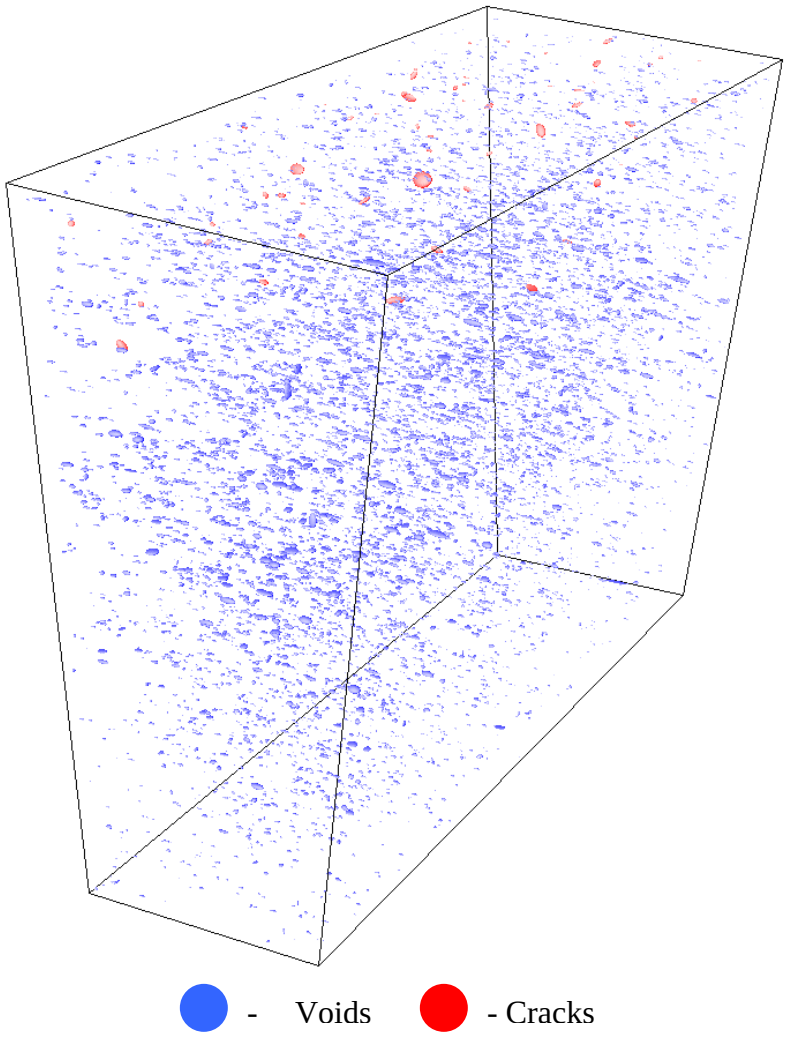

Figure 7.10: Nucleated voids and cracks in AA5182 with intact *Fe*-rich particle population (100% of particles that can nucleate voids) during bending in the rolling direction before the onset of fracture (angular deformation 8.8 degrees, 292x896x896μm volume originally).

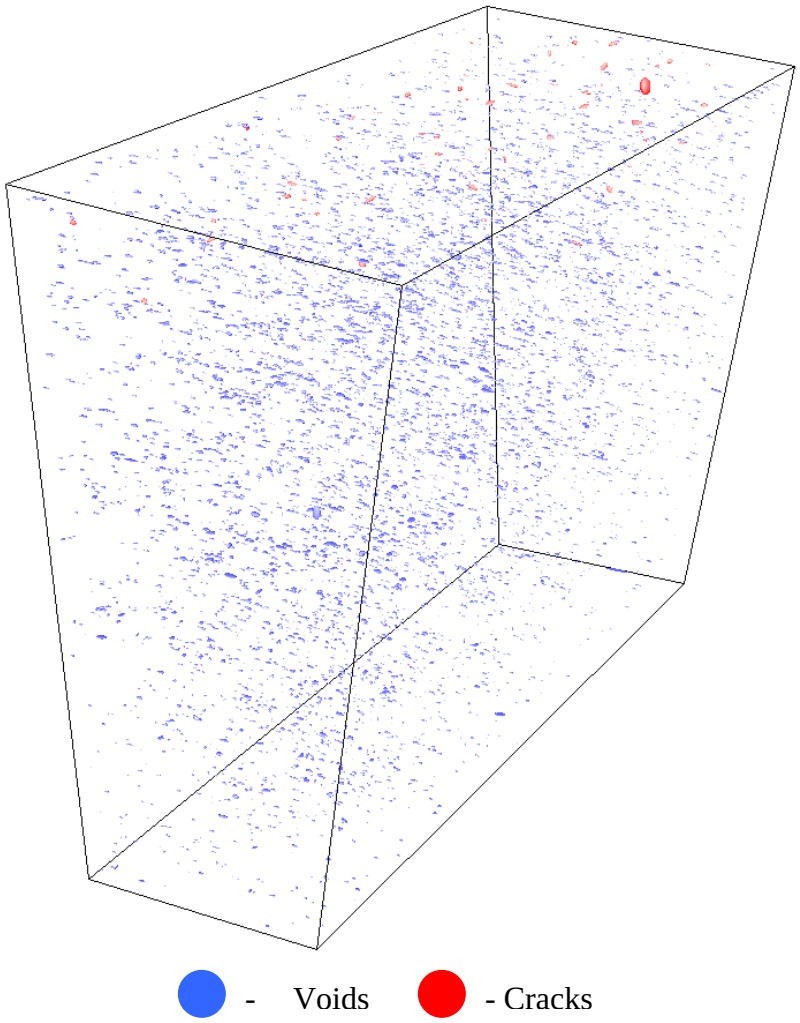

Figure 7.11: Nucleated voids and cracks in AA5182 with reduced *Fe*-rich particle population (50% of particles that can nucleate voids) during bending in the rolling direction before the onset of fracture (angular deformation 10.4 degrees, 292x896x896μm volume originally).

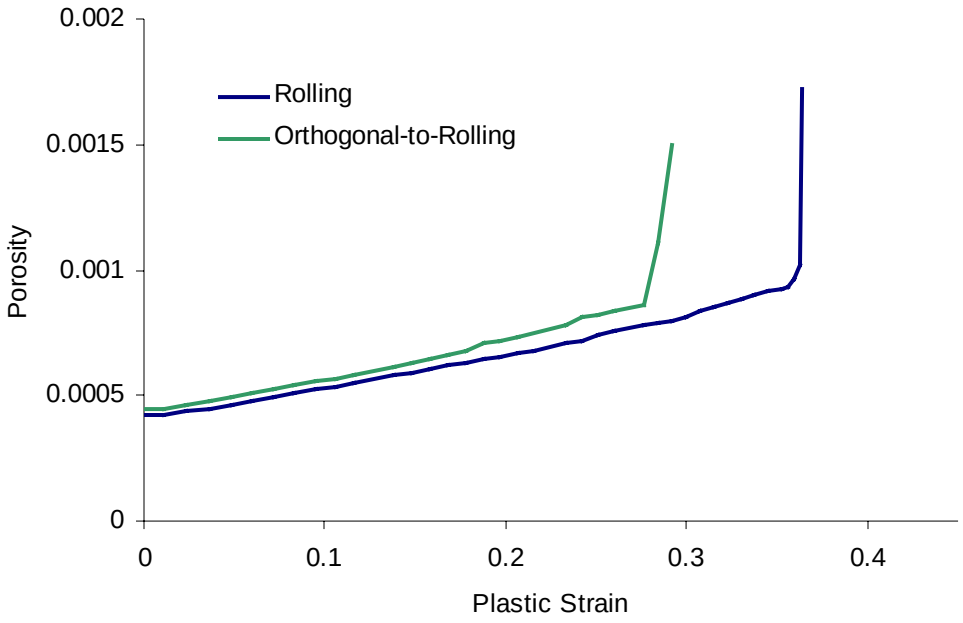

Figure 7.12: Porosity evolution in second phase particle fields (100% of particles that can nucleate voids) during bending in the rolling and orthogonal-to-rolling directions.

Table 7.2: Plastic strain at failure in second phase particle fields (100% of particles that can nucleate voids) during bending in the rolling and orthogonal-to-rolling directions.

Loading Direction	Rolling	Orthogonal-To-Rolling
Plastic Strain at Failure	0.36	0.29

Figure 7.13 shows the distribution of porosity in the modelled block of material during bending in the orthogonal-to-rolling direction. The character of the porosity distribution is similar to that shown in Figure 7.9 for the case of bending in the rolling direction.

The voids and cracks present in the second phase particle field in the case of bending in the orthogonal-to-rolling direction are shown in Figure 7.14. As in the case of bending in the rolling direction (Figure 7.10), cracking develops at the strained outer surface of the block; however, the damage development occurs earlier. This fact can be attributed to the spatial orientation of particle stringers (parallel to the axis of bending) that facilitates void coalescence. The decrease in the calculated plastic strain compared to the case of bending in the rolling direction is 7% strain.

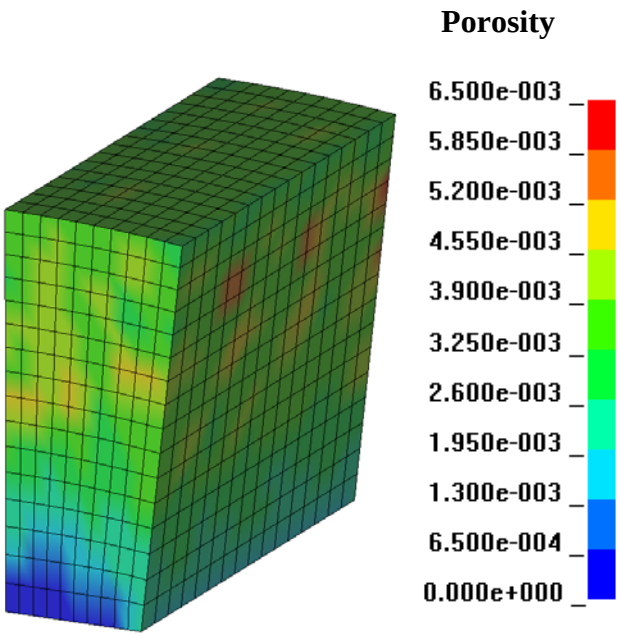

Figure 7.13: Distribution of porosity in deformed material (bending in the orthogonal-to-rolling direction, 6.7 degree bend, 100% *Fe*-rich particles).

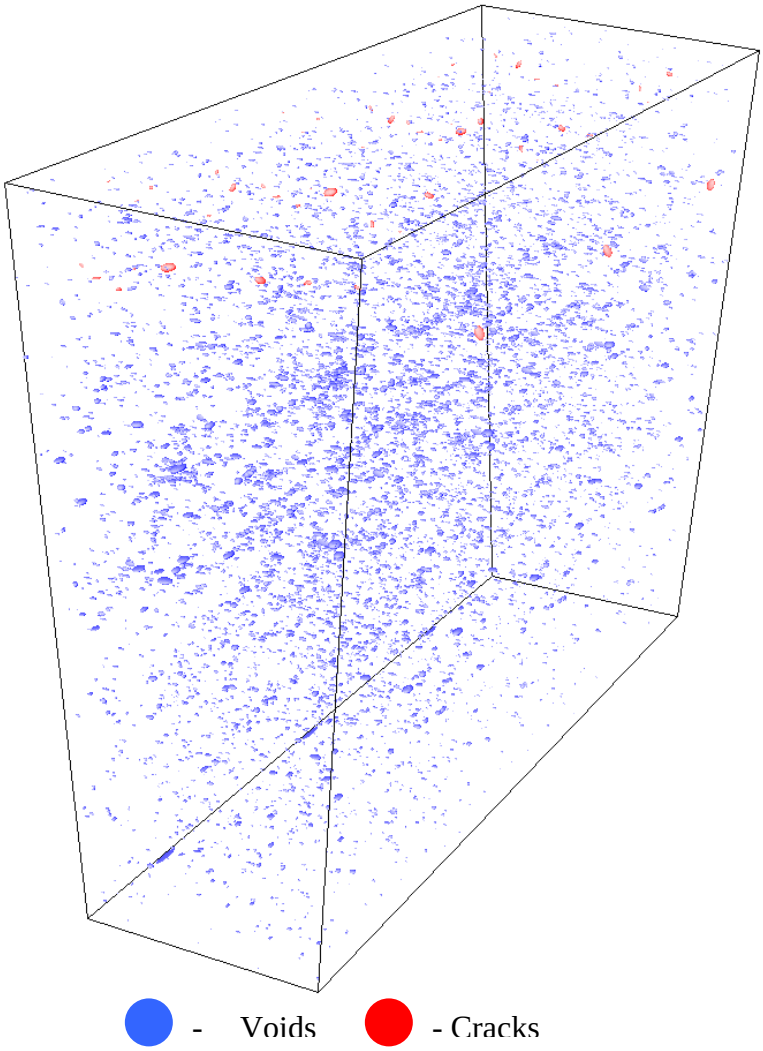

Figure 7.14: Nucleated voids and cracks in AA5182 with intact *Fe*-rich particle population (100% of particles that can nucleate voids) during bending in the orthogonal-to-rolling direction before the onset of fracture (angular deformation 6.7 degrees, 292x896x896μm volume originally).

Another important aspect of simulations of this kind, as mentioned in Chapter 5, is that a non-uniform porosity distribution in the material due to nucleating second phase particles may give rise to shear banding without any surface imperfection. In this case, nucleating voids would create sites to trigger shear bands, which would in turn facilitate further void nucleation. The modelling of shear banding is not the focus of the current work. However, the coupling of the DPM with a finite element simulation better able to capture shear banding may lead to additional insight.

Summary

This chapter has presented the application of the three-dimensional damage percolation model to the simulation of bending. The simulation of this type of forming operation should consider several processes contributing to the final rupture of material. Normally, surface roughening due to grain rotation is modelled with crystal plasticity. Such "wavy" surfaces facilitate shear banding (Lloyd *et al.*, 2002) that originates at the highly strained outer surface of the bent specimen and propagates through specimen thickness. Damage due to second phase particles is also present, which results in specimen ductile fracture.

The results of the DPM simulations show that such an approach is applicable to damage initiation and evolution prediction during bending. The damage predictions are based on criteria validated using an *in situ* tensile test. The effect of *Fe* content level on the formability of AA5182 sheet through the variation of *Fe*-rich particle population has been shown to have a significant effect. The reduction of the number of *Fe*-rich particle that can nucleate voids by only 10% (removing larger particles) results in increased

formability (average plastic strain at failure increased by about 3%strain). The effect of metal sheet orientation during deformation (bending in the rolling or orthogonal-to-rolling direction) is also significant. Bending in the rolling direction leads to higher (7% strain) average plastic strain at failure.

The DPM can be used together with a finite element simulation capturing shear banding. The loss of stability through necking (as described in the previous chapters) or through shear banding will allow the modelling of damage development in the majority of sheet metal forming operations.

Chapter 8

Discussion, Conclusions and Recommendations

8.1 Discussion

The DPM requires an input second phase particle field. The choice of the second phase particle field acquisition method depends on the availability of microstructural data, such as three-dimensional X-ray tomographic images and optical micrographs. High-resolution tomographic images normally comprise only a limited material volume due to restrictions of the tomography apparatus. Such images differentiate between phases present in the material and can be used in the DPM after ellipsoidal approximation of the particle field objects. Replicating the acquired particle field and creating a 3D array of such fields can be used for obtaining larger material volumes. The second phase particle field reconstruction method also can be used together with results of

characterization of a 3D particle field acquired with X-ray tomography. In this case, microstructural volumes of any size can be obtained and various types of second phase particle field objects can be reconstructed. Optical micrographs of two orthogonal sections of the long- and short-transverse planes can also be used for 3D microstructure reconstruction; however, different object types within the second phase particle field cannot be distinguished. The cumulative characteristics of all object types extracted from the micrographs are used for particle size/shape reconstruction. The methods of particle field acquisition based on X-ray tomography are preferred since they provide more accurate information on particle clustering, which affects material damage accumulation rates.

In situ tensile testing was used for acquiring input data for the analysis of damage initiation and evolution within AA5182. This work has provided initial insight into the nature of damage nucleation, but cannot be considered complete. The tensile test was stopped at the onset of necking before fracture. Measured numbers of nucleated voids in the most strained region were treated as upper limits on the number of nucleated voids that can be achieved; however, further deformation to an onset of ductile fracture could result in a higher number. Also, the shape of the curve for the evolution of the number of nucleated voids per unit volume (Figure 3.10) was approximated based on the five available points. The assumption of normality of the nucleation process PDF can be confirmed or dismissed through acquiring more points.

The three-dimensional damage percolation model has been fully coupled with a commercial finite element code, LS-DYNA. The calculation of stresses and strains is performed within the FE code and the damage processes are accounted for in the damage percolation part of the model. A dilational yield surface utilized in the GTN model is used to correlate calculated damage in the DPM with material softening in the FE

simulation. Such an approach allows taking into account both material softening, as in continuum damage models, and the irregular nature of real second phase particle fields.

The three-dimensional damage percolation model has both advantages and disadvantages. Damage modelling at the level of discrete particles and voids accounts for the material degradation process during deformation. Void nucleation, growth, and coalescence responsible for damage initiation and evolution are modelled, taking into account loading conditions and microstructure irregularity. However, the computational cost of such calculations is relatively high. For example, one cubic millimetre of material contains up to 800,000 objects. Modelling of large material volumes would involve considerable computational power. Thus, the model is more useful for research-type calculations. For example, it can be used for the study of the effect of optimized second phase particle field characteristics on formability.

The predicted damage propagation in the simulations with cluster-insensitive and cluster-sensitive nucleation criteria can be summarized as follows. The chosen nucleation criterion defines the spatial distribution of nucleating voids. If no preference of nucleation sites is imbedded in the nucleation criterion, diffuse nucleation takes place, as in the case of the cluster-insensitive criterion. The cluster-sensitive criterion favours void nucleation within particle-void clusters, which corresponds to the observed real nature of damage accumulation. According to the X-ray tomography microstructural data, damage initiates at large particles (Figures 2.11, 2.13, and 2.14) and within particle clusters (Figures 2.11 and 2.12).

Geometric variation in porosity causes increased local damage and material softening. Due to this effect, softer regions accumulate more strain and may act as defects, triggering shear banding. The presence of a macroscopic crack in the specimen and the irregular porosity field should result in shear localization and ductile fracture. However, this kind of behavior is not observed in the specimens since the specimen shape

(Figure 2.7a) has been developed to promote strain localization at the center of the specimen. However, shear banding can be studied using standard flat tensile specimens (not considered in the current work).

The DPM is mesh sensitive in the sense that the mesh should be chosen to take into account the characteristic size of the simulated material and the average particle size. Since discrete voids are considered in the model, the medium is no longer continuous and the use of the yield function is, strictly speaking, inappropriate. The minimum element edge length should be greater than the average particle size. In the current simulation the element edge length was 89.6 μm, and the average particle size was 7.25 μm. Higher numbers of elements are needed to better capture the strain gradient; however, this number affects the minimal element edge length, which, in turn, is limited by the average particle size.

The DPM calculates porosity as the ratio of the volume of all voids in an element to the element volume. The DPM can be used in two modes: with or without element deletion. The first mode would substitute big voids with deleted elements providing similar overall softening at the region, but would not allow predictions of crack propagation within the DPM due to void link-up after the deletion. Thus, this mode is not considered in the current work. The second mode (used in the current simulations) leads to high local porosity values.

8.2 Conclusions

The development and application of the DPM to simulation of the *in situ* tensile test has provided insight into the nature of damage initiation and evolution in materials

containing clustered second phase particle fields. The major conclusions stemming from this research are:

i. The onset of failure is triggered after the plastic strains exceed the Considere criterion. Necking initiates, after which ductile fracture, through void nucleation, growth, and coalescence, progresses rapidly.

ii. The *Fe*-rich and Mg_2Si particles present in AA5182 both nucleate voids during the manufacturing stage of cold rolling. In subsequent plastic deformation of the as-received sheet, only the large *Fe*-rich particles continue to nucleate voids, whereas the Mg_2Si particles no longer take active part in void nucleation.

iii. Damage processes such as void nucleation, growth, and coalescence are accelerated in particle clusters. In particular, void coalescence depends on the relative size of the coalescing voids and inter-void distance. Voids nucleated from large particles in particle clusters have closely located neighbours that facilitate void coalescence.

iv. There exist two coalescence stages of ductile rupture that include intra- and inter-cluster coalescence. The cracks formed by coalescence of two or more voids within a cluster, namely intra-cluster coalescence, can be relatively stable. The final rupture of material occurs when inter-cluster coalescence takes place and cracks in particle clusters start to coalesce with other isolated voids or cracks formed at other clusters.

v. The simulation of AA5182 microstructures with reduced *Fe*-rich of Mg_2Si particle content have predicted that higher formability can be achieved by reducing *Fe* content level in AA5182. This results in a smaller maximum *Fe*-rich particle size in the as-cast material, which in turn affects the degree of particle clustering and the maximum particle size in clusters within the as-rolled sheet.

vi. The bending test simulation results have revealed that the rate of damage development also depends upon the orientation of the sheet relative to the loading direction. Loading applied transverse to the rolling direction (acting perpendicular to the cluster axis) results in lower fracture strains than loading along the rolling direction.

8.3 Recommendations for future work

The accuracy of the three-dimensional damage percolation model can be increased and its applicability to various types of deformation other than tensile should be validated. The following steps would improve the model and make it a reliable tool for formability studies regardless of stress-strain state in the modelled material.

An important property of void growth still needs to be addressed in the second phase particle reconstruction method and the DPM. The reconstruction method does not differentiate between voids formed by matrix decohesion and particle fracture. The difference in void growth may stem from the effect of void propping by hard particles inside or adjacent to voids. All voids are considered to contain hard particles from which they nucleate, an assumption that corresponds to the matrix decohesion mechanism of nucleation. Certain portions of voids nucleate by particle fracture during cold rolling. The effect of this nucleation mechanism on void growth still has to be accounted for in future research.

Void coalescence is highly affected by particle clustering. The clustering method utilized in the reconstruction method employs several parameters such as the degree of Mg_2Si particle clustering, and the mean and standard deviation of the IPD normal distribution. The values of these parameters used in the simulation (m=0.8μm, σ=3μm,

and p=80%) provided a reasonably accurate prediction of material second phase particle clustering. The predicted plastic strain at failure is close to that of the simulation with the measured particle field. All of these parameters, as well as the IPD distribution type (for example, log-normal), should be further studied and rectified.

Further *in situ* tensile testing with X-ray tomography is needed to support improved damage characterization during material deformation. Specimens of different geometries can be used to achieve various stress and strain states. For example, notched specimens can be used to increase stress triaxiality in the center of the specimen. The notch radius can be varied to achieve desired triaxiality values, ultimately approaching a slit-like notch.

In situ tensile tests with more loading stages will provide more information about damage development. More points on the plots of the number of particle-void interfaces per unit volume and porosity versus plastic strain corresponding to the additional loading stages will allow better calibration of the void nucleation and coalescence criteria.

Damage characterization using three-dimensional second phase particle fields obtained with X-ray tomography will bring more understanding if more characterization parameters are introduced. In the current model, larger particle nucleate voids sooner. Quantification of the dependence of void nucleation on particle size will contribute to greater fidelity in the void nucleation model.

Calculating local porosity through three-dimensional tessellation during each loading step will provide better estimates of strain localization in inter-void ligaments and void coalescence onset. Currently, element porosity, which can be considered global, is used for that purpose.

References

Argon, A.S., Im, J., and Safoglu, R. (1975), Cavity formation from inclusions in ductile fracture, *Metallurgical Transactions A*, **6A**, pp. 825-837.

Argon, A.S. and Im, J. (1975), Separation of second phase particles in spheroidized 1045 steel, Cu-0.6Pct Cr alloy, and maraging steel in plastic straining, *Metallurgical Transactions A*, **6A**, pp. 839-851.

Argon A.S. (1976), Formation of cavities from nondeformable second-phase particles in low temperature ductile fracture, *Journal of Engineering Materials and Technology*, **98**, pp. 60-68.

Ashby, M.F. (1966), Work hardening of dispersion-hardened crystals, *Philosophical Magazine*, **14**, pp. 1157-1178.

Bandstra, J.P., Goto, D.M., and Koss, D.A. (1998), Ductile failure as a result of a void-sheet instability: experiment and computational modeling, *Materials Science and Engineering*, **A249**, pp. 46-54.

Bandstra, J.P. and Koss, D.A. (2001), Modeling the ductile fracture process of void coalescence by void-sheet formation, *Materials Science and Engineering*, **A319-321**, pp. 490-495.

Bandstra, J.P. and Koss, D.A., (2004) A simulation of growth and coalescence of voids during ductile fracture, *Materials Science and Engineering*, **A387-389**, pp. 399-403.

Bandstra, J.P., Koss, D.A., Geltmacher, A., Matic, P., and Everett, R.K. (2004), Modeling void coalescence during ductile fracture of a steel, *Materials Science and Engineering*, **A366**, pp.269-281.

Beachem, C.D. (1963), An electron fractographic study of the influence of plastic strain conditions upon ductile rupture processes in metals, *Transactions of the ASM*, **56**, pp. 318-326.

Becker, R. (1992), Analysis of shear localization during bending of a polycrystalline sheet, *Journal of Applied Mechanics*, **59**, pp. 491-496.

Benson, D.J. (1995), The effect of void cluster size on ductile fracture, *International Journal of Plasticity*, **11**, pp. 571-582.

Benzerga, A.A. (2002), Micromechanics of coalescence in ductile fracture, *Journal of the Mechanics and Physics of Solids*, **50**, pp. 1331-1362.

Bourcier, R.J., Smeller, R.E., Richmond, O., and Koss, D.A. (1984), Deformation and fracture at isolated holes in plane-strain tension, *International Journal of Fracture*, **24**, pp. 289-297.

Broek, D. (1973), The role of inclusions in ductile fracture and toughness, *Engineering Fracture Mechanics*, **5**, pp. 55-66.

Brown, L.M. and Embury, J.D. (1973), The initiation and growth of voids at second phase particles, *Proceedings of Conference on Microstructure and Design of Alloys, Institute of Metals and Iron and Steel Insitute, London*, **1 (33)**, pp. 164-169.

Brown, L.M. and Stobbs, W.M. (1976), The work-hardening of copper-silica. V. Equilibrium plastic relaxation by secondary dislocations, *Philosophical Magazine*, **34**, pp. 351-372.

Brownrigg, A., Spitzig, W.A., Richmond, O., Teirlinck, D., and Embury, J.D. (1983), The influence of hydrostatic pressure on the flow stress and ductility of a spheroidized 1045 steel, *Acta Metallurgica*, **31**, pp.1141-1150.

Budiansky, B., Hutchinson, J.W., and Slutsky, S. (1982), Void growth and collapse in viscous solids. In *Mechanics of solids – The Rodney Hill 60th anniversary volume*, Pergamon press, pp.13-45.

Burger, G., Koken, E., Wilkinson D.S., and Embury, J.D. (1988), The influence of spatial distributions on metallurgical processes, *Advances in Phase Transitions*, Pergamon Press, pp. 247-262.

Chen, Z.T., Worswick, M.J., Cinotti, N., Pilkey, A.K., and Lloyd, D.J. (2003), A linked FEM-damage percolation model of aluminum alloy sheet forming, *International Journal of Plasticity*, **19**, pp. 2099-2120.

Cinotti, N., Shakeri, H., Worswick, M.J., Finn, M.J., Jain, M., and Lloyd, D.J. (2000), Stretch flange formability of aluminum alloy sheet, *Proceedings of Plasticity 2000 Conference*, Whistler, Canada.

Corson, P. B. (1974), Correlation functions for predicting properties of heterogeneous materials. I. Experimental measurement of spatial correlation functions in multiphase solids, *Journal of Applied Physics*, **45**, pp. 3159-3164.

Cox, T.B. and Low, J.R.Jr. (1974), An investigation of the plastic fracture of AISI 4340 and 18 Nickel-200 grade maraging steels, *Metallurgical Transactions*, **5**, pp. 1457-1470.

Cruz-Orive, L-M. (1976), Particle size-shape distributions: the general spheroid problem. I. Mathematical model, *Journal of Microscopy*, **107**, pp. 235-253.

Cruz-Orive, L-M. (1978), Particle size-shape distributions: the general spheroid problem. II. Stochastic model and practical guide, *Journal of Microscopy*, **112**, pp. 153-167.

Dubensky, E.M. and Koss, D.A. (1987), Void/pore distributions and ductile fracture, *Metallurgical Transactions A*, **18**, pp.1887-1895.

Everett, R.K. and Chu, J.H. (1993), Modeling of non-uniform composite microstructures, *Journal of Composite Materials*, **27**, pp. 1128-1144.

Fisher, J.R. and Gurland, J. (1981a), Void nucleation in spheroidized carbon steels, Part 1: Experimental, *Metal Science*, **May**, pp. 185-192.

Fisher, J.R. and Gurland, J. (1981b), Void nucleation in spheroidized carbon steels, Part 2: Model, *Metal Science*, **May**, pp. 193-202.

Fleck, N.A. and Hutchinson, J.W. (1986), Void growth in shear, P*roceeding of the Royal Society of London*, **A407**, pp. 435-458.

Floreen, S. and Hayden, H.W. (1970), Some observations of void growth during the tensile deformation of a high strength steel, *Scripta Metallurgica*, **4**, pp. 87-94.

Forero, L.E. and Koss, D.A. (1994), On the strain-induced growth of neighbouring voids, *Scripta Metallurgica et Materialia*, **31**, pp.419-422.

Garrison, W.M.Jr. and Moody, N.R. (1987), Ductile fracture, *Journal of Physics and Chemistry of Solids*, **48**, pp. 1035-1074.

Geltmacher, A.B., Koss, D.A., Matic, P., and Stout, G. (1996), A modelling study of the effect of stress state on void linking during ductile fracture, *Acta Materialia*, **44**, pp. 2201-2210.

Gokhale, A.M. and Drury, W.J. (1994), Efficient measurement of microstructural surface area using trisector, *Metallurgical and Materials Transcation*, **25A**, pp. 919-928.

Gologanu, M., Leblond, J.B., and Devaux, J. (1993), Approximate models for ductile metals containing non-spherical voids – case of axisymmetric prolate ellipsoidal cavities, *Journal of the Mechanics and Physics of Solids*, **41**, pp. 1723-1754.

Gologanu, M., Leblond, J.B., and Devaux, J. (1994), Approximate models for ductile metals containing non-spherical voids – case of axisymmetric oblate ellipsoidal cavities, *Transaction of ASME,* **116**, pp. 290-297.

Goods, S.H. and Brown, L.M. (1979), The nucleation of cavities by plastic deformation, *Acta Metallurgica,* **27**, pp. 1-15.

Goodwin, G.M. (1968), Application of strain analysis to sheet metal forming problems in the press shop, *Society of Automotive Engineers*, Paper no. 680093.

Goto, D.M. and Koss, D.A. (1996), An experimental model of the growth of neighbouring voids during ductile fracture, *Scripta Materialia*, **35**, pp.459-463.

Gupta, A.K., Lloyd D.J., and Court, S.A. (2001), Precipitation hardening in Al-Mg-Si alloys with and without excess Si, *Materials Science and Engineering*, **A316**, pp. 11-17.

Gurland, J. and Plateau, J. (1963), The mechanism of ductile rupture of metals containing inclusions, *Transactions of the ASM*, **56**, pp. 442-454.

Gurland, J. (1972), Observations on the fracture of cementite particles in a spheroidized 1.05% C steel deformed at room temperature, *Acta Metallurgica*, **20**, pp. 735-741.

Gurson, A.L. (1975), Plastic flow and fracture behaviour of ductile materials incorporating void nucleation, growth, and interaction, PhD Thesis, Brown University, Providence, RI.

Gurson, A.L. (1977a), Porous rigid-plastic materials containing rigid inclusiond – yield fuction, plastic potential, and void nucleation, *Fracture*, **2**, pp. 19-24.

Gurson, A.L. (1977b), Porous rigid-plastic materials containing rigid inclusions - yield function, plastic potential, and void nucleation, *Proceeding of International Conference on Fracture*, **2A**, p. 357.

Gurson, A.L. (1977c), Continuum theory of ductile rupture by void nucleation and growth: Part I – yield criteria and flow rules for porous ductile media, *Journal of Engineering Materials and Technology*, **99**, pp. 2-15.

Hallquist, J.O. (1998), LS-DYNA theoretical manual, Livermore Software Technology Corporation, Livermore, CA.

Hancock, J.W. and Mackenzie, A.C. (1976), On the mechanisms of ductile failure in high-strength steels subjected to multi-axial stress-states, *Journal of the Mechanics and Physics of Solids*, **24**, pp. 147-169.

Hancock, J.W. and Thomson, R.D. (1985), Strain and stress concentrations in ductile fracture by void nucleation growth and coalescence, *Materials Science and Technology*, **1**, pp. 684-690.

Hill, R. (1962), Acceleration waves in solids, *Journal of the Mechanics and Physics of Solids*, **10**, pp. 1-16.

Keeler, S.P. and Backofen, W.A. (1963), Plastic instability and fracture in sheets stretched over rigid punches, *Truncations of the ASM*, **56**, pp. 25-48.

Kwon, D. and Asaro, R.J. (1990), A study of void nucleation, growth, and coalescence in spheroidized 1518 steel, *Metallurgical Transactions*, **21**, pp. 117-134.

LeRoy, G., Embury, J.D., Edward, G., and Ashby, M.F. (1981), A model of ductile fracture based on the nucleation and growth of voids, *Acta Metallurgica*, **29**, pp. 1509-1522.

Li, M., Ghosh, S., Richmond, O., Weiland, H., and Rouns, T.N. (1999), Three dimensional characterization and modelling of particle reinforced metal matrix composites: Part I quantitative description of microstructural morphology, *Materials Science and Engineering*, **A265**, pp. 153-173.

Lievers, W.B., Pilkey, A.K., and Worswick, M.J. (2003), The co-operative role of voids and shear bands in strain localization during bending, *Mechanics of Materials*, **35**, pp. 661-674.

Lievers, W.B., Pilkey A.K., and Lloyd, D.J. (2003), The influence of iron content on the bendability of AA6111 sheet, *Materials Science and Engineering*, **A361**, pp. 312-320.

Lievers, W.B. (2004), Tesselation3D Software Suite, A Manual.

Lloyd, D.J., Evans, D., Pelow, C., Nolan, P., and Jain, M. (2002), Bending in aluminum alloys AA6111 and AA5754 using the cantilever bend test, *Materials Science and Technology*, **18**, pp. 621-628.

Magnusen, P.E., Dubensky, E.M., and Koss, D.A. (1988), The effect of void arrays on void linking during ductile fracture, *Acta Metallurgica*, **36**, pp. 1503-1509.

Maire, E., Buffiere, J.Y., Salvo, L., Blandin, J.J., Ludwig, W., and Letang, J.M. (2001), On the application of X-ray tomography in the field of materials science, *Advanced Engineering Materials*, **3**, pp. 539-546.

Marini, B., Murdi, F., and Pineau, A. (1985), Experimental study of cavity growth in ductile rupture, *Engineering Fracture Mechanics*, **22**, pp. 989-996.

McClintock, F.A. (1968), A criterion for ductile fracture by the growth of holes, *Journal of Applied Mechanics*, **35**, pp. 353-371.

McMahon, C.J.Jr. and Cohen, M. (1965), Initiation of cleavage in polycrystalline iron, *Acta Metallurgica*, **13**, pp. 591-604.

Melander, A. (1980), Void growth during wire drawing and tensile testing of copper, *Scandinavian Journal of Metallurgy*, **9**, pp. 267-272.

Morris, M.D. (1991), Factorial sampling plans for preliminary computational experiments, *Technometrics*, **33**, pp. 161-174.

Norris, D.M., Reaugh, J.E., Moran, B., and Quinones, D.F. (1978), A plastic-strain, mean-stress criterion for ductile fracture, *Journal of Engineered Materials and Technology, transactions of ASME,* **100**, pp. 279-286.

Orlov, O., Winkler, S.L., Worswick, M.J., Lloyd, D.J. (2004), and Finn, M.J., A three-dimensional damage percolation material model, *Proceedings of the 7th Esaform Conference on Material Forming*, Trondheim, Norway.

Orlov, O. S., Winkler, S.L., Worswick, M.J., Lloyd, D.J., and Finn, M.J. (2005), Damage localization prediction using the three-dimensional damage percolation model, *Proceedings of the 8th International Conference on Technology of Plasticity*, Verona, Italy.

Orlov, O., Maire, E., Adrien, J., Worswick, M.J., Lloyd, D.J. (2006), Damage evolution prediction using X-ray tomography and the three-dimensional damage percolation model, *Proceedings of the 9th European Mechanics of Materials Conference, Local Approach to Fracture*, Moret sur Loing, France.

Orlov, O., Maire, E., Adrien, J., Worswick, M. J., and Lloyd, D.J. (2006), Application of the three-dimensional damage percolation model and X-ray tomography for damage evolution prediction in aluminum alloys, *Proceedings of the International Conference on Aluminum Alloys,* Vancouver, Canada.

Oyane, M. (1972), Criteria of ductile fracture strain, *Bulletin of JSME,* **15**, pp. 1507-1513.

Pardoen, T. and Hutchinson, J.W. (2000), An extended model for void growth and coalescence, *Journal of the Mechanics and Physics of Solids*, **48**, pp. 2467-2512.

Perrin, G. and Leblond, J.B. (1990), Analytical study of a hollow sphere made of plastic porous material and subjected to hydrostatic tension – application to some problems in ductile fracture of metals, *International Journal of Plasticity*, **6**, pp. 677-699.

Petch, N.J. (1961), In *Toughness and Brittleness of Metals*, Institution of metallurgists, Interscience Publishers Inc., New York.

Pilkey, A.K., Worswick M.J., Thomson C.I.A., Burger G., and Lloyd D.J. (1998), Effect of second phase particle distribution on the formability of Al-Si sheet, In *Advances in Industrial Materials*, The Metallurgical Society of CIM, Montreal.

Puttick, K.E. (1959), Ductile fracture in metals, *Philosophical magazine*, **4**, pp. 964-969.

Ragab, A.R. (2000), Prediction of ductile fracture in axisymmetric tension by void coalescence, *International Journal of Fracture,* **105**, pp. 391-409.

Rice, J.R. and Tracey, D.M. (1969), On the Ductile Enlargement of Voids in Triaxial Stress Fields, *Journal of the Mechanics and Physics of Solids*, **17**, pp. 201-217.

Rice, J.R. (1976), The localization of plastic deformation, In *Theoretical and Applied Mechanics*, North-Holland, pp. 207-220.

Rogers, H.C. (1960), The tensile fracture of ductile metals, *Transactions of the Metallugrical Society of AIME*, **218**, pp. 498-506.

Rosenfield, A.R., and Hahn, G.T. (1966), Numerical descriptions of the ambient low-Temperature and high-strain rate flow and fracture behavior of plain carbon steel, *Transactions of the ASM*, **59**, pp. 962-980.

Rosenfield, A.R. (1968), Criteria for ductile fracture of two-phase alloys, *Metallurgical Reviews*, **13**, pp. 29-40.

Rousselier, G. (1987), Ductile fracture models and their potential in local approach of fracture, *Nuclear Engineering and Design*, **105**, pp. 97-111.

Rudnicki, J.W and Rice, J.R. (1975), Conditions for the localization of deformation in pressure-sensitive dilatant materials, *Journal of the Mechanics and Physics of Solids*, **23**, pp. 371-394.

Saltelli, A., Tarantola, S., Campolongo, F., and Ratto, M. (2004), Sensitivity analysis in practice, John Wiley & Sons, UK.

Selcuk, A. and Rawlings, R.D. (1991), A cantilever-type bend test technique for formability analysis of strip/plate metals, *ASTM Journal of Testing and Evaluation*, **19**, pp. 349-358.

Smerd R., Winkler S., Salisbury C., Worswick M.J., Lloyd D.J., and Finn M.J. (2005), High strain rate tensile testing of automotive aluminum alloy sheet, *International Journal of Impact Engineering*, **32**, pp. 541-560.

Sowerby, R. and Chandrasekaran, N. (1986), Application of McClintock's ductile fracture model by the growth of holes to the tensile straining of some spheroidized steels under superimposed hydrostatic pressures, *Materials Science and Engineering*, **79**, pp. 15-25.

Stauffer, D. (1985), Introduction to percolation theory, Taylor and Francis, London.

Stoughton, T.B. (2001), Stress-based forming limits in sheet-metal forming, *Journal of Engineering Materials and Technology*, **123**, pp. 417-422.

Spitzig, W.A., Kelly, J.F., and Richmond, O. (1985), Quantitative characterization of second-phase populations, *Metallography*, **18**, pp. 235-261.

Tanaka, K., Mori, T., and Nakamura, T. (1970), Cavity formation at the interface of a spherical inclusion in a plastically deformed matrix, *Philosophical Magazine*, **21**, pp. 267-279.

Teirlinck, D., Zok, F., Embury, J.D., and Ashby, M.F. (1988), Fracture mechanism maps in stress space, *Acta Metallurgica*, **36**, pp.1213-1228.

Tewari, A., Gokhale, A.M., Spowart, J.E., and Miracle, D.B. (2004), Quantitative characterization of spatial clustering in three-dimensional microstructures using two-point correlation functions, *Acta Materialia*, **52**, pp. 307-319.

Thomason, P.F. (1968), A Theory for ductile fracture by internal necking of cavities, *Journal of the Institute of Metals*, **96**, pp. 360-365.

Thomason, P.F. (1981), Ductile fracture and the stability of incompressible plasticity in the presence of microvoids, *Acta Metallurgica*, **29**, pp. 763-777.

Thomason, P.F. (1985), A three-dimensional model for ductile fracture by the growth and coalescence of microvoids, *Acta Metallurgica*, **33**, pp. 1087-1095.

Thomason, P.F. (1990), Ductile fracture of metals, Pergamon Press plc, Headington Hill Hall, Oxford, UK.

Thomason, P.F. (1993), Ductile fracture by the growth and coalescence of microvoids of non-uniform size and spacing, *Acta Metallurgica et Materialia*, **41**, pp. 2127-2134.

Thomson, R.D. and Hancock, J.W. (1984), Ductile failure by void nucleation, growth, and coalescence, *International Journal of Fracture*, **26**, pp. 99-112.

Thomson, C.I.A., Worswick, M.J., Pilkey, A.K., Lloyd, D.J., and Burger, G. (1999), Modelling void nucleation and growth within periodic clusters of particles, *Journal of the Mechanics and Physics of Solids*, **47**, pp. 1-26.

Thomson, C.I.A. (2001), Modelling the effects of particle clustering on ductile failure, PhD Thesis, Carleton University, Canada.

Thomson, C.I.A., Worswick, M.J., Pilkey, A.K., and Lloyd, D.J. (2003), Void coalescence within periodic clusters of particles, *Journal of the Mechanics and Physics of Solids*, **51**, pp. 127-146.

Tonks, D.L. (1994), Percolation wave propagation, and void link-up effects in ductile fracture, *Journal de Physique IV*, **4**, pp. 665-670.

Triantafyllidis, N., Needleman, A., and Tvergaard, V. (1982), On the development of shear bands in pure bending, *International Journal of Solid Structures*, **18**, pp. 121-138.

Tvergaard, V. (1981), Influence of voids on shear band instabilities under plane strain conditions, *International Journal of Fracture*, **17**, pp. 389-407.

Tvergaard, V. (1982), On localization in ductile materials containing spherical voids, *International Journal of Fracture*, **18**, pp. 237-252.

Tvergaard, V. (1987), Effect of yield surface curvature and void nucleation on plastic flow localization, *Journal of the Mechanics and Physics of Solids*, **35**, pp. 43-60.

Tvergaard, V. (1990), Material failure by void growth to coalescence, *Advances in Applied Mechanics*, **27**, pp. 83-151.

Tvergaard, V. (1996), Effect of void size difference on growth and cavitation instability, *Journal of the Mechanics and Physics of Solids*, **44**, pp. 1237-1253.

Tvergaard, V. and Needleman, A. (1984), Analysis of the cup-cone fracture in a round tensile bar, *Acta Metallurgica*, **32**, pp.157-169.

Tvergaard, V. and Needleman, A. (1995), Effects of nonlocal damage in porous plastic solids, *International Journal of Solid Structures*, **32**, pp. 1063-1077.

Van Stone, R.H., Cox, T.B., Low, J.R.Jr., and Psioda, J.A. (1985), Microstructural aspects of fracture by dimpled fracture, *International Metals Reviews*, **30**, pp. 157-179.

Watt, D.F. and Xu, X.Q. (1996), A finite element analysis of plastic relaxation and plastic accumulation at second phase particles, *Acta Materialia*, **44**, pp. 801-811.

Wicksell, S.D. (1925), The corpuscle problem: A mathematical study of a biometric problem, *Biometrica*, **17**, pp. 84-99.

Wicksell, S.D. (1926), The corpuscle problem: Second memoir: Case of ellipsoid corpuscles, *Biometrica*, **18**, pp. 151-172.

Worswick, M.J., Plikey, A.K., Thomson, C.I.A., Lloyd, D.J., and Burger, G. (1998), Percolation damage predictions based on measured second phase particle distributions, *Microstructural Science*, **26**, pp. 507-514.

Worswick, M.J., Pilkey, A.K., and Lalbin, X. (2000), Introduction of material length scale through damage percolation modelling, *Proceedings of the 2000 International Conference on Fundamental Issues and Applications of Shock-Wave and High-Strain-Rate Phenomena*, Albuquerque, New Mexico.

Worswick, M. J., and Finn, M.J. (2000), The numerical simulation of stretch flange forming, *International Journal of Plastisity,* **16**, pp. 701-720.

Worswick, M.J., Chen, Z.T., Pilkey, A.K., Lloyd, D.J., and Court, S. (2001), Damage characterization and damage percolation modeling in aluminum alloy sheet, *Acta Materialia,* **49**, pp. 2791-2803.

Wray, P.J., Richmond, O., and Morrison, H.L. (1983), Use of the dirichlet tessellation for characterizing and modelling nonregular dispersions and second-phase particles, *Metallography*, **18**, pp. 39-58.

Yamamoto, H. (1978), Conditions for shear localization in the ductile fracture of void-containing materials, *International Journal of Fracture*, **14**, pp. 347-365.

Appendix A

Second Phase Particle Field Reconstruction Method Sensitivity Analysis

There are three primary parameters that are set manually by the researcher and, therefore, are biased. These are the three grey-scale thresholds used to separate second phase particles and voids from the matrix. To show the effect of the threshold choice, a sensitivity analysis (SA) has been undertaken.

Ideally, a Monte Carlo simulation method could be used to establish the relationship between uncertainties in the input and output of the studied model. A thorough SA can be rather computationally expensive to run large numbers of model evaluations. At the same time, simple sensitivity analyses that rely on derivatives with regard to a model parameter fail to account for the effects of all other changing parameters. Therefore, a SA method is needed that is computationally inexpensive (requires small number of model evaluations) and global. A local method, as opposed to

global, examines model output variations with one varying parameter and all the other parameters being kept constant at their nominal values. Following the recommendations for the choice of sensitivity analysis provided by Saltelli *et al.* (2004), the method proposed by Morris (1991) has been utilized. The method of Morris is qualitative in principal when used with small sample size, but it gives an idea of how much a parameter influences the output of a model. The choice of qualitative versus quantitative method is defined by the second phase particle field reconstruction model's computational cost. The method of Morris requires fewer model evaluations than variance-based methods, but there are similarities in result interpretation.

The method examines so-called elementary effects of input parameters on the output using incremental ratios of the change in the output to the change in the input:

$$d_i = \frac{y(x_1,...,x_{i-1},x_i+\Delta,x_{i+1},...,x_k) - y(x_1,x_2,...,x_k)}{\Delta} \tag{A.1}$$

where Δ is the predetermined change in the parameter scaled to take discrete values between 0 to 1.

One parameter is varied at a time. Each parameter takes a discrete number of values within the parameter range of variation. Two sensitivity measures are used for each parameter: the mean (μ) and standard deviation (σ) of the distribution of elementary effects of a parameter on the output.

$$\mu = \sum_{i=1}^{r} \frac{d_i}{r}, \qquad \sigma = \sqrt{\sum_{i=1}^{r} \frac{(d_i-\mu)^2}{r}} \tag{A.2}$$

where r is the number of elementary effects.

The first measure estimates the overall effect of the parameter on the output; whereas, the second estimates higher-order effects in which the parameter is involved. Even though the method relies on the elementary effects, which use the incremental ratios that are local in nature, the final measures are calculated by averaging several elementary effects at different points of the input space. Thus, the method can be considered global. Full details of the method can be found in the work of Morris (1991).

A deviation of 6 shades of grey from the threshold values used in the previous chapter has been chosen as a reasonable visual uncertainty affecting the inter-phase boundaries. The total change in the thresholds was therefore 12 shades of grey. The three thresholds studied were: void/Mg_2Si particle (T_1=36±6), Mg_2Si particle/matrix (T_2=85±6), and *Fe*-rich particle/matrix (T_3=185±6) thresholds. It should be noted that the first threshold affects the sizes of voids and Mg_2Si particles at the same time.

The threshold values were assigned discrete values: T_1=(30, 34, 38, 42); T_2=(79, 83, 87, 91), and T_3= (179, 183, 187, 191). The following parameters obtained by scaling the threshold values were used in the SA: t_i = (0, 0.3333, 0.6667, 1) (i=1, 2, 3). A series of 40 second phase particle field reconstruction simulation (tests) was performed using a test matrix (Table A.1) developed with the method of Morris. The total number of 6 material volumes of 200x200x200μm was constructed for each test case (0.048mm^3 total volume). The variation in the results of the simulation was characterized based on the ellipsoid axes of the three types of objects: voids, Mg_2Si particles, and *Fe*-rich particles. Measures characterizing the output axis size distributions, means (M) and standard deviations (Σ) (not to be confused with those of the elementary effects), were calculated for each simulation. The measures of the elementary effect distributions were established based on the entire population of all 40 sets of ellipsoid axis distribution means (M) and standard deviations (Σ).

Table A.1: Test matrix of the method of Morris.

Test #	T_1	T_2	T_3	Test #	T_1	T_2	T_3
0	42	87	187	20	30	83	187
1	42	87	183	21	34	83	187
2	42	83	183	22	34	83	191
3	38	83	183	23	34	79	191
4	38	83	183	24	42	91	183
5	34	83	183	25	38	91	183
6	34	83	187	26	38	91	179
7	34	87	187	27	38	87	179
8	38	87	183	28	38	79	187
9	42	87	183	29	38	83	187
10	42	83	183	30	38	83	183
11	42	83	187	31	42	83	183
12	38	83	183	32	34	83	191
13	42	83	183	33	34	87	191
14	42	87	183	34	34	87	187
15	42	87	179	35	30	87	187
16	34	87	179	36	30	79	183
17	38	87	179	37	34	79	183
18	38	87	183	38	34	83	183
19	38	91	183	39	34	83	179

Table A.2: Mean (M^0) and standard deviation (Σ^0) of nominal ellipsoid axis distribution mean (M) and standard deviation (Σ).

	Fe-rich			Voids			Mg_2Si		
	X	Y	Z	X	Y	Z	X	Y	Z
$M^0(M)$	2.7635	1.8968	2.3835	2.8915	1.9326	2.7178	2.8959	1.7473	2.3840
$\Sigma^0(M)$	0.0167	0.0063	0.0130	0.0249	0.0074	0.0160	0.0188	0.0041	0.0144
$M^0(\Sigma)$	1.2136	0.4951	0.8068	1.4942	0.4300	1.1324	1.2867	0.3792	1.1191
$\Sigma^0(\Sigma)$	0.0283	0.0078	0.0225	0.0480	0.0050	0.0436	0.0234	0.0068	0.0739

To provide an estimate of variation in the output, a series of 40 particle field reconstruction simulations was conducted using the threshold nominal values (T_1=36, T_2=85, T_3=185) and output axis size distribution characteristics' (M, Σ) means (M^0) and standard deviations (Σ^0) were calculated (Table A.2). Assuming that each reconstruction result in the Morris method has similar variation in the predictions, the standard deviation of the elementary effects d_i on output j can be estimated (Table A.3):

$$\sigma_d^j = \frac{\sqrt{2}}{\Delta}\Sigma_j^0 \tag{A.3}$$

Table A.3: Standard deviations of the elementary effects of ellipsoid axis mean (M) and standard deviation (Σ).

σ_d	*Fe*-rich			Voids			Mg_2Si		
	d^X	d^Y	d^Z	d^X	d^Y	d^Z	d^X	d^Y	d^Z
M	0.0707	0.0268	0.0553	0.1058	0.0312	0.0678	0.0797	0.0175	0.0613
Σ	0.1199	0.0333	0.0955	0.2035	0.0214	0.1851	0.0992	0.0287	0.3135

The results of the method of Morris are presented in Figures A.1 – A.6. Each of the 6 figures shows the effect of the input parameters on measures M and Σ of the three types of objects (*Fe*-rich particles, voids, and Mg_2Si particles). Each figure contains a set of 9 points corresponding to pairs of measures μ and σ of the effects of the input parameters t_1, t_2, and t_3 on each ellipsoid axis (X, Y, and Z). For example, the point on the top of Figure A.1 marked "Z" represents the effect of the first input parameter t_1 on the *Fe*-rich particle ellipsoid Z-axis distribution mean (M). Larger point marks denote the

ellipsoid dimensions directly affected by the change in the corresponding input parameter. For instance, the same point on the top has a small point mark because all the three axes of Fe-rich particles are not affected by the change in parameter t_1, which is the threshold separating voids from *Mg_2Si* particles. Vertical lines in the figures are the confidence limits ($\pm 2\sigma_d^j$) for measures μ to show the magnitude of the effect of an input parameter on an output compared to its uncertainty.

While interpreting the SA results presented in Figures A.1 – A.6, most attention has been paid to the spread of measures μ since they indicate overall influence of the input parameters on the model output. The first two figures (Figures A.1 and A.2) show the SA results for the *Fe*-rich particle ellipsoid reconstruction. In this case, no significant deviation from 0 can be observed. This can be explained by the fact that the lower values of the threshold T_3 change the number of dispersoids included in the *Fe*-rich particle population. It has little effect of the population size distribution. The dispersoids do not affect the final axis distributions since particles of very small volume ($2\mu m^3$) are filtered before the particle field data is used in the reconstruction procedure. The results of void ellipsoid reconstruction (Figures A.3 and A.4) indicate that one ellipsoid axis (X) is affected significantly by the change in the parameter t_1 corresponding to the threshold T_1. Both ellipsoid X-axis distribution characteristics M and Σ are affected by T_1. The total change (on average) in these characteristics over the entire range of change in T_1 can be roughly estimated as 11.6% (μ_M/M^0) and 37.9% (μ_Σ/Σ^0). All the other measures μ remain within their confidence intervals showing little dependence on their respective parameters. In the case of *Mg_2Si* particle results (Figures A.5 and A.6), the effect of the parameter t_2 on the Y-axis distribution mean (M) lies outside its confidence interval. Its overall change is 2.8% (μ_M/M^0).

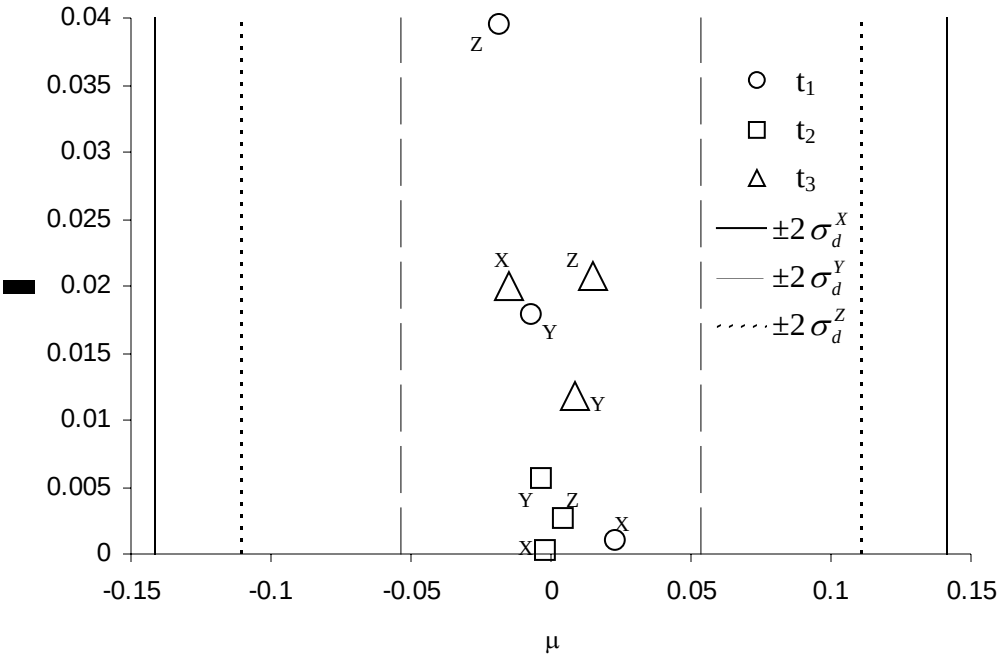

Figure A.1: Sensitivity measures μ and σ for mean (M) of *Fe*-rich particle ellipsoid axes.

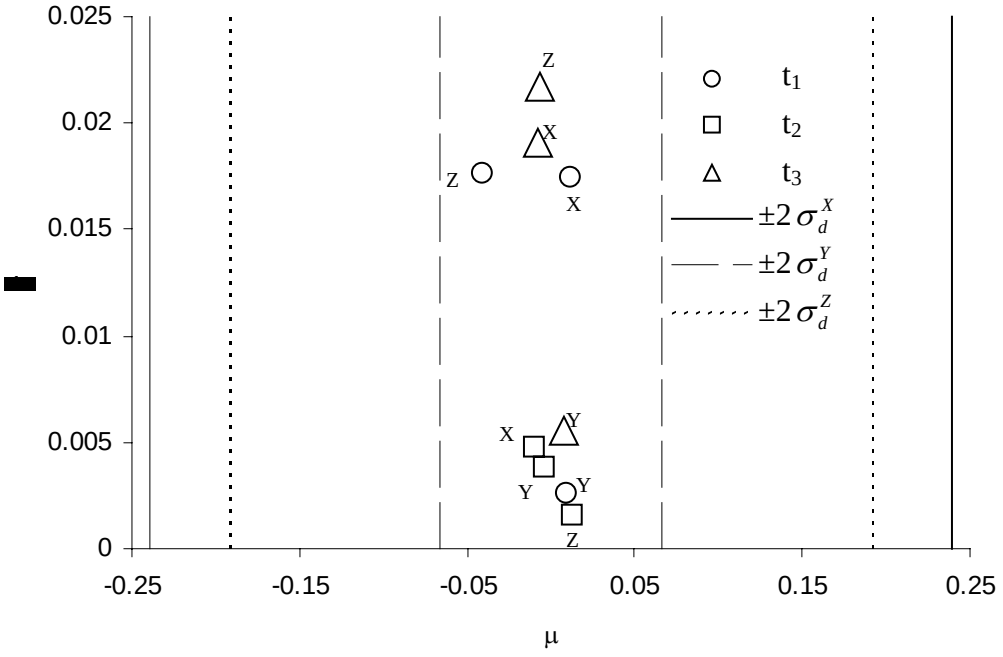

Figure A.2: Sensitivity measures μ and σ for standard deviation (Σ) of *Fe*-rich particle ellipsoid axes.

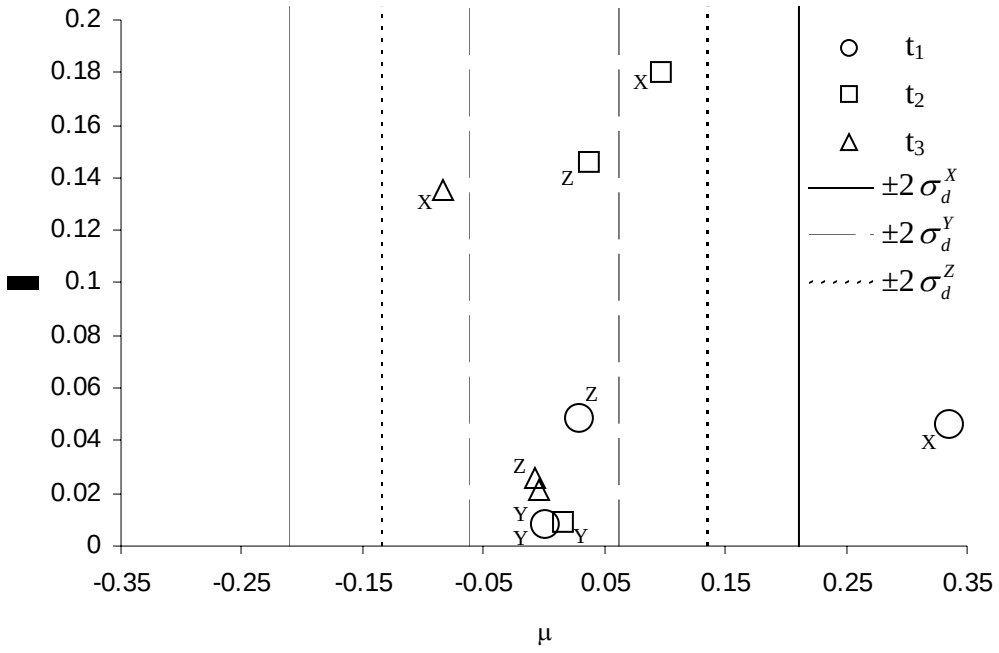

Figure A.3: Sensitivity measures μ and σ for mean (M) of void ellipsoid axes.

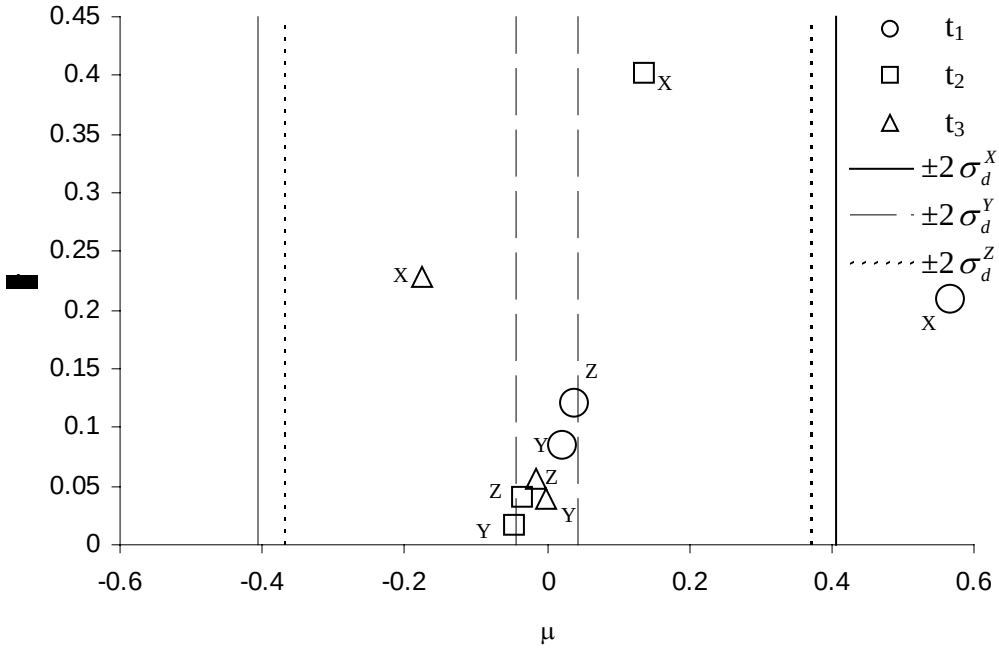

Figure A.4: Sensitivity measures μ and σ for standard deviation (Σ) of void ellipsoid axes.

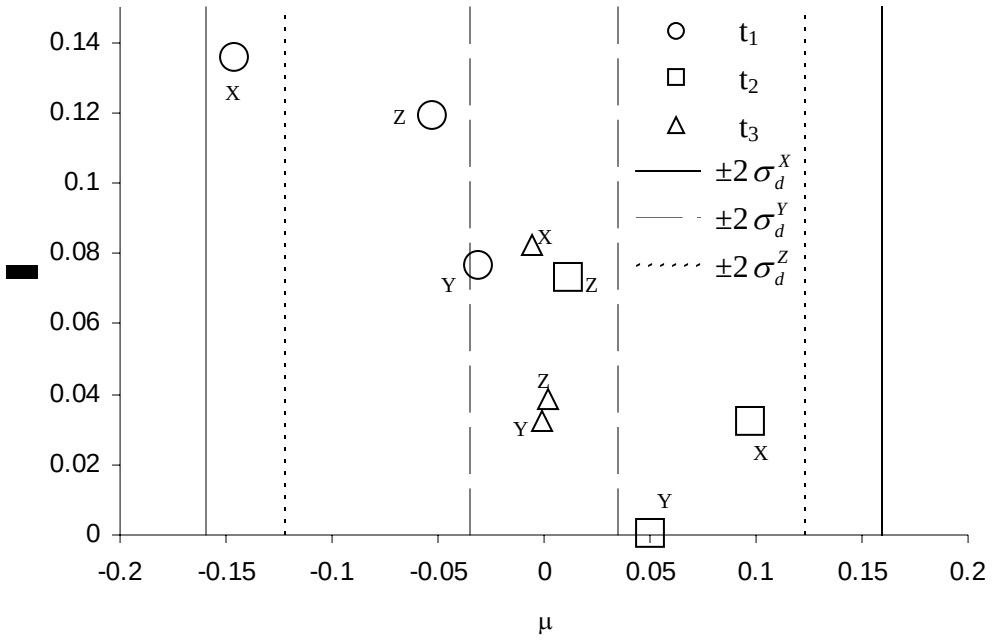

Figure A.5: Sensitivity measures μ and σ for mean (M) of *Mg_2Si* particle ellipsoid axes.

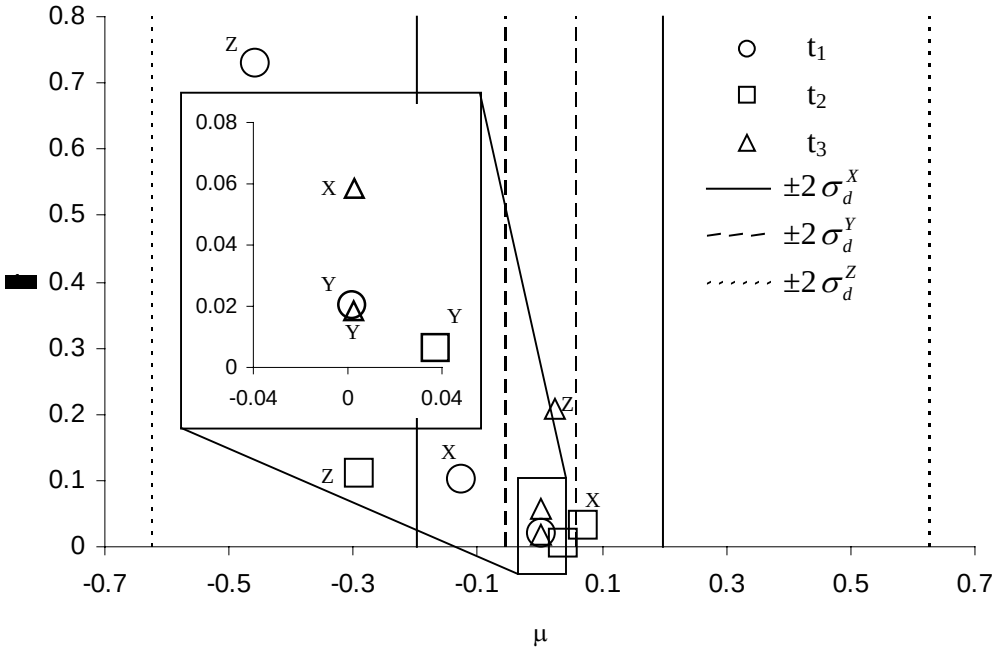

Figure A.6: Sensitivity measures μ and σ for standard deviation (Σ) of *Mg_2Si* particle ellipsoid axes.

The overall behaviour of the model can be summarized as follows. The deviation in the thresholds does not affect dramatically most of the output ellipsoid axis distributions. Their characteristics, mean M and standard deviation Σ, lie within their confidence intervals defined by the reconstruction model prediction scatter at the chosen particle field volume scale. The threshold T_1 has the highest influence on the output particle/void fields as it affects significantly void ellipsoid X-axis distribution. This leads to the change in material porosity, a critical parameter in many material damage models. It should be noted that the actual porosity is a very small quantity for this material; hence, this level of sensitivity is not surprising. The effect of change in the threshold T_2 is noticeable in Mg_2Si particle ellipsoid Y-axis distribution, but is not as severe.

Appendix B

Three-Dimensional Damage Percolation Model Sensitivity Analysis

Various parameters of the DPM input were studied to estimate their effect on the predictions of the DPM. Among the sources of uncertainty, the following parts of a DPM simulation were considered: the input second phase particle field, finite element model, and DPM criteria. The sensitive parameters in the case of second phase particle field acquisition were the thresholds T_1 and T_2, as it was discussed in Chapter 2. Both parameters were included in the sensitivity analysis (SA). The finite element model parameters considered were the number of through-thickness elements and DPM elongation step. The cross sections of the studied specimen meshes are square with equal numbers of elements per edge. The former parameter (elongation step) was chosen since it was responsible for better capture of the non-uniform strain gradient at the final deformation stage. The latter parameter (number of through-thickness elements) defined

the accuracy of the prediction of the onset of final fracture since the results of void coalescence are monitored only at the end of each elongation step. Finer elongation steps allow more accurate determination of abrupt catastrophic macro crack propagation. Finally, the DPM includes criteria governing void nucleation, growth, and coalescence. Among these three criteria, the void nucleation criterion accounting for particle clustering was thought to have the highest impact on the process of material damage initiation and evolution. Its effect was included in the SA by considering nucleation criteria with various numbers of IPD discretization.

The five parameters considered in the SA were the threshold T_1 and T_2, number of through thickness elements, elongation step, and nucleation criterion modification with respect to the number of IPD classes. The method of Morris (1991) was employed to perform the five-parameter SA of the relatively computationally expensive DPM. The parameters were assigned four different values that are relevant to the type of considered DPM simulation. The threshold values were taken from the second phase particle field reconstruction method SA described in Chapter 2. These were T_1=(30, 34, 38, 42) and T_2=(79, 83, 87, 91). The number of through-thickness elements took the values of 5, 10, 15, and 20 (Figures B.1 and B.2). The elongation step ranged from 0.00067 to 0.001675 mm with the step of 0.000335 mm (the total elongation was 0.81mm). The considered void nucleation criteria had the following numbers of IPD classes: 1, 17, 33, and 49 (Figures 3.36 – 3.39).

A test matrix for the SA was created according to the method of Morris (Table 3.4). For each test case, a tomographic image of the undeformed AA5182 alloy was thresholded with the corresponding T_1 and T_2 (T_3=185) and used in a DPM simulation utilizing one of the four element meshes (Figures B.1 and B.2) and nucleation criteria (Figures B.3 – B.6). The results of the simulations can also be found in Table B.1 in the

form of plastic strain at the onset of final fracture. This moment was defined by the beginning of abrupt inter-cluster void-crack coalescence.

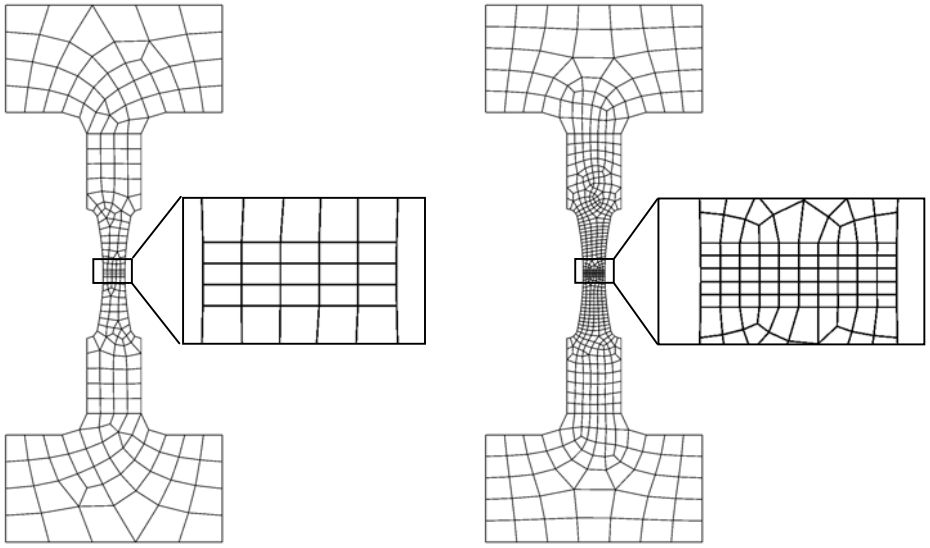

(a) (b)

Figure B.1: Finite element meshes with 5 (a) and 10 (b) through-thickness elements.

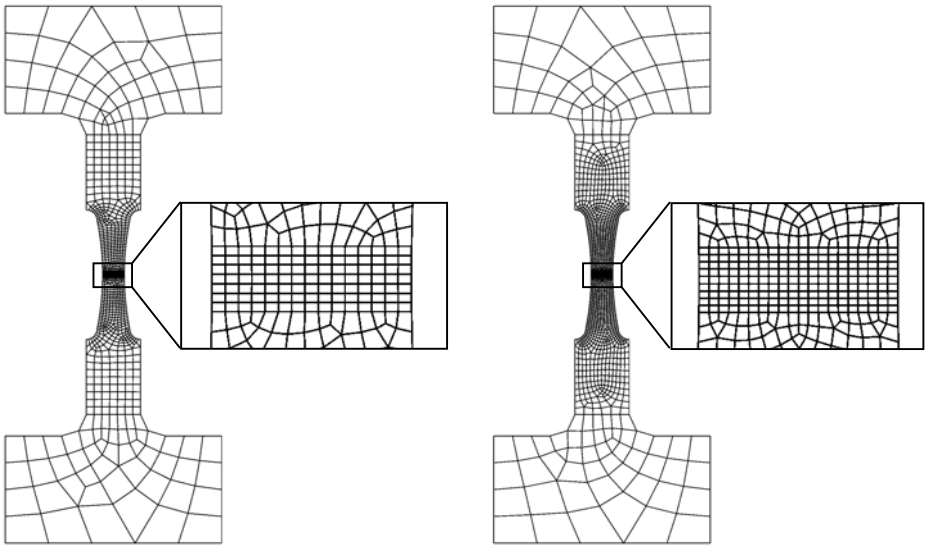

(a) (b)

Figure B.2: Finite element meshes with 15 (a) and 20 (b) through-thickness elements.

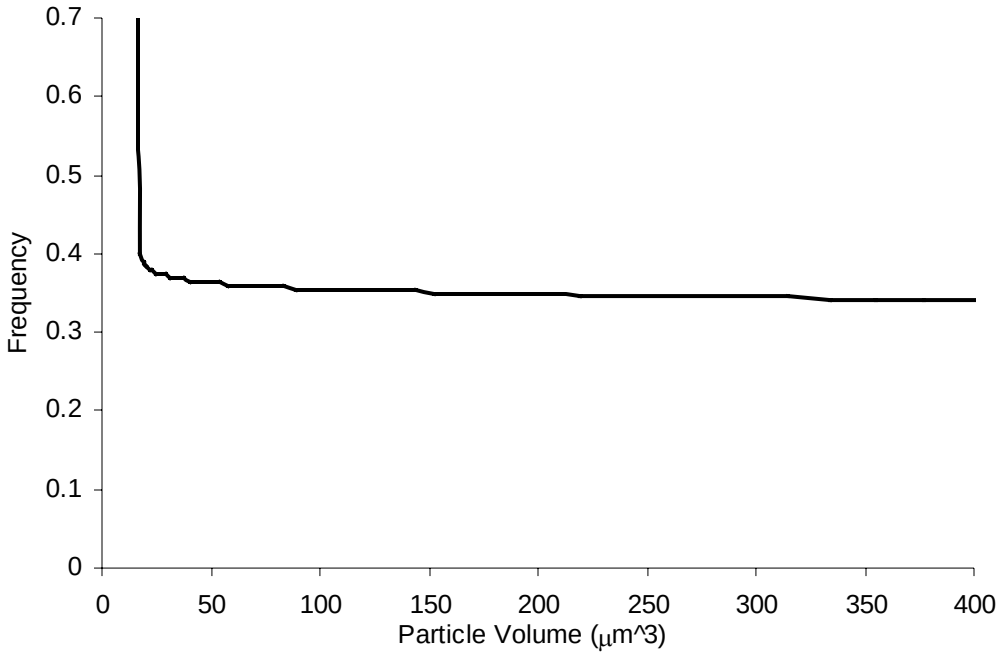

Figure B.3: Nucleation criterion (1 IPD class, T_1=42, T_2=91).

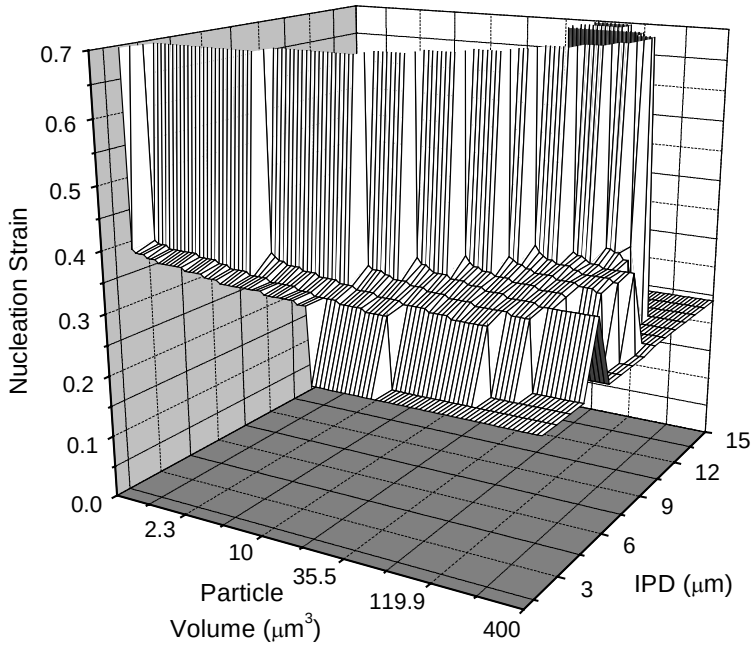

Figure B.4: Nucleation criterion (17 IPD classes, T_1=42, T_2=91).

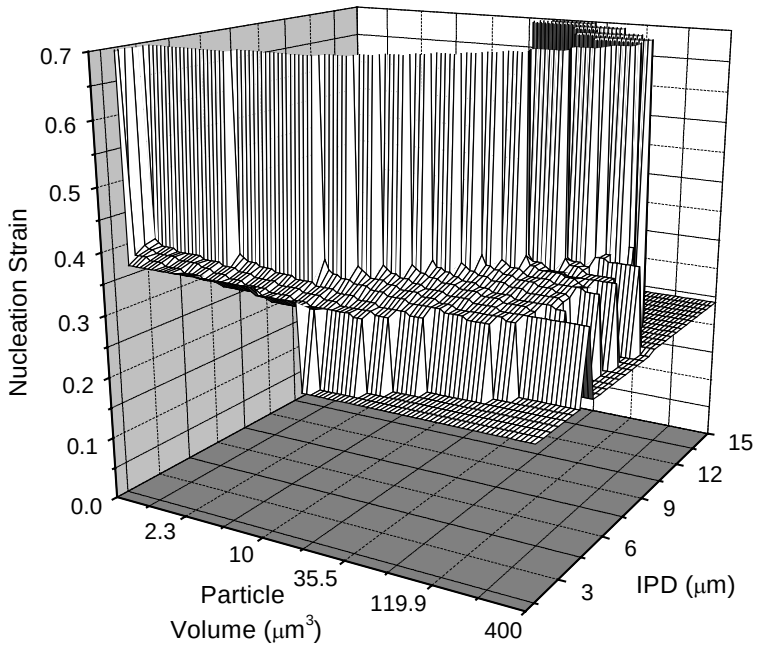

Figure B.5: Nucleation criterion (33 IPD classes, T_1=42, T_2=91).

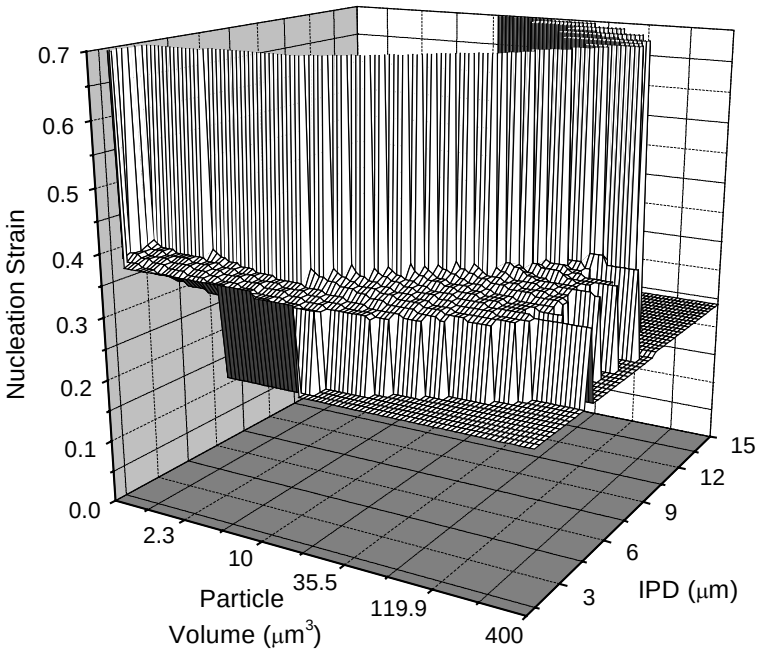

Figure B.6: Nucleation criterion (49 IPD classes, T_1=42, T_2=91).

Table B.1: DPM sensitivity analysis test matrix and results.

Test	T_1	T_2	Mesh	Elongation Step (mm)	Nucl. Criterion	Failure Strain
0	38	83	20	0.001675	17	0.384989
1	38	83	20	0.00134	17	0.381135
2	38	87	20	0.00134	17	0.381135
3	42	87	20	0.00134	17	0.381135
4	42	87	20	0.00134	33	0.381135
5	42	87	15	0.00134	33	0.383482
6	34	79	15	0.001005	17	0.386758
7	34	79	15	0.001005	1	0.386758
8	34	83	15	0.001005	1	0.386758
9	34	83	15	0.00134	1	0.383482
10	34	83	10	0.00134	1	0.405802
11	30	83	10	0.00134	1	0.405802
12	30	83	10	0.001675	49	0.419262
13	30	83	5	0.001675	49	0.382600
14	30	79	5	0.001675	49	0.382600
15	34	79	5	0.001675	49	0.382600
16	34	79	5	0.00134	49	0.398533
17	34	79	5	0.00134	33	0.400303
18	34	83	5	0.001675	17	0.350913
19	30	83	5	0.001675	17	0.350913
20	30	83	10	0.001675	17	0.416572
21	30	87	10	0.001675	17	0.416572
22	30	87	10	0.001675	33	0.424708
23	30	87	10	0.00134	33	0.420878
24	34	83	10	0.001005	33	0.401360
25	30	83	10	0.001005	33	0.401360
26	30	87	10	0.001005	33	0.401360
27	30	87	5	0.001005	33	0.383196
28	30	87	5	0.00134	33	0.386341
29	30	87	5	0.00134	17	0.358760

Table B.1 (Continued): DPM sensitivity analysis test matrix and results.

Test	T_1	T_2	Mesh	Elongation Step (mm)	Nucl. Criterion	Failure Strain
30	38	87	10	0.00067	49	0.382401
31	38	87	5	0.00067	49	0.372332
32	38	87	5	0.00067	33	0.365290
33	42	87	5	0.00067	33	0.365290
34	42	87	5	0.001005	33	0.365262
35	42	91	5	0.001005	33	0.365262
36	30	79	10	0.001005	49	0.407711
37	30	79	10	0.001005	33	0.401360
38	34	79	10	0.001005	33	0.401360
39	34	79	10	0.00134	33	0.420878
40	34	79	5	0.00134	33	0.400303
41	34	83	5	0.00134	33	0.400303
42	30	83	5	0.00067	33	0.365290
43	34	83	5	0.00067	33	0.365290
44	34	83	5	0.00067	17	0.379330
45	34	83	5	0.001005	17	0.378050
46	34	79	5	0.001005	17	0.378050
47	34	79	10	0.001005	17	0.410911
48	38	91	15	0.001005	1	0.386758
49	38	91	10	0.001005	1	0.406059
50	38	91	10	0.00067	1	0.383374
51	34	91	10	0.00067	1	0.383374
52	34	91	10	0.00067	17	0.382401
53	34	87	10	0.00067	17	0.382401
54	34	83	15	0.001005	33	0.386758
55	34	83	15	0.001005	17	0.386758
56	34	87	15	0.001005	17	0.386758
57	34	87	10	0.001005	17	0.432105
58	34	87	10	0.00134	17	0.438542
59	38	87	10	0.00134	17	0.438542

The method of Morris examines elementary effects of input parameters on the output using incremental ratios of the change in the output to the change in the input as described in Appendix A.

$$d_i = \frac{y(x_1,...,x_{i-1},x_i+\Delta,x_{i+1},...,x_k) - y(x_1,x_2,...,x_k)}{\Delta} \qquad \text{(B.1)}$$

where Δ is the predetermined change in the parameter scaled to take discrete values between 0 to 1.

The sensitivity measures μ (mean) and σ (standard deviation) were found for each parameter.

$$\mu = \sum_{i=1}^{r} \frac{d_i}{r}, \qquad \sigma = \sqrt{\sum_{i=1}^{r} \frac{(d_i-\mu)^2}{r}} \qquad \text{(B.2)}$$

where *r* is the number of elementary effects.

The results of the method of Morris are presented in Figure B.7. The first observation that can be made is that the thresholds T_1 and T_2 have no effects on the output function (plastic strain at failure). Changes in these parameters affect the size and shape of second phase particles to an extent that does not affect significantly the predicted damage processes (void nucleation, growth, and coalescence). The number of through-thickness elements has the largest effect on plastic strain at failure. However, the sign of the average elementary effect was not expected to be positive. It means that failure should be postponed (plastic strain at fracture increased) as the parameter decreases. A more detailed analysis of the data in Table 3.4 revealed that the positive sign is associated with test cases considering the mesh with 5 through-thickness elements. Eliminating these cases from the calculation brought a consistent result (Figure B.7). This

fact was attributed to the following hypothesis. Finer meshes allow reproduction of the material strain gradient in the considered region with better accuracy and lead to accelerated void nucleation in elements with higher plastic strain. On the other hand, a very coarse mesh, such as that with 5 through-thickness elements, predicts the plastic strain field to be more uniform. In this case, plastic strain peaks in the middle of the specimen are smoothed by averaging with less strained regions while overall strain level in surrounding material increases leading to void nucleation in regions where it is not observed.

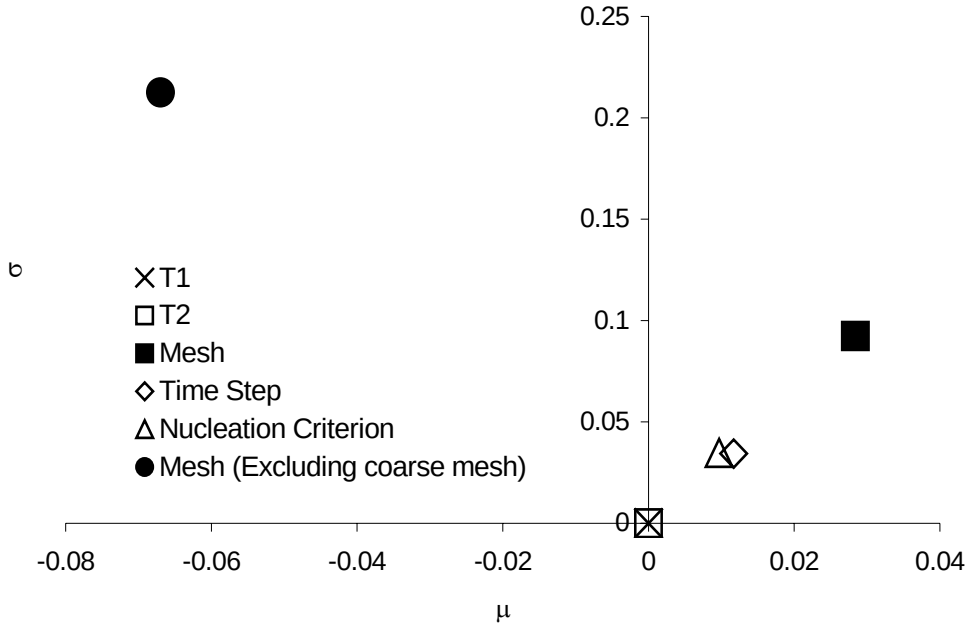

Figure B.7: Results of the DPM sensitivity analysis.

The last two parameters, the elongation step and nucleation criterion type, have moderate effects on the predicted final fracture onset compared to the effect of the number of through-thickness elements. Both of these parameters have positive and negative elementary effects. However, their average effects on model performance can be estimated. The average effect of the elongation step choice introduces a change in failure

plastic strain of 0.0097 (2.5% of 0.394, plastic strain at the last loading stage prior to failure during the *in situ* tensile test) over the range of considered parameter values. The same change due to the nucleation criterion choice is 0.012 (2.96%). The largest effect of the number of through-thickness elements introduces a variation of 0.067 (17%). The case of the 5 through-thickness element mesh is not considered here and it should not be used for simulation.